

**Investigation of Starting and Ignition Transients in the
Thermally Choked Ram Accelerator**

by

Edward A. Burnham, Jr.

A dissertation submitted in partial fulfillment
of the requirements for the degree of

Doctor of Philosophy

University of Washington

1993

Approved by _____
(Chairperson of Supervisory Committee)

Program Authorized
to Offer Degree _____ Aeronautics and Astronautics

Date _____ December 10, 1993

Doctoral Dissertation

In presenting this dissertation in partial fulfillment of the requirements for the Doctoral degree at the University of Washington, I agree that the Library shall make its copies freely available for inspection. I further agree that extensive copying of this dissertation is allowable only for scholarly purposes, consistent with "fair use" as prescribed in the U.S. Copyright Law. Requests for copying or reproduction of this dissertation may be referred to University Microfilms, 1490 Eisenhower Place, P.O. Box 975, Ann Arbor, MI 48106, to whom the author has granted "the right to reproduce and sell (a) copies of the manuscript in microform and/or (b) printed copies of the manuscript made from microform."

Signature _____

Date _____

© Copyright 1993

Edward A. Burnham, Jr.

University of Washington

Abstract

**Investigation of Starting and Ignition Transients in the
Thermally Choked Ram Accelerator**

by Edward A. Burnham, Jr.

Supervisory Committee Chairperson: Professor Abraham Hertzberg
Dept. of Aeronautics and Astronautics

An experimental investigation of the starting transients of the thermally choked ram accelerator is presented in this dissertation. A highly instrumented tube section and instrumentation inserts provide high resolution experimental pressure, luminosity, and electromagnetic data of the starting transients. Detonations are used to estimate induction and reaction times at elevated pressures. Data obtained prior to and following the entrance diaphragm show detailed development of shock systems in both combustible and inert mixtures. With an evacuated launch tube, starting the diffuser is possible at any Mach number above the Kantrowitz Mach number. The detrimental effects and possible solutions of higher launch tube pressures and excessive obturator leakage (blow-by) are discussed. Ignition of a combustible mixture is demonstrated with both perforated and solid obturators. The relative advantages and disadvantages of each are discussed. The source of ignition is identified and discussed. Numerical simulations of various features using Van Leer splitting or Advection Upstream Splitting Method (AUSM) are shown and related to experimental observations. Data obtained from these starting experiments enhance the understanding of the ram accelerator, as well as assist in the validation of unsteady, chemically reacting CFD codes.

Table of Contents

	Page
List of Figures	iii
List of Tables	xi
Nomenclature	xii
I. INTRODUCTION	1
1.1 Experimental Setup	3
1.2 Pressure and Luminosity Sensor Response	6
1.3 Non-Ideal Sensor Response	7
II. DETONATION OF THE COMBUSTIBLE GAS MIXTURE	19
2.1 Spinning Detonation	19
2.2 Obturator Initiation of a Detonation	23
III. THREE DIMENSIONAL EFFECTS	41
3.1 Experimental Three-Dimensional Results	41
3.2 Numerical Three-Dimensional Results	44
IV. THE STARTING PROCESS	52
4.1 Idealized Starting Process	52
4.2 Diffuser Starting	54
4.3 Ignition Transients	60
4.4 Solid Obturator Starting	64
4.5 High Launch Tube Pressure	66
4.6 Obturator Leakage	71
4.7 Buffer Sections	73
4.7 Further Ignition Source Studies	76
4.8 Larger Scale Facilities	79
V. COMPUTATIONAL MODELING	126
5.1 Choice of Methods	126
5.2 Heat Release Model - Induction/Reaction	127
5.3 Governing Equations	129

5.3.1	Van Leer equations and discussion	130
5.3.2	Advection Upwind Splitting Method (AUSM)	133
5.4	Boundary Conditions	135
5.5	Numerical Results	135
5.5.1	Launch tube simulations	135
5.5.2	Induction/Reaction simulations	139
5.5.3	Detonation simulations	141
5.5.4	Ram Accelerator Starting Simulation	144
5.6	Future work	146
VI.	CONCLUSION	163
	REFERENCES	165

List of Figures

	Page
Fig. 1.1 Comparison of a conventional ramjet with the ram accelerator.	10
Fig. 1.2 Operational regimes of the ram accelerator.	11
Fig. 1.3 Ram accelerator facility.	12
Fig. 1.4 Geometry of projectile, obturator, and backplate.	13
Fig. 1.5 Highly instrumented tube section, inserts and tube couplers.	14
Fig. 1.6 Instrument station numbering and distance between stations for the majority of starting experiments.	15
Fig. 1.7 Typical pressure and luminosity data obtained from the thermally choked regime.	16
Fig. 1.8 Pressure sensor response to a normal shock in argon.	17
Fig. 1.9 Luminosity sensor response to the initiation of a detonation.	18
Fig. 2.1 Schematic representation of a spinning detonation.	26
Fig. 2.2 Pressure data from the passage of a spinning detonation in the mixture $2.7\text{CH}_4+2\text{O}_2+5.8\text{N}_2$ at 21 atm and 298 K.	27
Fig. 2.3 Pressure data from Fig. 2.2 on longer time scale.	28
Fig. 2.4 Three-dimensional representation of the pressure data of Fig. 2.2.	29
Fig. 2.5 Lead and secondary shock locations of the data in Fig. 2.2.	30
Fig. 2.6 First two sets of pressure data from the passage of a spinning detonation in the mixture $2.7\text{CH}_4+2\text{O}_2+5.8\text{N}_2$ at 21 atm.	31
Fig. 2.7 Two sets of luminosity data from the passage of the spinning detonation shown in Fig. 2.6.	32
Fig. 2.8 Second two sets of pressure data from the passage of the spinning detonation shown in Fig. 2.6.	33

Fig. 2.9	Shock and luminosity locations of the data shown in Figs. 2.6 -2.8.	34
Fig. 2.10	First two sets of pressure data from the passage of a spinning detonation in a 21 atm mixture of $2.7\text{CH}_4+2\text{O}_2+5.8\text{N}_2$.	35
Fig. 2.11	Two sets of luminosity data from the passage of the spinning detonation shown in Fig. 2.10.	36
Fig. 2.12	Second two sets of pressure data from the passage of the spinning detonation shown in Fig. 2.10.	37
Fig. 2.13	Shock and luminosity locations of the data shown in Figs. 2.10 - 2.12.	38
Fig. 2.14	Pressure data from the initiation of a detonation with an obturator in a 24 atm mixture of $2.7\text{CH}_4+2\text{O}_2+5.8\text{N}_2$.	39
Fig. 2.15	Luminosity data from the same experiment as shown in Fig. 2.14.	40
Fig. 3.1	Experimental pressure and luminosity data from a channel and from over a fin for a projectile traveling 1540 m/s.	46
Fig. 3.2	Pressure data from an experiment where the projectile was traveling 1440 m/s.	47
Fig. 3.3	Three-dimensional representation of the pressure data of Fig. 3.2.	48
Fig. 3.4	Comparison of experimental pressure data from Fig. 3.2 with axisymmetric and 3-dimensional CFD calculations.	49
Fig. 3.5	Three-dimensional representation of the tube wall pressure obtained from a non-reacting, 3-dimensional CFD simulation.	50
Fig. 3.6	Representation of the pressure on the projectile surface obtained from a non-reacting, 3-dimensional CFD simulation.	51
Fig. 4.1	Schematic of the idealized starting process.	80

Fig. 4.2	Schematic of the measured starting process.	81
Fig. 4.3	Tube wall pressure traces from the launch tube for a projectile traveling 1170 m/s in a mixture of $2.7\text{CH}_4+7.8\text{N}_2$.	82
Fig. 4.4	Tube wall pressure traces from the accelerator section for a projectile traveling 1170 m/s in a mixture of $2.7\text{CH}_4+7.8\text{N}_2$.	83
Fig. 4.5	Tube wall pressure traces from farther down the accelerator section for the experiment shown in Figs. 4.3 and 4.4.	84
Fig. 4.6	Comparison of tube wall pressure and luminosity data from station 3 in the launch tube for the experiment shown in Fig. 4.3.	85
Fig. 4.7	Distance-time (x-t) diagram of the experimental data shown in Figs. 4.3 and 4.4.	86
Fig. 4.8	Tube wall pressure traces from the launch tube for a projectile traveling 955 m/s in a mixture of $2.7\text{CH}_4+7.8\text{N}_2$.	87
Fig. 4.9	Tube wall pressure traces from the accelerator section for a projectile traveling 955 m/s in a mixture of $2.7\text{CH}_4+7.8\text{N}_2$.	88
Fig. 4.10	Tube wall pressure traces from farther down the accelerator section for the experiment shown in Figs. 4.8 and 4.9.	89
Fig. 4.11	Tube wall pressure traces from the launch tube for a projectile traveling 910 m/s in a mixture of $2.7\text{CH}_4+7.8\text{N}_2$.	90
Fig. 4.12	Tube wall pressure traces from the accelerator section for a projectile traveling 910 m/s in a mixture of $2.7\text{CH}_4+7.8\text{N}_2$.	91
Fig. 4.13	Tube wall pressure traces from farther down the accelerator section for the experiment shown in Figs. 4.11 and 4.13.	92
Fig. 4.14	Instrumentation station numbering for Figs 4.15 - 4.18.	93
Fig. 4.15	Tube wall pressure traces from the launch tube for a projectile traveling 1160 m/s in a mixture of $2.7\text{CH}_4+2\text{O}_2+5.8\text{N}_2$.	94
Fig. 4.16	Luminosity data from the launch tube for the experiment shown in Fig. 4.15.	95

Fig. 4.17	Tube wall pressure traces from the accelerator section for a projectile traveling 1160 m/s in a mixture of $2.7\text{CH}_4+2\text{O}_2+5.8\text{N}_2$.	96
Fig. 4.18	Luminosity data from the accelerator section for the experiment shown in Fig. 4.17.	97
Fig. 4.19	Tube wall pressure traces from the launch tube for a projectile traveling 1190 m/s in a mixture of $2.7\text{CH}_4+2\text{O}_2+5.8\text{N}_2$ with a solid obturator.	98
Fig. 4.20	Tube wall pressure traces from the accelerator section for a projectile traveling 1190 m/s in a mixture of $2.7\text{CH}_4+2\text{O}_2+5.8\text{N}_2$ with a solid obturator.	99
Fig. 4.21	Tube wall pressure traces from farther down the accelerator section for the experiment shown in Figs. 4.19 and 4.20.	100
Fig. 4.22	Comparison of tube wall pressure and luminosity data for the experiment shown in Figs. 4.19 and 4.20.	101
Fig. 4.23	Tube wall pressure traces from the launch tube for a projectile traveling 1180 m/s in a mixture of $2.7\text{CH}_4+2\text{O}_2+5.8\text{N}_2$ with 1.0 psi of air in the launch tube and five 0.014" mylar diaphragms.	102
Fig. 4.24	Tube wall pressure traces from the accelerator section for a projectile traveling 1180 m/s in a mixture of $2.7\text{CH}_4+2\text{O}_2+5.8\text{N}_2$ with 1.0 psi of air in the launch tube and five 0.014" mylar diaphragms.	103
Fig. 4.25	Tube wall pressure traces from farther down the accelerator section for the experiment shown in Figs. 4.23 and 4.24.	104
Fig. 4.26	Comparison of tube wall pressure and luminosity data for the experiment shown in Figs. 4.23 and 4.24.	105
Fig. 4.27	Distance-time (x-t) diagram of the experimental data shown in Figs. 4.23 and 4.24.	106

Fig. 4.28	Tube wall pressure traces from the launch tube for a projectile traveling 1140 m/s in a mixture of $2.7\text{CH}_4+2\text{O}_2+5.8\text{N}_2$ with 1.0 psi of air in the launch tube and two 0.014" mylar diaphragms.	107
Fig. 4.29	Tube wall pressure traces from the accelerator section for a projectile traveling 1140 m/s in a mixture of $2.7\text{CH}_4+2\text{O}_2+5.8\text{N}_2$ with 1.0 psi of air in the launch tube and two 0.014" mylar diaphragms.	108
Fig. 4.30	Tube wall pressure traces from farther down the accelerator section for the experiment shown in Figs. 4.28 and 4.29.	109
Fig. 4.31	Tube wall pressure traces from the launch tube for a projectile traveling 1100 m/s in a mixture of $2.7\text{CH}_4+2\text{O}_2+5.8\text{N}_2$ with obturator leakage (5%) and 0.1 psi of air in the launch tube and five 0.014" mylar diaphragms.	110
Fig. 4.32	Tube wall pressure traces from the accelerator section for a projectile traveling 1100 m/s in a mixture of $2.7\text{CH}_4+2\text{O}_2+5.8\text{N}_2$ with obturator leakage (5%) and 1.0 psi of air in the launch tube and five 0.014" mylar diaphragms.	111
Fig. 4.33	Tube wall pressure traces from farther down the accelerator section for the experiment shown in Figs. 4.31 and 4.32.	112
Fig. 4.34	Instrumentation station numbering and diaphragm location for Figs. 4.35 - 4.40.	113
Fig. 4.35	Tube wall pressure traces from the launch tube for a projectile traveling 1150 m/s in a mixture of $2.7\text{CH}_4+2\text{O}_2+5.8\text{N}_2$ with a buffer section filled with a mixture of $2.7\text{CH}_4+2\text{O}_2+5.8\text{N}_2$.	114
Fig. 4.36	Tube wall pressure traces from the accelerator section for a projectile traveling 1150 m/s in a mixture of	115

- 2.7CH₄+2O₂+5.8N₂ with a buffer section filled with a mixture of 2.7CH₄+2O₂+5.8N₂.
- Fig. 4.37 Tube wall pressure traces from farther down the accelerator section for the experiment shown in Figs. 4.35 and 4.36. 116
- Fig. 4.38 Tube wall pressure traces from the launch tube for a projectile traveling 1150 m/s in a mixture of 2.7CH₄+2O₂+5.8N₂ with a buffer section filled with a mixture of 2.7CH₄+7.8N₂. 117
- Fig. 4.39 Tube wall pressure traces from the accelerator section for a projectile traveling 1150 m/s in a mixture of 2.7CH₄+2O₂+5.8N₂ with a buffer section filled with a mixture of 2.7CH₄+7.8N₂. 118
- Fig. 4.40 Tube wall pressure traces from farther down the accelerator section for the experiment shown in Figs. 4.38 and 4.39. 119
- Fig. 4.41 Tube wall pressure traces from the launch tube for a projectile traveling 1190 m/s in a mixture of 2.7CH₄+2O₂+5.8N₂ with 0.01 psi of air in the launch tube and a solid non-leaking obturator. 120
- Fig. 4.42 Tube wall pressure traces from the accelerator section for a projectile traveling 1190 m/s in a mixture of 2.7CH₄+2O₂+5.8N₂ with 0.01 psi of air in the launch tube and a solid non-leaking obturator. 121
- Fig. 4.43 Tube wall pressure traces from farther down the accelerator section for the experiment shown in Figs. 4.41 and 4.42. 122
- Fig. 4.44 Tube wall pressure traces from the launch tube for a projectile traveling 1170 m/s in a mixture of 2.7CH₄+2O₂+5.8N₂ with 0.01 psi of air in the launch tube and a solid non-leaking obturator. 123
- Fig. 4.45 Tube wall pressure traces from the accelerator section for a projectile traveling 1170 m/s in a mixture of 124

	2.7CH ₄ +2O ₂ +5.8N ₂ with 0.01 psi of air in the launch tube and a solid non-leaking obturator.	
Fig. 4.46	Tube wall pressure traces from farther down the accelerator section for the experiment shown in Figs. 4.41 and 4.42.	125
Fig. 5.1	Induction and reaction times for various initial pressures and temperatures.	148
Fig. 5.2	Simulated launch tube pressure contours of a solid obturator accelerated to 1170 m/s in 0.1 psi air.	149
Fig. 5.3	View close to the entrance diaphragm of the simulation shown in Fig. 5.2	150
Fig. 5.4	Simulated launch tube pressure contours of a solid obturator and projectile accelerated to 1170 m/s in 0.1 psi air.	151
Fig. 5.5	Simulated launch tube pressure contours of a solid obturator and projectile accelerated to 1170 m/s in 0.1 psi air with a 1/1000 obturator area helium leak.	152
Fig. 5.6	Temperature contours from the same simulation shown in Fig 5.5.	153
Fig. 5.7	Simulated launch tube pressure contours of a solid obturator and projectile accelerated to 1170 m/s in 1.0 psi air with a 1/1000 obturator area helium leak.	154
Fig. 5.8	Simulated density contours of a 38 mm diameter sphere/cylinder body traveling Mach 6.0 in a 10 atm mixture of 2.7CH ₄ +2O ₂ +5.8N ₂ .	155
Fig. 5.9	Simulated density contours of a 38 mm diameter sphere/cylinder body traveling Mach 5.0 in a 10 atm mixture of 2.7CH ₄ +2O ₂ +5.8N ₂ .	156
Fig. 5.10	Simulated time evolution of the centerline density contours of a 38 mm diameter sphere/cylinder body traveling Mach 5.0 in a 10 atm mixture of 2.7CH ₄ +2O ₂ +5.8N ₂ .	157

Fig. 5.11	Simulated impact of a 35 gm solid obturator traveling 1250 m/s with a 23 atm stationary mixture of $2.7\text{CH}_4+2\text{O}_2+5.8\text{N}_2$.	158
Fig. 5.12	Simulated impact of a 13 gm solid obturator traveling 1125 m/s with a 23 atm stationary mixture of $2.7\text{CH}_4+2\text{O}_2+5.8\text{N}_2$.	159
Fig. 5.13	Simulated initiation of a 2-dimensional detonation in a 20 atm mixture of $2.7\text{CH}_4+2\text{O}_2+5.8\text{N}_2$.	160
Fig. 5.14	Simulated pressure and density contours for a projectile entering a 23 atm mixture of $2.7\text{CH}_4+2\text{O}_2+5.8\text{N}_2$ from a launch tube initially at 0.1 psi with 1/1000 obturator leakage area.	161
Fig. 5.15	Simulated pressure and density contours for a projectile entering a 23 atm mixture of $2.7\text{CH}_4+2\text{O}_2+5.8\text{N}_2$ from a launch tube initially at 1.0 psi with 1/100 obturator leakage area.	162

List of Tables

	Page
Table 5.1: Induction and Reaction Coefficients	128

Nomenclature

c	Speed of sound
F	Flux vector in the ξ direction
f	Van Leer flux term
G	Flux vector
g	Van Leer flux term
H	Axisymmetric source vector
h	Enthalpy
I	Induction parameter
I_S	Induction parameter source term
J^{-1}	Jacobian
K	Induction and reaction source vector
M	Mach number
M_ξ	Mach number in the ξ direction
M_η	Mach number in the η direction
m	Molecular mass
P	Pressure
Q	Vector of conservative variables
q	Heat addition term
R	Reaction parameter
r	Radial distance
R_m	Gas constant

R_S	Reaction parameter source term
R_u	Universal gas constant
T	Temperature
U	Contravariant velocity in the ξ direction
\bar{U}	Normalized contravariant velocity in the ξ direction
u	Velocity in the ξ direction
\bar{u}	Normalized velocity in the ξ direction
V	Contravariant velocity in the η direction
\bar{V}	Normalized contravariant velocity in the η direction
v	Velocity in the η direction
\bar{v}	Normalized velocity in the η direction

Greek Symbols

α	Axisymmetric source term switch
Φ^C	Convected part of the vector of conservative variables
$\bar{\gamma}$	Ratio of specific heats
η	Generalized space coordinate
ρ	Density
τ	Generalized time coordinate
ξ	Generalized space coordinate

Acknowledgments

The author wishes to express his appreciation to the members of his supervisory committee: Abraham Hertzberg, Adam P. Bruckner, Scott Eberhardt, David T. Pratt, and Ken Y. Lin. Their support and criticisms were extremely valuable and greatly improved the quality of this work. Dr. Pratt is also to be thanked for sharing his CFDK computer program. Malcolm Saynor is greatly appreciated for his skillful machining of projectiles, obturators, and other custom instrumentation. My fellow graduate students Andrew J. Higgins and Gilbert Chew have provided significant contributions to this work and tolerated long discussions concerning the starting process and other miscellaneous topics. The contributions of my colleague John B. Hinkey have indeed been immense: from design of the HITS and inserts to performing experiments, processing data, and proofreading this and other documents. His assistance has been invaluable. My parents, Ed and Candice Burnham, have always been there to support my college endeavors. Last, but not least, the author wishes to thank Lisa Townsend for her continued support and proofreading of this dissertation.

I. INTRODUCTION

The ram accelerator is a ramjet in-tube which operates in a manner similar to a conventional ramjet,¹ as shown in Fig. 1.1. The projectile resembles the centerbody of a ramjet and travels supersonically through a tube filled with a combustible gas mixture. The combustion process travels with the projectile, generating a pressure distribution which produces thrust. For a given velocity, the thrust can be controlled within limits by changing the pressure and the chemical composition of the mixture.

There are three distinct regimes of ram accelerator operation which are determined by the projectile velocity relative to the Chapman-Jouguet (C-J) detonation speed of the mixture and the method of heat release.² The regime investigated most thoroughly to date is the thermally choked regime which operates at velocities below 90% of the C-J detonation speed of the propellant mixture.³ In this regime the bulk of the heat release occurs behind the projectile at full tube area, as depicted in Fig. 1.2a. Theoretically, this regime is characterized by decreasing thrust as velocity increases until it equals zero at the point which the projectile reaches the C-J detonation velocity of the mixture. The transdetonative regime occurs between 90% and 110% of the C-J detonation speed of the mixture. In this regime the heat release moves from mainly behind the projectile to on and behind the projectile body as depicted in Fig. 1.2b. The superdetonative regime, shown in Fig. 1.2c, occurs at projectile speeds greater than 110% of the C-J speed of the mixture. In this regime the bulk of the heat release is thought to occur on the projectile body. The heat release may be caused by oblique detonations or supersonic combustion. In the superdetonative regime the bulk of the flow over the body is supersonic, while in the transdetonative and subdetonative regimes the flow is mixed subsonic and supersonic.

Currently, large scale ram accelerators are a topic of experimental research at other institutions, such as the U.S. Army Research Laboratory,⁴ the U.S. Air

Force at Eglin AFB,⁵ and at ISL, the French-German Research Institute.^{6,7} Computationally, the ram accelerator is a topic of study at the Naval Research Laboratory,⁸ Science Applications International Corp.,⁹ and Amtec Engineering, Inc.,^{10,11} among others. The information presented in this dissertation will aid in the understanding of the starting process in large and small scale facilities, as well as assist in the validation of unsteady, chemically reacting CFD codes.

The majority of analysis done to date on the ram accelerator has made the assumption that the flow is steady in the reference frame of the projectile. Neglecting the unsteady aspects of the flow greatly simplifies modeling of the ram accelerator and generally gives satisfactory results. Phenomena that are inappropriate to model using the steady state assumption include the starting process, mixture transition and high acceleration.

The understanding of these unsteady flows is important for several reasons. To make accurate predictions of thrust under extreme acceleration conditions the unsteady nature of the flow around the projectile must be considered. The transients caused by transitions between combustible gas mixtures can, under the wrong conditions, lead to the projectile "unstaring". In an unstart a shock is disgorged from the projectile throat either by choking at the throat or by the normal shock on the projectile body passing through the throat and onto the nose cone. Establishing stable combustion in the thermally choked regime and in the other regimes always involves unsteady flows. The transients associated with starting are the most important unsteady phenomena in all ram accelerators; before the projectile can undergo high acceleration or make mixture transitions, the diffuser must be gasdynamically started and combustion must be stabilized behind the projectile.¹²⁻¹⁴ This dissertation details the starting process in inert and reacting mixtures and discusses simulations which clarify the interpretation of the experimental results.

The transients of the starting process are important for all ram accelerator sizes, regimes of operation, operating pressures, and gas mixtures. The

understanding of these transients can prevent many discouraging and expensive experiments when new conditions, such as changing scale or operating pressure, are encountered. Experimental data on the starting process not only enhance the understanding of the ram accelerator, but also provide data for the evaluation of unsteady, chemically reacting CFD codes.

1.1 Experimental Setup

The ram accelerator facility, Fig. 1.3, consists of a light gas gun, helium dump tank, ram accelerator section, final dump tank and projectile decelerator (the final dump tank and decelerator are not shown). The 38 mm bore, 6.4 m long, single-stage light gas gun is capable of accelerating the projectile assembly (typical combined mass of 60-100 gm) to speeds of up to 1300 m/s. The muzzle of the light gas gun is connected to a perforated-wall tube that passes through an evacuated tank which serves as a vent for the helium driver gas.

The 16 m long ram accelerator section consists of eight steel tubes with a bore of 38 mm, and an outer diameter of 100 mm. There are a total of 144 instrumentation ports at 40 regular intervals of 40 cm along the accelerator tube. At twenty-four axial stations there are four ports at right angles to each other and at sixteen stations there are 3 ports separated by 120 degrees. This permits the use of either three or four transducers at each station. Piezoelectric pressure transducers can be located in any of these instrument stations. The remaining ports are used to mount electromagnetic transducers (copper wire coiled around a Lexan core) or fiber-optic light guides. There is an additional instrument station 11.5 cm ahead of the entrance to the first tube. A 32 channel, 1 MHz digital data acquisition system is used to acquire the data. Multiplexing permits monitoring of up to 100 separate input signals.

The end of the accelerator tube is connected by a 0.76 m long drift tube to a 2.4 m long evacuated dump tank where the projectile flies free. The tank has a pair of 25 cm dia. viewing ports for photography and additional velocity measurements. The free-flying projectile is brought to a stop in tightly packed

rug remnants in a 20 cm inner diameter, 1 m long tube attached to the far end of the dump tank.

The ram accelerator tube is designed to operate at propellant fill pressures up to 50 atm. Thin Mylar diaphragms are used to close off each end of the accelerator tube and to separate sections of the tube filled with different propellant mixtures. The fuel, oxidizer, and diluent gases are metered using sonic orifices and directed to the appropriate sections of the ram accelerator tube.

The basic projectile geometry that has been used in the majority of the experimental work to date is illustrated in Fig. 1.4. The projectile is fabricated from an aluminum or magnesium alloy in two pieces, the nose cone and the body, and has a range in mass of 45 to 90 gm. The fins serve only to center the projectile in the tube. Thin magnetic rings are mounted in the nose/body joint and may also be placed in the base of the body. When the projectile passes electromagnetic transducers mounted in the accelerator tube, the magnetic material induces signals which are used to determine the distance-time history of the projectile, and hence, its velocity and acceleration.

The obturator (Fig. 1.4) is fabricated from polycarbonate (Lexan) and consists of two pieces whose typical combined mass is 15 gm. The main body has a length to diameter ratio of 0.42 and is perforated axially with a series of regularly spaced holes whose total cross-sectional area is approximately 40% of that of the tube. A thin flat plate of the same material is used to seal these perforations against the driving gas in the light gas gun. This plate, subsequently referred to as the backplate, is snugly fitted into a shallow cavity machined in the back of the main body of the obturator.

The existing ram accelerator is inadequate for the study of transient phenomena because the instrumentation stations are separated by 40 cm, or about 2.6 times the length of a projectile. It is clear that to study the transients of the starting process a much higher instrumentation density is needed.

There are several design requirements for any method of improving instrumentation density. First, any additional ram accelerator tube must fit into the system with little or no modification of the existing facility. Second, to study as many phenomena as possible, it is necessary for the high density instrumentation to be placed anywhere in the system. For investigation of the starting process, only the location where the projectile enters the combustible gas mixture needs the high density instrumentation; however, for mixture transition, high acceleration and normal operation studies, other locations will need the high density instrumentation. Third, for the study of transitions and starting, it is necessary to have an instrumentation station as close as possible to the entrance diaphragm. Finally, the instrumentation stations must be close enough together to provide adequate resolution to study transient wave motion. The above requirements prohibit the modification of an existing tube section because with their design, the closest an instrumentation station can be to a diaphragm is about 6 cm to 8 cm. Consequently, it was decided to construct a short section of ram accelerator tube and a new coupling method to meet the above design requirements. The tube couplers and highly instrumented tube section (HITS) are shown in Fig. 1.5. The tube couplers (one with right handed threads, the other with left) screw on to the existing ram accelerator tubes. They provide a flush mounting surface to which the HITS is bolted. Unlike the original tube couplers, they permit an instrumentation station to be as close to the diaphragm as desired. The length of the HITS was constrained by the available spacing in the system. The spacing of the instrumentation stations was chosen to be 20 mm for structural and instrumentation density reasons.

The 20 mm spacing is approximately three times the diameter of a pressure transducer and 1/20 the spacing of the instrumentation stations in the original ram accelerator tubes. For a typical projectile length of 153 mm, this provides eight sensors over the length of the projectile at some time during an experiment. For a starting type experiment the typical projectile velocity is 1200 m/s, which corresponds to approximately 17 ms for the same location on

the projectile to pass two adjacent instrumentation stations. At each instrumentation station there are four ports separated by 90° . There are eight axial stations with each station rotated by 45° relative to the previous one. Under proper conditions, these can be used to determine the orientation of the projectile and to determine the three-dimensional character of the flow.¹⁵⁻¹⁷

In addition to the HITS, several short sections of tube (subsequently referred to as inserts) were constructed. Inserts with both four and eight equispaced ports at a single station have been used. The inserts may be used alone, stacked together or combined with the HITS to provide the required resolution. The arrangement used in the majority of starting experiments is shown in Fig. 1.6. The end of the launch tube after the vent section is shown at the left of the figure with the projectile traveling from left to right. Three inserts and the HITS are shown installed between the end of the launch tube and accelerator section. The entrance diaphragm was placed between the inserts and the HITS. The station numbering in this configuration is shown at the top of the figure. Together with the existing instrument station in the launch tube, there were four stations prior to the diaphragm and eight stations after the diaphragm.

The HITS and tube couplers were made from a solid 6" diameter rod of AISI 4150 hot rolled heat treated stress relieved steel alloy while the inserts were made from a 4" diameter rod. This material has a Brinell hardness of 302 (Rockwell C 32), a tensile strength of 156,000 psi and a yield point of 138,000 psi. This material also has high resistance to impacts and good machinability which makes it ideal for ram accelerator applications.

1.2 Pressure and Luminosity Sensor Response

It is important to examine typical data obtained from the thermally choked regime of operation to provide a common point of reference for future discussions. Fig. 1.7 shows typical pressure and luminosity data from an experiment in which the projectile was traveling 1540 m/s (approximately 90%

C-J or Mach 4.25) in a mixture of $2.7\text{CH}_4+2\text{O}_2+5.8\text{N}_2$ with an initial fill pressure of 24 atm. The first rise in pressure is the conical shock generated from the nose of the projectile reflecting from the tube wall. This reflected shock in turn reflects from the projectile nose cone and then reflects once again from the tube wall as indicated by the second small rise in pressure. The flow expands as it passes over the throat of the projectile and is indicated as the first reduction of pressure. The next large increase and decrease in pressure is a result of the three dimensional structure of the projectile and its origin will be discussed in a later section.¹⁵⁻¹⁷ The final rise in pressure is what is referred to as the "normal" shock on the projectile body. In this case the "normal" shock is actually an oblique shock at the base of the projectile.

The luminosity data has typically been used to determine regions of combustion or "hot spots" in the flow.¹⁸⁻²⁰ The luminosity data indicates that there are "hot spots" just past the projectile throat, at the base of the projectile and behind the projectile at the full tube area. The luminosity near the throat will be explained in the section on three dimensional effects. It should be noted that at lower Mach numbers the light in the region of the throat vanishes. The luminosity on the base of the projectile may indicate combustion in the separated boundary layer of the projectile as predicted by Higgins.²¹ The bulk of the luminosity is emitted from the flow behind the projectile which is consistent with the assumption of combustion at the full tube area.

This pressure and luminosity data provide a baseline to which other experimental conditions may be compared. A projectile that has successfully started or is in the process of a successful start should show similar pressure and luminosity data. As will be shown in the next section, some care must be used in interpreting the data from both pressure and luminosity probes.

1.3 Non-Ideal Sensor Response

In an ideal environment the pressure sensors would output the exact pressure at a point on the tube wall. Unfortunately the sensor is not a point device; in

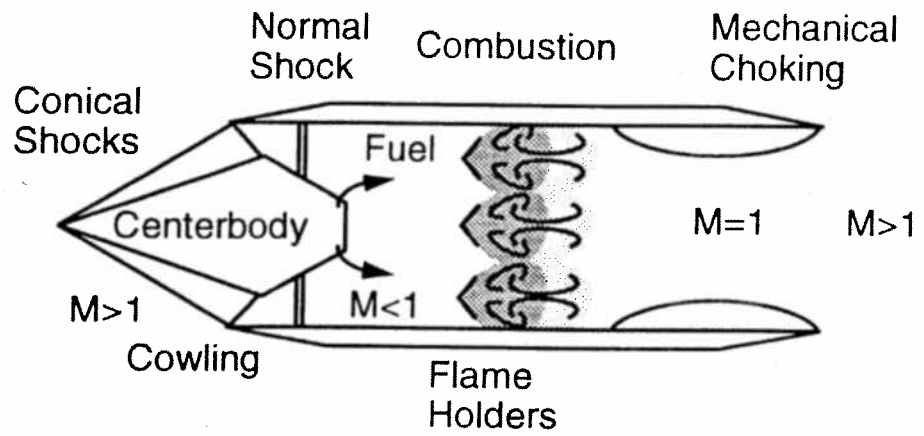
fact, it has a diameter of approximately 6 mm and is typically recessed from the tube wall 0.25 mm to 0.5 mm to prevent impact damage. In addition to these problems, the sensor is an electro-mechanical device which has a dynamic response. The typical response of a pressure transducer to a normal shock is shown in Fig. 1.8. The shock is in argon and has a pressure ratio of about 3.3. The ideal response of a point pressure transducer is shown by the dashed line and is seen to jump from a value of 1 prior to time zero and to a constant value of 3.3 after time zero. As expected, the actual sensor response to the shock is not instantaneous but requires several micro-seconds to respond. The response begins prior to time zero because of the 6 mm diameter of the sensor (but not as early as if it were flush mounted). What is not expected is the large overshoot in pressure, approximately 35%, for 30 to 40 μ sec. Two possible causes come to mind: the sensors' dynamic response and the recession of the sensor in the tube wall. The natural frequency and damping ratio found from the response of a second order system with similar overshoot amplitude and duration provide a frequency response much lower than advertised by the manufacturer. In addition, the longer term oscillations of the 2nd order system require much longer to damp out than in the actual response. This indicates that the dynamic response alone does not account for the overshoot. A complete model of the recession of the pressure transducers is beyond the scope of this work; however, it is reasonable to expect the response of a recessed sensor to be delayed in time and to have a different amplitude measurement than a flush mounted sensor. The measurement overshoot may be caused by the reflection of the shock from the downstream edge of the recess and is thought to decay away because of viscous effects of the flow.

It is not only the pressure sensors that provide incorrect or misleading information. The luminosity sensors have been plagued with operational problems so that on the average, in any given experiment, only 30%-40% are operational. The luminosity sensors respond to light entering at the appropriate angle, whether from a local (near tube wall) or distant (far tube

wall or scattered light) source. Figure 1.9 shows the response of two luminosity sensors separated by a distance of 140 mm. The first trace shows a very bright region that saturated the data acquisition system. At the same time at a station 140 mm away an increase and decrease in luminosity can be seen. This "blip" recorded by the second sensor is a reflection inside the tube of the bright light seen at the first sensor.

This demonstrates that data obtained from pressure and luminosity sensors may not always be correct. Pressure data may lag in time, be averaged in space, and have an overshoot compared to data from a point surface mounted transducer. Luminosity data may be from reflections or from distant locations. When examining pressure and luminosity data, these possible errors should be kept in mind.

Conventional Ramjet



Ram Accelerator

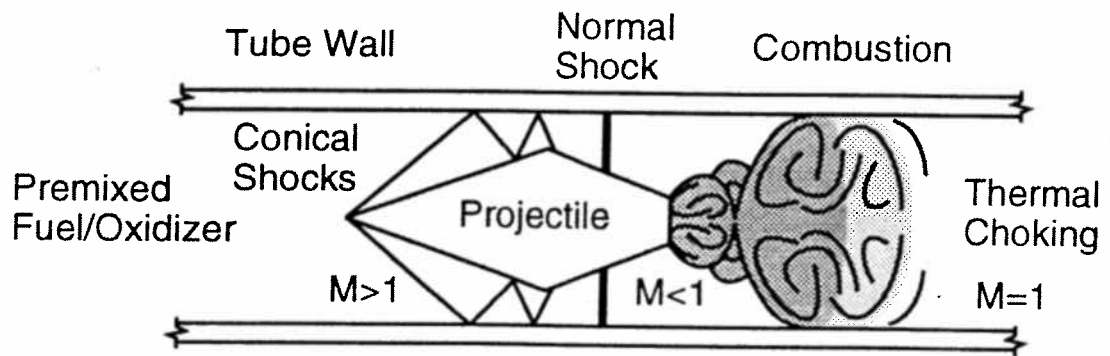


Fig. 1.1 Comparison of a conventional ramjet with the ram accelerator.

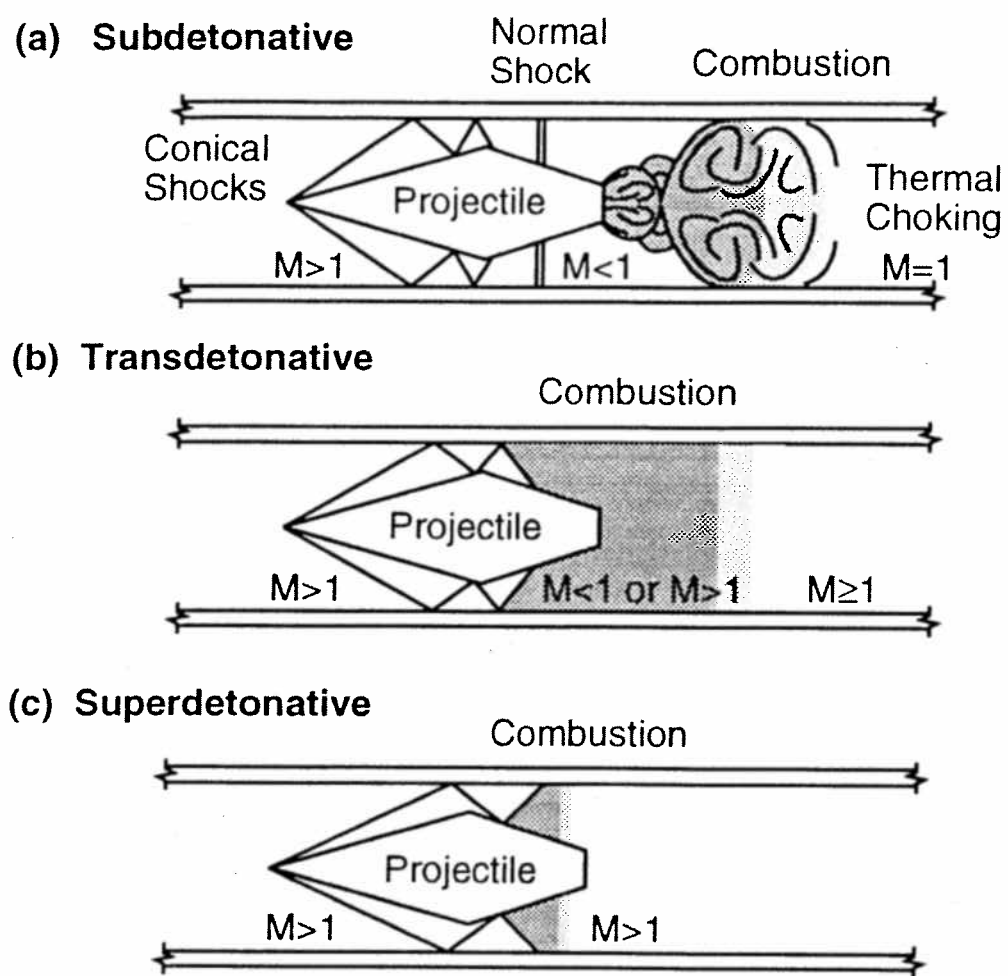


Fig. 1.2 Operational regimes of the ram accelerator.

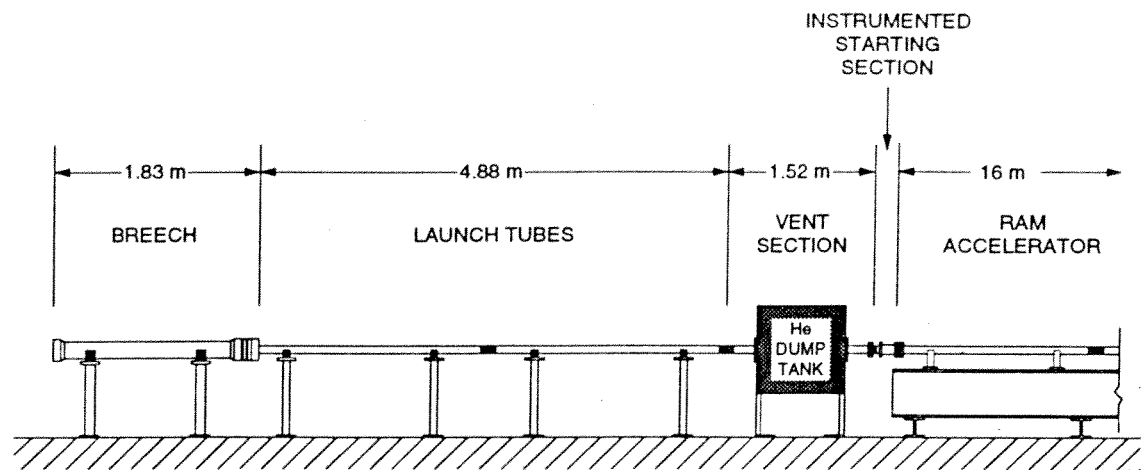


Fig. 1.3 Ram accelerator facility (final dump tank and decelerator not shown).

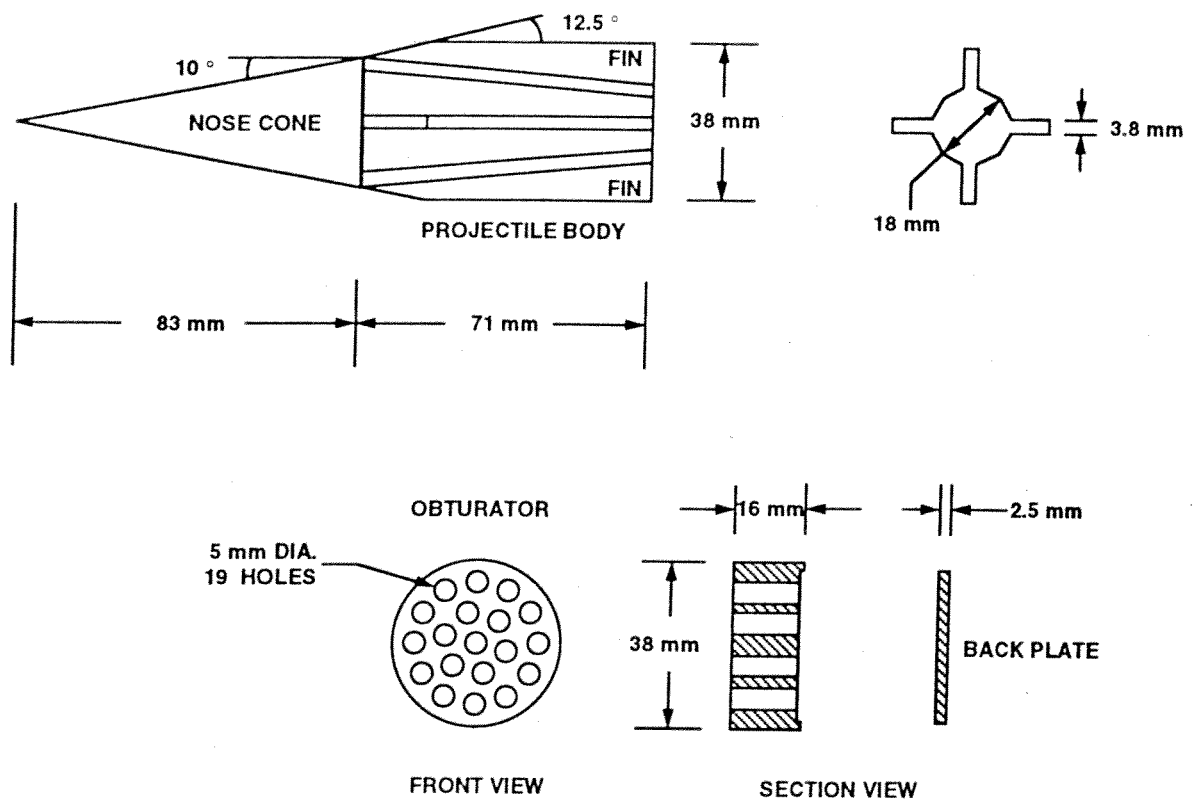


Fig. 1.4 Geometry of projectile, obturator, and backplate used in these experiments.

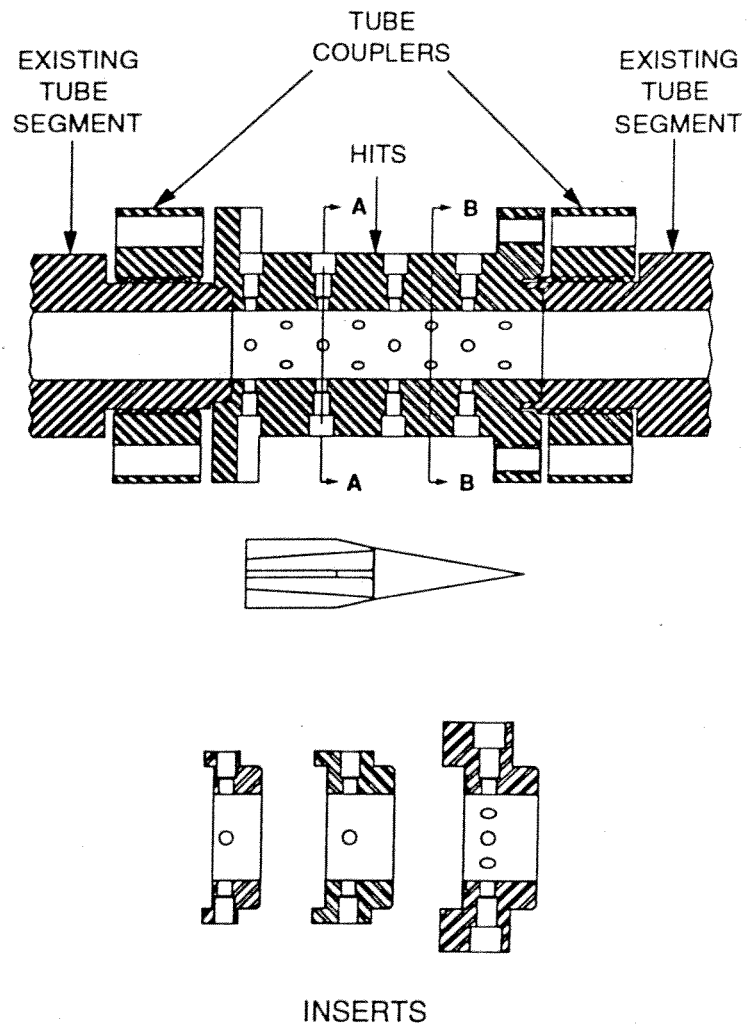


Fig. 1.5 Highly instrumented tube section, inserts and tube couplers. Projectile shown for scale.

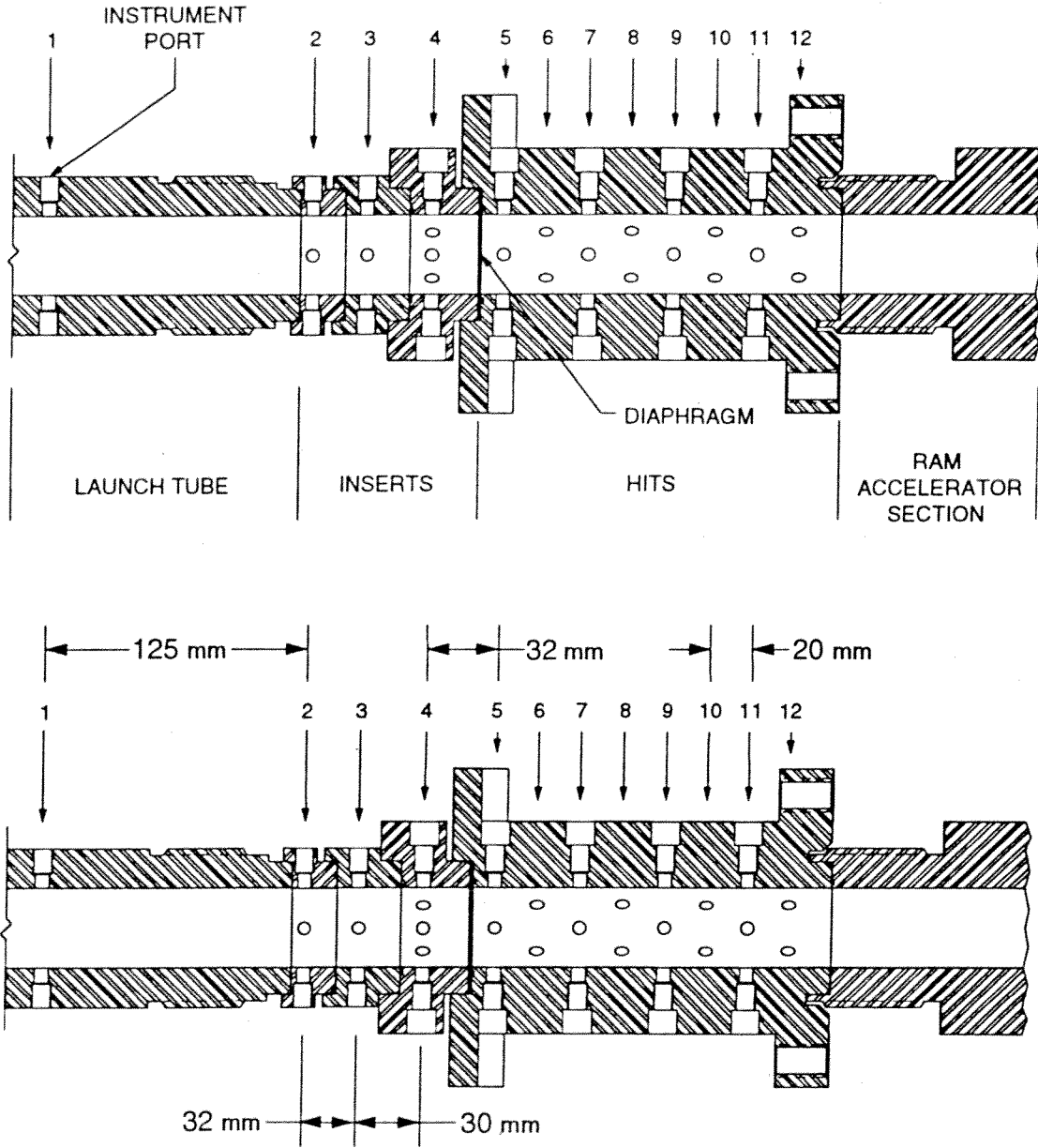


Fig. 1.6 Instrument station numbering and distance between stations for the majority of starting experiments.

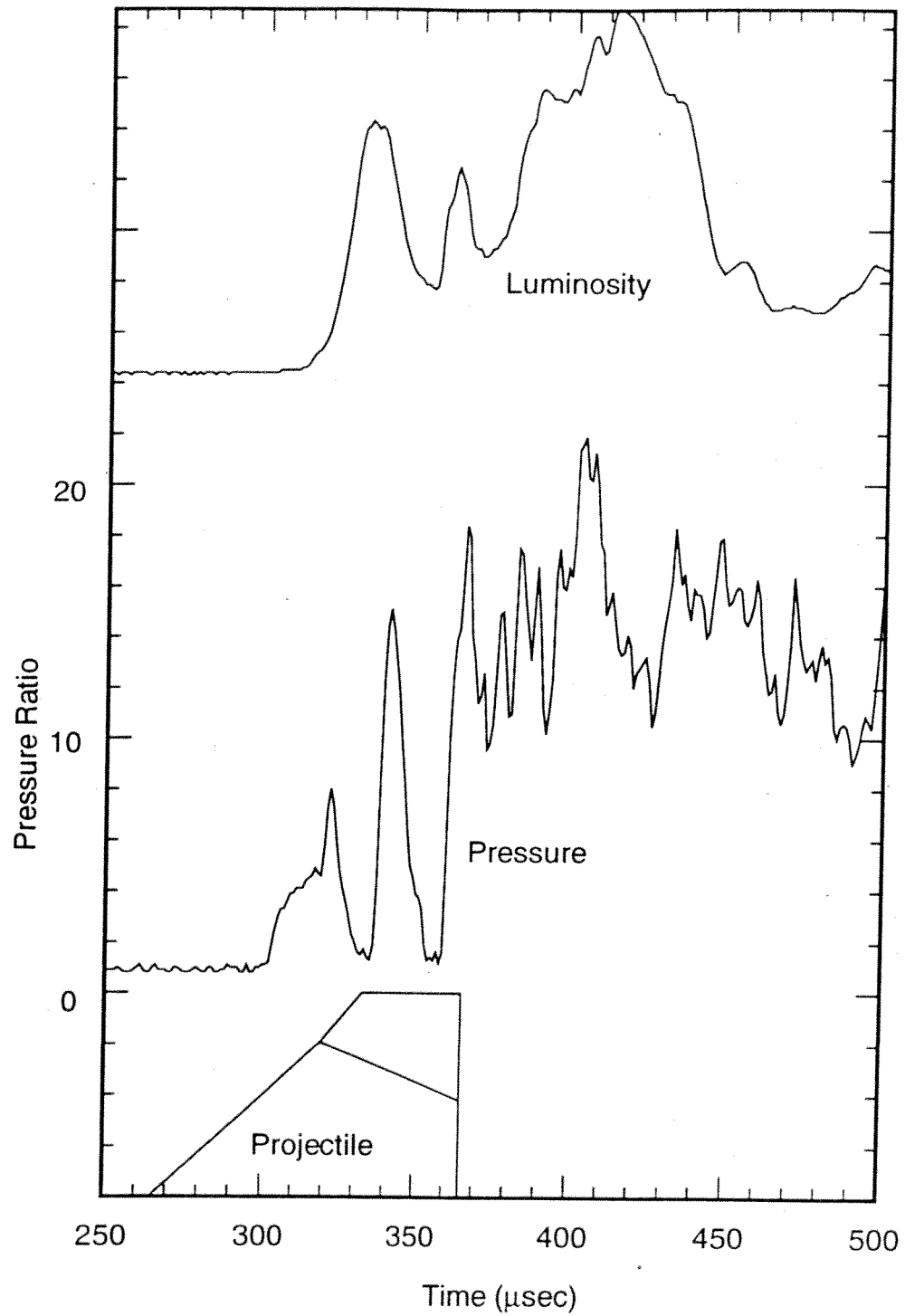


Fig. 1.7 Typical pressure and luminosity data obtained from the thermally choked regime.

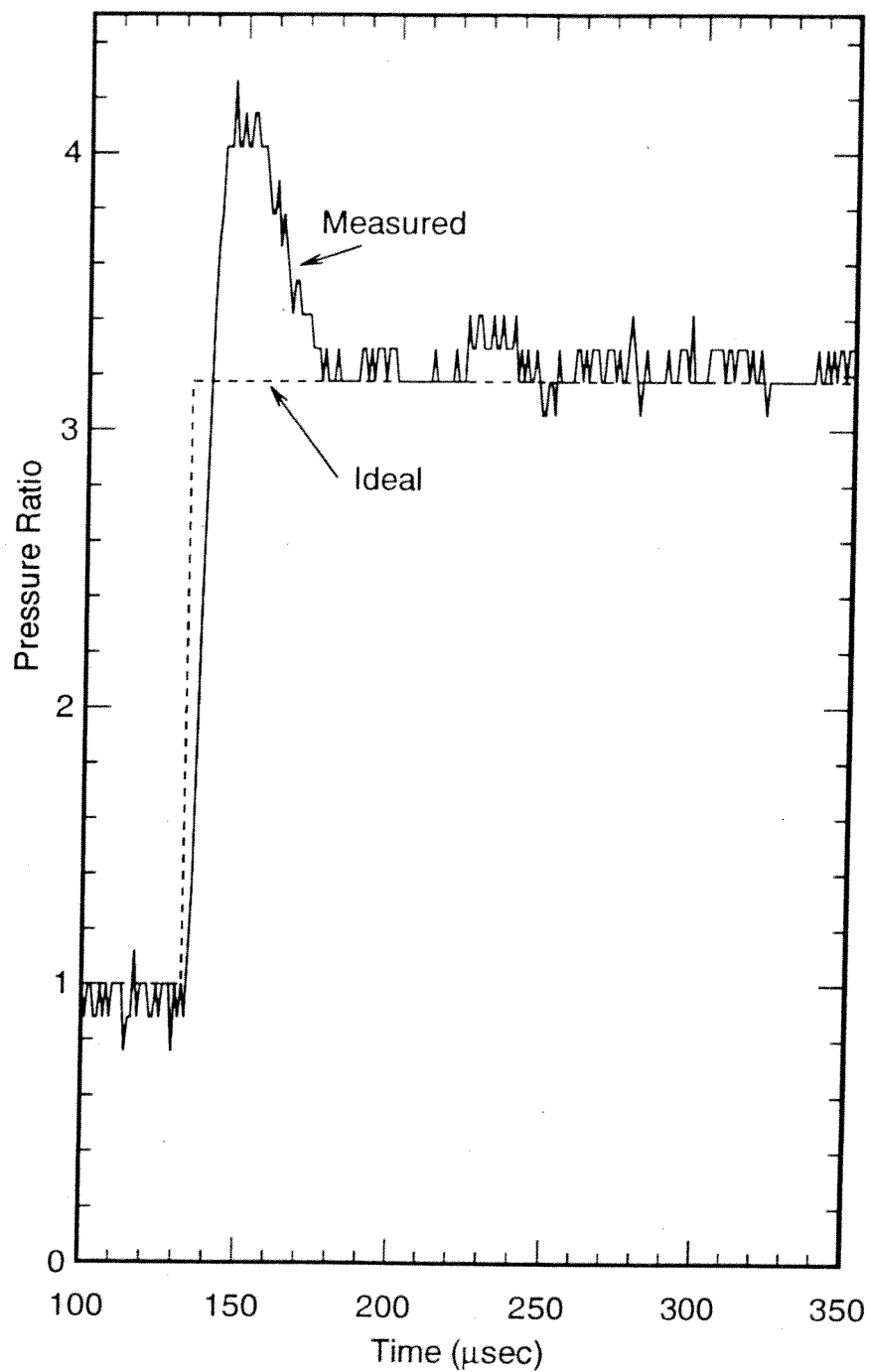


Fig. 1.8 Pressure sensor response to a normal shock in argon.

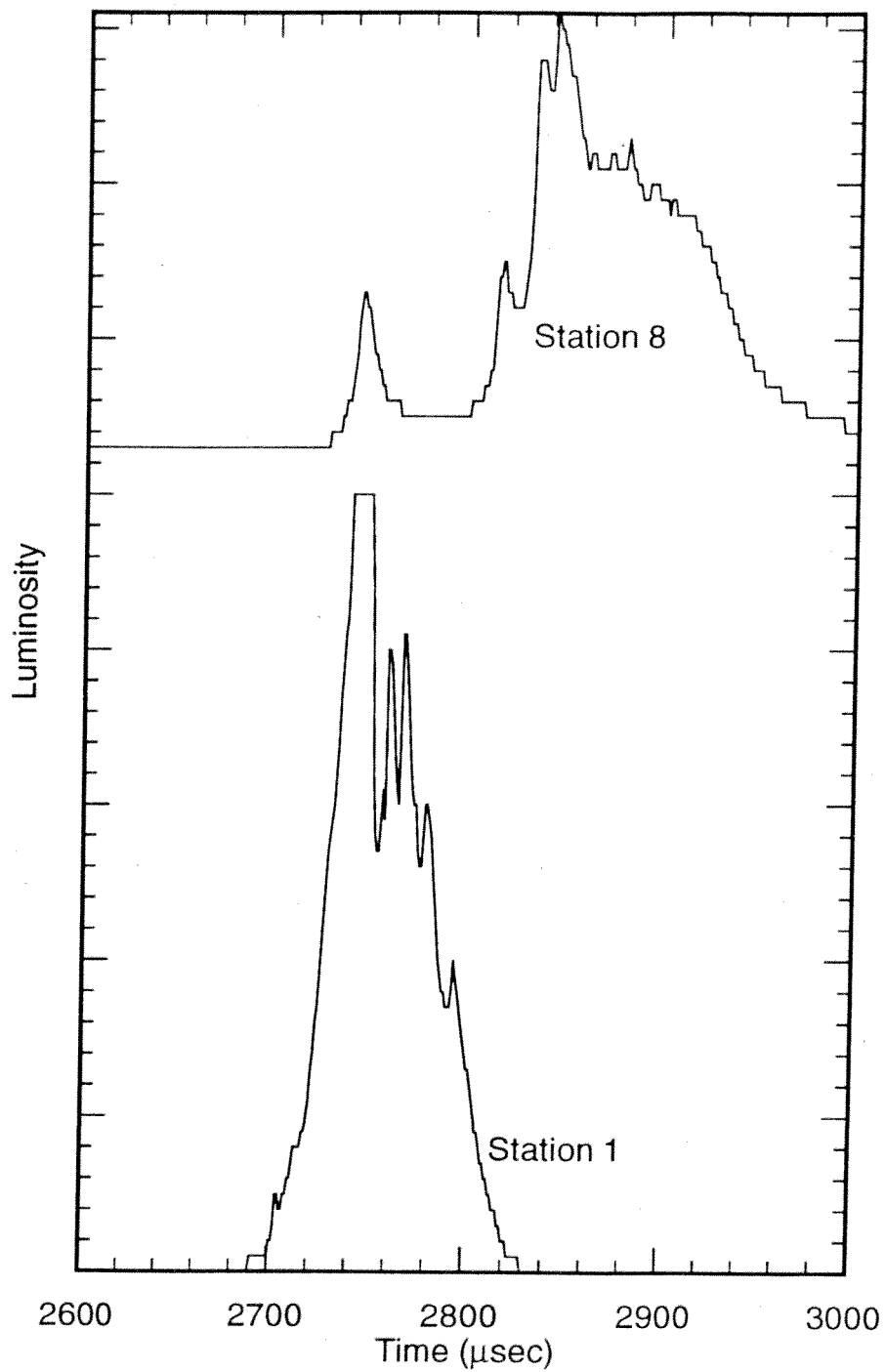


Fig. 1.9 Luminosity sensor response to the initiation of a detonation.

II. DETONATION OF THE COMBUSTIBLE GAS MIXTURE

The C-J detonation velocity of a premixed combustible gas mixture may be calculated from algebraic considerations.²²⁻²⁴ This model makes no statements on the structure of the wave or if it is at all physically possible. For the mixture $2.7\text{CH}_4+2\text{O}_2+5.8\text{N}_2$ at 21 atm and 298 K, the theoretical C-J detonation velocity is 1700 m/s. By assuming a one-dimensional ZND (Zel'dovich, von Neumann, and Doring) wave structure²²⁻²⁴ the peak shock pressure ratio is 25.2 and the post reaction pressure ratio is 13.4.

2.1 Spinning Detonation

The mixture $2.7\text{CH}_4+2\text{O}_2+5.8\text{N}_2$ is very dilute to be detonated in a 38mm diameter tube. To study the detonation characteristics of this mixture, a solid slug was launched from the gas gun and impacted the premixed gas at approximately 1250 m/s. This creates an overdriven detonation which decays in velocity. At initial pressures of 7.8 atm and 14.6 atm the combustion eventually, prior to 10 m into the accelerator section, decoupled from the shock and propagated as a shock deflagration. At 21 atm a marginal detonation was propagated down the 16 m length of the accelerator section and was observed to have a velocity of approximately 1750 m/s. This detonation was not what would be expected from one-dimensional considerations. The detonation propagated as a single headed spinning detonation.²²⁻²⁴

Figure 2.1 shows a schematic representation of a spinning detonation. The detonation has been "unrolled" and tracked relative to the shock triple point. The lead shock varies in strength and location relative to the triple point. At 1 the lead shock and combustion front are closely coupled. Traveling toward 2 the shock becomes weaker and the reaction zone becomes more removed from the shock. At 3 a detonation that travels transversely around the tube reacts the gas that has passed through the lead shock but has not made it to the reaction front. This is the source of the triple point shock and the shock (4) which trails away from the reaction front. The dashed line represents the

conditions to which a pressure or luminosity probe at one location in the tube would be exposed. This is a somewhat simplified view of a spinning detonation, but it provides a sufficient description for the discussion of the experimental data.

Figure 2.2 shows the pressure data from two 8 port inserts separated by 31 mm and rotated by 22.5° relative to each other. The lead shock can be seen to arrive at different times and to have a large variation in amplitude. The peak shock strength gives a pressure ratio of 110. This is a factor of 4.4 greater than the peak shock strength predicted by the ZND model. Many of the pressure traces show the passage of the lead shock and then a second rise in pressure which is the shock between 3 and 4 in Fig 2.1. Figure 2.3 shows the same data as Fig. 2.2 only at a longer time scale. The variations in pressure in the far field carry on for a long period of time and form a spiral pattern. The variations appear to be relatively low in amplitude, but are typically 140 atm. The pressure distribution on the tube wall as the detonation passes can be visualized by representing the tube wall pressure as the radial distance of a point away from the surface of a cylinder representing the ram accelerator tube wall at the fill pressure. The different angular stations in the inserts correspond to the same angles on the hypothetical tube, while the length of the tube represents time. Another way to explain this visualization is as if the detonation were traveling through an infinitely thin, flexible tube that deforms radially outward proportionally to the instantaneous pressure on the tube wall. Figure 2.4 is such a representation of the data of Fig 2.2 corrected for front rotation. Both the surface shading and radial distance are proportional to pressure. The large amplitude initial shocks are evident, as well as the spiral oscillations in the far flow field. Figure 2.5 is the "unrolled" format similar to Fig. 2.1 of the data in Fig. 2.2. It shows the curved shock front and the shock trailing into the far flow field.

The importance of this gas mixture propagating a spinning detonation is twofold. First, it characterizes the combustible gas mixture in the tube

diameter and at pressures comparable to all of the starting data presented in this dissertation. Second, it provides a mechanism by which the induction and reaction times of the mixture at high pressure may be roughly measured. If the end of the induction and reaction zones can be found relative to the shock front, measurements of pressure and estimates of temperature and flow velocity provide a means of estimating induction and reaction times. Even if the estimates are only accurate to an order magnitude, they are still valuable because of the lack of dilute, methane rich, high pressure kinetic data.

To locate the end of the induction and reaction zones, spinning detonation experiments were done that utilized not only pressure transducers but also used luminosity probes. In these experiments the HITS was used with 2 sets of 4 pressure transducers, followed by 2 sets of 4 luminosity sensors, followed by another 2 sets of 4 pressure transducers. In the first case the HITS was 12 m from the entrance to the accelerator section. The pressure data from the first 2 sets of pressure transducers are shown in Fig. 2.6. They show similar character to the data in Fig. 2.2 in the variation of the lead shock strength, a second strong shock arriving at different times depending on the position of the sensor, and long term pressure variations in the far flow field. Figure 2.7 shows the data from the luminosity sensors. There is a wide variation in the arrival time of the first light and time of peak amplitude. The oscillations that appear in the pressure data also appear in the luminosity data. The differences in peak amplitude and decay rate may be explained by different views of the reaction zone and variations in each of the luminosity sensors. Figure 2.8 shows the data from the last 2 sets of pressure transducers. These again show the variation in shock arrival time and strength as well as the far field pressure oscillations.

In this form the data just discussed are interesting, but it is difficult to obtain a measure of the induction and reaction times. For this reason the data on shock arrival times, first luminosity, peak luminosity and secondary shock arrival times have been put in the format of Fig. 2.1 and is shown in Fig. 2.9.

The dashed lines represent the path in this coordinate system to which a pressure or luminosity probe at one location in the tube would be exposed. The symbols represent experimental data points. It is now assumed that the beginning of luminosity, not associated with a shock, indicates the end of the induction zone and the peak indicates the end of the reaction zone. In general the character of Fig 2.9 is similar to that of Fig. 2.1; however, it is obvious that there is some error in the measurement of shock and luminosity positions. The errors may be explained by the difficulty in assembling the figure from data taken at many different positions and then being reassembled into a single picture with corrections for the rotation of the front.

With complete knowledge of the flow, a single spinning detonation would provide induction and reaction times for a wide variation in pressure and temperature. With the limited resolution of this method and assumptions made in obtaining velocity and temperature, only one or two "best guesses" can be made. For an estimated pressure of 525 atm and temperature of 1150 K, the induction time is estimated to be 30 μ sec while at 380 atm and 1100 K the reaction time is estimated to be 9 μ sec. At 380 atm and 1100 K the induction time is estimated to be 40 μ sec and at 320 atm and 1050 K the reaction time is estimated to be 9 μ sec. These values may be considered to be of an order of magnitude accuracy due to the assumptions made in their calculation. The accuracy of these values may be improved with a sophisticated numerical model of a spinning detonation so that velocity and temperature may be more accurately estimated; however, that is beyond the scope of this work. As rough as these estimates are, they do provide a "ball park" range of induction and reaction times to which a chemical kinetics model may be compared. This is necessary because of the high pressures and type of mixture.

For the next data set the HITS was placed 8 m from the entrance to the accelerator section. Figure 2.10 shows the first two sets of pressure data, while Figs. 2.11 and 2.12 show the luminosity and second set of pressure data. As in the previous spinning detonation experiments, there is a variation of the shock

arrival time and strength and there are far field oscillations in both pressure and luminosity. The data have been reduced to the "unrolled" form in Fig. 2.13. The figure shows a much more irregular initial shock. This is from difficulties in correcting for rotation of the front. Using the same procedure described above, the induction time at 440 atm and 1100 K was estimated as 26 μ sec and the reaction time at 400 atm and 1080 K was estimated as 7 μ sec.

This method of measuring induction and reaction times from a spinning detonation could be much improved by using inserts with 8 or 16 sensor locations at one axial location. Alternating pressure and luminosity sensors in one insert would help to remove difficulties of correcting for the rotation of the front. By using multiple inserts instrumented in this way, much better data could be obtained to improve the accuracy of the measurements. The development of a 3-dimensional CFD code to model the spinning detonation would also improve the accuracy by giving better values of temperature and velocity.

2.2 Obturator Initiation of a Detonation

The final detonation experiment performed was one with the HITS placed at the entrance to the accelerator section. A combustible gas mixture of $2.7\text{CH}_4+2\text{O}_2+5.8\text{N}_2$ was used at a pressure of 24 atm. The HITS and 4 m of the ram accelerator tube were filled with the combustible gas mixture. The detonation was initiated by launching a 35 gm Lexan solid obturator to a speed of 1250 m/s with the light gas gun, which impacted the entrance diaphragm and combustible gas mixture.

The obturator impact with the entrance diaphragm was 10 mm prior to the first sensor in the HITS. Figures 2.14 and 2.15 show the pressure and luminosity history of this detonation experiment. The peak pressure ratio at station 1 is 83 which rapidly decreased to an average of approximately 47 at later stations. The base of the obturator can be identified by the beginning of

the low pressure region behind the shock. The distance between the obturator and shock increases as they propagate down the axis of the tube because the obturator is traveling at about 1250 m/s and decelerating while the shock is traveling at about 2000 m/s. It should be noted that if there were no combustion (an inert mixture), the maximum pressure ratio would be approximately 25 and the shock speed would be approximately 1600 m/s. The higher pressure and shock speed ensure that combustion is occurring. The shock and combustion activity in this experiment couple and travel as an overdriven detonation wave. As the obturator slows and its influence diminishes, the speed of the overdriven detonation wave decreases and stabilizes near the C-J detonation speed of the combustible gas mixture. As with the previous experiments, the marginal detonation propagates in a spiral.

The luminosity history from this experiment, shown in Fig. 2.5, provides some interesting information. The first peak in luminosity, which occurs at the same time for all stations, approximately corresponds to the sabot impact with the entrance diaphragm. The fiber optic light guides in the luminosity probes are recessed about 1.5 cm, so ideally they only view activity within a small angle of their location. It is obvious that this is not the case (station 8 is 150 mm from the entrance diaphragm), and as discussed earlier, interpretation of the luminosity data must be done with care. The secondary peaks in luminosity correspond well with the location of the overdriven detonation wave, and the rapid rise in luminosity seems to match well the point where the heat release is thought to occur. At station 1 the strong shock seems to detonate the mixture immediately, while at station 8, where the shock strength has decayed, the peak in luminosity lags behind the shock. This is not the typical view of an overdriven detonation; however, this mixture is very dilute and is known to propagate a single headed spinning detonation at this initial pressure. At some point the combustion must decouple from the overdriven shock structure to establish the spinning detonation. Using the method described above, the induction time at 850 atm and 1300 K is estimated to be 32 μ sec and the

reaction time at 750 atm and 1250 K is estimated to be 12 μ sec. These values are close to those obtained previously even though the pressure has increased by a factor of 2 and the temperature is 150 K higher. This is not surprising since the method of estimation is not very accurate. Improved resolution in space (smaller probe size) may allow improved measurements in the induction and reaction zone.

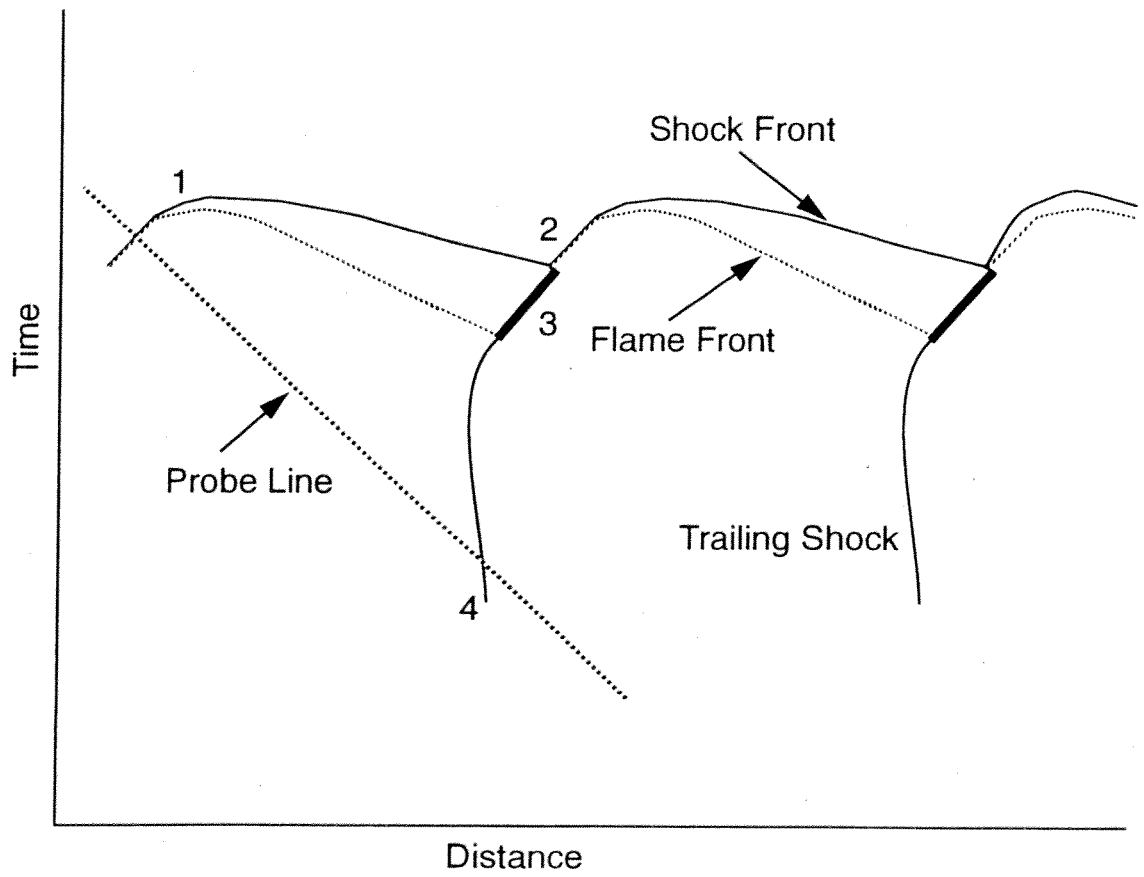


Fig. 2.1 Schematic representation of a spinning detonation.

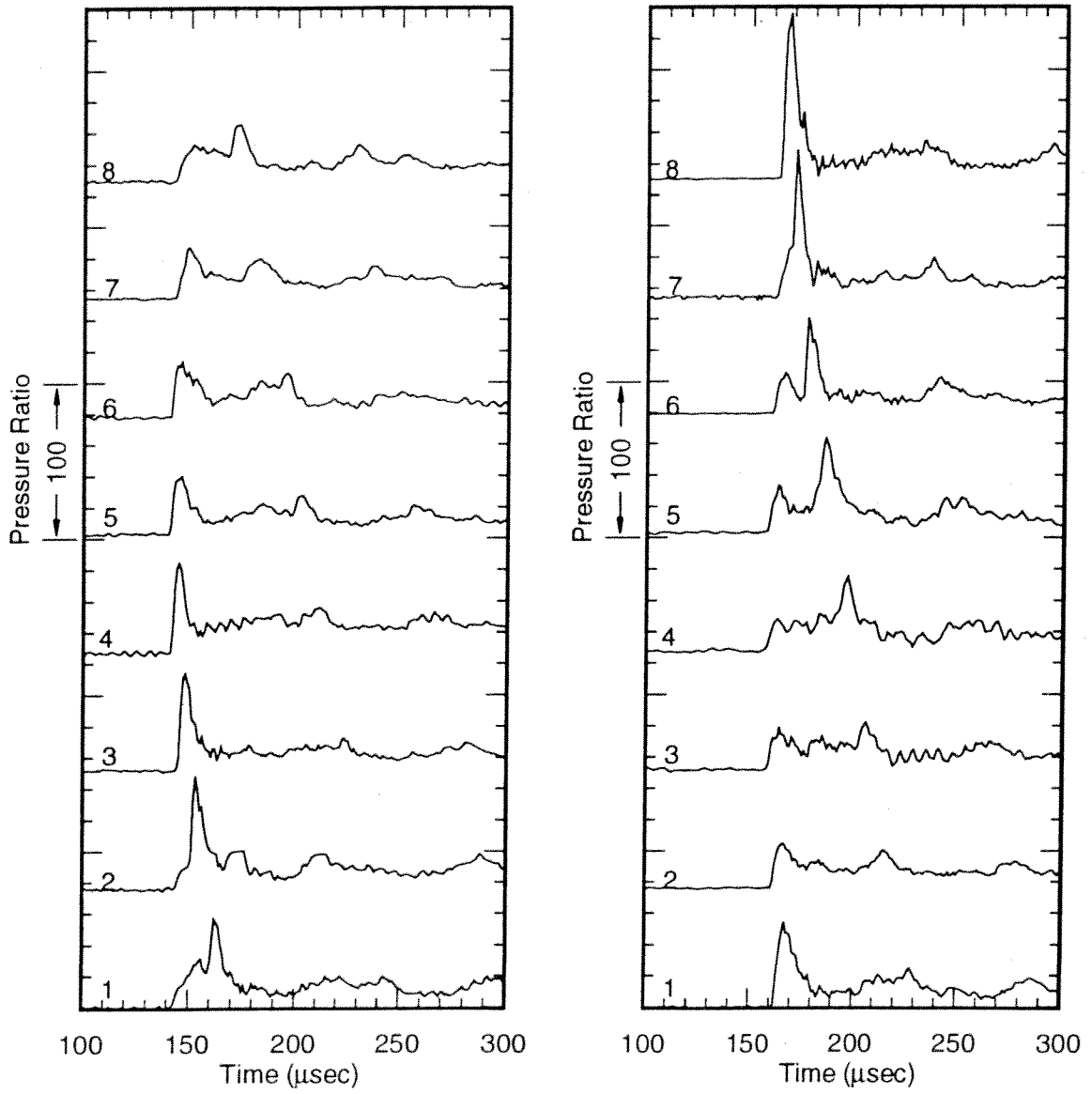


Fig. 2.2 Pressure data from the passage of a spinning detonation in the mixture $2.7\text{CH}_4+2\text{O}_2+5.8\text{N}_2$ at 21 atm and 298 K.

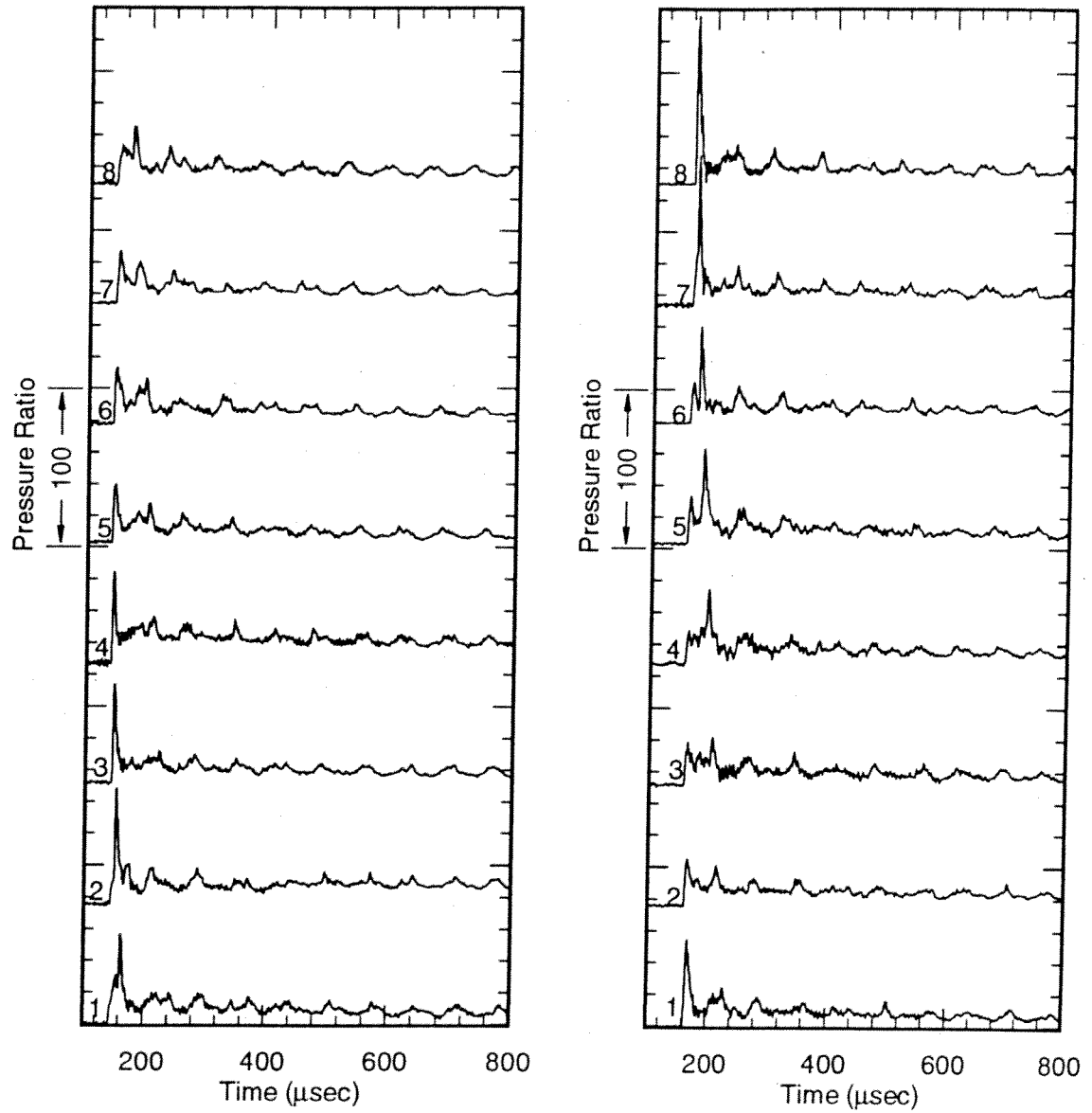


Fig. 2.3 Pressure data from Fig. 2.2 on longer time scale.

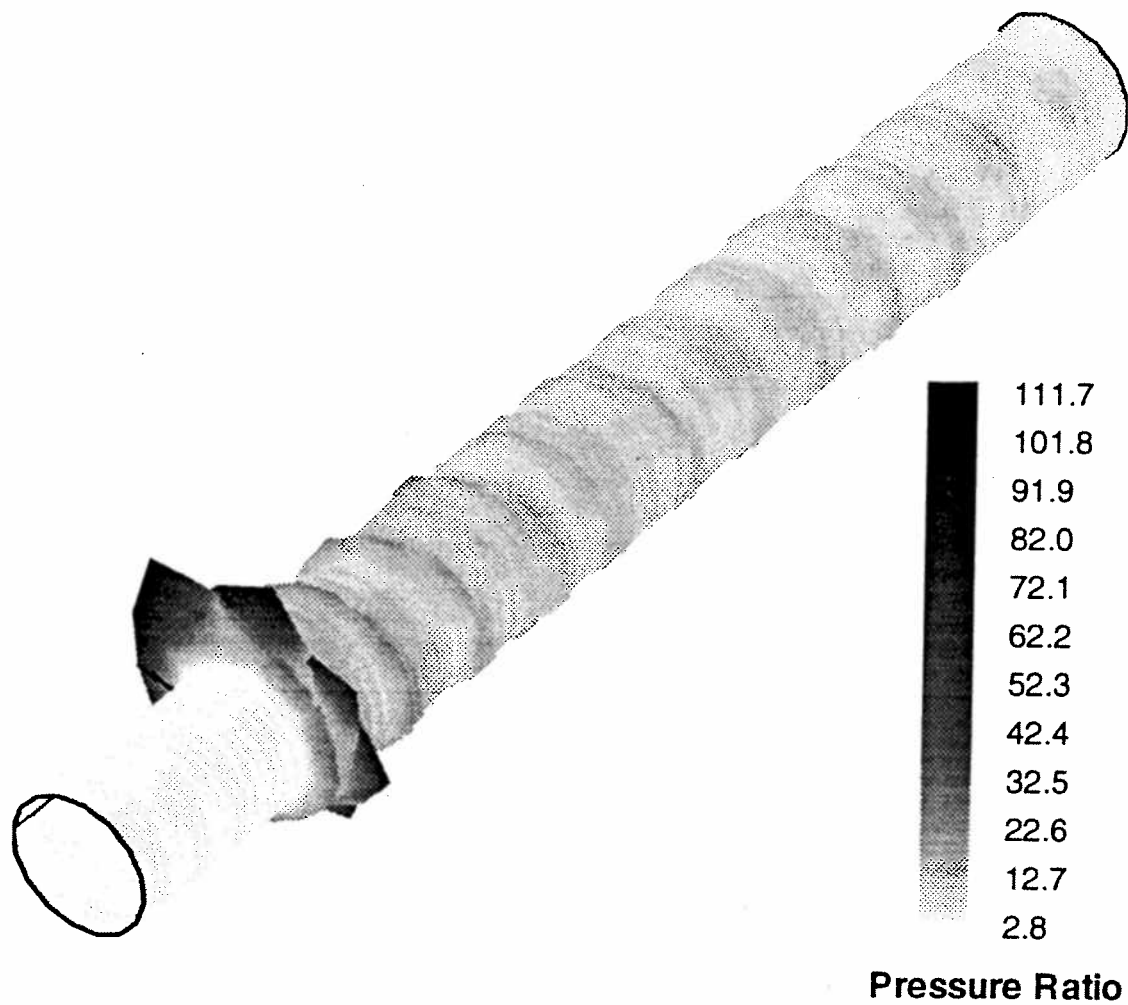


Fig. 2.4 Three-dimensional representation of the pressure data of Fig. 2.2.

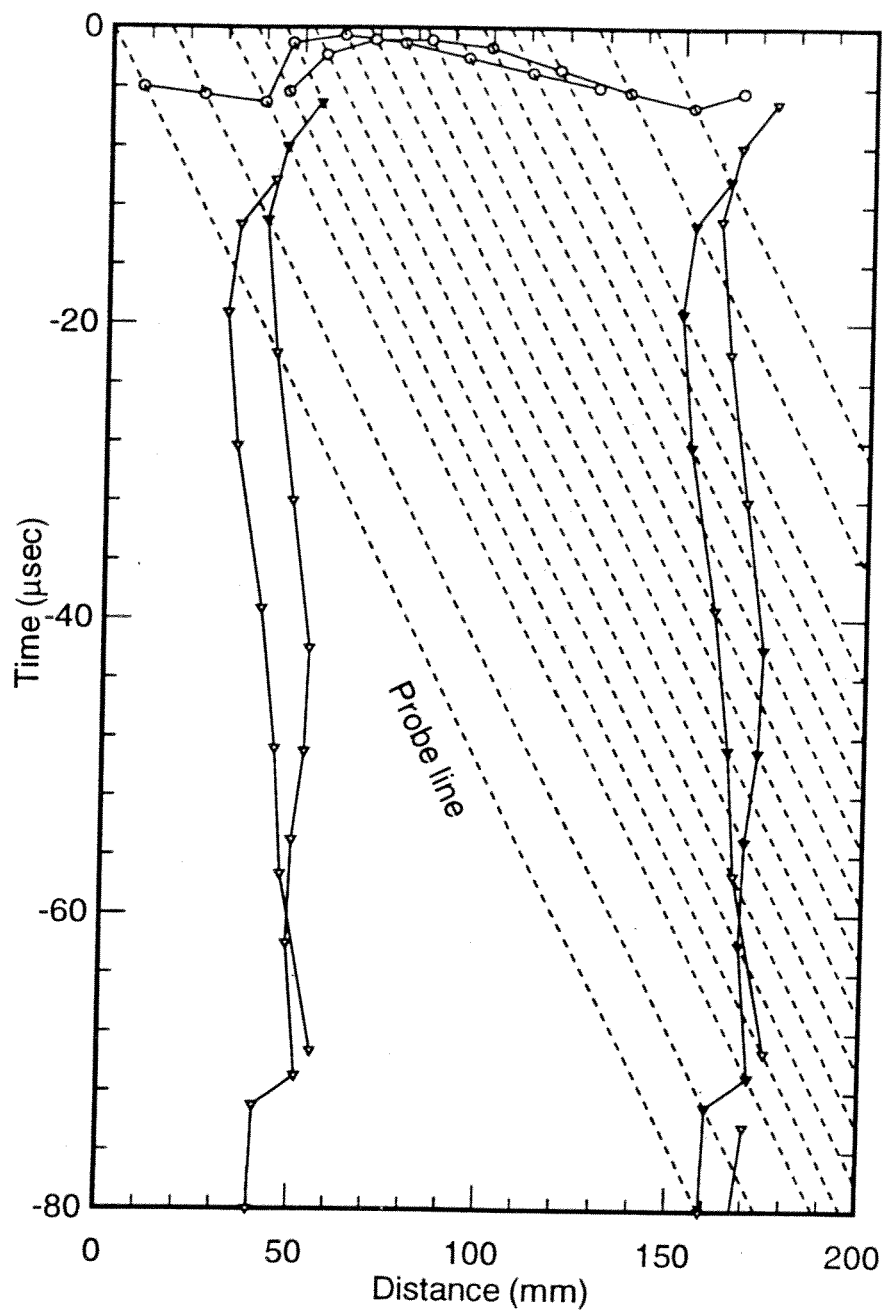


Fig. 2.5 Lead and secondary shock locations of the data in Fig. 2.2.

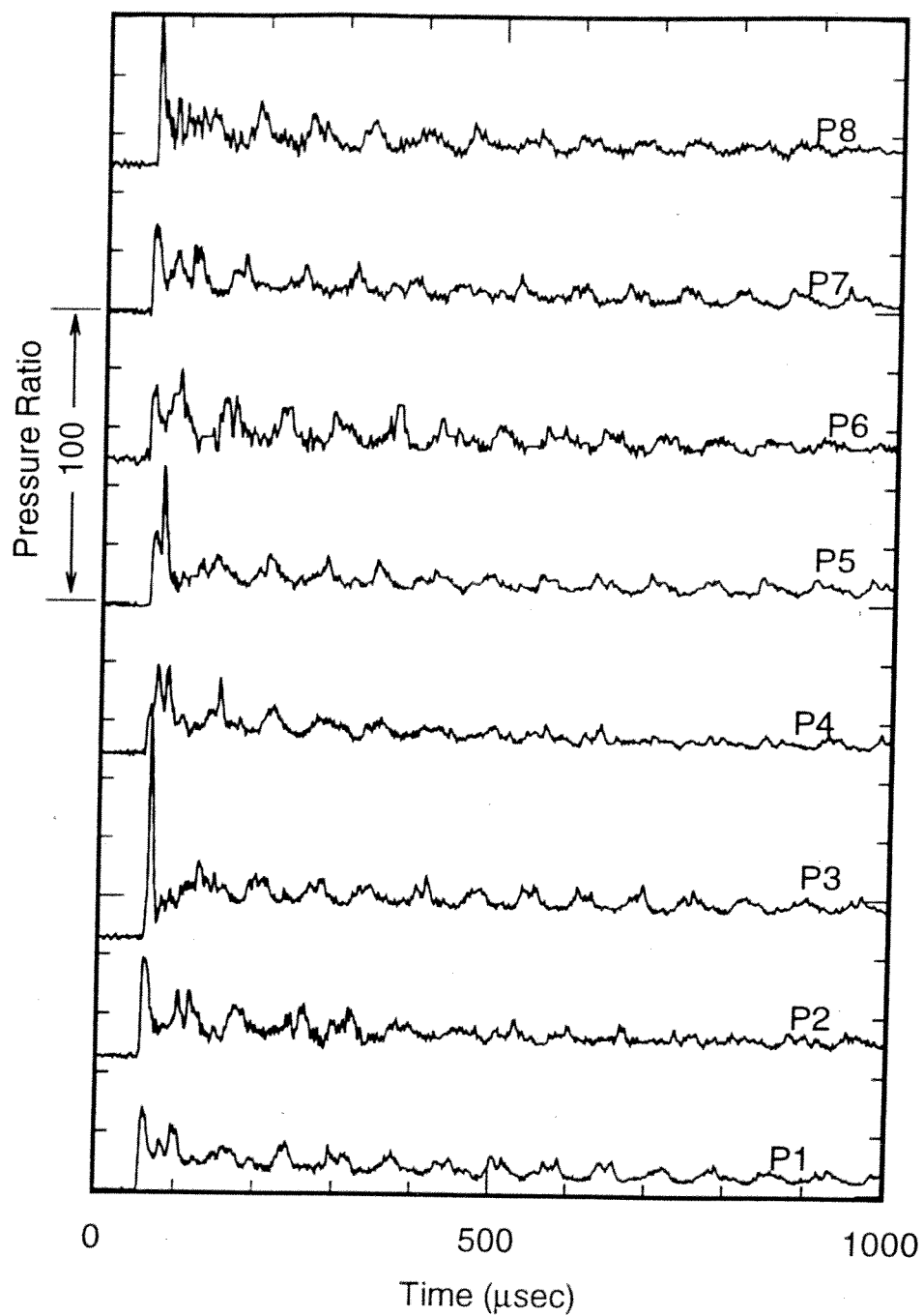


Fig. 2.6 First two sets of pressure data from the passage of a spinning detonation in the mixture $2.7\text{CH}_4+2\text{O}_2+5.8\text{N}_2$ at 21 atm.

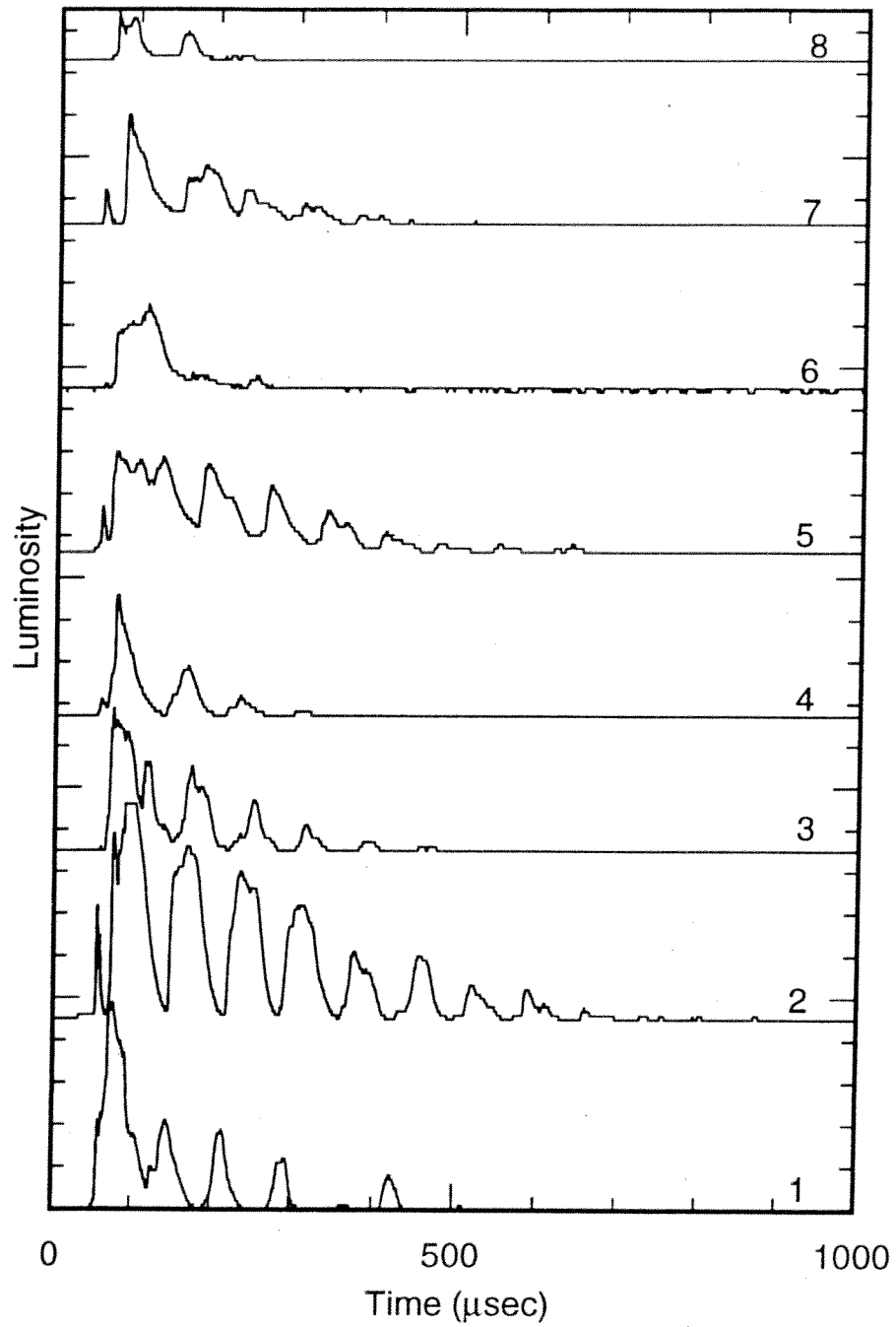


Fig. 2.7 Two sets of luminosity data from the passage of the spinning detonation shown in Fig. 2.6.

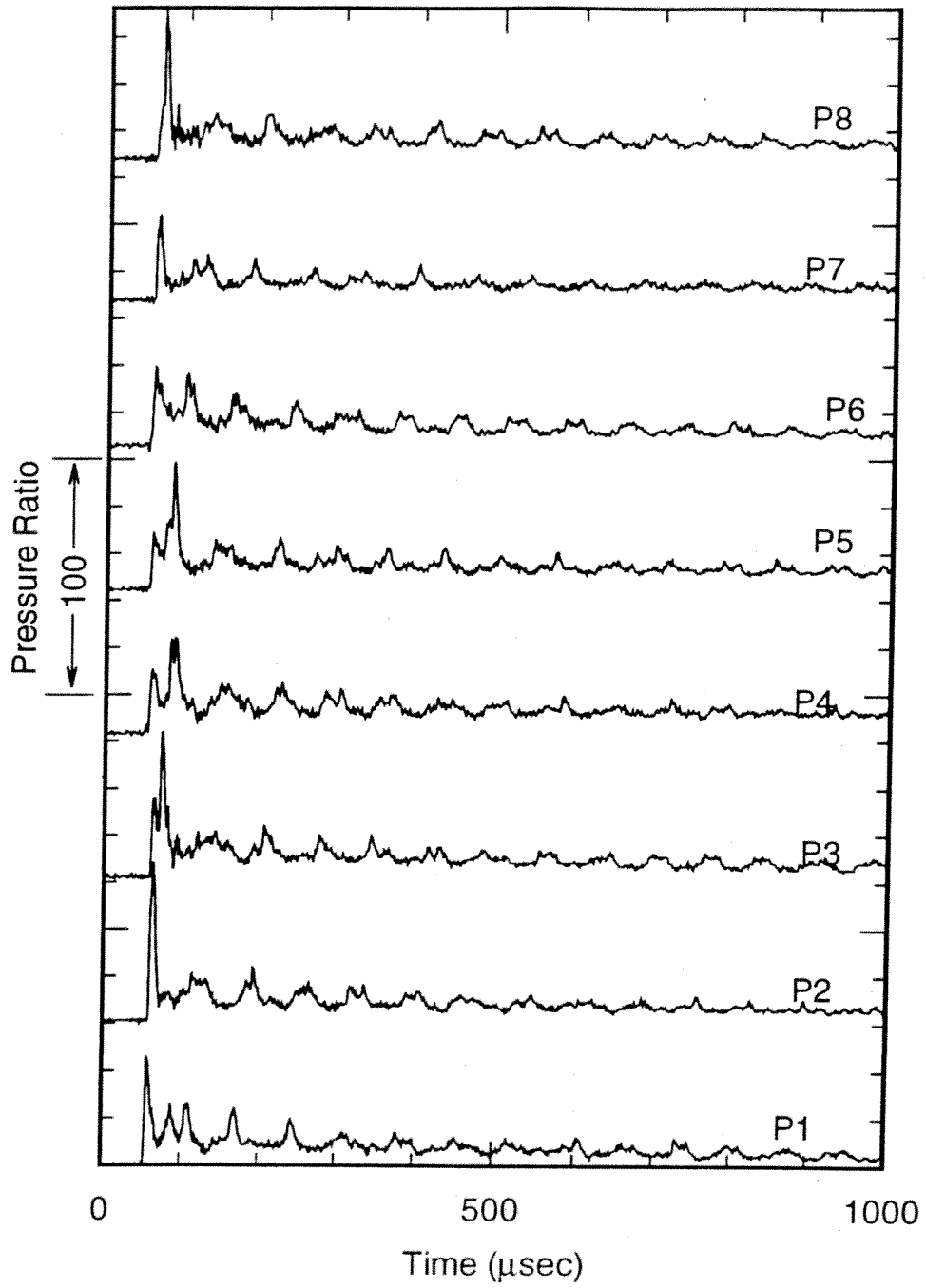


Fig. 2.8 Second two sets of pressure data from the passage of the spinning detonation shown in Fig. 2.6.

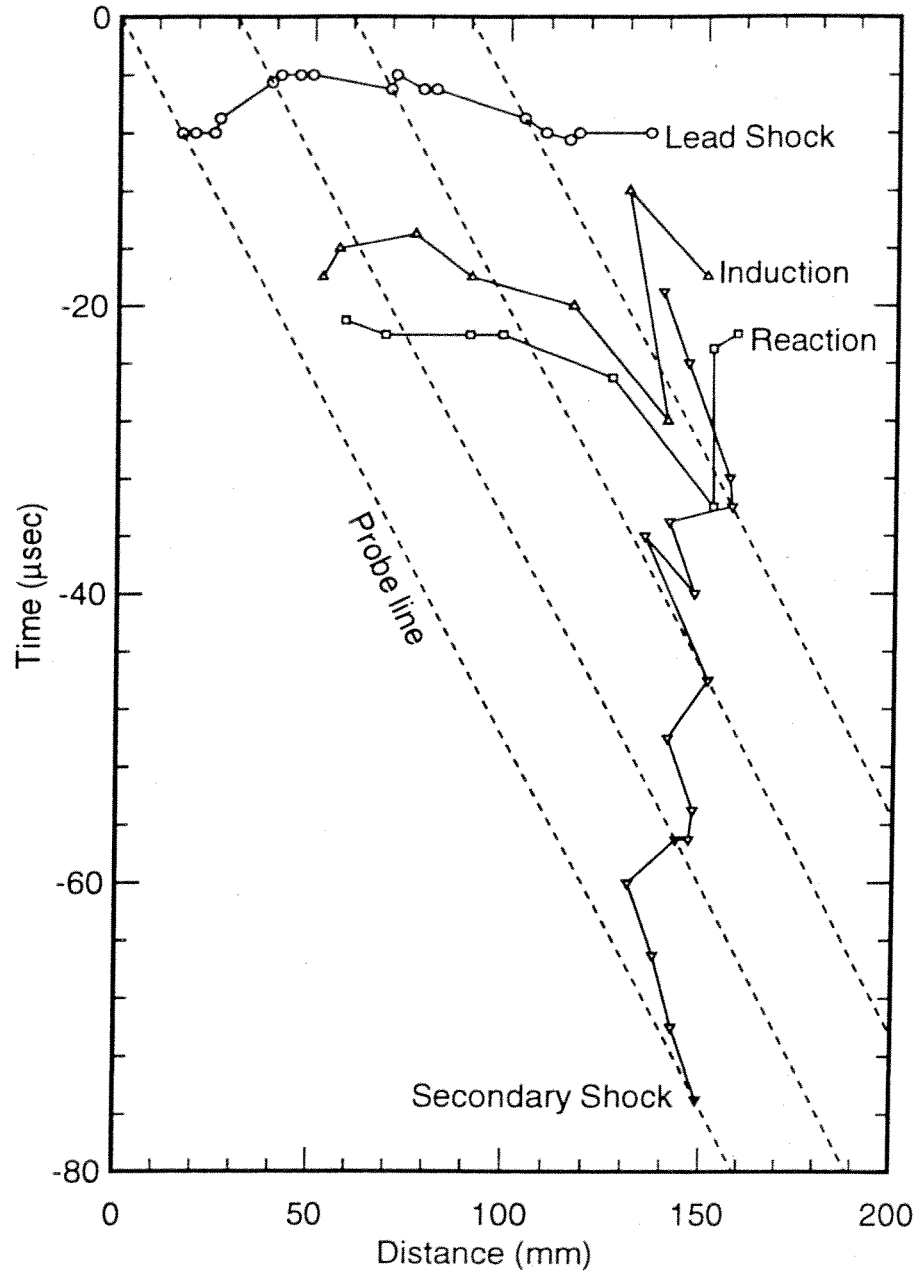


Fig. 2.9 Shock and luminosity locations of the data shown in Figs. 2.6 -2.8 .

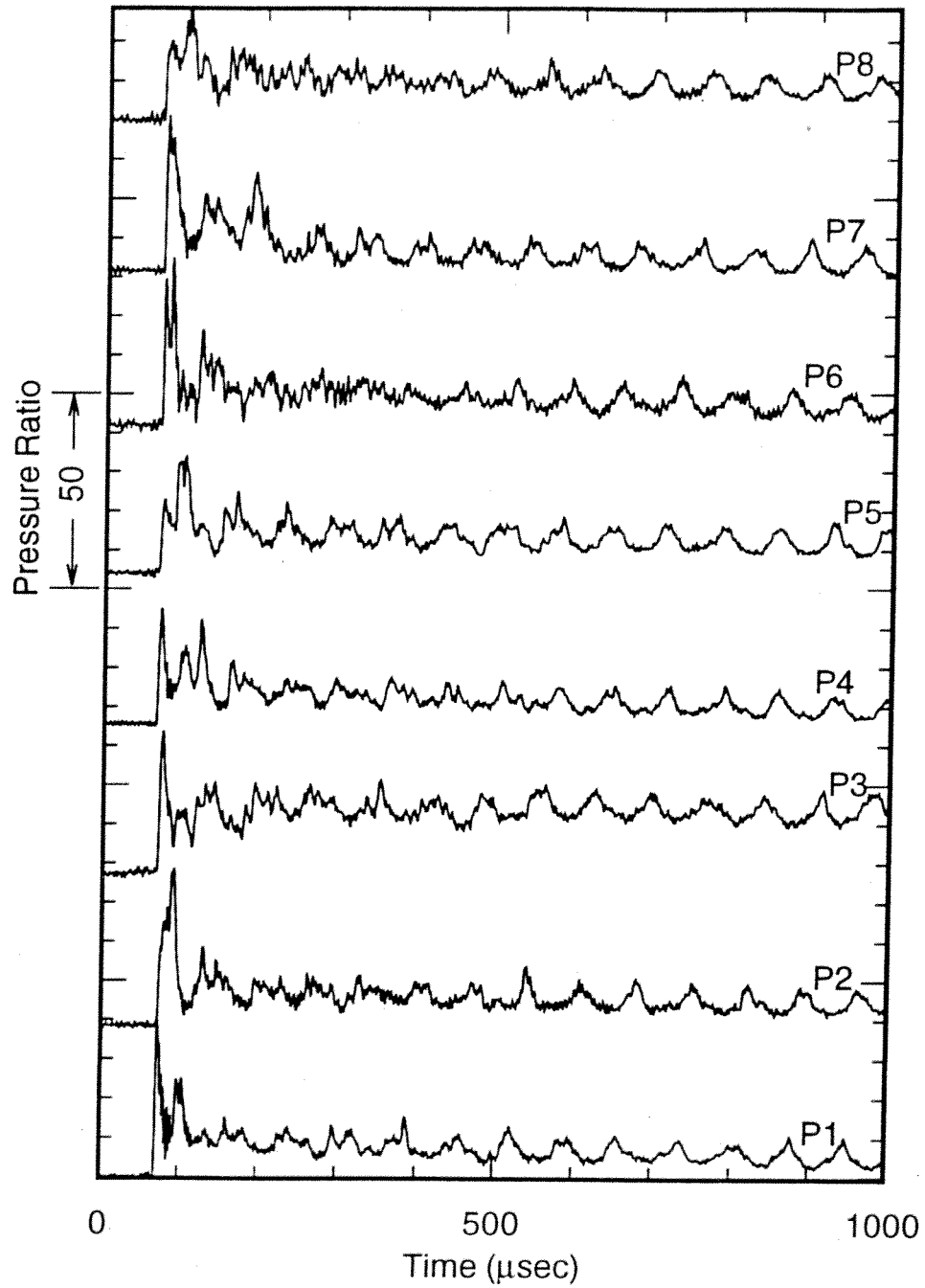


Fig. 2.10 First two sets of pressure data from the passage of a spinning detonation in a 21 atm mixture of $2.7\text{CH}_4 + 2\text{O}_2 + 5.8\text{N}_2$.

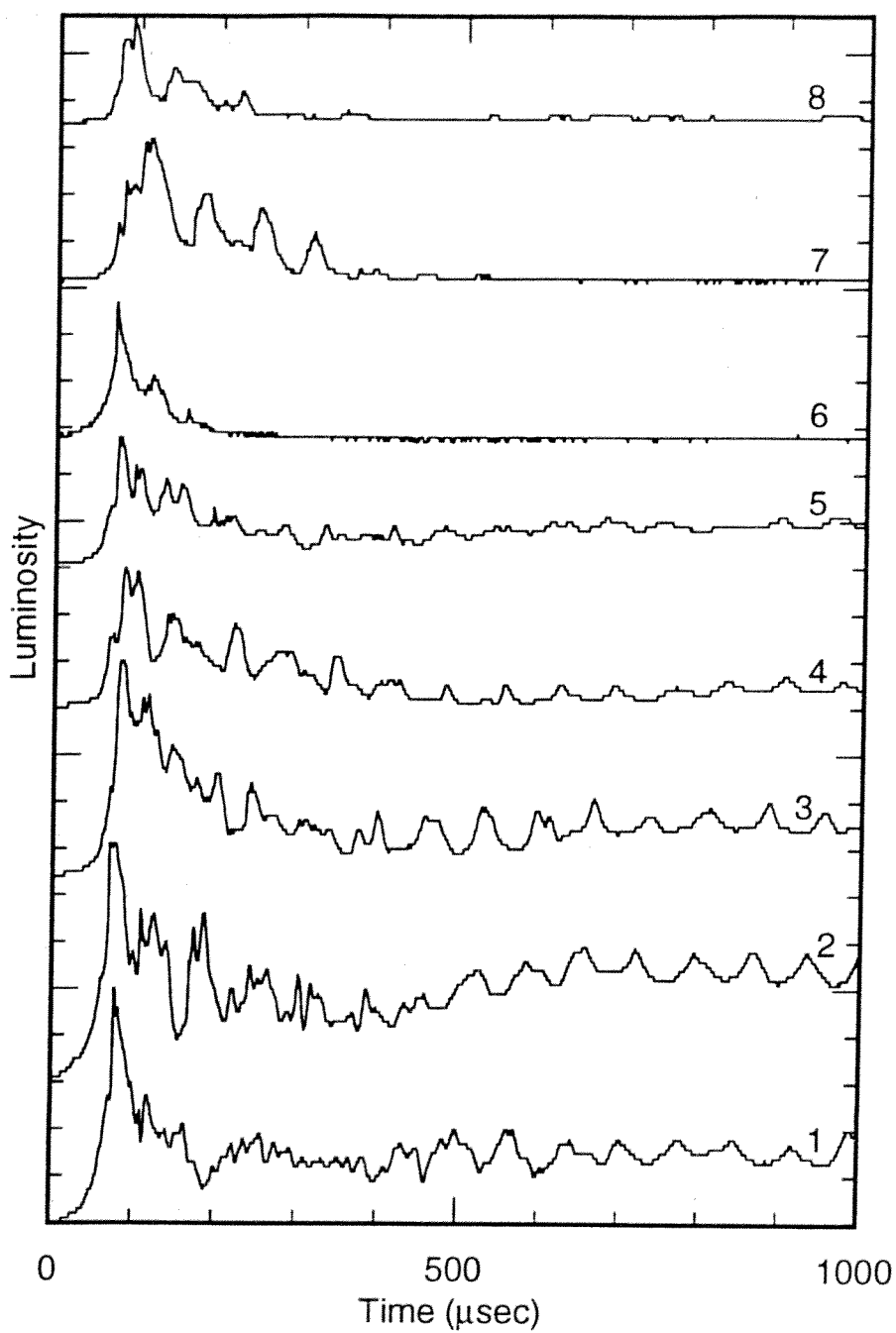


Fig. 2.11 Two sets of luminosity data from the passage of the spinning detonation shown in Fig. 2.10.

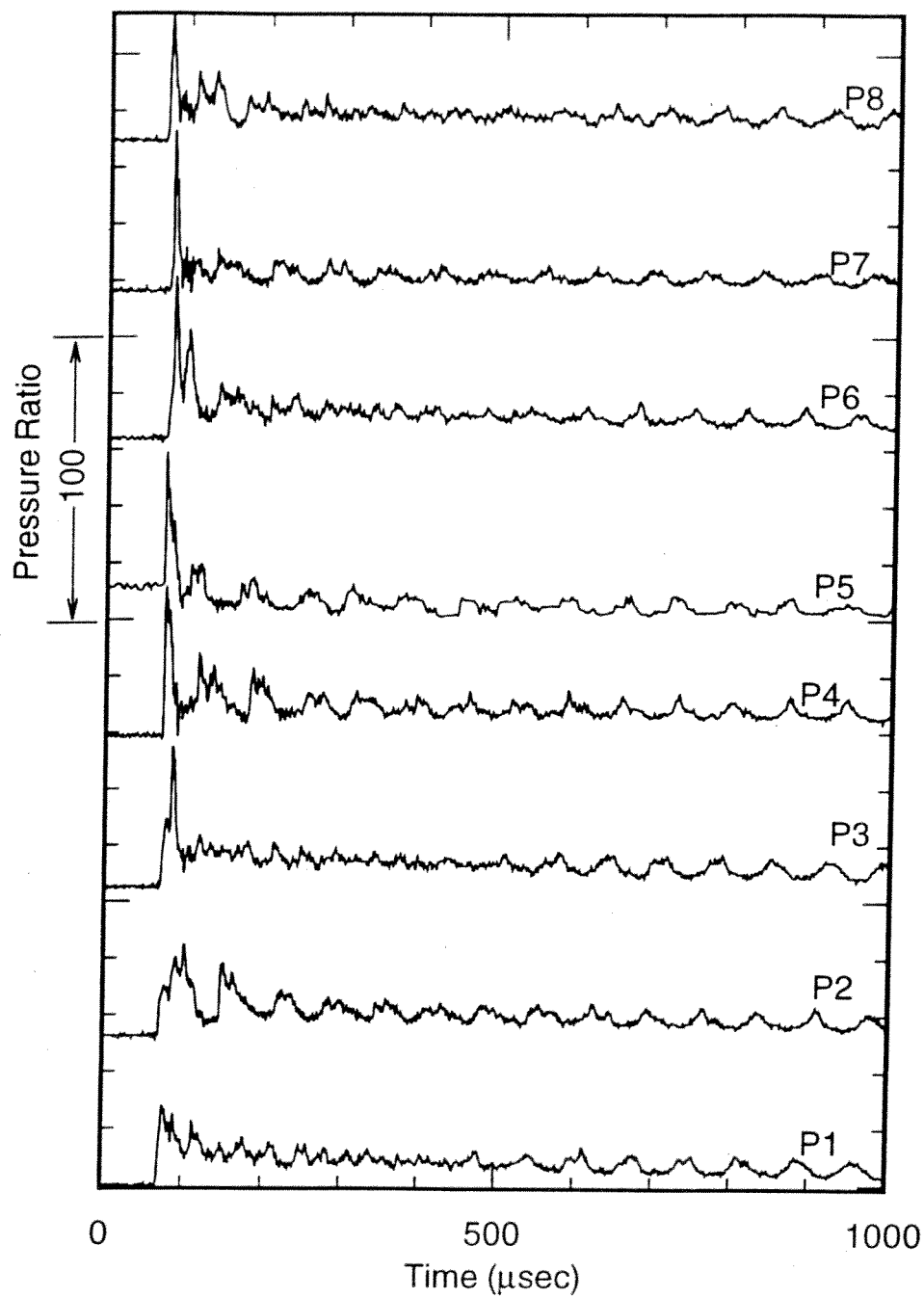


Fig. 2.12 Second two sets of pressure data from the passage of the spinning detonation shown in Fig. 2.10.

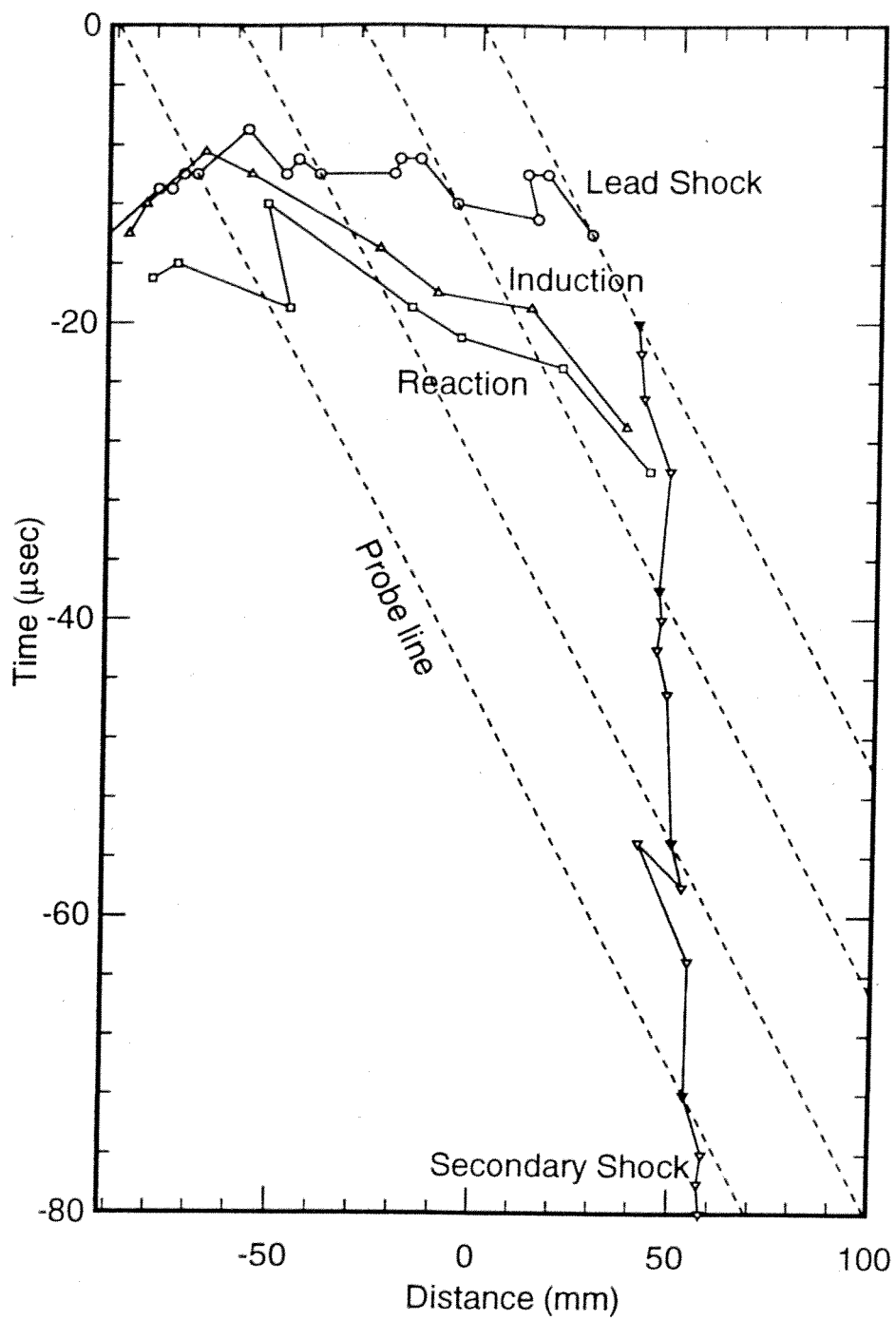


Fig. 2.13 Shock and luminosity locations of the data shown in Figs. 2.10 - 2.12.

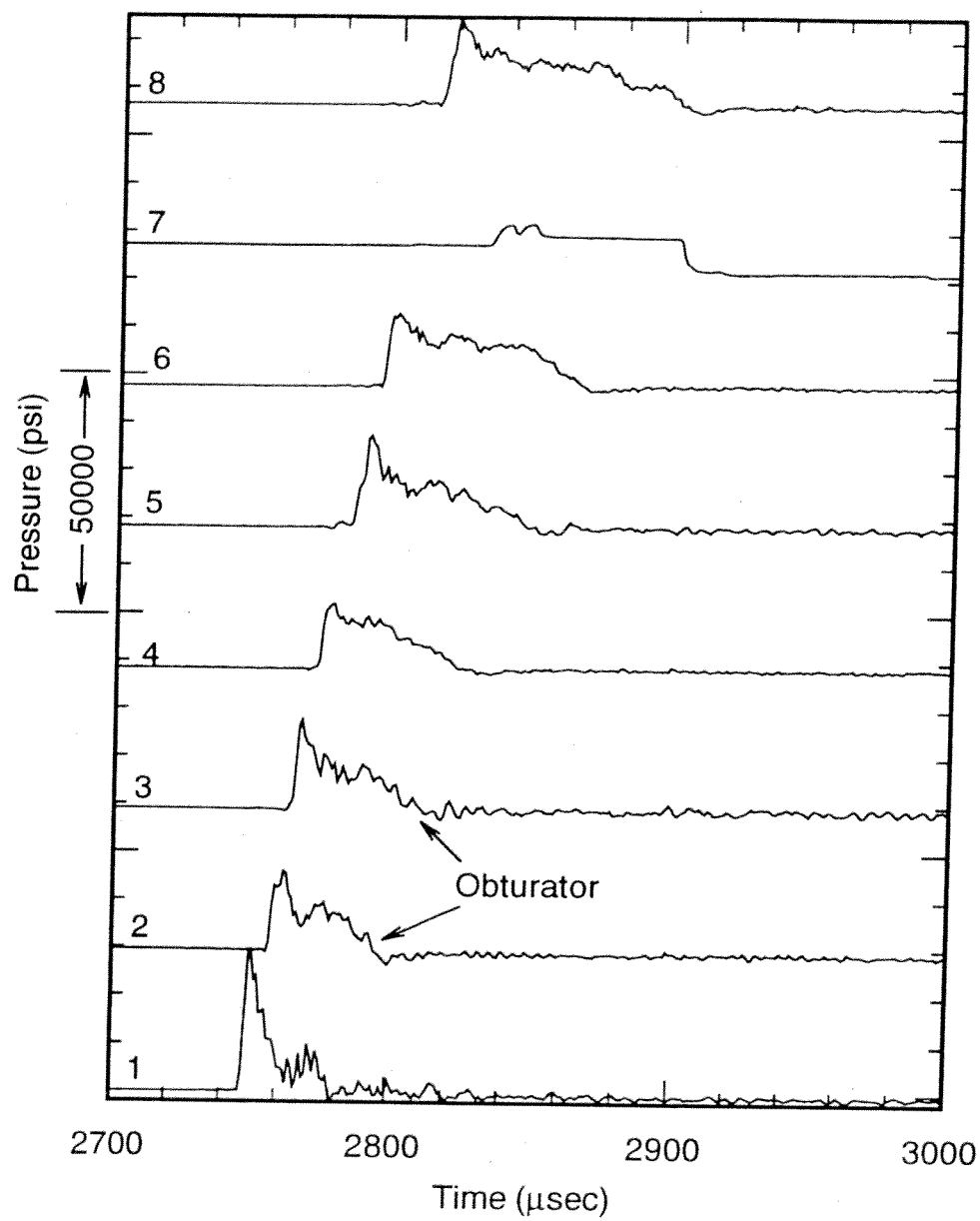


Fig. 2.14 Pressure data from the initiation of a detonation with an obturator in a 24 atm mixture of $2.7\text{CH}_4+2\text{O}_2+5.8\text{N}_2$.

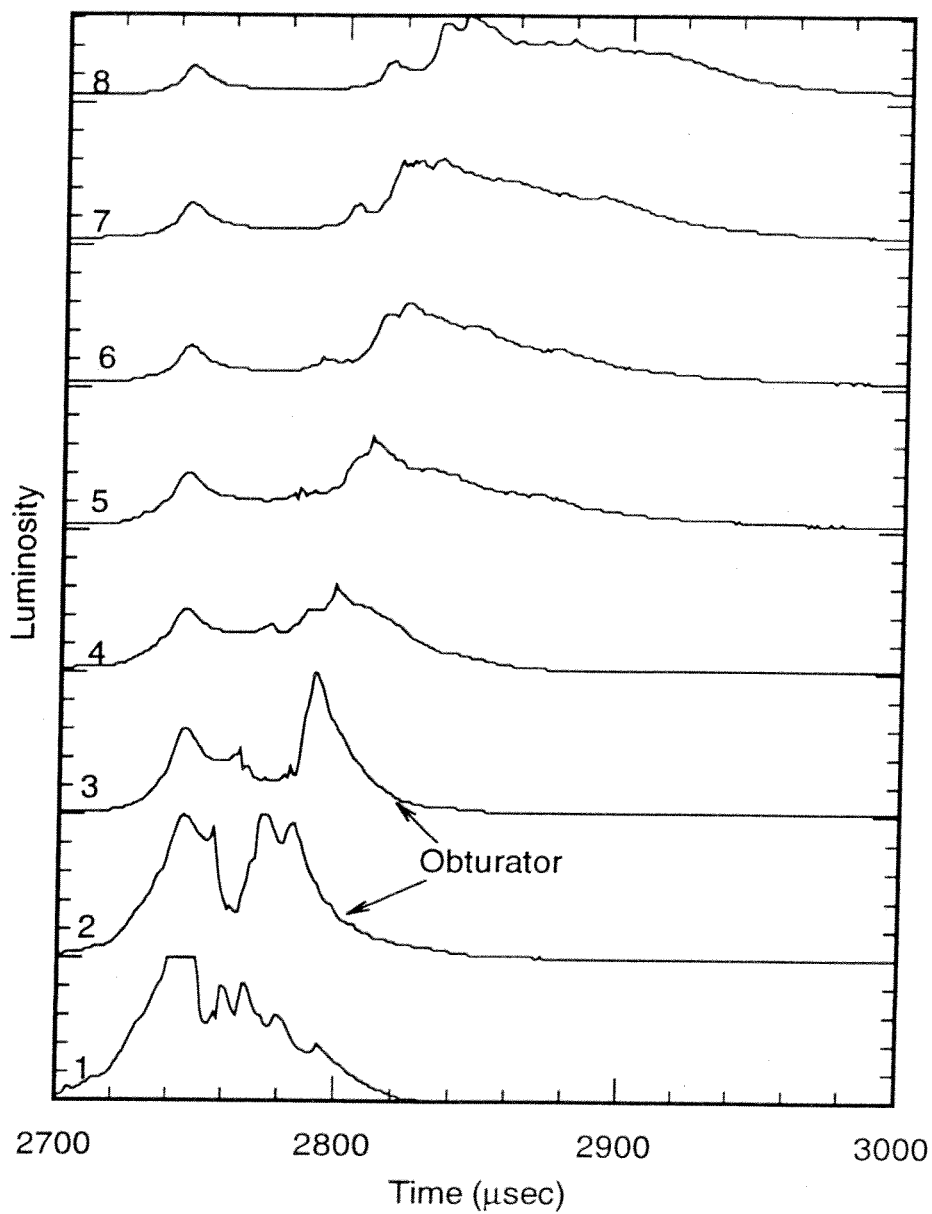


Fig. 2.15 Luminosity data from the same experiment as shown in Fig. 2.14.

III. THREE DIMENSIONAL EFFECTS

For the remainder of the experiments discussed, projectiles were launched into both inert and reacting gas mixtures. The main emphasis of these experiments is on the starting of the projectile diffuser and ignition of the combustible gas. It now becomes important to discuss the influences of the three dimensional effects of the projectile fins on the flow so that they may be distinguished from transients due to starting.

Recently many papers have discussed experimental and numerical influences of projectile fins and canting of the projectile.^{11,15-17} During the starting process the projectile is in good condition and has not been observed to cant in the tube. For this reason canting will not be discussed here. The influence of projectile fins during starting has been observed and may be confused with shock motions on the projectile body; therefore, the influence of the fins on steady flow will be discussed to prevent future confusion.

3.1 Experimental Three-Dimensional Results

Several experiments were performed in a single 16 m long, methane-based mixture consisting of $2.7\text{CH}_4+2\text{O}_2+5.8\text{N}_2$, which has an experimentally determined detonation speed of approximately 1750 m/s.¹⁵⁻¹⁷ Four-fin projectiles were manufactured from 7075-T651 aluminum alloy by computer numerical control (CNC) machines. These were used for this series of experiments because the CNC machines produced projectiles that were nearly geometrically identical. All projectile masses are approximately 74 gm with a maximum deviation of 0.3 gm. Using a light gas gun, the projectiles were pre-accelerated to a velocity of approximately 1150 m/s before entrance into the ram accelerator section of the facility. The HITS or a pair of inserts were then installed at a position along the tubes where the projectile would have the desired velocity.

Figure 3.1 shows pressure and luminosity data for a projectile traveling 1540 m/s in a 24 atm mixture. The lower traces correspond to flow 45° from a fin (in the center of a channel) and the upper traces correspond to the flow directly over a fin. There is an enormous difference in the character of the tube wall pressure data. The reflection of the initial conical shock from the tube wall is equal in amplitude, but that is where the similarity ends. The data from directly over a fin show a large pressure and luminosity spike just past the projectile throat. This is caused by multiple shock reflections between the tube wall and the fin leading surface and possible stagnation of the flow near the tube wall/fin junction. The pressure and temperature are both high and it is possible that this causes some localized combustion of the flow. The high pressure caused by the fin then expands around the side of the fin and generates a shock seen later in time in the center of the channel. The luminosity seen in the middle of the projectile body in the channel flow is associated with the hot gas generated by the fins. Both sets of data then show a shock near the base of the projectile and luminosity behind the projectile. These traces demonstrate that large shocks and luminosity spikes just past the projectile throat, as well as shocks in the channel between two fins, may be due to 3-dimensional effects rather than to transients of the flow.

A complete set of pressure data from around the circumference of the tube is shown in Fig. 3.2. The resulting pressure traces from each angular position in the HITS are denoted by numbers 1 through 8 as shown in the top of the figure. This also shows the projectile fin orientation relative to the pressure traces. In this experiment the fill pressure was 18 atm and the projectile velocity was 1440 m/s. A small outline of one half of a projectile is placed at the bottom of the figure to indicate the position of the projectile body and fins relative to the pressure traces. The first rise in pressure, which appears similar in all traces, is the reflection from the tube wall of the conical shock generated by the projectile nose. Traces 2, 4, 6, and 8 are unlike those of 1, 3, 5, and 7 because of the large pressure spikes that appear slightly before the point where the

projectile fins' leading surfaces contact the tube wall. These pressure spikes coincide with the passage of the projectile fins directly over the pressure sensors. Traces 1, 3, 5, and 7 are then the tube wall pressures measured along the centers of the channels (the spaces between adjacent fins). The character of the flow appears to be radically different depending on the fin orientation relative to a sensor. The initial conical shocks are unaffected by the fin location; however, the fins have a tremendous influence on the remainder of the flow. A large pressure spike (pressure ratio ~ 35) is formed near a fin while the pressure in the channel drops due to the expansion over the nose cone/body joint. Later in time a lower amplitude pressure spike is seen in the channel and the pressure over the fins is reduced. The high pressure spike near the fin in traces 2, 4, 6, and 8 of Fig. 3.2 is a result of the reflected shock system between the leading surface of the fin and the tube wall. The disturbances caused by each fin intersect and result in the high pressure spike seen later in the channel.

The pressure distribution on the tube wall as the projectile passes through the tube can be visualized, as done with the previous spinning detonation, by representing the measured (or calculated) tube pressure as the radial distance of a point away from the surface of a cylindrical tube representing the ram accelerator tube wall. The different angular stations in the HITS or the inserts correspond to the same angles on the hypothetical tube. The length of the tube represents time in the stationary (lab) reference frame or distance in the projectile (moving) reference frame (assuming steady flow). Another way to explain this visualization is as if the projectile were traveling through an infinitely thin, flexible tube that deforms radially outward proportional to the instantaneous pressure on the tube wall. Figure 3.3 represents such a visualization with the experimental pressure data of Fig. 3.2. Both the surface shading and radial distance from the tube wall are proportional to the pressure. Data between angular stations were linearly interpolated. A projectile with the correct fin orientation with respect to the pressure surface

is also shown for reference. The surface is cut along the centerline of a channel and a fin in this and all similar figures. The fin and channel shocks are more apparent in this format as opposed to the line plots of Fig. 3.2.

3.2 Numerical Three-Dimensional Results

The measured tube wall pressure profile in the channel between the fins more closely matches those pressure traces produced by axisymmetric CFD simulations. The difference between the axisymmetric simulation and the experiment is shown by a large pressure rise after the initial set of conical shocks and is a result of the intersection of the disturbances caused by the high pressure regions generated by the flat leading surface of the fins. Figure 3.4 compares the tube wall pressure distributions from an experiment with two calculations using inviscid, nonreacting, axisymmetric and three-dimensional CFD codes. All three traces are from a projectile traveling at Mach 4.0 while the assumption of steady flow has been made to translate time into distance for the experimental data. The strengths of the first two shock reflections from the tube wall are similar for all three plots, while the subsequent waves are dissimilar for the axisymmetric and three-dimensional traces. Conversely, the experimental results are closely approximated by the three-dimensional simulation. Discrepancies between the experimental data and the three-dimensional simulation can be explained by a slight canting of the projectile, differences in the fin gap and/or localized combustion near the leading surface of the fin.¹⁵⁻¹⁷ These comparisons to experiment by nonreacting codes may be done because at this Mach number the normal shock is at the very end of the projectile body, leaving most of the flow around the projectile supersonic and unreacted.

Figure 3.5 shows the corresponding plot of the computed tube wall pressure distribution over the projectile utilizing the three-dimensional, inviscid, nonreacting CFD code. The computed distribution is much smoother than the experimental results, but they generally correlate very well. Both show the

large pressure spikes associated with the leading surfaces of the fins, as well as the pressure reduction as the high pressure gas expands from the fin gap into the channel. The shocks from the leading surfaces of the fins intersect along the center of the channel and form a pressure rise which then decays in both plots. These data illustrate that the flow around the projectile body is affected by the shocks generated at the leading surface of the fins; therefore, two-dimensional axisymmetric simulations are inadequate to model the details of the flow field around the projectile body.

Because the tube wall pressure distribution calculated with the three-dimensional CFD code correlates well with the experimental data, there is confidence in the calculated pressure distribution on the projectile body, shown in Fig. 3.6. The plot is of a three-dimensional projectile with the surface shading corresponding to the calculated pressure. Note the effect of the intersecting fin shocks on the body pressure distribution and the very high pressure on the faces of the leading surfaces of the fins. Also notice the high pressure regions on the conical part of the body near where the fin and body join. Experimentally, it has been observed that material is often eroded from this area of the projectile as well as from the leading surfaces of the fins. These observations lend support to the accuracy of the three-dimensional simulations.

This data further eliminates the difficulty in tracking transient shock activity if the flow is assumed to be 2-dimensional. By knowing the projectile orientation and the character of the steady 3-dimensional flow around the projectiles, it is possible to accurately track the transients of the starting and ignition process.

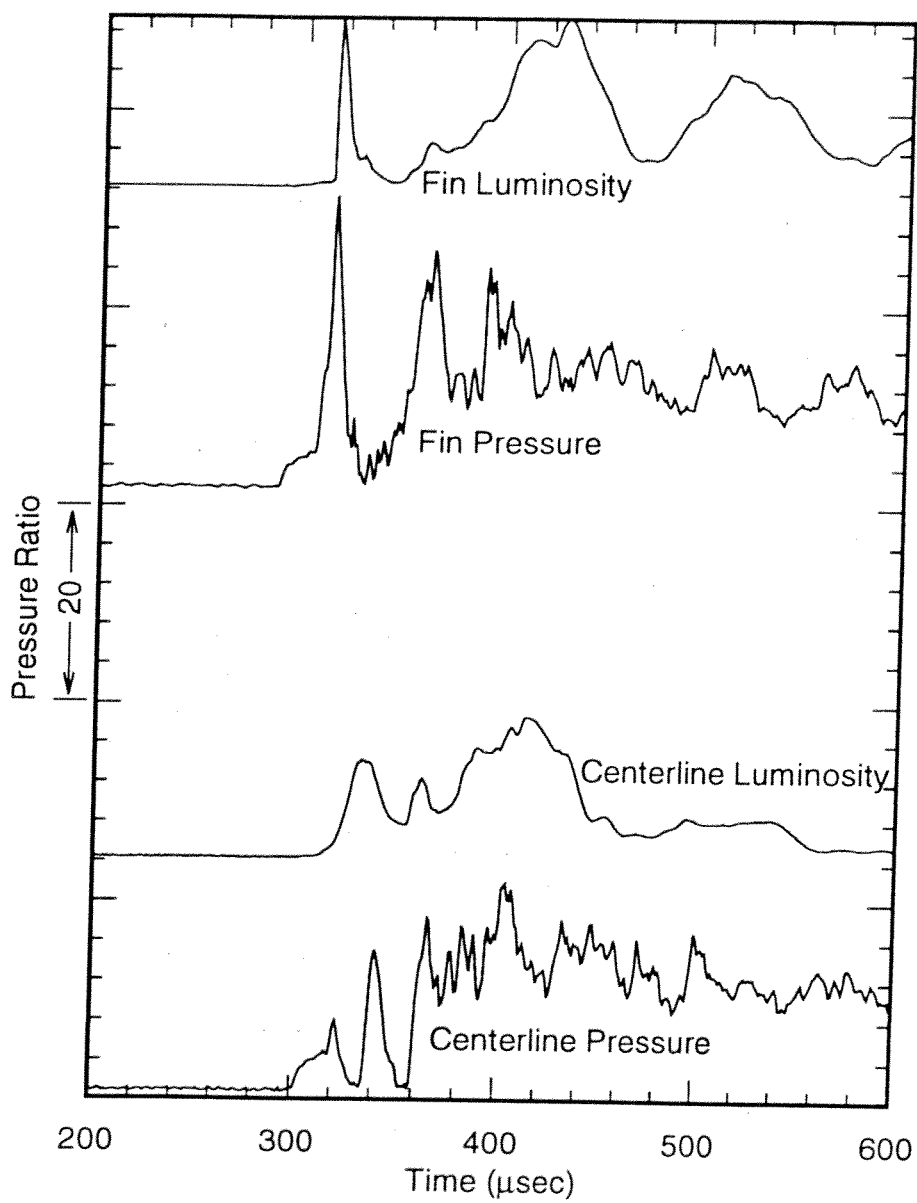


Fig. 3.1 Experimental pressure and luminosity data from a channel and from over a fin for a projectile traveling 1540 m/s.

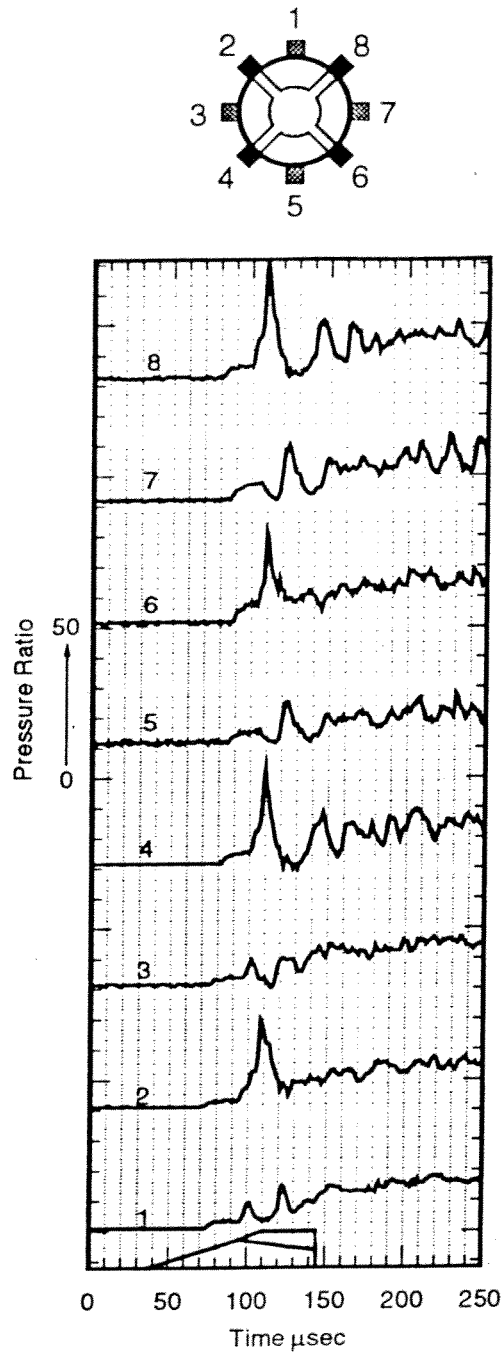


Fig. 3.2 Pressure data from an experiment where the projectile was traveling 1440 m/s.

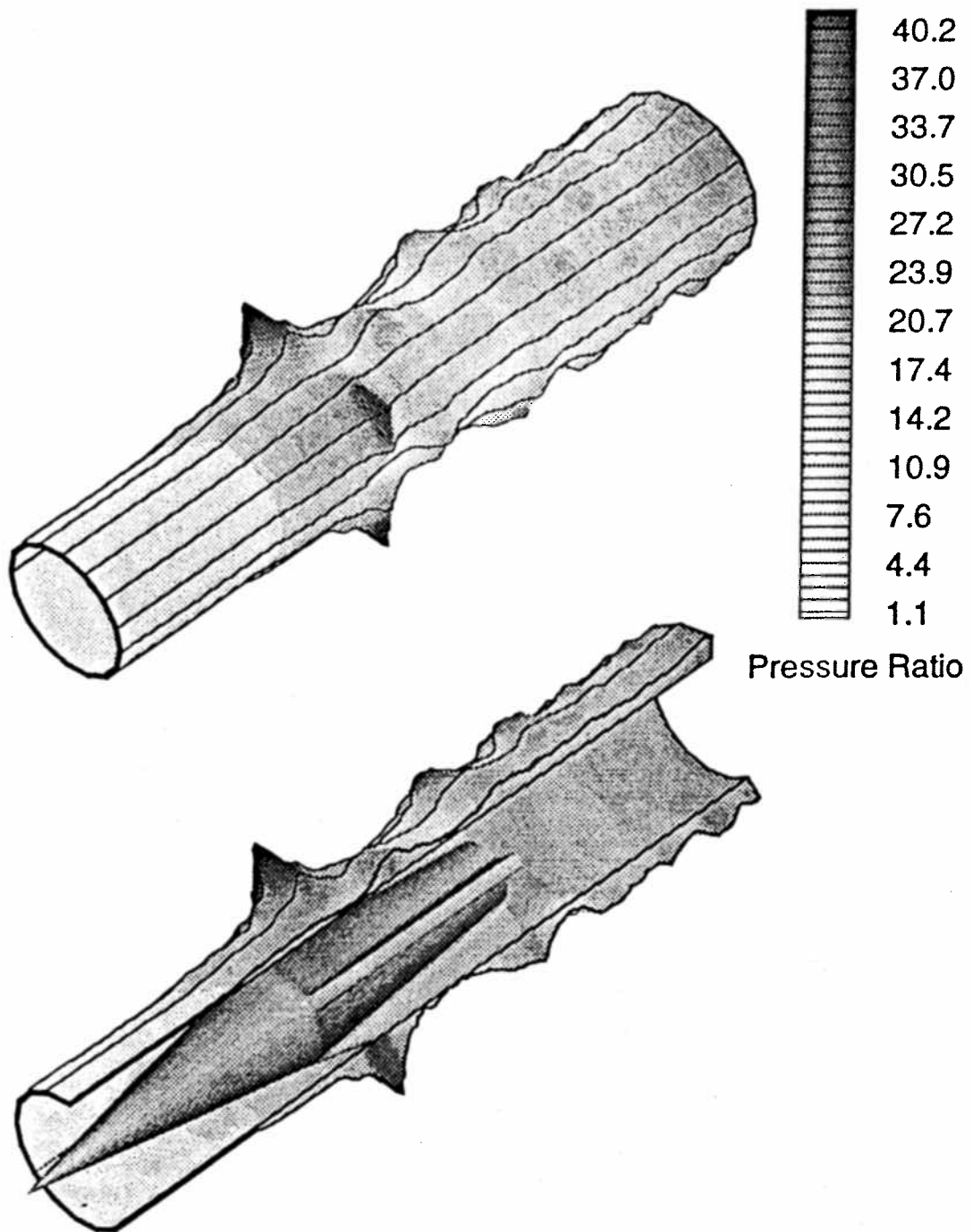


Fig. 3.3 Three-dimensional representation of the pressure data of Fig. 3.2.

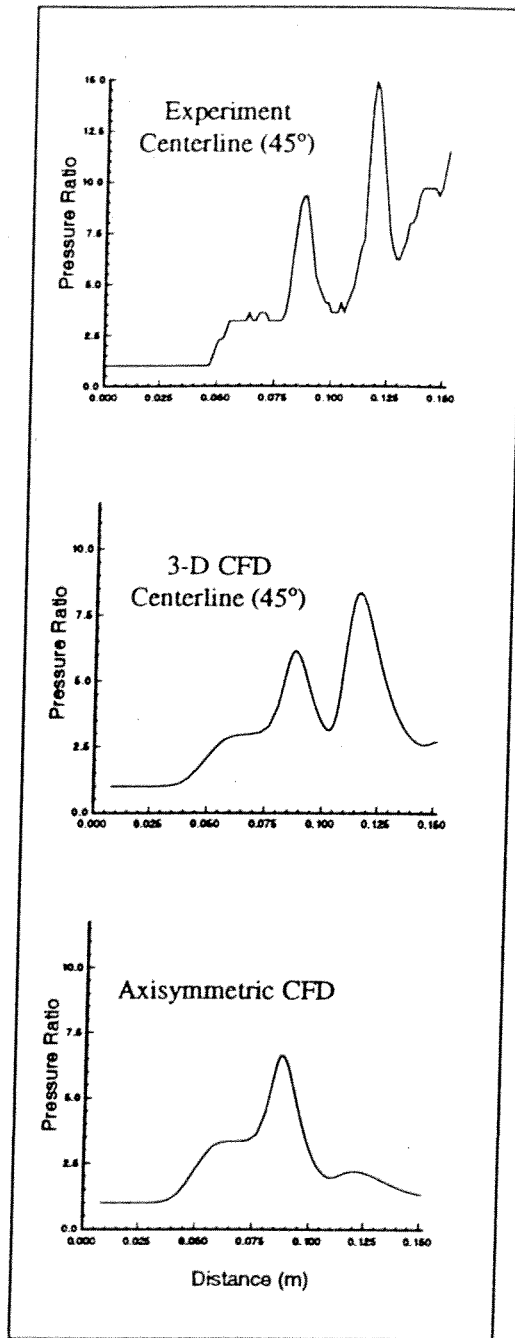


Fig. 3.4 Comparison of experimental pressure data from Fig. 3.2 with axisymmetric and 3-dimensional CFD calculations.

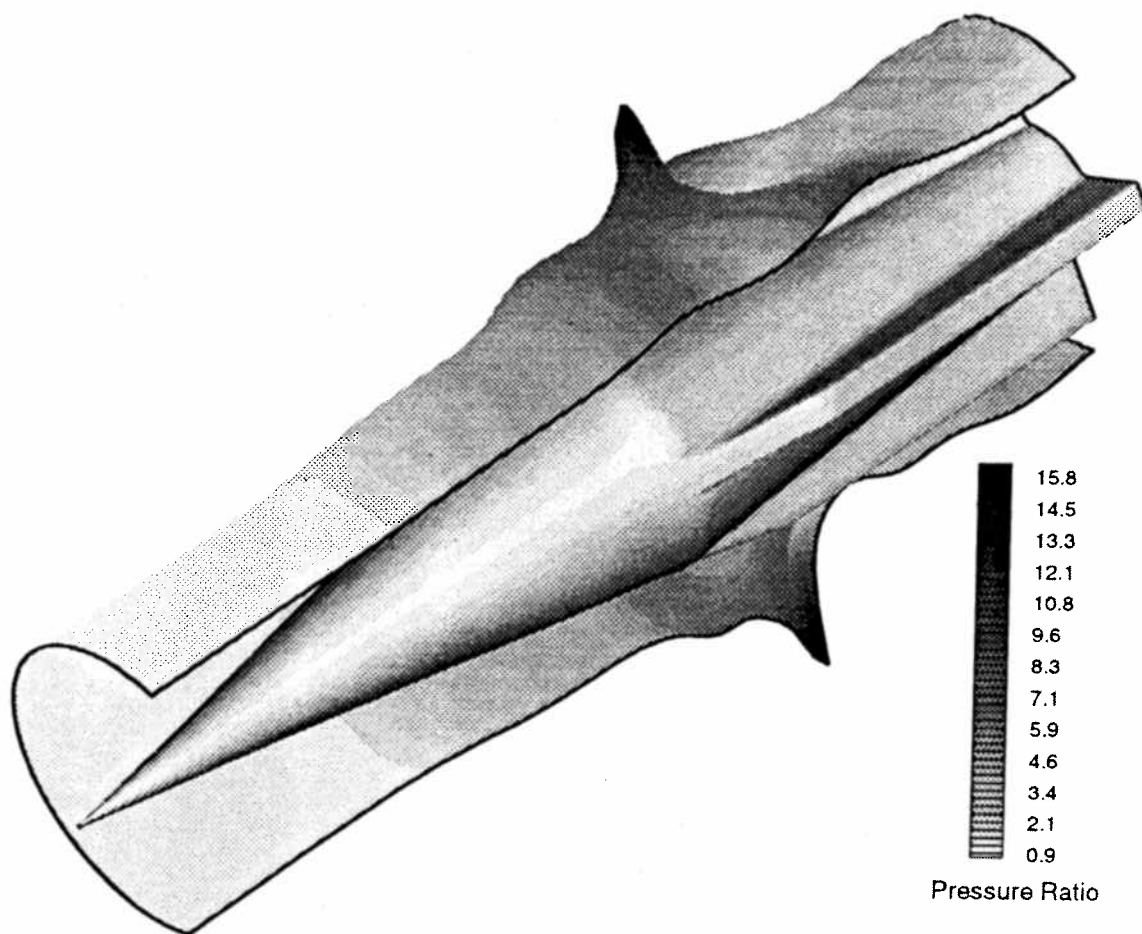


Fig. 3.5 Three-dimensional representation of the tube wall pressure obtained from a non-reacting, 3-dimensional CFD simulation.

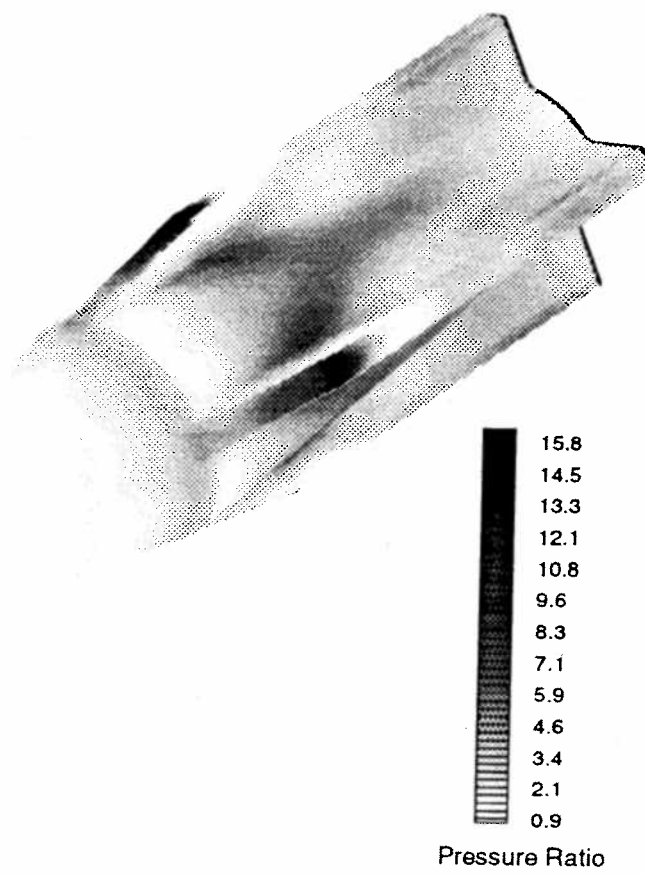


Fig. 3.6 Representation of the pressure on the projectile surface obtained from a non-reacting, 3-dimensional CFD simulation.

IV. THE STARTING PROCESS

The starting process of the ram accelerator is relatively broad in its scope.¹²⁻¹⁴ The topics range from starting the diffuser and igniting the flow to establishing stable combustion behind the projectile. The transients of the starting process are important for all ram accelerator sizes, regimes of operation, operating pressures, and gas mixtures. The understanding of these transients can prevent many discouraging and expensive experiments when new conditions, such as changing scale or operating pressure, are encountered. This chapter details the starting process in inert and reacting mixtures from an experimental point of view and discusses various conditions which inhibit the successful starting of a ram accelerator.

4.1 Idealized Starting Process

A description of an idealized starting process provides a convenient reference when discussing the actual process. In the ideal case, the backplate and obturator seal the tube completely and prevent leakage of the helium driver gas during the launch process. In the evacuated launch tubes the assembly of projectile, obturator, and backplate are accelerated to the desired entrance velocity. Before the projectile impacts the Mylar entrance diaphragm, it passes through a vent section where the helium driver gas is vented. Figure 4.1 shows schematically the following description of the projectile entering the accelerator section. The projectile pierces the entrance diaphragm and enters the combustible gas mixture. Any effect of the diaphragm on the gas or projectile is neglected. The diffuser starts upon entering the stationary gas when the projectile Mach number is greater than its Kantrowitz Mach number. (The Kantrowitz Mach number is the supersonic Mach number at which the flow at the throat of the diffuser of the projectile is sonic.) Once the diffuser is started the relative flow velocity over the entire projectile is supersonic. The supersonic flow then encounters the obturator and backplate resulting in the generation of a normal shock. The backplate is dislodged from the obturator

and the shock is driven onto the body of the projectile. The high temperature zone caused by this interaction causes the flow to begin reacting. The holes in the obturator act as choked orifices which interact with the normal shock for a long enough period of time that combustion stabilizes at the base of the projectile. The obturator rapidly decelerates and typically within 1 to 2 m, depending on the initial fill pressure of the accelerator section, no longer interacts with the projectile. This is because the combustion of the gas thermally chokes the flow between the projectile and obturator preventing interaction of the obturator with the projectile. The projectile continues to accelerate and is no longer affected by the obturator.

The idealized view of the starting process is relatively accurate, but much of the detail is missing. The major assumptions are that the backplate and obturator completely seal the tube, that the launch tubes are completely evacuated, that the diaphragm has no effect on the combustible gas or projectile, and that the flow is ignited by the shock generated by the obturator in the combustible gas. It is known from experimental observations, however, that the launch tubes are not completely evacuated and that the obturator does not always completely seal the tubes. Therefore, it should be expected that a shock will form and propagate in front of the projectile in the launch tube due to helium leakage and the "piston" effect of the obturator. Figure 4.2 shows a more realistic view of the shock dynamics in the launch tube and accelerator section. A shock is created in the launch tube from the acceleration of the projectile and leakage of helium past the obturator. This shock reflects from the entrance diaphragm and travels back up the launch tube toward the projectile. The reflected shock in turn reflects from the projectile and obturator and travels back toward the entrance diaphragm where, assuming the diaphragm does not burst, it reflects back toward the projectile. As the projectile enters the accelerator section, the highly compressed launch tube gas may have a variety of effects on the accelerator gas ranging from virtually no effect to pre-ignition of the combustible gas, depending on initial launch tube

pressure and severity of helium leakage. The following sections discuss the conditions that affect the starting of the ram accelerator and outline problem areas and their solution.

4.2 Diffuser Starting

To simplify the investigation of the starting process two different sets of experiments were performed. Three experiments were performed with a noncombustible gas mixture in the ram accelerator section to study the starting of the diffuser under a nonreacting or "cold" condition. "Hot" experiments, in which a combustible gas mixture of $2.7\text{CH}_4+2\text{O}_2+5.8\text{N}_2$ was used, were performed mainly to study ignition transients. In the hot experiments certain aspects of diffuser starting were also investigated.

The first experiment done to investigate diffuser starting was performed with approximately 0.1 psi of air in the launch tubes and a "cold" (nonreacting) mixture of $2.7\text{CH}_4+7.8\text{N}_2$ in the accelerator section (2 moles of nitrogen were used to replace 2 moles of oxygen of the standard "hot" or reacting mixture) at 360 psi. The 0.1 psi of air in the launch tubes was used to aid in measuring the initial shocks created by helium leakage and projectile acceleration. Two 0.014" Mylar diaphragms separated the launch tubes from the accelerator section. This is the standard diaphragm thickness for accelerator fill pressures below 600 psi (static burst pressure of 750 psi) and low launch tube pressure. The projectile, obturator, and backplate masses were 70.3 gm, 11.8 gm, and 3.4 gm, respectively. The assembly was launched from the light gas gun with 4450 psi of helium and achieved an entrance speed of 1170 m/s at the point of diaphragm impact. The configuration of the experiment is shown in Fig. 1.6. Three instrumented inserts were placed prior to the entrance diaphragm (the 0.1 psi side) and the HITS was placed immediately after. This arrangement allows for four viewing stations in the evacuated section and eight stations in the acceleration section to be near the entrance diaphragm.

Figure 4.3 shows the pressure data obtained from the launch tube side of the entrance diaphragm using the station numbers of Fig. 1.6. An initial shock, created from the acceleration of the projectile and minor helium blow-by, and its reflection from the entrance diaphragm are too low in amplitude to be seen on this pressure scale. The first pressure rise, seen at station 1, is the reflected compression wave from the projectile/obturator combination of the low amplitude reflected shock which was traveling from the diaphragm toward the projectile. Initially this pressure rise is not a single shock, but is a combination of shocks and compressions created by the reflections of a shock from the nose cone, fins, obturator and backplate. This series of compressions has coalesced into two shocks at station 2. By station 3 these two shocks have merged into a single, stronger shock. Station 4 shows the arrival of this shock and a short time later its reflection from the entrance diaphragm. This reflected shock travels toward the projectile as seen at stations 4, 3, and 2. This shock in turn reflects from the obturator and is seen again at stations 2, 3, and 4. The passage of the obturator and backplate is marked by a jump up in pressure (to the expanded gas gun pressure) at station 1 and a jump down in pressure at stations 2, 3, and 4. The pressure across the obturator and backplate jumps up to the expanded gas gun pressure at station 1 because the reflected shock from the diaphragm has not yet reached the projectile at this station. The pressure jumps down to the expanded gun gas pressure at stations 2, 3, and 4 because the second reflection has reached the obturator and has reflected from it by these stations, thereby increasing the pressure in front of the obturator above that of the expanded gun gas pressure.

Figure 4.4 shows the pressure data obtained from the accelerator section (HITS) during the same experiment discussed above. A general description of traces 5 through 12 follows. The first rise in pressure is the reflection from the tube wall of the conical shock generated by the passage of the projectile nose. This reflected shock reflects from the nose cone and in turn reflects again from the tube wall where it is seen as the second rise in pressure. An expansion from

the nose/body joint is then seen as a decrease in tube wall pressure. A normal shock can be seen on the body of the projectile and the base of the obturator can be identified as a rapid decrease in pressure. The separation of the backplate from the obturator can be seen at stations 5 through 12 as an increase and then a decrease in pressure behind the obturator. It should be noted that in this experiment the diffuser starts upon entrance to the acceleration section and remains started for more than 4 m. This can be seen in Fig. 4.5 which is the pressure data from the first five stations, numbered here 13 to 17, of the standard accelerator section. The traces show the supersonic profile associated with the projectile, followed by a slower, decelerating shock caused by the obturator. This demonstrates that there are no long term transients occurring near the projectile. Upon entrance to the accelerator section, the projectile was traveling at Mach 3.22, which is well above the experimentally determined Kantrowitz Mach number of 2.6.

It is of some interest here to compare luminosity and pressure data obtained from the same station in the launch tube section. Figure 4.6 compares luminosity and pressure from station 3. In the ideal model of starting there would be no pressure rise except for the small amount of helium driver gas that was not vented and there would be no luminosity at all because a nonreacting mixture was used. (It would be possible to get scattered or direct light from a combustible gas after it was ignited). It is clear from the figure that the gas in the launch tube does modify the ideal view substantially. The gas in the launch tube has been processed by many shock reflections and is hot as indicated by the luminosity sensor. The rise and decrease in luminosity seems to agree well with the passage of shocks and expansions that would increase and decrease the temperature of the flow respectively.

Figure 4.7 shows a distance-time ($x-t$) diagram of the experimental data of Figs. 4.3 and 4.4. This $x-t$ diagram clarifies the origin and motion of shocks that are typically encountered during the starting of a projectile. The entrance diaphragm defines the zero of the distance axis with values to the left

corresponding to the launch tube and values to the right corresponding to the accelerator section. Dashed lines represent the portions of the figure where extrapolation of the experimental data was used to complete the x-t diagram. Shocks are identified by letters on the figure and will be referred to in the following discussion. The incident shock (a), which is too low in amplitude to be seen in Fig. 4.3, travels in the direction of projectile motion until it reflects from the entrance diaphragm (b). The reflection (b) travels opposite to the direction of projectile motion until it is partially reflected from the nose cone of the projectile (c) and then the remainder is completely reflected from the obturator (d). The reflections from the nose cone (c) and obturator (d) both travel in the direction of projectile motion with the reflection from the obturator (d) traveling at a higher speed than either the projectile or the reflection from the nose cone (c). The reflections from the nose cone (c) and obturator (d) coalesce into a single shock (e) at approximately 0.06 m from the entrance diaphragm. In this case a shock reflected back into the launch tube (f) and a shock transmitted into the accelerator section (g) were detected. This reflection from the entrance diaphragm (f) travels opposite to the direction of projectile motion and is then reflected from the obturator (h). This reflection (h) travels in the direction of projectile motion toward the projectile throat until entering into the accelerator section where it is swept back toward the obturator. When the obturator enters the accelerator section, a normal shock (i) is generated which travels in the direction of projectile motion and is initially driven toward the projectile throat, eventually merging with the shock generated in the launch tube (h). The normal shock (i) begins to travel away from the projectile throat as the obturator continues to decelerate.

The second experiment done to investigate diffuser starting was performed with the same conditions and instrumentation configurations (Fig. 1.6) as the previous experiment, approximately 0.1 psi of air in the launch tubes and a 360 psi mixture of $2.7\text{CH}_4 + 7.8\text{N}_2$ in the accelerator section. Two 0.014" Mylar diaphragms separated the launch tubes from the accelerator section. The

projectile, obturator, and backplate masses were 68.3 gm, 11.9 gm, and 3.5 gm, respectively. The assembly was launched from the light gas gun with 2500 psi of helium and achieved an entrance speed of 955 m/s at the point of diaphragm impact.

The pressure traces from this experiment are shown in Figs. 4.8, 4.9, and 4.10. These traces show the same character as those discussed earlier even though the entrance Mach number is 2.63, just slightly above the minimum steady state Mach number of operation. In Fig. 4.8 (trace 1) the first reflected compression from the projectile/obturator is more disperse than in the previous experiment, but the trend in shock development is similar. In Fig. 4.9 the shock development is also similar to the previous experiment. The conical and reflected shocks, as well as the normal shock and obturator location, can be clearly seen. The diffuser in this experiment started and remained started for more than 4 m of travel. Figure 4.10 shows the pressure data from the first five stations of the standard accelerator section. The traces show the supersonic profile associated with the projectile, followed by a slower, decelerating shock caused by the obturator. This demonstrates that starting the diffuser with low initial launch tube pressure does not limit the low speed operation of the ram accelerator; instead, it is the Kantrowitz Mach number and the conditions behind the projectile which are the limiting factors. When heavy obturators or combustible gas mixtures are used, the diffuser may be unstarted at Mach numbers above the Kantrowitz Mach number by a normal shock being driven past the projectile throat, thereby limiting low speed operation.

The final experiment done to investigate diffuser starting was again done with approximately 0.1 psi of air in the launch tubes, a 360 psi mixture of $2.7\text{CH}_4+7.8\text{N}_2$ in the accelerator section, and the same instrumentation configuration as that of the previous experiments. Two 0.014" Mylar diaphragms separated the launch tubes from the accelerator section. The projectile, obturator, and backplate masses were 78.2 gm, 11.9 gm, and 3.5 gm, respectively. The assembly was launched from the light gas gun with 2360 psi

of helium and achieved an entrance speed of 910 m/s at the point of diaphragm impact.

The pressure traces from this the launch tube portion of this experiment are shown in Fig. 4.11. The traces in Fig. 4.11 show the same character as those discussed earlier in Figs. 4.3 and 4.8. Even though the Mach number is 2.51, just slightly below the minimum steady state Mach number of operation, traces 5 through 7 of Fig. 4.12 appear similar to those of Figs. 3.4 and 4.9. The conical and reflected shocks can be clearly seen, as well as the normal shock and obturator location. It appears that the diffuser in this experiment has started; however, traces 8 through 12 show that this is not the case. The pressure spike at the throat of the projectile (see Fig. 4.12 for the throat location), which in previous experiments was the reflected shock from the projectile nose cone, grows in amplitude as the projectile travels into the mixture. This is because the flow chokes at the throat and pressure builds, causing a shock to be disgorged from the diffuser. Although these pressure spikes near the projectile throat are very similar in appearance to the spikes caused by the passage of a projectile fin shown earlier, this is not the case. It is a high pressure region caused by choking of the flow at the throat of the projectile and not related to a fin shock. At station 13 in Fig. 4.13, which is 0.22 m downstream of station 12, the pressure spike is even larger and it is clear that the projectile is unstarted. This is more obvious from traces 14 through 17 which show a normal shock followed by the projectile that is decelerating and acting like a piston to augment the shock. At Mach numbers lower than the Kantrowitz Mach number, the diffuser cannot be started and typical ram accelerator operation is not possible.

During normal operation, the typical entrance Mach number into the first stage of the ram accelerator is about 3.2. There are several reasons that this is well above the Kantrowitz Mach number. Although the diffuser can be started at Mach numbers as low as 2.6, it may be unstarted by a shock being disgorged by conditions behind the projectile. Excessive obturator, backplate,

or projectile mass, insufficient obturator hole area, or excessive heat addition will raise the minimum Mach number of starting. When the entrance Mach number is well above the Kantrowitz Mach number, a greater range of obturator, projectile, backplate mass, or heat release can be tolerated.

4.3 Ignition Transients

A set of experiments was performed to investigate the starting transients of a projectile in a combustible ("hot") gas mixture. For all hot experiments the gas mixture composition was $2.7\text{CH}_4+2\text{O}_2+5.8\text{N}_2$. This is the same mixture in which spinning detonations, three-dimensional effects and subdetonative, transdetonative and superdetonative regimes have been studied and is the most thoroughly investigated mixture to date.^{2,3,12-17}

The first experiment to investigate starting transients was performed with approximately 0.1 psi of air in the launch tubes and 355 psi of combustible gas mixture in the accelerator section. Two 0.014" Mylar diaphragms separated the launch tubes from the accelerator section. The projectile, obturator, and backplate masses were 61.2gm, 11.8 gm, and 3.5 gm, respectively. The assembly was launched from the light gas gun with 3950 psi of helium and achieved an entrance speed of 1160 m/s at the point of diaphragm impact. The HITS was placed ahead of the entrance diaphragm, as shown in Fig. 4.14a.

The tube wall pressure traces from this experiment are shown in Fig. 4.15. This is a more detailed view of the launch tube data than shown in Figs. 4.3, 4.8, and 4.11. The station numbering of this experiment is shown in Fig. 4.14a. The initial shock, created from the acceleration of the projectile and helium blow-by, and its reflection from the entrance diaphragm are too low in amplitude to be seen on this plot. The first two pressure rises seen at station 1 are the reflected compressions from the projectile/obturator combination of the shock which had previously reflected from the diaphragm and traveled toward the projectile. The second shock is overtaking the first shock as shown

by the two pressure jumps coming closer together from station 1 to station 8. These two shocks merge, reflect from the entrance diaphragm and travel back toward the projectile. The reflected shock from the diaphragm passes over the projectile and impacts the obturator at nearly the same time that the tip of the projectile nose impacts the entrance diaphragm. The shock reflects from the obturator and backplate and travels toward the entrance diaphragm. By station 8 this reflected shock is near the projectile throat. The rapid decrease in pressure on the right of traces 4 through 8 is the abrupt change in gas pressure from the shock compressed gas to the expanded helium driver gas across the obturator and backplate.

Even more illuminating is the luminosity data from the same locations in the launch tube. This data is shown in Fig. 4.16. Stations 1 and 2 show no luminosity at those locations in the launch tube. At these stations the gas has only passed through three sets of shocks, the incident, reflection from the diaphragm, and the reflection from the projectile and obturator. The other stations view locations that are also shocked by the second reflection from the diaphragm and second reflection from the projectile and obturator. It is interesting that all of the locations that are exposed to these additional shocks show luminosity. The lead luminosity signature in stations 8 through 3 agrees well with the passage of the second reflected shock from the diaphragm. The rapid increase and later decrease in luminosity in traces 3 through 8 agrees well with the passage of the second shock reflected from the obturator and the passage of the obturator, respectively. The presence of luminosity in the launch tube indicates that the gas is very hot from being multiply shock heated.

Even though the accelerator section was filled with combustible gas there was little change in the shock dynamics in the launch tube. Comparing station 8 in Fig. 4.15 and station 4 in Fig. 4.3 it can be seen that the form and amplitude of the pressure traces are nearly the same. The presence of a combustible gas mixture in the accelerator section does not significantly change the short term

pressure data recorded in the launch tubes. On the contrary, the launch tube gas may affect the results obtained from the combustible gas filled accelerator section. After the launch tube gas has been compressed by the multiple shock reflections, it is at a relatively high temperature and pressure as indicated by the data. This high temperature gas provides a possible ignition source for the combustible gas in the accelerator section. Upon rupture of the entrance diaphragm, the high temperature launch tube gas is in contact with the combustible gas of the accelerator section. Through heat transfer and mixing, the high temperature gas may ignite the combustible gas in the accelerator section, thereby beginning the combustion process. At this point this is only a hypothesis; however, later sections will discuss data that will show that shock heated gas in the launch tubes is the source of ignition and without it the mixture will not ignite.

The understanding of the shock dynamics in the launch tube is necessary in order to obtain reliable ignition and diffuser starting in not so highly evacuated systems. Using a launch tube filled with 0.1 psi of air, multiple shock reflections between the projectile and entrance diaphragm raise the pressure for a short time to nearly 2000 psi, well above the breaking pressure of the entrance diaphragm. In a system using a higher launch tube pressure, the pressure from the multiple shock reflections could easily break the entrance diaphragm and ignite a detonation well in front of the projectile. For these reasons it may be necessary to create a special venting or buffer section⁷ to prevent premature rupturing of the entrance diaphragm or ignition of the combustible gas.

The second experiment to investigate starting transients was performed with the same conditions as the previous experiment, with the exception that the HITS was placed in the combustible gas mixture adjacent to the entrance diaphragm as shown in Fig. 4.14b. The tube wall pressure traces from this experiment are shown in Fig. 4.17. Station 1 shows that the conical shock system on the nose is already established and that a strong (6,000 psi) normal

shock has been generated by the obturator on the base of the projectile. The base of the obturator can be identified by the rapid reduction in pressure following the normal shock. At the stations farther from the entrance diaphragm, there is very little change in the conical shock system, but the normal shock propagates closer to the projectile throat. Beginning at station 3 and continuing through station 8, the location of the backplate can be identified as a small rise and then decay in pressure behind the obturator. By comparing station 8 of Fig. 4.17 and station 12 of Fig. 4.4, it can be seen that the normal shock is larger in amplitude and closer to the throat of the projectile in the hot experiment. This is due to the heat release of the combustible gas augmenting the normal shock. The difference between cold and hot experiments is more dramatic farther from the entrance diaphragm. In the cold experiment the normal shock does not keep up with the projectile, while in the hot experiment the shock remains on the body due to thermal choking of the flow.

Figure 4.18 shows the luminosity data for this experiment. The sensors at station 3, 5, and 8 gave only low amplitude signals while the ones at stations 6 and 7 did not work at all. There is sufficient data to provide some insight to what is happening. At station 1 the luminosity begins at the throat with the peak about 15 μ sec later. At first this seems to be a strange location for hot gas or combustion. In the ideal model the combustion should begin at the base of the projectile and stabilize there. The luminosity could be from shock induced combustion around a fin, but the Mach number is fairly low and this sensor is not over a fin. The explanation is that this is luminosity from the reaction front and the interface between the hot launch tube gas and the reacting gas mixture. In the launch tube the pressure builds to over 2000 psi behind the second reflection from the obturator. When the entrance diaphragm is broken by this pressure or pierced by the projectile, a shock is propagated into the reactive mixture and an interface with a great temperature difference is created. The shock propagates into the reacting mixture and the mixture begins to react at the interface. Initially the interface and shock are on the

nose of the projectile. By station 1 the projectile has overtaken the shock and reaction zone which are traveling into the accelerator section. The transmitted shock can be seen at station 1 of Fig. 4.17. By station 2 both the pressure and luminosity data indicate that the transmitted shock and interface have been swept toward the base of the projectile. If the pressure in the launch tube had been higher, the transmitted shock and reaction interface would have been more difficult to overtake and the flow may have choked at the projectile throat, causing an immediate unstart.

The idealized starting process discussed earlier ignores important information on the source of ignition and diffuser starting. The lack of realism in the ideal model may not allow proper modeling of the starting process, especially at higher launch tube pressures or with significant obturator blow-by. This makes the information obtained from the hot and cold starting experiments important for proper design of new ram accelerator facilities.

4.4 Solid Obturator Starting

A solid obturator has several advantages over the existing perforated design. It can be made stronger and lighter than a perforated obturator and, therefore, is able to survive more severe launch conditions. The solid obturator is also simpler and less expensive to fabricate. The disadvantages are that the range of pressure, heat release, and entrance speed which a given mass of solid obturator will allow successful starting is more narrow than that of a perforated obturator. However, there will be cases when the advantage of strength and simplicity will outweigh the constraints on operating conditions. A solid obturator starting experiment is presented for these reasons and is used to clarify problems that may arise from its use.

A solid obturator experiment was done with approximately 0.1 psi of air in the launch tubes and 360 psi of combustible gas mixture ($2.7\text{CH}_4+2\text{O}_2+5.8\text{N}_2$) in the accelerator section. As in previous experiments, two 0.014" Mylar

diaphragms separated the launch tubes from the accelerator section. The projectile and solid obturator masses were 71.2 gm and 10.1 gm, respectively. The assembly was launched from the light gas gun with 4330 psi of helium and achieved an entrance speed of 1190 m/s at the point of diaphragm impact. The configuration of the experiment is shown in Fig. 1.6. Three inserts were placed prior to the entrance diaphragm (the 0.1 psi side) and the HITS was placed immediately after.

The tube wall pressure traces from this experiment are shown in Figs. 4.19 and 4.20. Figure 4.19 shows the data obtained from the launch tube side of the entrance diaphragm using the station numbers of Fig. 1.6. The initial shock, created from the acceleration of the projectile and helium blow-by, and its reflection from the entrance diaphragm are too low in amplitude to be seen on this plot. The first two pressure rises seen at station 1 are the reflections from the projectile/obturator combination of the shock which was traveling from the diaphragm toward the projectile. By station 3 these two shocks have merged into a single, stronger shock. Station 4 shows the arrival of this shock and a short time later its reflection from the entrance diaphragm. This shock travels toward the projectile and then reflects from the obturator as seen at stations 2, 3, and 4. The passage of the obturator is marked by a jump up in pressure to the expanded gas gun pressure at station 1 and a jump down in pressure at stations 2, 3, and 4. These traces are very similar to those of Figs. 4.3, and 4.15, as would be expected.

Figure 4.20 shows the data obtained from the accelerator section during the same experiment. The first rise in pressure is the reflection from the tube wall of the conical shock generated by the passage of the projectile nose. The second rise in pressure is the reflection from the tube wall of the shock which has reflected from the nose cone. These two pressure rises are then followed by an expansion from the nose/body joint. A normal shock which is on the body of the projectile, as well as the rapid decrease in pressure which identifies the base of the solid obturator, can be seen. The major differences between this

experiment and either of the previous hot or cold experiments (Fig. 4.4 and Fig. 4.17) are that there is no pressure variation due to the backplate and that the normal shock is much closer to the throat of the projectile than in the other cases. This is because there is no gas released through the obturator, so a stronger shock is driven toward the projectile throat. Even with the normal shock closer to the throat at station 12, the projectile remained started and accelerated for more than 4 m as indicated by the data in Fig. 4.21. The supersonic profile as seen in the nonreactive experiments is still present, but now the "normal" shock remains close to the projectile, accelerating it down the tube. The normal shock remaining with the projectile for such a long period of time indicates that combustion has been stabilized at the base of the projectile. Figure 4.22 compares luminosity and pressure data from one station in the launch tube and one station in the accelerator section. The launch tube luminosity again matches the passage of shocks and indicates that there is hot gas present long before the entrance diaphragm is ruptured. The first rise in luminosity in the accelerator section indicates that the hot reaction zone is near the base of the projectile. The second rise in luminosity is the hot launch tube gas being moved past the sensor because it is confined by the obturator. The dip in between the two peaks is likely a cool region of gas caused by an expansion that traveled into the launch tube gas from the bursting of the entrance diaphragm or some accelerator gas that reacted to a lower temperature because of the way it was processed. It is also possible that this is simply gas that has not yet had time to react. This experiment demonstrates that starting with a solid obturator is possible, but it may be somewhat less forgiving than using a perforated obturator.

4.5 High Launch Tube Pressure

A pair of experiments was performed to investigate the effect of elevated launch tube pressures on the starting transients of a combustible gas mixture. For both experiments the combustible gas mixture was the same as used in the previous hot experiments.

The first experiment to investigate the effect of elevated launch tube pressures on the starting transients was performed with approximately 1.0 psi of air in the launch tubes and 360 psi of combustible gas mixture in the accelerator section. Five 0.014" Mylar diaphragms (static burst pressure of 1870 psi) separated the launch tubes from the accelerator section. The projectile, obturator, and backplate masses were 71.1 gm, 11.9 gm, and 3.5 gm, respectively. The assembly was launched from the light gas gun with 4600 psi of helium and achieved an entrance speed of 1180 m/s at the point of diaphragm impact. Three inserts were placed prior to the entrance diaphragm (the 1.0 psi side) and the HITS was placed immediately after, as shown in Fig. 1.6.

The initial shock, created from the acceleration of the projectile and helium blow-by, is not visible in traces 1 through 4 in Fig. 4.23, but the reflection of this shock from the entrance diaphragm is visible on the left of the traces in the figure. When the initial shock arrives at the entrance diaphragm in this experiment, it is closer to the projectile than in the earlier experiments. It is possible that the higher launch tube pressure impeded the generation of a shock caused by helium blow-by, thus causing the initial shock to be closer to the projectile. Station 1 shows the origin of the double wave system seen in earlier traces. The first shock is the coalesced reflection from the nose cone of the projectile and the second shock is the reflection from the obturator of the original acceleration/blow-by shock. These two shocks can be seen at station 2 and are nearly equal to the gas gun pressure. The maximum pressure at station 4 is only about double the pressure seen in the cold and previous hot experiments. Fewer shock reflections have occurred because the incident shock was closer to the projectile, thereby keeping the pressure lower than expected. By comparing station 5 of Fig. 4.24 and station 1 of Fig. 4.17, it appears that there is higher pressure gas near the nose and throat of the projectile. The pressure rise at station 5 of Fig. 4.24 has a longer duration and higher amplitude in the region of the projectile throat. This implies that a shock was transmitted into the combustible gas slightly ahead of the projectile

throat and that the reaction of the gas mixture is more vigorous than the case of low launch tube pressure. Stations 6 through 12 of Fig. 4.24 confirm that the diffuser started even with the higher launch tube pressure. Figure 4.25 shows the supersonic projectile profiles with the "normal" shock on or near the projectile base indicating that combustion was stabilized behind the projectile. In this case the normal shock does not shift locations relative to the projectile throat as much as seen with the solid obturator data of Fig. 4.21. This is because the perforations of the obturator allow a smoother, less "shocking" starting process by relieving some of the high pressure gas while at the same time remaining in contact with the projectile for a longer time because of its slower deceleration. The longer contact time allows smooth establishment of the combustion zone at the base of the projectile and inhibits large normal shock motions.

Figure 4.26 shows the pressure and luminosity data from one station in the launch tube and one station in the accelerator section. These are the same locations as the solid obturator data in Fig. 4.22. The launch tube luminosity data agree with the passage of shocks but differ from the luminosity in Fig. 4.22 because there are fewer shock reflections. The luminosity data from the accelerator section indicate a hot region at the projectile base, a cool region of either launch tube or accelerator gas, and a region of high temperature launch tube gas. This is very similar to the luminosity in Fig. 4.22.

Figure 4.27 shows a distance-time ($x-t$) diagram of the experimental data of Figs. 4.23 and 4.24. The entrance diaphragm defines the zero of the distance axis, with values to the left corresponding to the launch tube and values to the right corresponding to the accelerator section. Dashed lines represent portions of the figure where extrapolation of the experimental data was used to complete the $x-t$ diagram. Shocks are identified by letters on the figure and correspond to the following discussion. The low amplitude incident shock (a) travels in the direction of projectile motion until it reflects from the entrance diaphragm (b). The reflection (b) travels opposite to the direction of projectile

motion until it is partially reflected from the nose cone of the projectile (c) and then the remainder is completely reflected from the obturator (d). The reflections from the nose cone (c) and obturator (d) both travel in the direction of projectile motion with the reflection from the obturator (d) traveling at a higher speed than either the projectile or the reflection from the nose cone (c). These two shocks reflect from the entrance diaphragm (e) and (f) which then coalesce into a single shock (g) approximately 0.05 m from the entrance diaphragm. This shock (g) is reflected from the obturator (h) and travels in the direction of projectile motion toward the projectile throat until entering into the accelerator section, where it is swept back toward the obturator. When the obturator enters the accelerator section, a normal shock (i) is generated which travels in the direction of projectile motion and is driven toward the projectile throat. It then merges with the shock generated in the launch tube (h). The normal shock (i) stabilizes at a constant distance from the projectile throat due to the heat release of the combustible gas. This x-t diagram differs from Fig. 4.7 in that the heat addition decelerates the obturator and backplate more rapidly and the timings of the shocks in the launch tube are different.

This experiment demonstrates that it is possible to start a ram accelerator projectile with a substantial amount of air in the launch tube. The thicker entrance diaphragm used in this experiment seem to have withstood the additional shock pressures caused by the higher launch tube pressure, but did allow the transmission of a relatively strong shock ahead of the projectile throat into the accelerator section. The projectile started in spite of the transmitted shock and possible combustion in front of the throat. The difficulties seen here can be anticipated to be worse when a higher launch tube pressure, a thinner entrance diaphragm, or a lower entrance speed are used.

The second experiment to investigate the effect of elevated launch tube pressures on the starting transients was also performed with approximately 1.0 psi of air in the launch tubes and 360 psi of combustible gas mixture in the accelerator section. In this case only two 0.014" Mylar diaphragms separated

the launch tube from the accelerator section. The projectile, obturator, and backplate masses were 73.0 gm, 11.9 gm, and 3.5 gm, respectively. The assembly was launched from the light gas gun with 4450 psi of helium and achieved an entrance speed of 1140 m/s at the point of diaphragm impact.

The tube wall pressure traces from the launch tube section of this experiment are shown in Fig. 4.28. The initial shock, created from the acceleration of the projectile and helium blow-by, and its reflection from the entrance diaphragm are too low in amplitude to be seen on this pressure scale except at station 1. The maximum pressure at station 4 is about 1000 psi less than station 4 of Fig. 4.23 even though there are more shock reflections and the initial launch tube pressure is the same. This is because the high pressure gas ruptured the entrance diaphragm before the projectile pierced it, propagating a shock into the combustible gas mixture. This transmitted shock can be seen as a small rise in pressure at station 5 of Fig. 4.29. Station 5 also shows that there is a great deal of high pressure gas near the nose and throat of the projectile. The initial pressure rise is farther in front of the projectile than in Fig. 4.24. The bursting of the entrance diaphragm exposed the accelerator gas to the hot launch tube gas long before the projectile was present. The accelerator gas then began to react as the projectile approached. If a large portion of the gas reacts then, the flow at the throat of the projectile will choke and the projectile will unstart. Stations 6 through 12 of Fig. 4.29 confirm that a large shock was formed in the throat of the projectile. As expected, the data from farther down the tube, Fig. 4.30, show a shock being propagated in front of the projectile and the projectile decelerating.

In many ways this is similar to entering the mixture at a Mach number below the Kantrowitz Mach number as shown by the cold experiment data of Figs. 4.11, 4.12, and, 4.13. In the cold experiment it was simply the Mach number that was too low. In this reactive experiment the combination of a strong transmitted shock and combustion in front of the projectile effectively made the Mach number too low. The premature bursting of the entrance diaphragm and

ignition of the combustible gas caused the diffuser not to start, which in turn forced the shock in front of the projectile throat. This experiment demonstrates that leaving a substantial amount of air in the launch tubes with an inadequate entrance diaphragm thickness can cause the diffuser not to start. Reducing the number of shock reflections and a thick entrance diaphragm seem to aid in starting the diffuser and in keeping the combustion behind the projectile when higher launch tube pressures are used.

4.6 Obturator Leakage

It has been shown that excessive air left in the launch tubes can cause difficulties in starting under certain circumstances. Another deleterious effect on starting is leakage or blow-by of helium gas past the obturator during the launch process. In almost all experiments some blow-by is present, but not in amounts significant enough to interfere with starting. To study the effects of blow-by on starting, an intentionally undersized solid obturator was used. The solid obturator was used because there are no major design changes needed when its outer dimensions are modified.

A blow-by experiment was done with approximately 0.1 psi of air in the launch tube and 360 psi of combustible gas mixture ($2.7\text{CH}_4+2\text{O}_2+5.8\text{N}_2$) in the accelerator section. Five 0.014" Mylar diaphragms separated the launch tubes from the accelerator section. The projectile and solid obturator masses were 65.1 gm and 9.4 gm, respectively. The diameter of the obturator was 37.1 mm, giving a 5% blow-by area. The assembly was launched from the light gas gun with 4170 psi of helium and achieved an entrance speed of 1100 m/s at the point of diaphragm impact.

Figure 4.31 shows the data obtained from the launch tube side of the entrance diaphragm. These traces appear quite different from those seen earlier. There is a gradual rise in pressure on all traces preceding the shock activity. The peak pressure at station 4 is about 5000 psi and is relatively broad. This

pressure is well above the breaking pressure of the entrance diaphragm (five 0.014" diaphragms have a static break pressure of approximately 1870 psi) and causes it to fail. Station 5 of Fig. 4.32 shows the effect of the diaphragm failure as a strong shock in front of the projectile throat. In this case the projectile was unstarted before it ever entered the combustible gas mixture. Figure 4.33 shows the pressure data from farther into the accelerator section which are typical of an unstart; a normal shock followed by a decelerating projectile. Even the five diaphragms that allowed a projectile to start with 1.0 psi in the launch tubes were insufficient for this extreme case of blow-by.

It is evident that significant leakage of helium past the obturator is a serious problem in starting the projectile. The blow-by gas caused the entrance diaphragm to fail and may have ignited the combustible gas mixture. For ram accelerators that use a powder gun rather than a helium gas gun to launch the projectile, the blow-by problem may be more severe. In a powder gun, both the pressure and temperature are significantly higher behind the obturator, causing a more severe environment for the obturator and possibly more leakage.

A possible solution to the blow-by and high launch tube pressure problems is to have multiple diaphragm/vent stations down the length of the of the launch tube. As the projectile is launched, the blow-by and acceleration cause a shock to form in front of the projectile. By reflecting this shock from a diaphragm early in the launch tube, it would not attain a significant distance from the projectile. The gas will be compressed by the approaching projectile and vented near the diaphragm location. The location of the first diaphragm/vent station could be tailored so that the driver gas was supersonic relative to the vent holes, thereby reducing the loss in drive pressure. The projectile would pierce the diaphragm and release the compressed gas into the next section of the launch tube. The expanding gas and the projectile acceleration will create another shock in front of the projectile which in turn will reflect off the next launch tube diaphragm. The process continues, keeping the initial shock in the

launch tube close to the projectile and venting high pressure gas at each diaphragm. Several closely spaced diaphragm/vent stations prior to the entrance diaphragm would vent additional gas and sweep the existing shocks back on the projectile to provide better conditions for entrance into the ram accelerator section. This multiple diaphragm technique would not only reduce the effect of blow-by and high launch tube pressures, but would protect the entrance diaphragm from stray pieces of material accelerated ahead of the projectile by the blow-by. The use of multiple vent/diaphragm stations may allow the use of atmospheric launch tube pressures in future ram accelerator designs.

4.7 Buffer Sections

In order to demonstrate that ignition of the combustible gas is caused by the launch tube gas, two experiments were done using either a reactive or nonreactive buffer section which separated the launch tube from the accelerator section. The buffer section filled with the reactive gas mixture would act as the "control" to ensure that introducing additional diaphragms would not change the typical starting and combustion stabilization process. If the diaphragms did not modify the process, then the data from the experiment with the inert buffer section would indicate whether the launch tube gas was important or not for ignition. The inert buffer section would separate the hot launch tube gas from the reactive gas mixture and if ignition occurred, the launch tube gas was not important; however, if the reactive mixture failed to ignite, the launch tube gas would be the key to ignition (in this gas mixture).

A buffer section type experiment was done with approximately 0.1 psi of air in the launch tube and 365 psi of combustible gas mixture ($2.7\text{CH}_4+2\text{O}_2+5.8\text{N}_2$) in the accelerator and buffer sections. Two 0.014" Mylar diaphragms separated the launch tubes from the buffer section and another two diaphragms separated the buffer section from the accelerator section. The projectile, obturator, and backplate masses were 62.4 gm, 12.3 gm, and 3.4 gm,

respectively. The assembly was launched from the light gas gun with 4200 psi of helium and achieved an entrance speed of 1150 m/s at the point of diaphragm impact. One insert was placed prior to the entrance diaphragm (the 0.1 psi side) to the buffer section, two inserts made up the buffer section which was followed by a diaphragm and the HITS, as shown in Fig. 4.34.

Figure 4.35 shows the data obtained from the launch tube and buffer section. The buffer section is filled with combustible gas so the data should not appear similar to previous launch tube data. Station 1 shows the jump in pressure going from the gas pressure in the launch tube to the residual helium gas gun pressure. Station 2 is in the launch tube, but is only 18 mm from the entrance diaphragm to the buffer section and shows the typical launch tube shocks. The data from station 3 show the conical and reflected shock, but then becomes a flat line due to saturation of the data acquisition system. At station 4 the conical shock system appears normal, but the pressure behind the projectile is high compared to trace 2 of Fig. 4.17. This may be explained by a partial reflection of the shock from the remnants of the diaphragm that separated the buffer section from the accelerator section. Figure 4.36 shows the data from the accelerator section. The conical shock system and obturator location can be clearly identified. The "normal" shock has a similar appearance to other experiments in reactive mixtures only the amplitude is slightly greater. This may be caused by the reflected shock in the buffer section detonating the buffer section gas and propagating a stronger shock and enhanced reaction zone into the accelerator section. Data from stations farther into the acceleration section are shown in Fig. 4.37, and indicate that the diffuser is started and that combustion stabilized behind the projectile. This experiment demonstrated that the additional diaphragms introduced when using buffer sections do not prevent stabilization of combustion behind the projectile.

A second buffer section type experiment was done with the same conditions as the previous experiment, approximately 0.1 psi of air in the launch tube and 365 psi of combustible gas mixture ($2.7\text{CH}_4+2\text{O}_2+5.8\text{N}_2$) in the accelerator

section. The difference between the two experiments was that in this case the buffer section was filled with 365 psi of noncombustible gas mixture ($2.7\text{CH}_4+7.8\text{N}_2$). As in the previous experiment, two 0.014" Mylar diaphragms separated the launch tubes from the buffer section and another two diaphragms separated the buffer section from the accelerator section. The projectile, obturator, and backplate masses were 64.8 gm, 12.3 gm, and 3.5 gm, respectively. The assembly was launched from the light gas gun with 4300 psi of helium and achieved an entrance speed of 1150 m/s at the point of diaphragm impact. One insert was placed prior to the entrance diaphragm (the 0.1 psi side) to the buffer section, two inserts made up the buffer section which was followed by a diaphragm and the HITS, as shown in Fig. 4.34.

Figure 4.38 shows the data obtained from the launch tube and buffer section. Even though the buffer section is filled with noncombustible gas, the data appear very similar to the previous experiment. Station 1 shows the jump in pressure going from the gas pressure in the launch tube to the residual helium gas gun pressure. Station 2 is in the launch tube and only 18 mm from the entrance diaphragm to the buffer section and shows the typical launch tube shocks. The data from station 3 is of poor quality because of a faulty pressure transducer. Station 4 of this experiment is very similar to station 4 of the previous experiment, Fig. 4.35. The conical shock system and the high pressure behind the projectile are similar. There is a slight difference in the shock structure near the throat of the projectile. This may be caused by 3-dimensional effects or combustion in the reacting case.

Figure 4.39 shows the data from the accelerator section which was filled with the combustible gas. The conical shock system and obturator location can be clearly identified. At stations 6, 8, 10, and 12 the shock near the projectile throat is augmented by close passage of the projectile fin while stations 5, 7, 9, and 11 are near the center of a channel. The normal shock in Fig. 4.39 is seen to decay in amplitude as the projectile enters the combustible gas. This is much different than in the data from the previous experiment, Fig. 4.36. Data

from stations farther into the acceleration section are shown in Fig. 4.40, and show that the diffuser is started and that there is a normal shock following the projectile. These are the profiles associated with nonreacting experiments, Figs. 4.5 and 4.10, where there was no possibility of combustion. In this case even though there was the possibility of combustion, it did not stabilize behind the projectile. This was caused by the inert buffer section gas preventing contact between the hot launch tube gas and the combustible gas in the accelerator section. For the combustible gas mixture at initial fill pressures and temperature, projectile configuration, tube diameter, and entrance velocity discussed in this thesis, the primary ignition source and the key to stabilizing combustion behind the projectile is the hot launch tube gas.

4.7 Further Ignition Source Studies

Since the ignition source for conditions of interest has been shown to be the gas in the launch tube, it should be possible to inhibit ignition by removing the source. If there was a perfect vacuum in the launch tube and no driver gas leakage through the obturator, the combustible gas should not ignite and combustion should not stabilize behind the projectile. Both a perfect vacuum and no blow-by are difficult to achieve, but attempts were made to improve upon the existing conditions. A second vacuum pump was installed and all leak sources were sealed. A new solid obturator was designed to prevent blow-by. The location where the projectile is loaded in the launch tube has been worn to a diameter of about 1.504" and tapers into the nominal tube diameter of 1.499". The exterior of the solid obturator was tapered from 1.506" to 1.499" over its length and a thin "Bridgman" seal was placed on the back. The solid obturator has no internal seal as the two piece perforated obturator does, and is therefore superior for this purpose.

A solid obturator experiment was done with approximately 0.01 psi of air in the launch tubes and 360 psi of combustible gas mixture ($2.7\text{CH}_4+2\text{O}_2+5.8\text{N}_2$) in the accelerator section. As in previous experiments, two 0.014" Mylar

diaphragms separated the launch tubes from the accelerator section. The projectile and solid obturator masses were 69.3 gm and 12.8 gm, respectively. The assembly was launched from the light gas gun with 4100 psi of helium and achieved an entrance speed of 1190 m/s at the point of diaphragm impact. Three inserts were placed prior to the entrance diaphragm (the 0.01 psi side), and the HITS was placed immediately after, as shown in Fig. 1.6.

Figure 4.41 shows the data obtained from the launch tube side of the entrance diaphragm. There are no shocks which arrive prior to the projectile that are clearly identifiable and no large build up in pressure at station 4 which is just prior to the entrance diaphragm. The only jump in pressure is the pressure change going across the obturator from the launch tube gas to the helium driver gas. This is much different than any launch tube results previously discussed. Figure 4.42 shows the data from the accelerator section of this experiment. The traces 5, 7, 9, and 11 are from directly over a fin while traces 6, 8, 10, and, 12 are from the center of a channel. The conical shock is apparent as well as the normal shock and the obturator. The normal shock created by the impact of the obturator with the combustible gas creates a strong shock seen at station 6 which is driven closer to the throat of the projectile going from station 6 to 12. The normal shock is much stronger than in Fig. 4.39, where the mixture failed to ignite, and comparable to Fig. 4.36 where the mixture did ignite and combustion stabilized behind the projectile. Figure 4.43 shows data from farther into the accelerator section. At station 13 the normal shock is very near the projectile throat, while at stations 16 and 17 the shock lags far behind the supersonic signature of the projectile. It is evident from these traces that combustion did not stabilize at the base of the projectile even though data from station 13 seems to indicate that the normal shock is stabilized on the projectile body. The lack of perforations in the solid obturator prevents the escape of gas and the only relief of the post shock gas is the deceleration of the obturator and the acceleration of the projectile. This effect causes the normal shock in the HITS and at station 13 to be strong and confuse the results with stabilized

combustion behind the projectile. The reduction in launch tube pressure and elimination of helium blow-by prevented the stabilization of combustion behind the projectile.

To confirm the previous results, a second solid obturator experiment was done with approximately 0.01 psi of air in the launch tubes and 360 psi of combustible gas mixture in the accelerator section. As in the previous experiment, two 0.014" Mylar diaphragms separated the launch tubes from the accelerator section. The projectile and solid obturator masses were 75.9 gm and 12.4 gm, respectively. The assembly was launched from the light gas gun with 4350 psi of helium and achieved an entrance speed of 1170 m/s at the point of diaphragm impact. The configuration of the experiment is shown in Fig. 1.6 and is the same as the previous experiment.

Figure 4.44 shows the data obtained from the launch tube side of the entrance diaphragm. The sensor at station 1 did not function. As in the last experiment, there are no shocks which arrive prior to the projectile and no large build up in pressure at station 4. The only jump in pressure is the pressure change going across the obturator from the launch tube gas to the helium driver gas. This is very similar to the data of Fig. 4.41. Figure 4.45 shows the data from the accelerator section of this experiment. As in the previous experiment, traces 5, 7, 9, and 11 are from directly over a fin while traces 6, 8, 10, and, 12 are from the center of a channel. The conical shock is apparent as well as the normal shock and the obturator. The normal shock created by the impact of the obturator with the combustible gas creates a strong shock seen at station 6, which is driven closer to the throat of the projectile going from station 6 to 12. This data is almost identical to the results of the previous experiment shown in Fig. 4.42. The amplitude and arrival times of all of the shocks, as well as the passage of the obturator, are for all practical purposes indistinguishable from the previous results. Figure 4.46 shows data from farther into the accelerator section. At station 13 the normal shock is very near the projectile throat, and can be seen to separate from the projectile going from trace 13 to 17. It is

evident from these traces that combustion did not stabilize at the base of the projectile, which is the same result obtained previously.

The reduction in launch tube pressure and elimination of helium blow-by prevented the stabilization of combustion behind the projectile. The strong shocks may have ignited part of the flow, but it was not sufficient to stabilize the combustion zone. For more energetic gas mixtures the shock alone may be sufficient to ignite the flow and stabilize combustion.

4.8 Larger Scale Facilities

For larger ram accelerators that use higher launch tube pressures and powder gun launchers, it has been observed that less energetic mixtures must be used to allow the diffuser to start.^{4,6,7} As shown in this work, the conditions in the launch tube are important for ignition of the flow. High launch tube pressure and excessive blow-by have been shown to enhance ignition of the combustible gas. It can be expected that simply increasing the diameter, and therefore the length of the projectile, will change the time scale for combustion to occur as the projectile pierces the entrance diaphragm. If all things are the same except scale as a projectile pierces the entrance diaphragm in a 38 mm and 120 mm bore facility, the interface between the hot launch tube gas and the combustible gas will be swept past the projectile throat in a shorter time in the smaller facility. This implies that for the same launch tube conditions a "hotter" (one with shorter induction and reaction times) combustible gas mixture may be successfully used in the smaller facility whereas an unstart would result in the larger facility. When the additional effects of higher launch tube pressures and hot blow-by from a powder gun are included, it should come as no surprise that larger facilities require less energetic, longer induction and reaction time, starting mixtures.

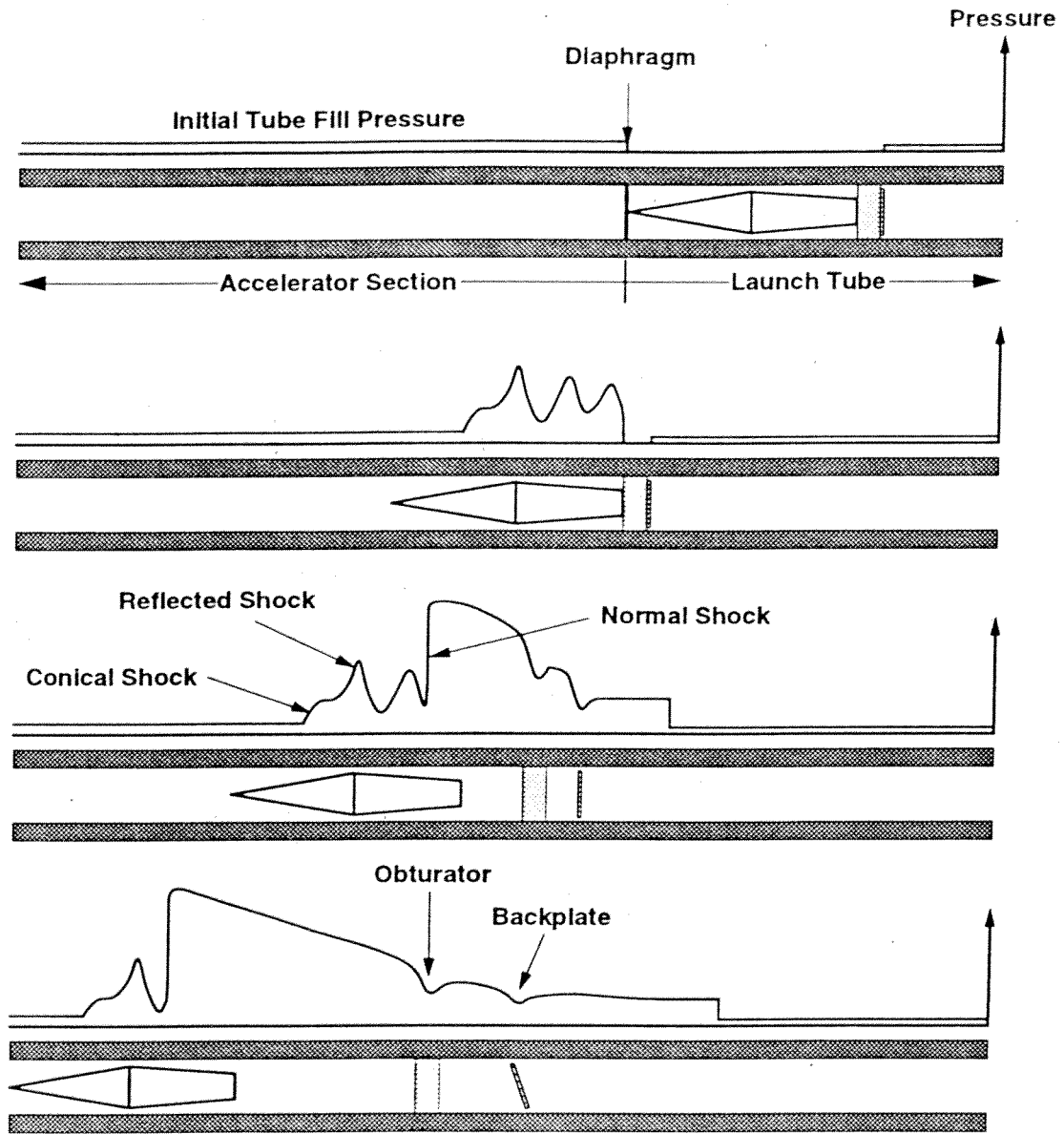


Fig. 4.1 Schematic of the idealized starting process.

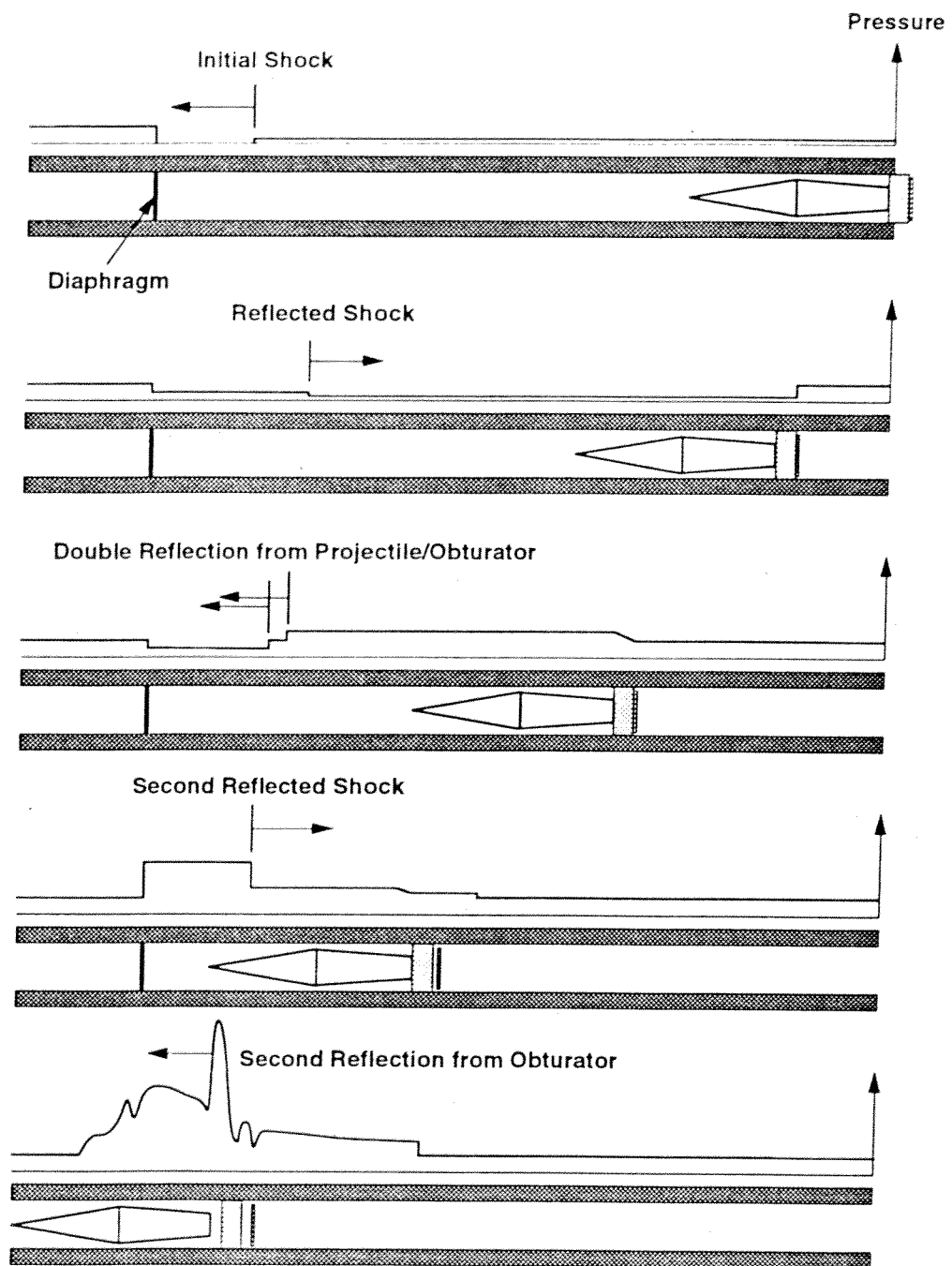


Fig. 4.2 Schematic of the measured starting process.

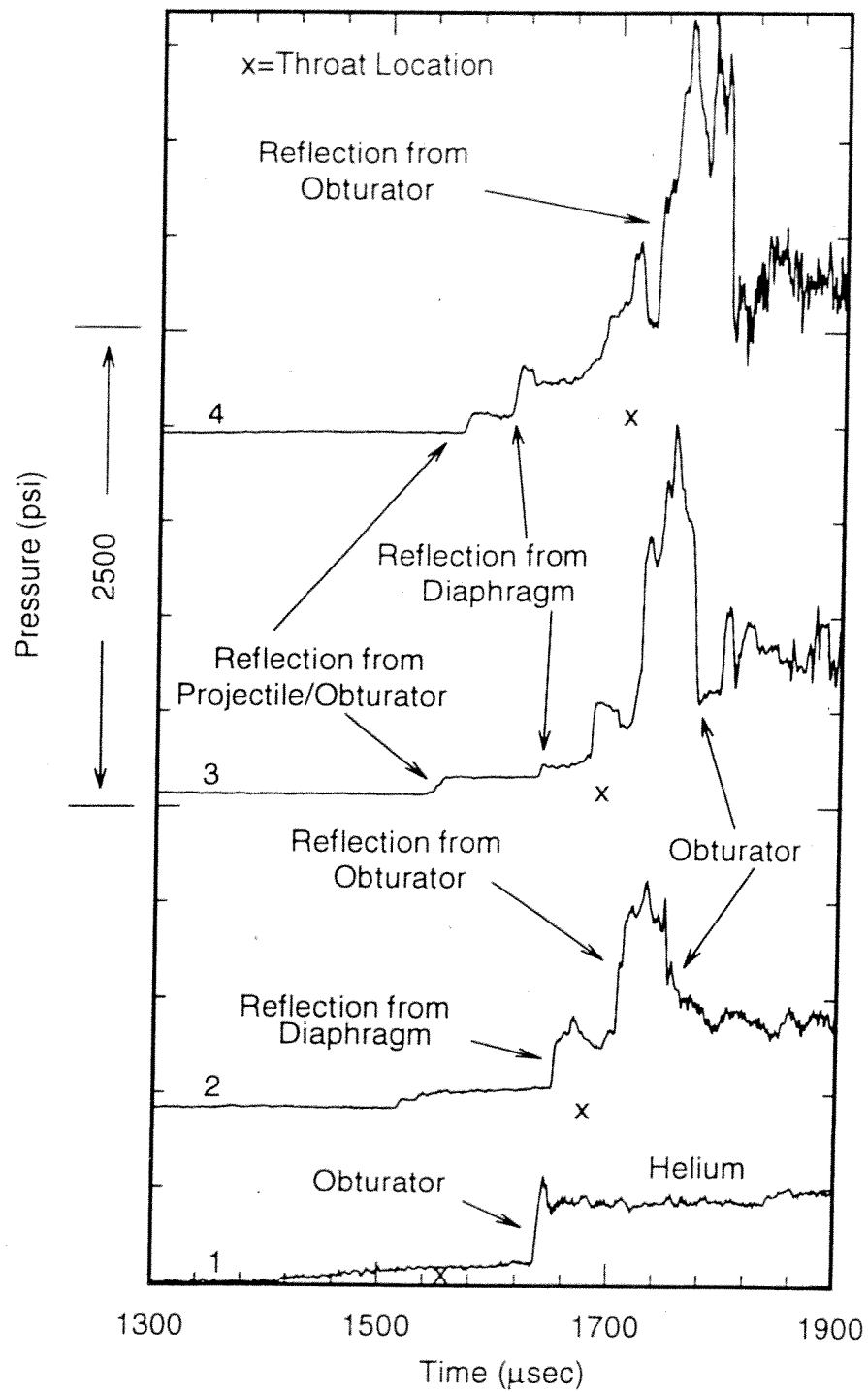


Fig. 4.3 Tube wall pressure traces from the launch tube for a projectile traveling 1170 m/s in a mixture of $2.7\text{CH}_4 + 7.8\text{N}_2$.

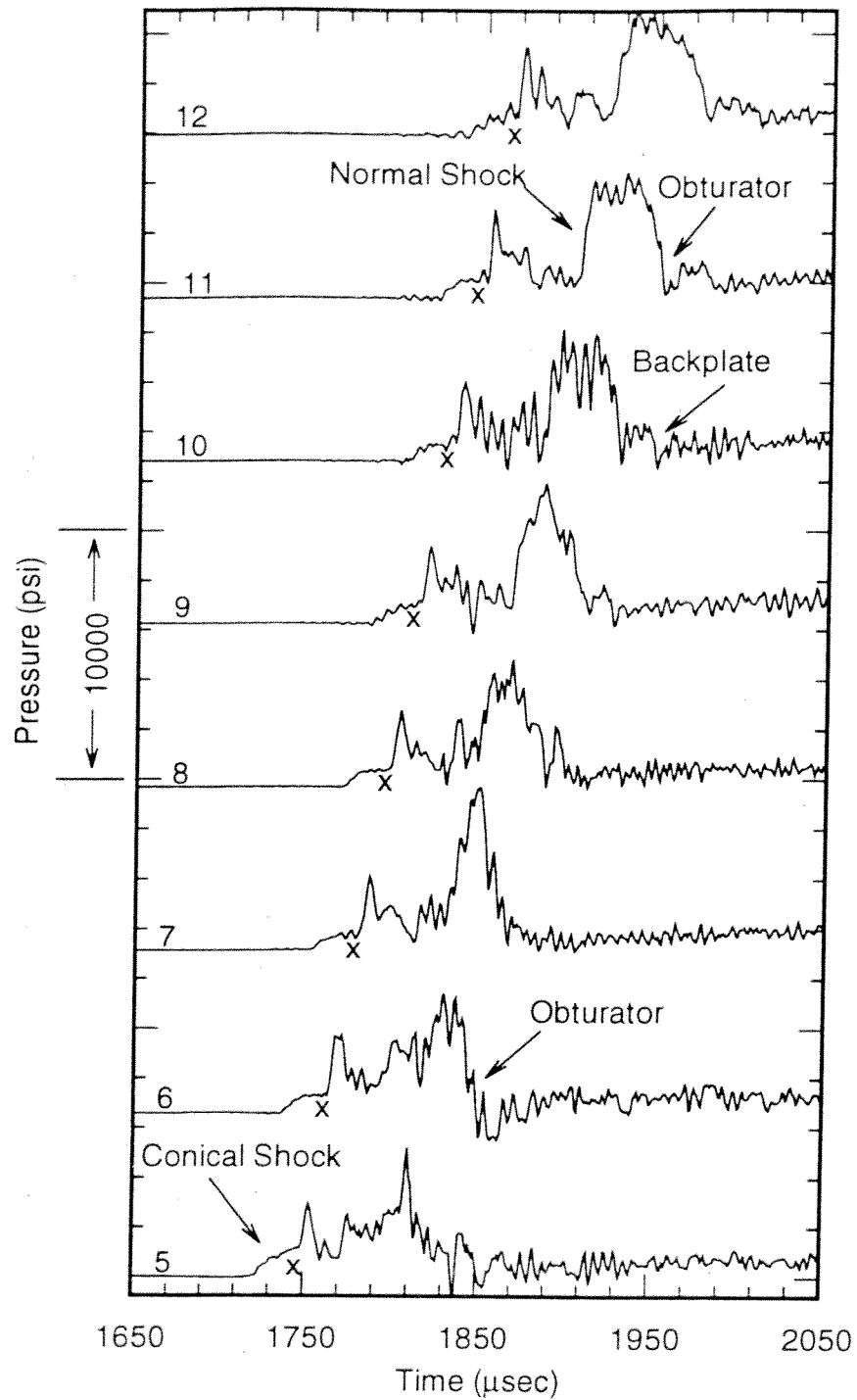


Fig. 4.4 Tube wall pressure traces from the accelerator section for a projectile traveling 1170 m/s in a mixture of $2.7\text{CH}_4 + 7.8\text{N}_2$.

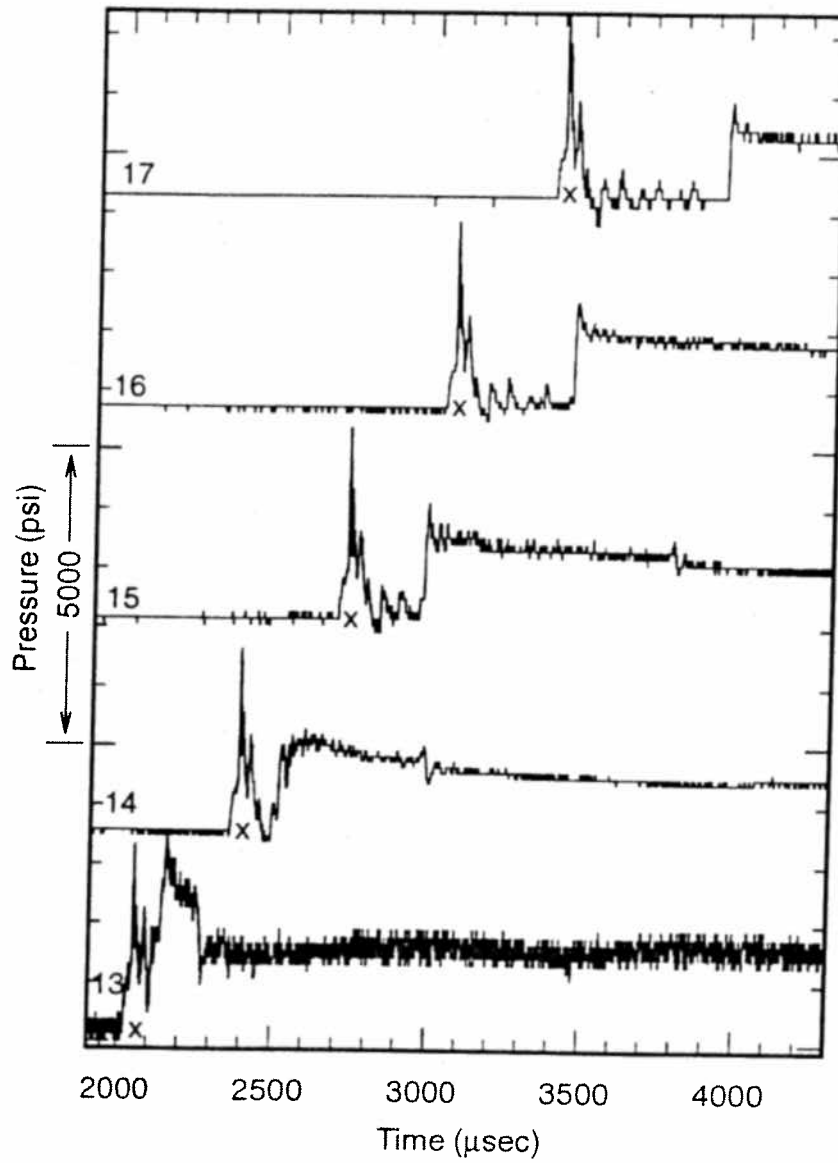


Fig. 4.5 Tube wall pressure traces from farther down the accelerator section for the experiment shown in Figs. 4.3 and 4.4.

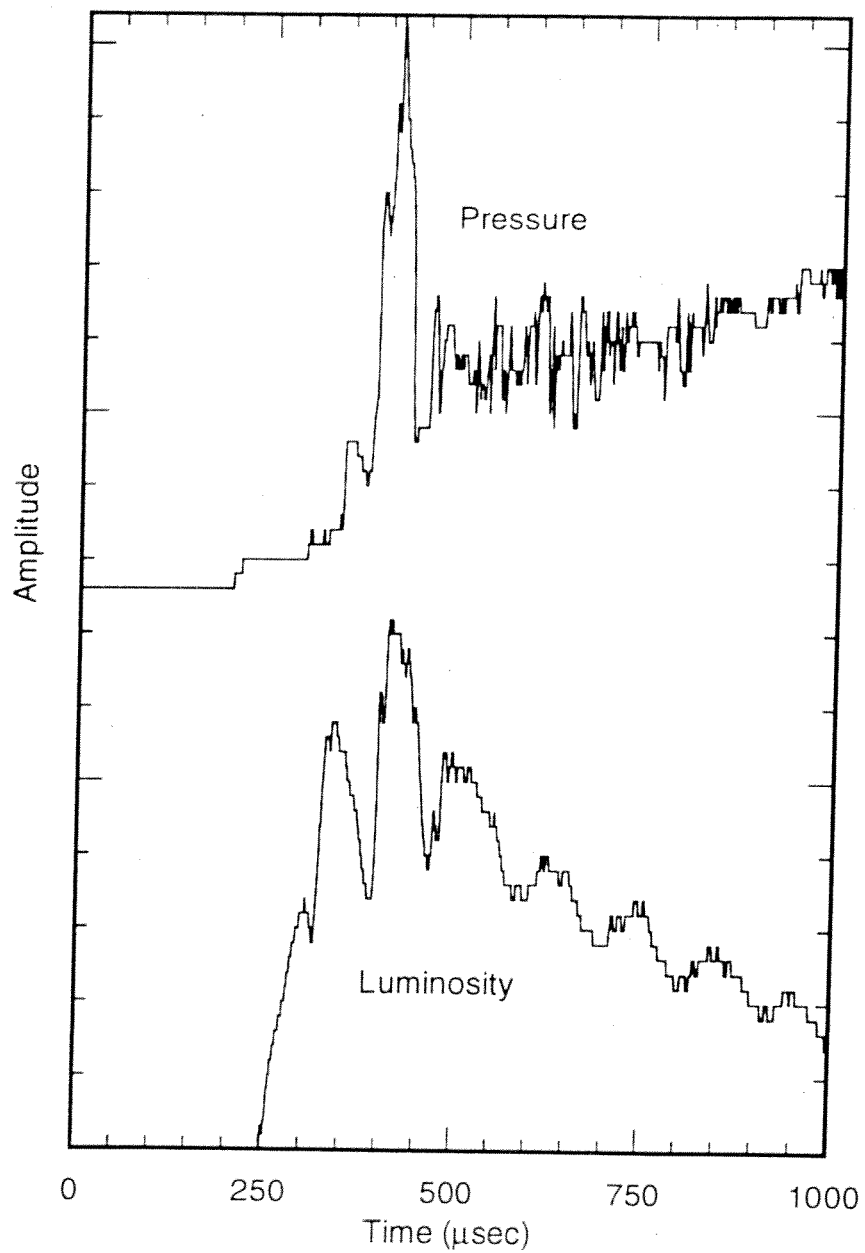


Fig. 4.6 Comparison of tube wall pressure and luminosity data from station 3 in the launch tube for the experiment shown in Fig. 4.3.

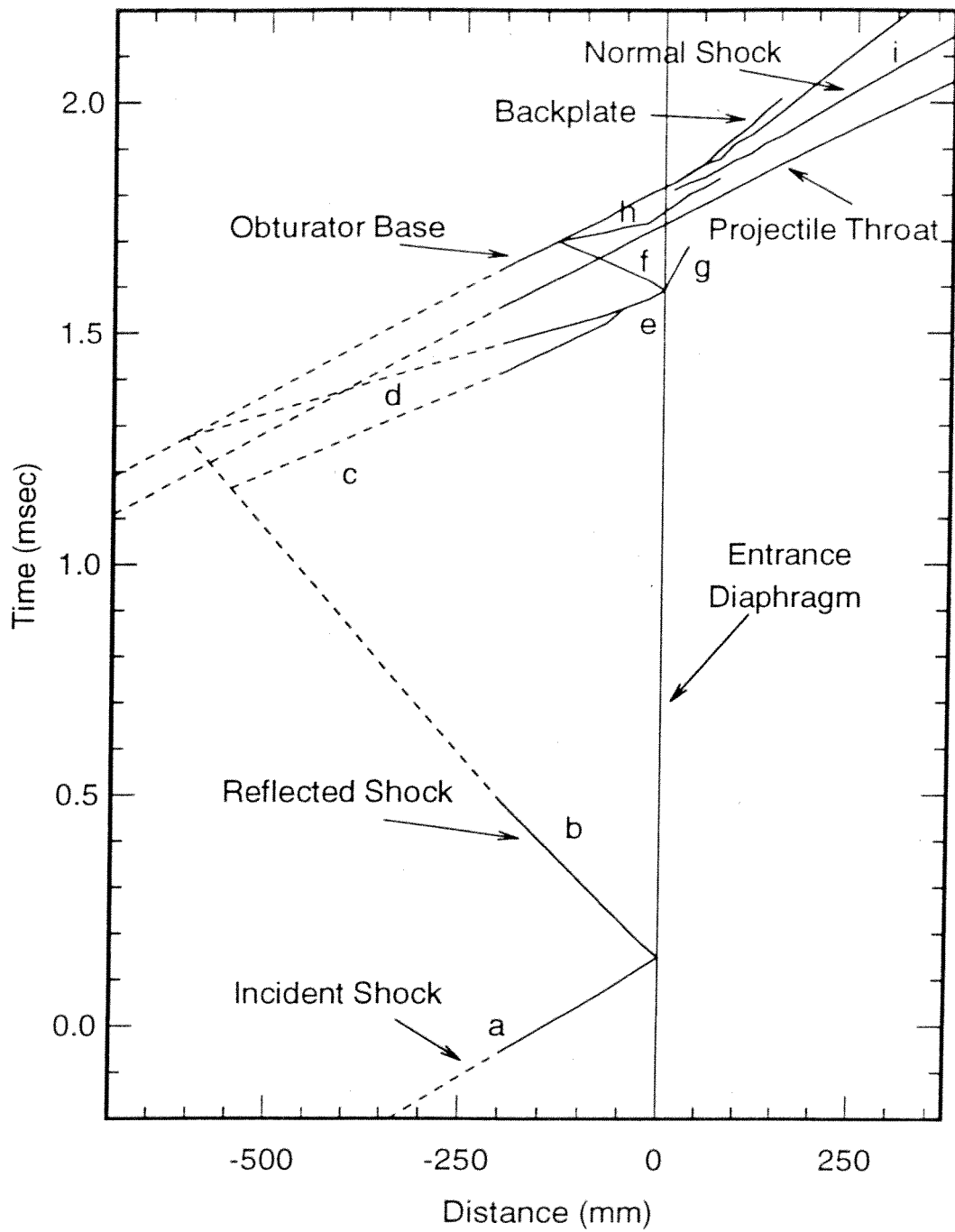


Fig. 4.7 Distance-time (x-t) diagram of the experimental data shown in Figs. 4.3 and 4.4.

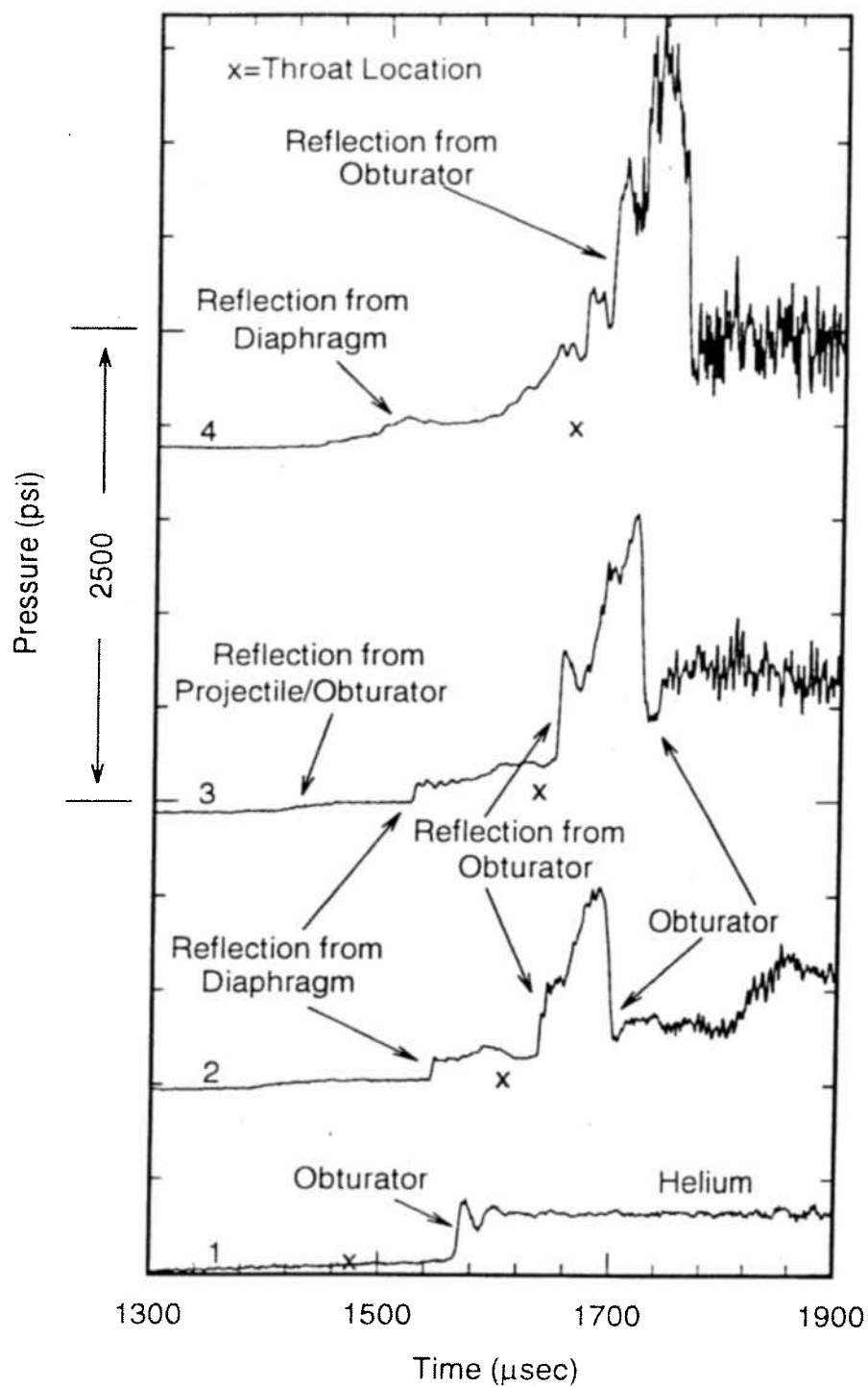


Fig. 4.8 Tube wall pressure traces from the launch tube for a projectile traveling 955 m/s in a mixture of $2.7\text{CH}_4+7.8\text{N}_2$.

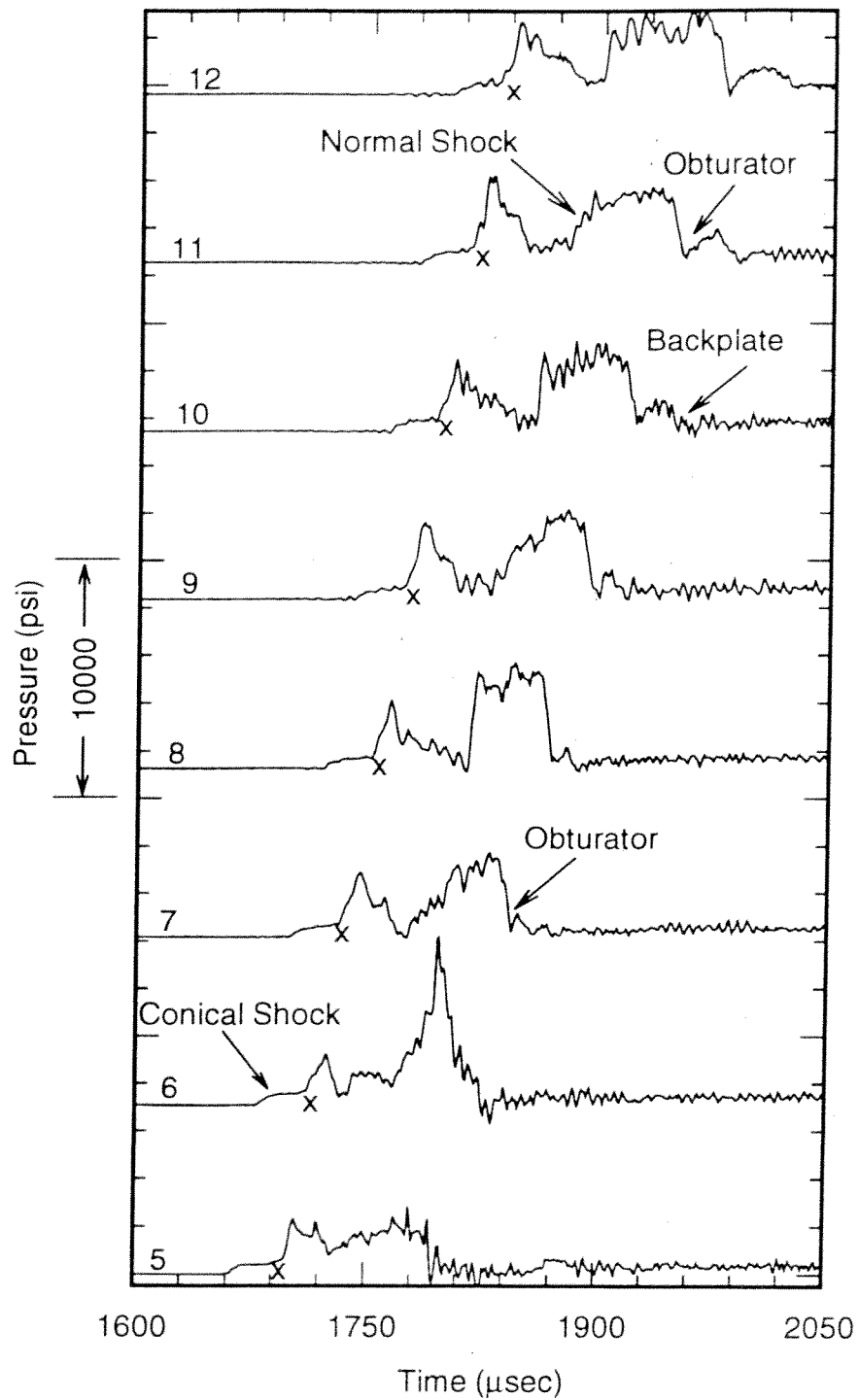


Fig. 4.9 Tube wall pressure traces from the accelerator section for a projectile traveling 955 m/s in a mixture of $2.7\text{CH}_4+7.8\text{N}_2$.

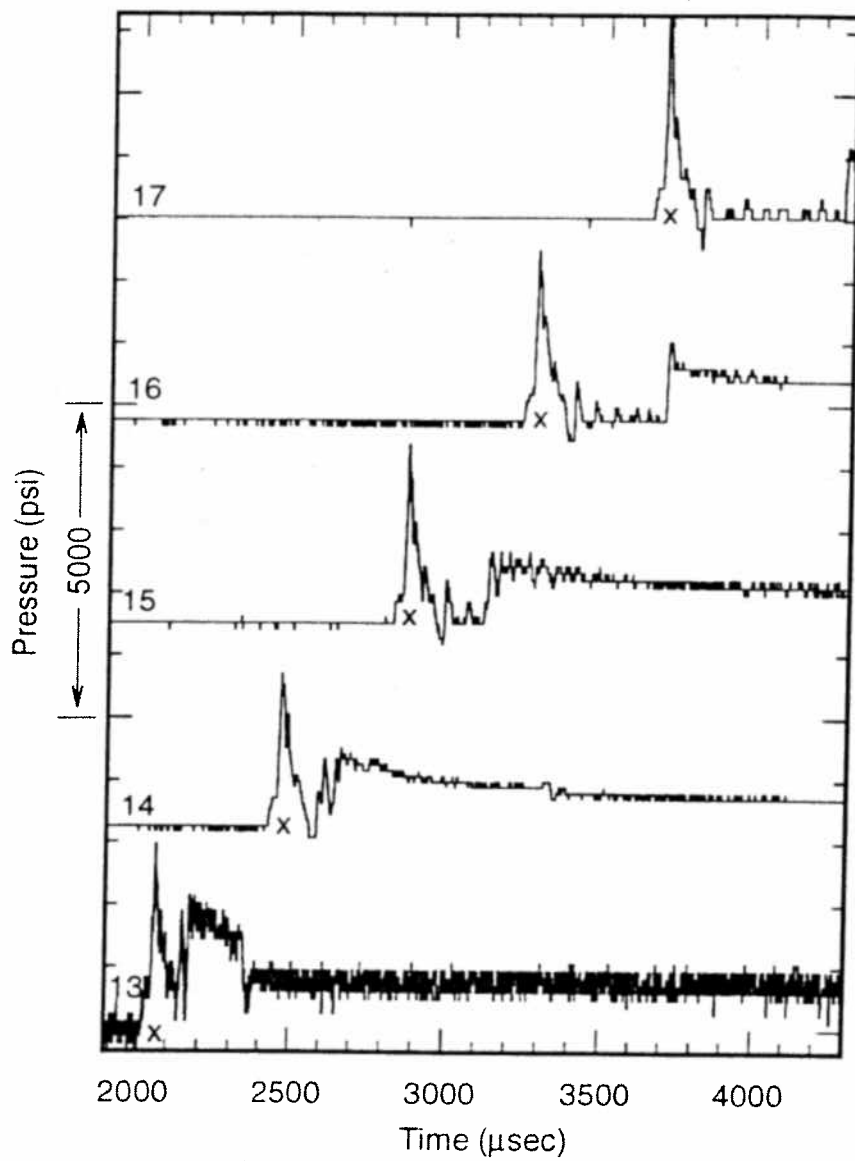


Fig. 4.10 Tube wall pressure traces from farther down the accelerator section for the experiment shown in Figs. 4.8 and 4.9.

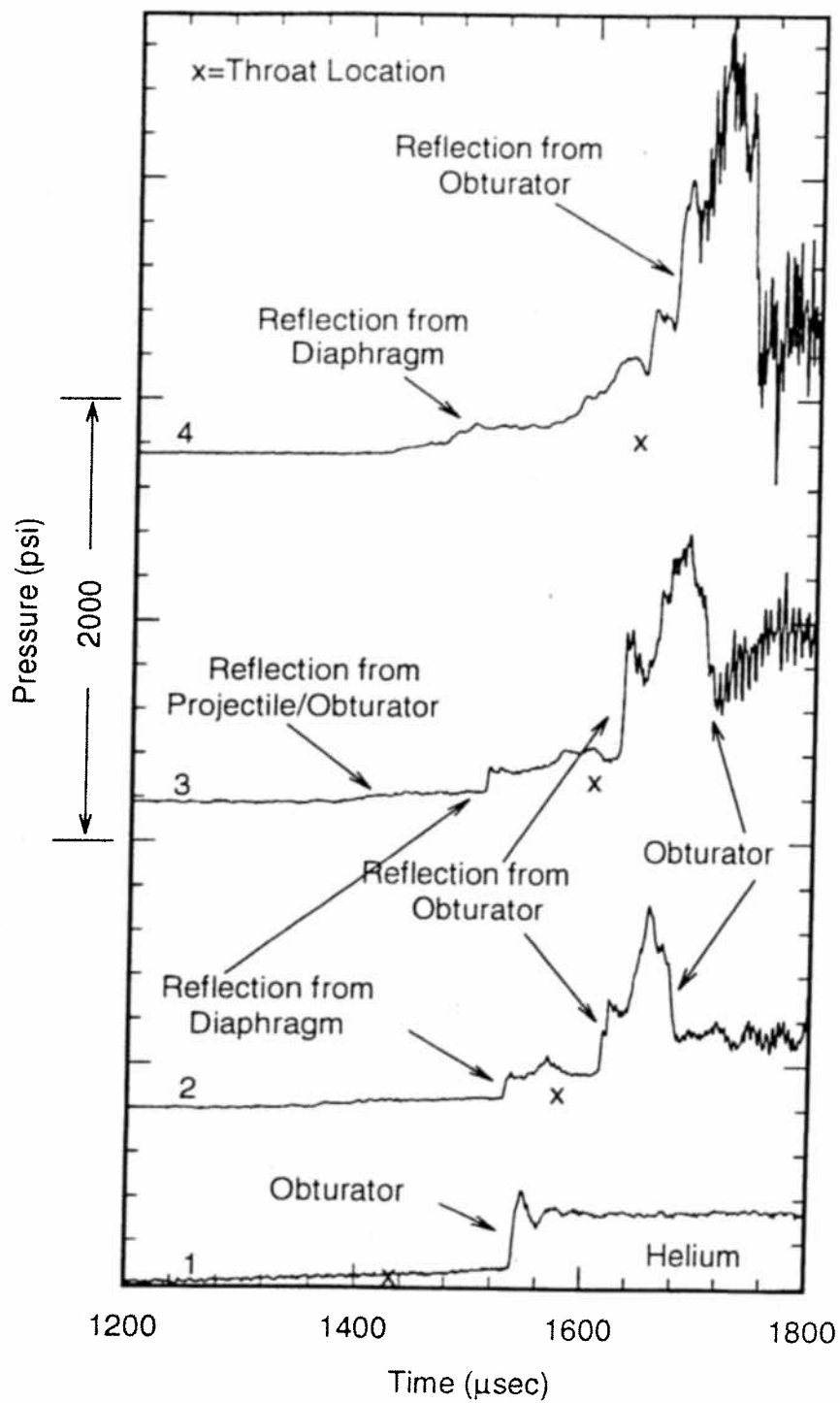


Fig. 4.11 Tube wall pressure traces from the launch tube for a projectile traveling 910 m/s in a mixture of $2.7\text{CH}_4+7.8\text{N}_2$.

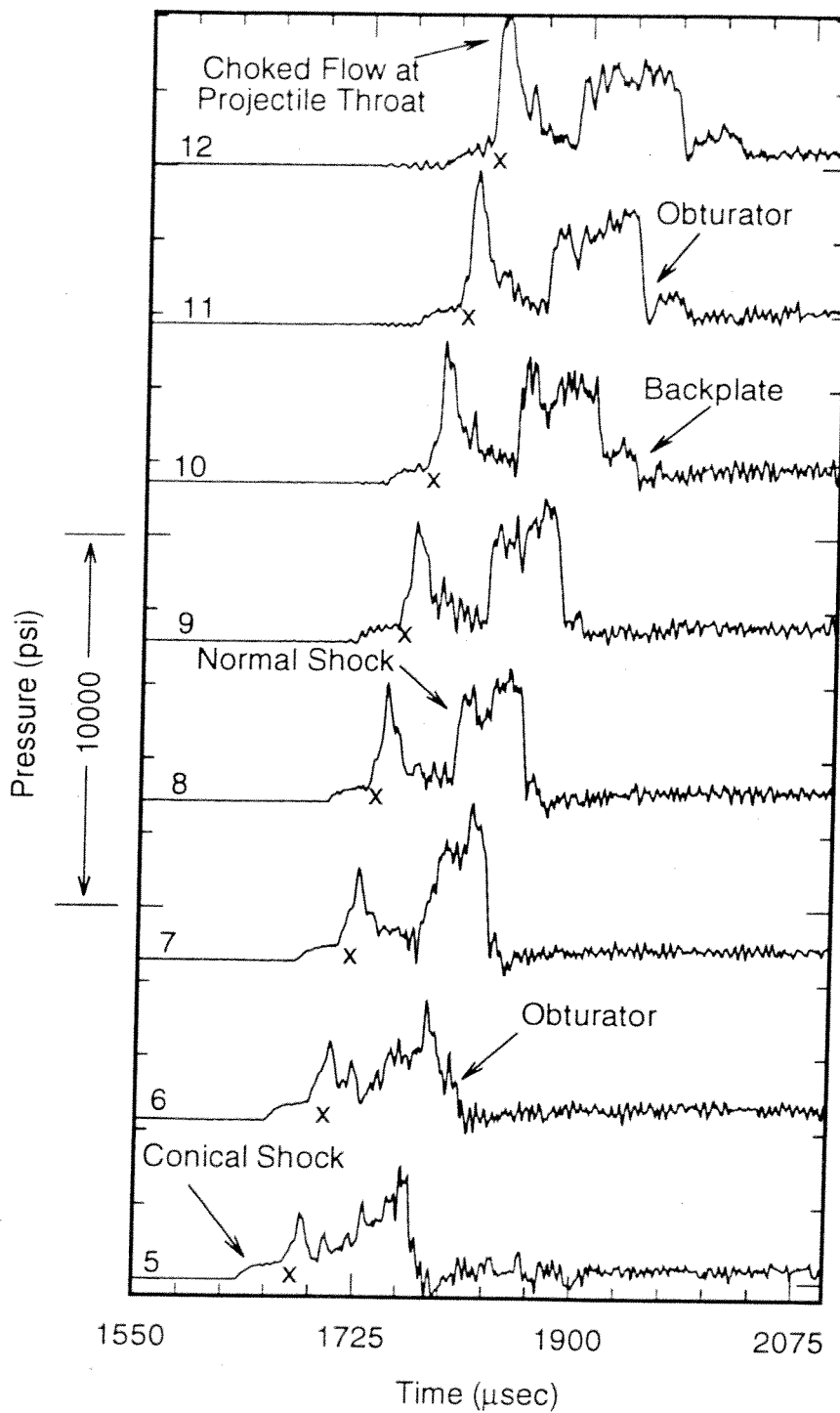


Fig. 4.12 Tube wall pressure traces from the accelerator section for a projectile traveling 910 m/s in a mixture of $2.7\text{CH}_4 + 7.8\text{N}_2$.

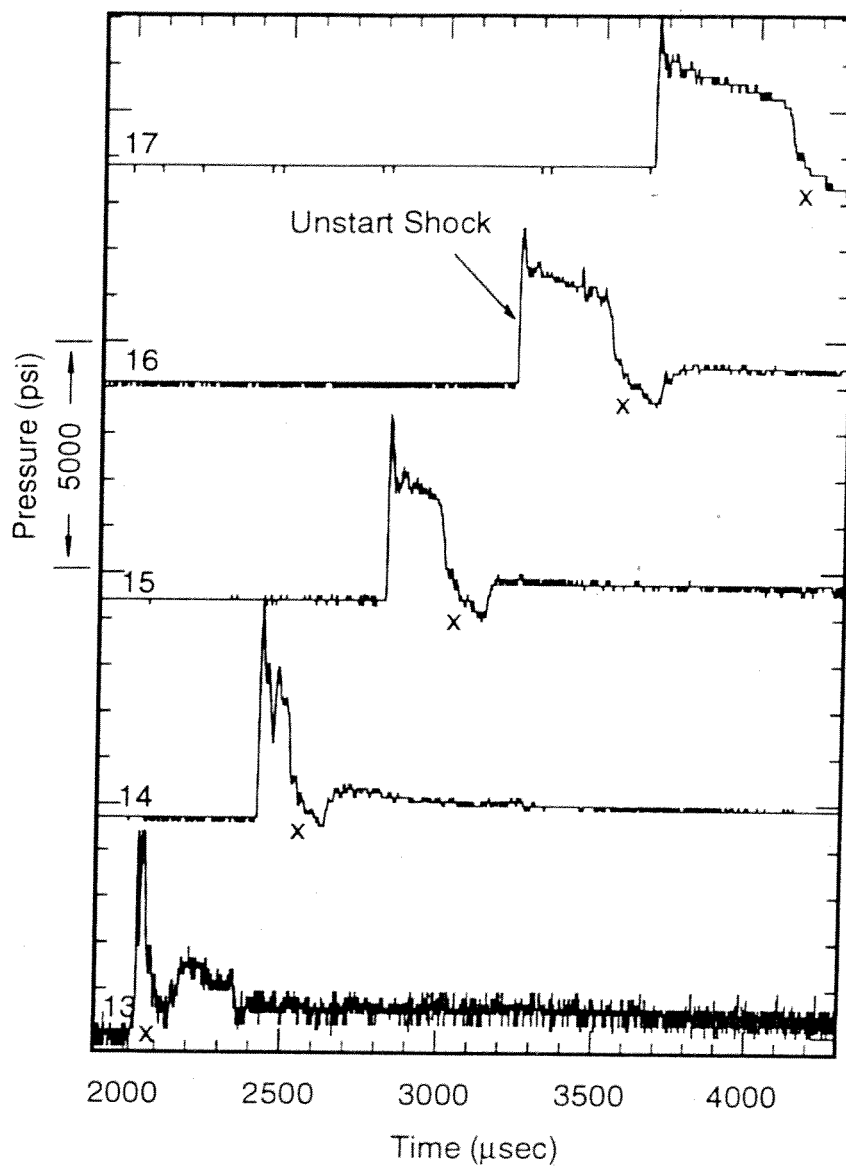


Fig. 4.13 Tube wall pressure traces from farther down the accelerator section for the experiment shown in Figs. 4.11 and 4.13.

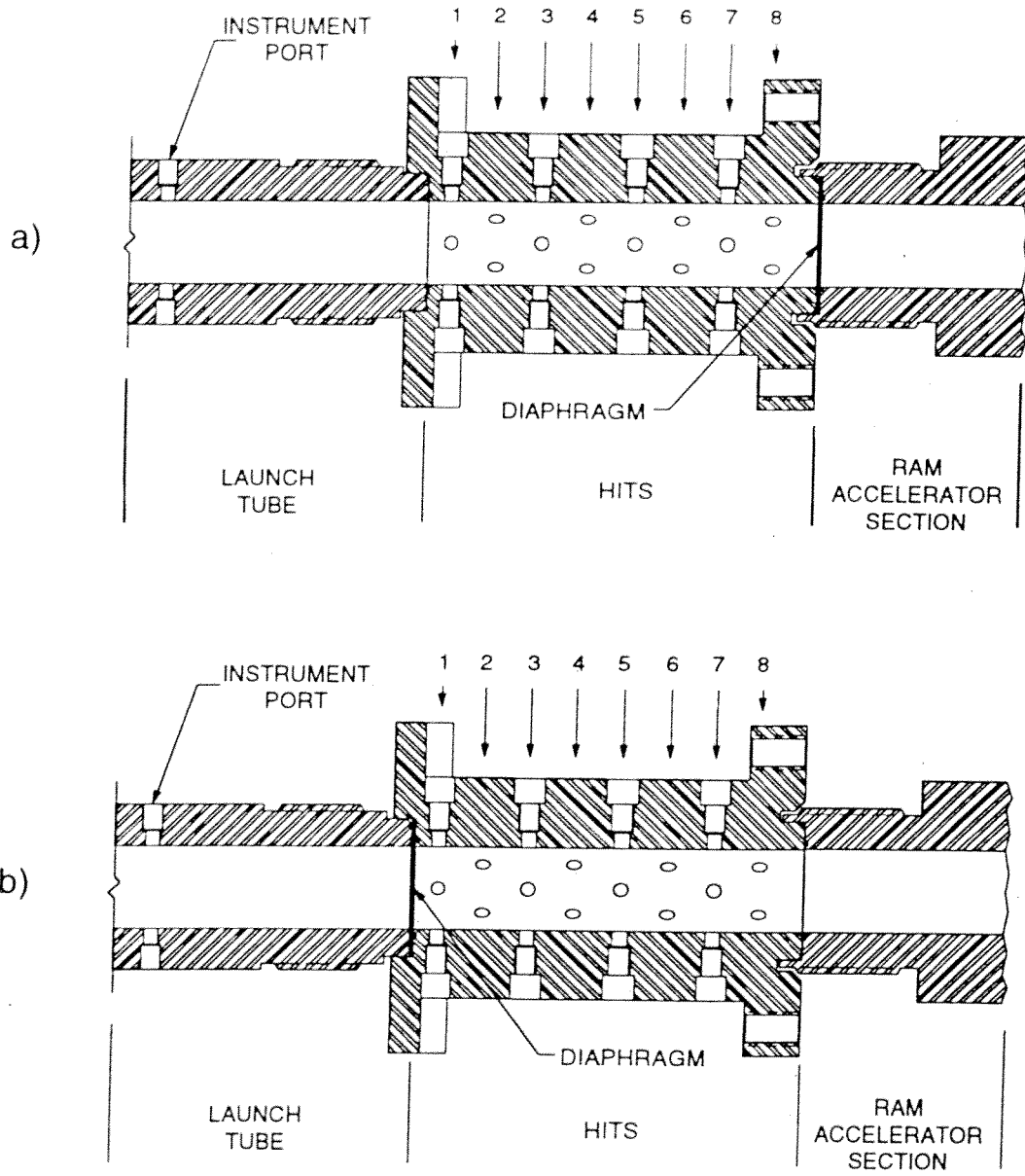


Fig. 4.14 Instrumentation station numbering for Figs 4.15 - 4.18.

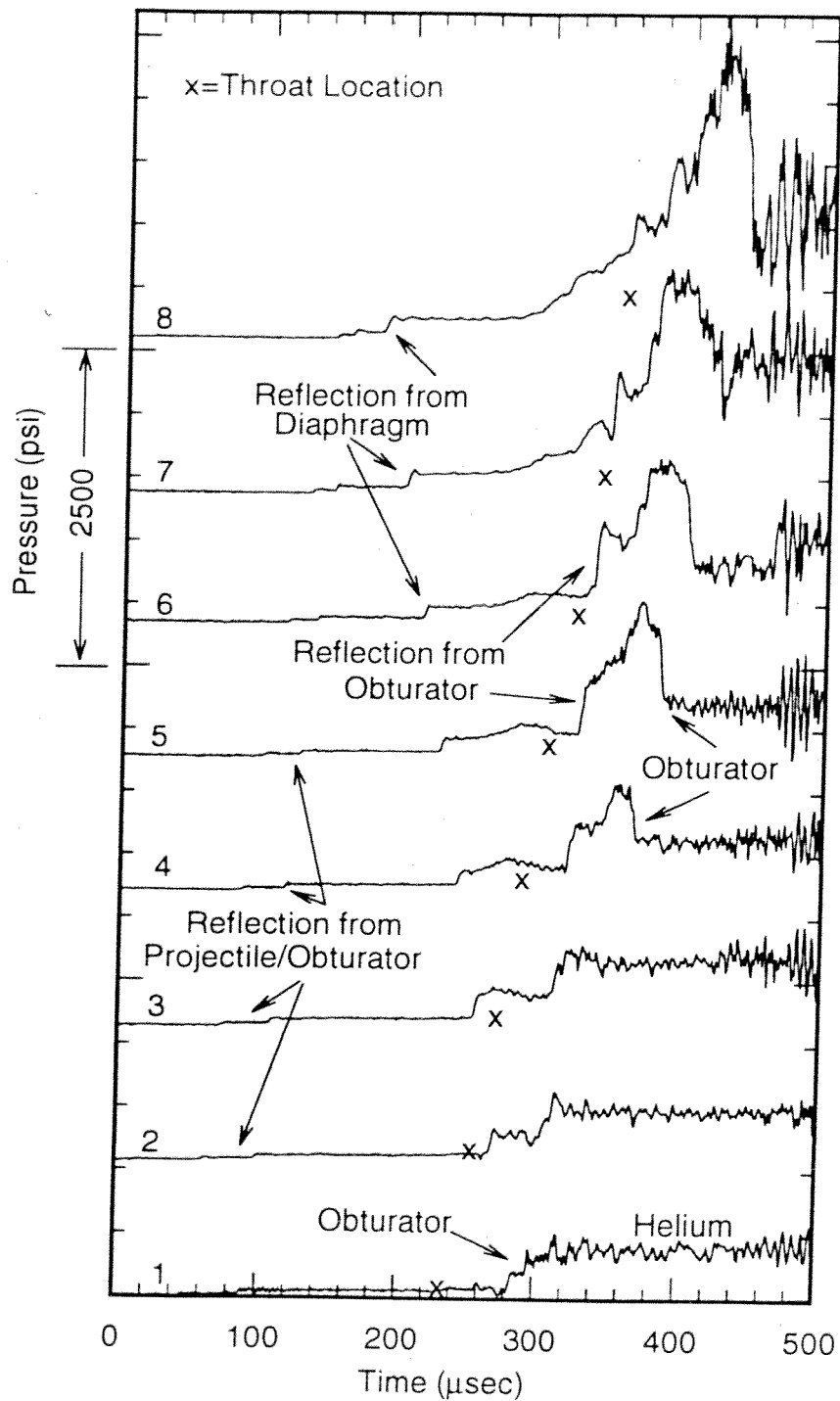


Fig. 4.15 Tube wall pressure traces from the launch tube for a projectile traveling 1160 m/s in a mixture of $2.7\text{CH}_4+2\text{O}_2+5.8\text{N}_2$.

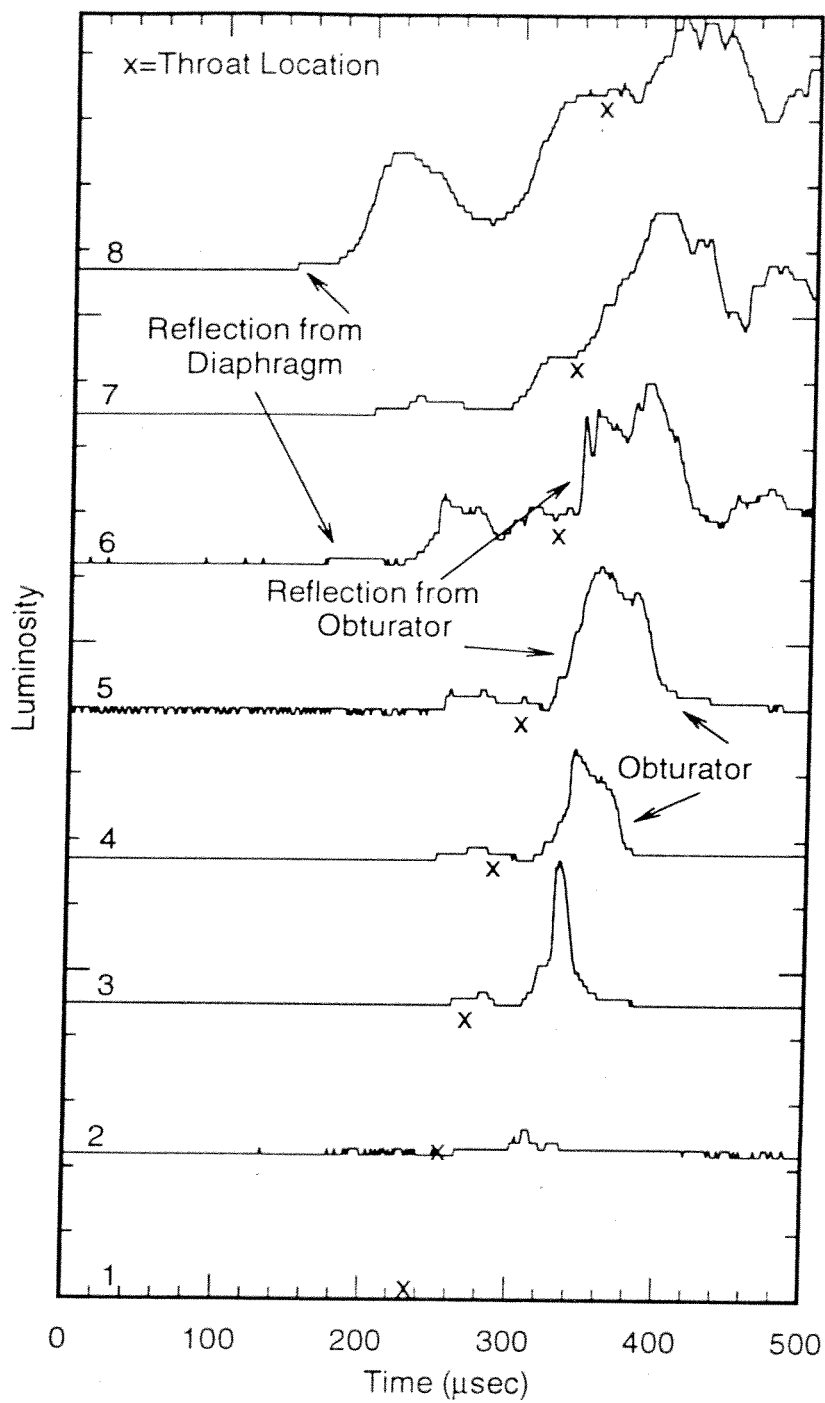


Fig. 4.16 Luminosity data from the launch tube for the experiment shown in Fig. 4.15.

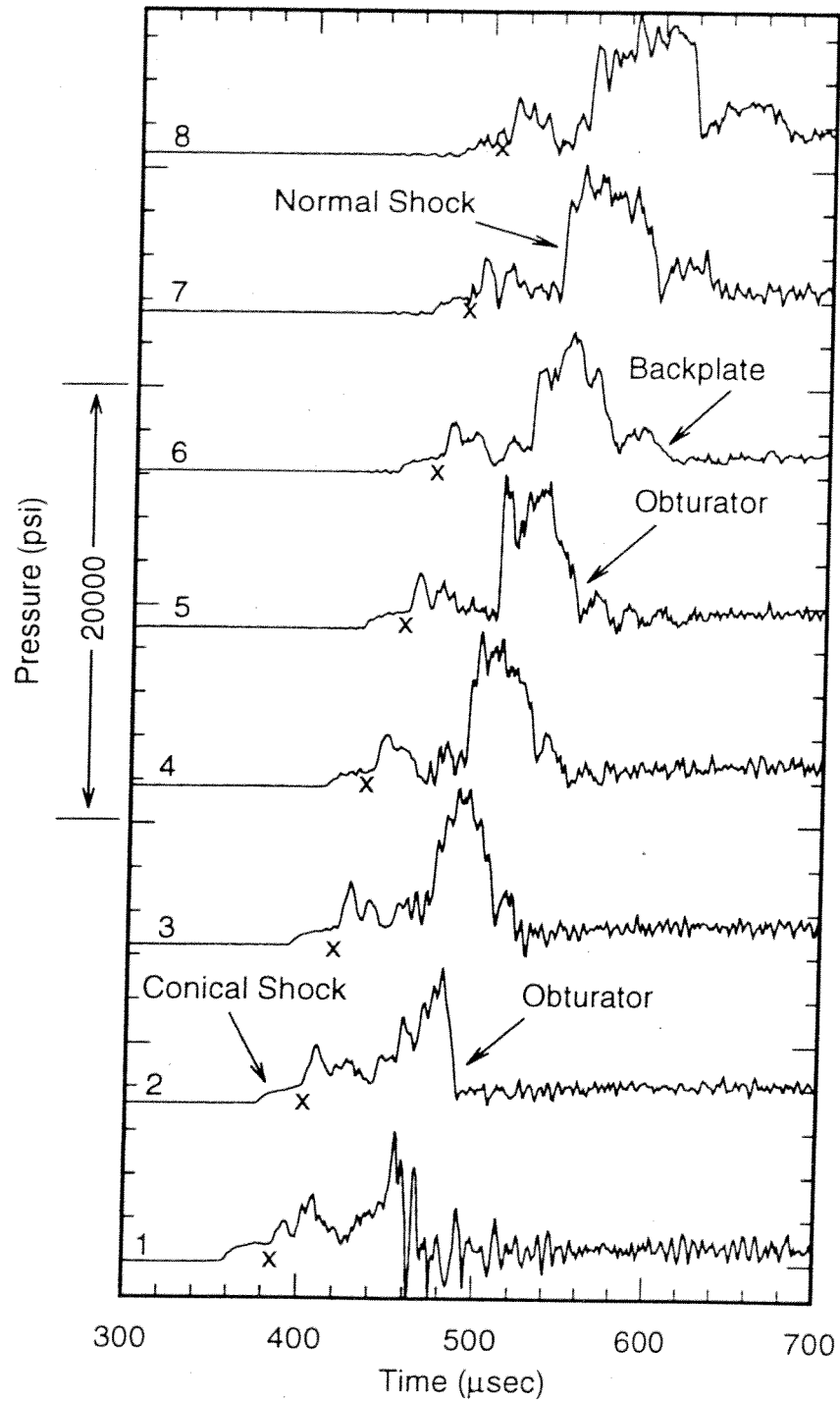


Fig. 4.17 Tube wall pressure traces from the accelerator section for a projectile traveling 1160 m/s in a mixture of $2.7\text{CH}_4 + 2\text{O}_2 + 5.8\text{N}_2$.

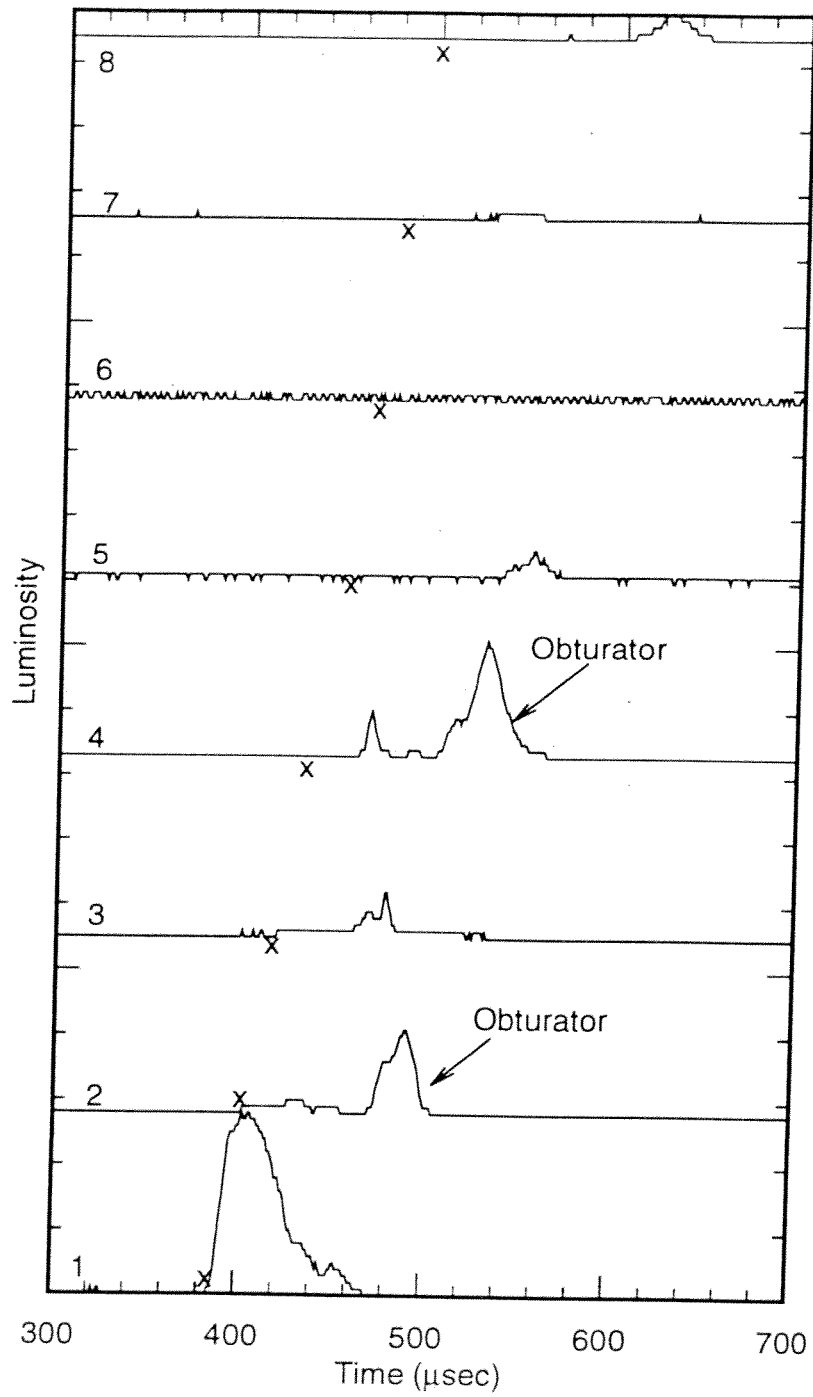


Fig. 4.18 Luminosity data from the accelerator section for the experiment shown in Fig. 4.17.

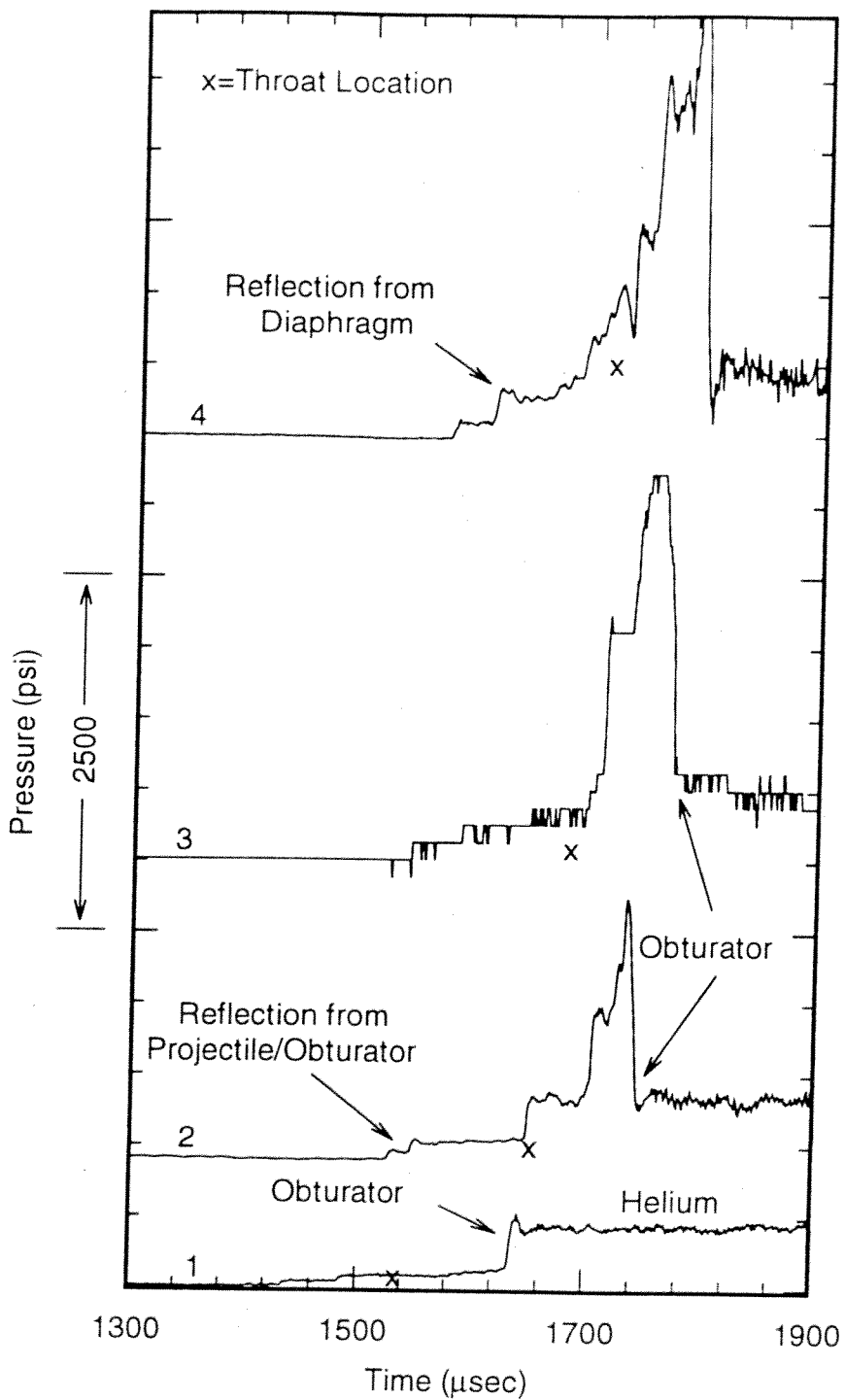


Fig. 4.19 Tube wall pressure traces from the launch tube for a projectile traveling 1190 m/s in a mixture of $2.7\text{CH}_4+2\text{O}_2+5.8\text{N}_2$ with a solid obturator.

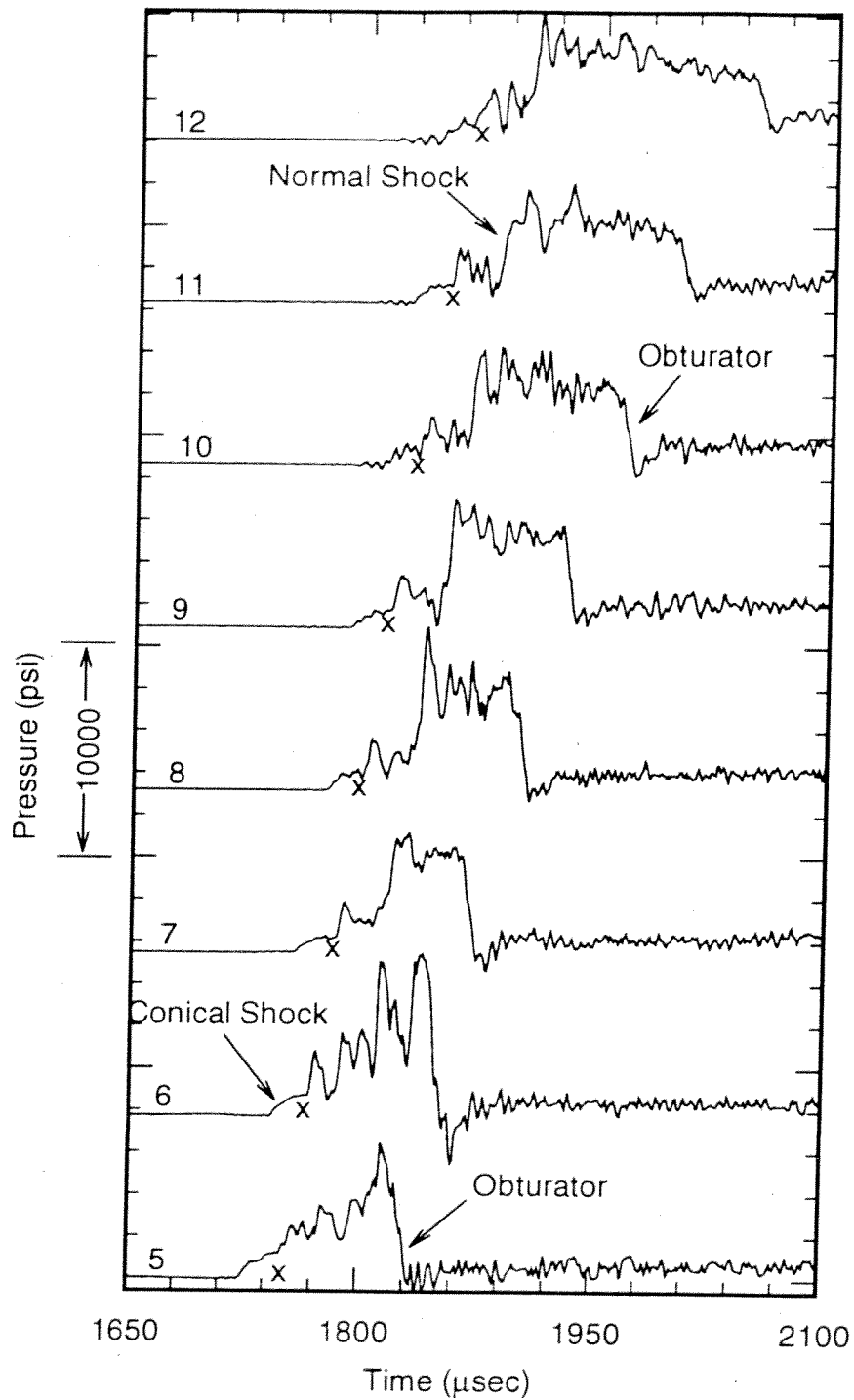


Fig. 4.20 Tube wall pressure traces from the accelerator section for a projectile traveling 1190 m/s in a mixture of $2.7\text{CH}_4 + 2\text{O}_2 + 5.8\text{N}_2$ with a solid obturator.

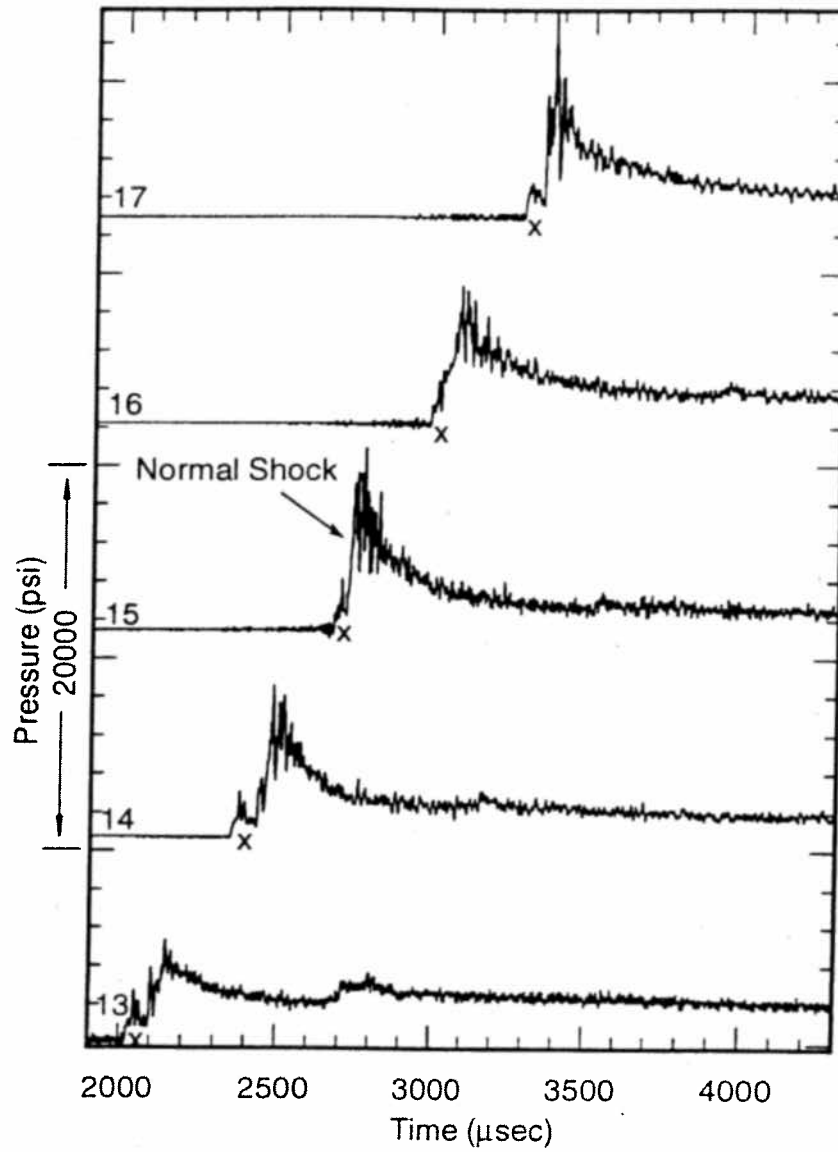


Fig. 4.21 Tube wall pressure traces from farther down the accelerator section for the experiment shown in Figs. 4.19 and 4.20.

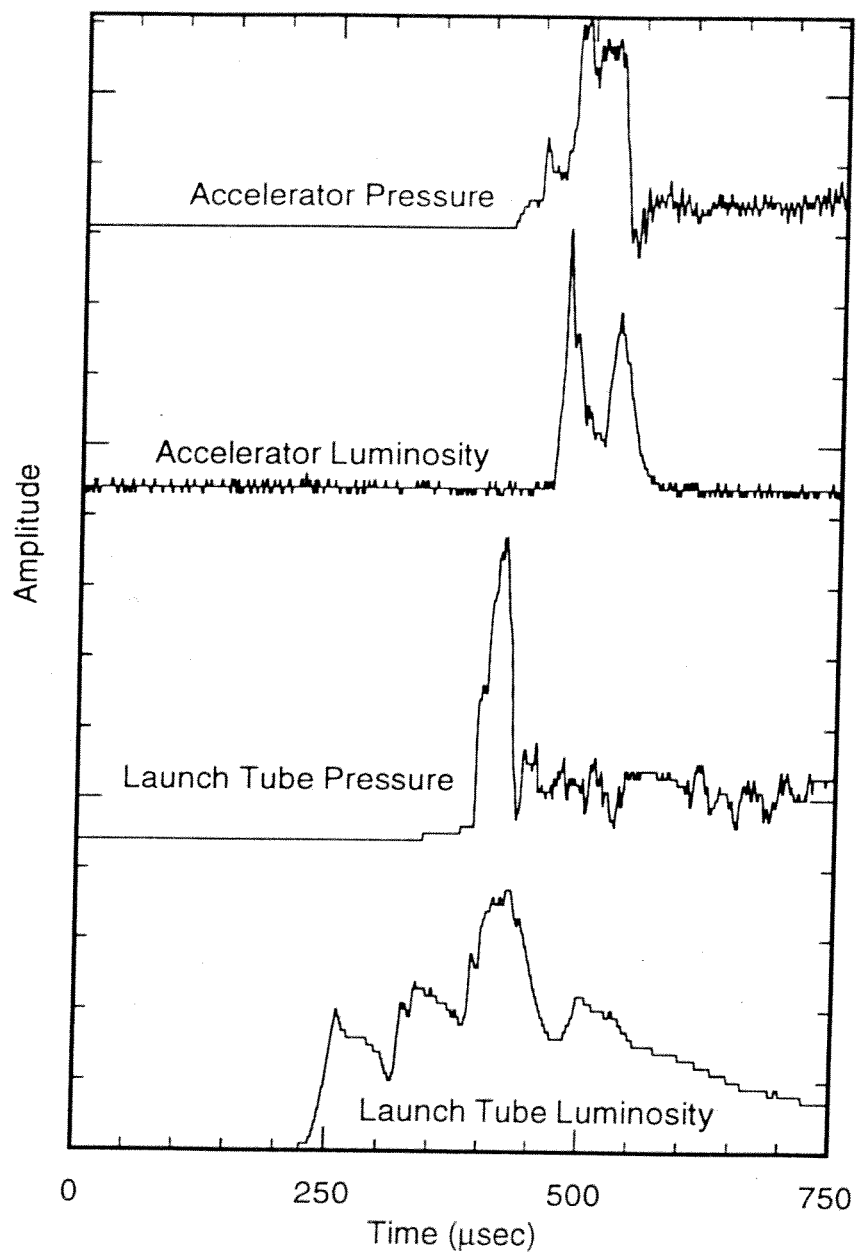


Fig. 4.22 Comparison of tube wall pressure and luminosity data for the experiment shown in Figs. 4.19 and 4.20.

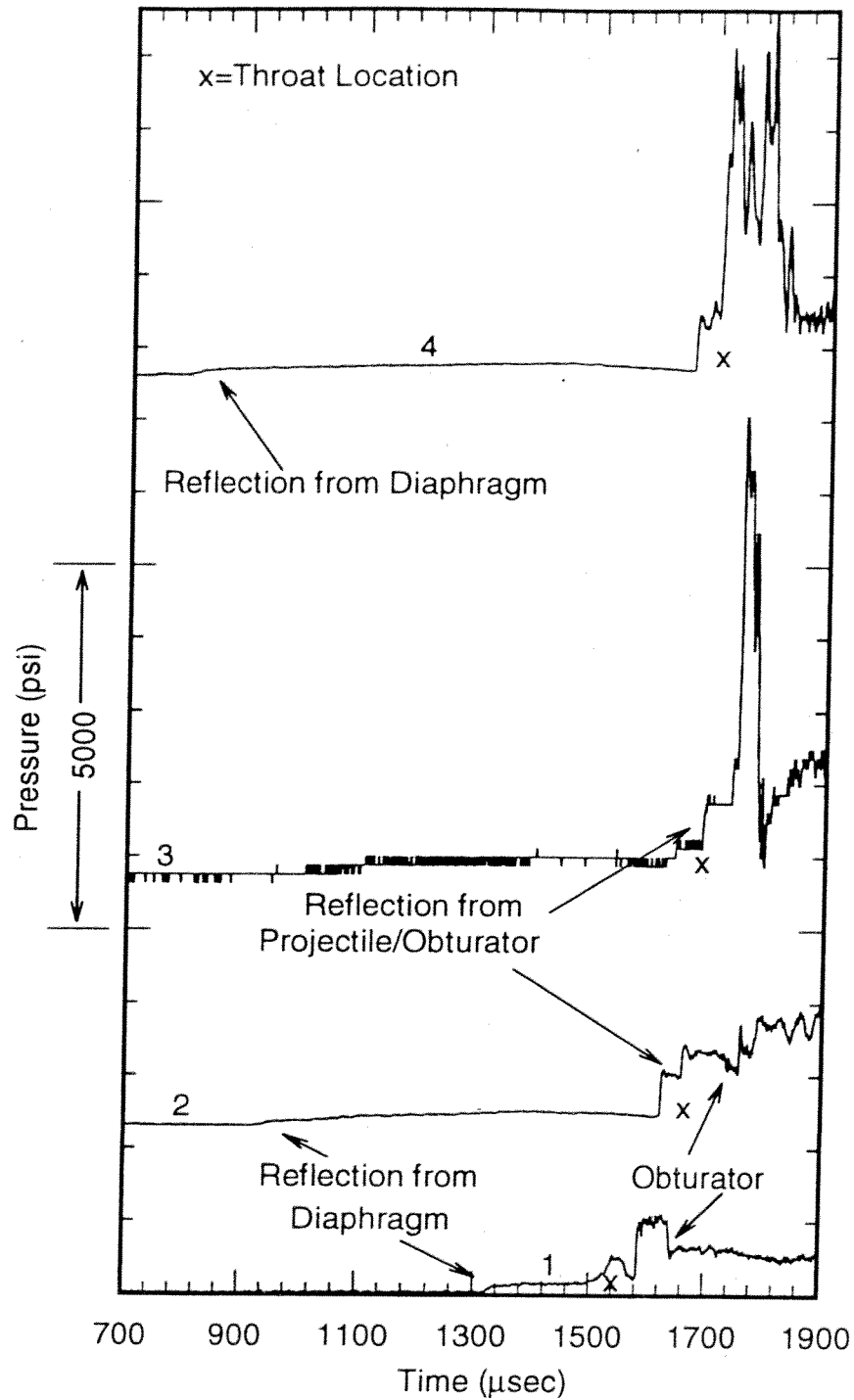


Fig. 4.23 Tube wall pressure traces from the launch tube for a projectile traveling 1180 m/s in a mixture of $2.7\text{CH}_4+2\text{O}_2+5.8\text{N}_2$ with 1.0 psi of air in the launch tube and five 0.014" mylar diaphragms.

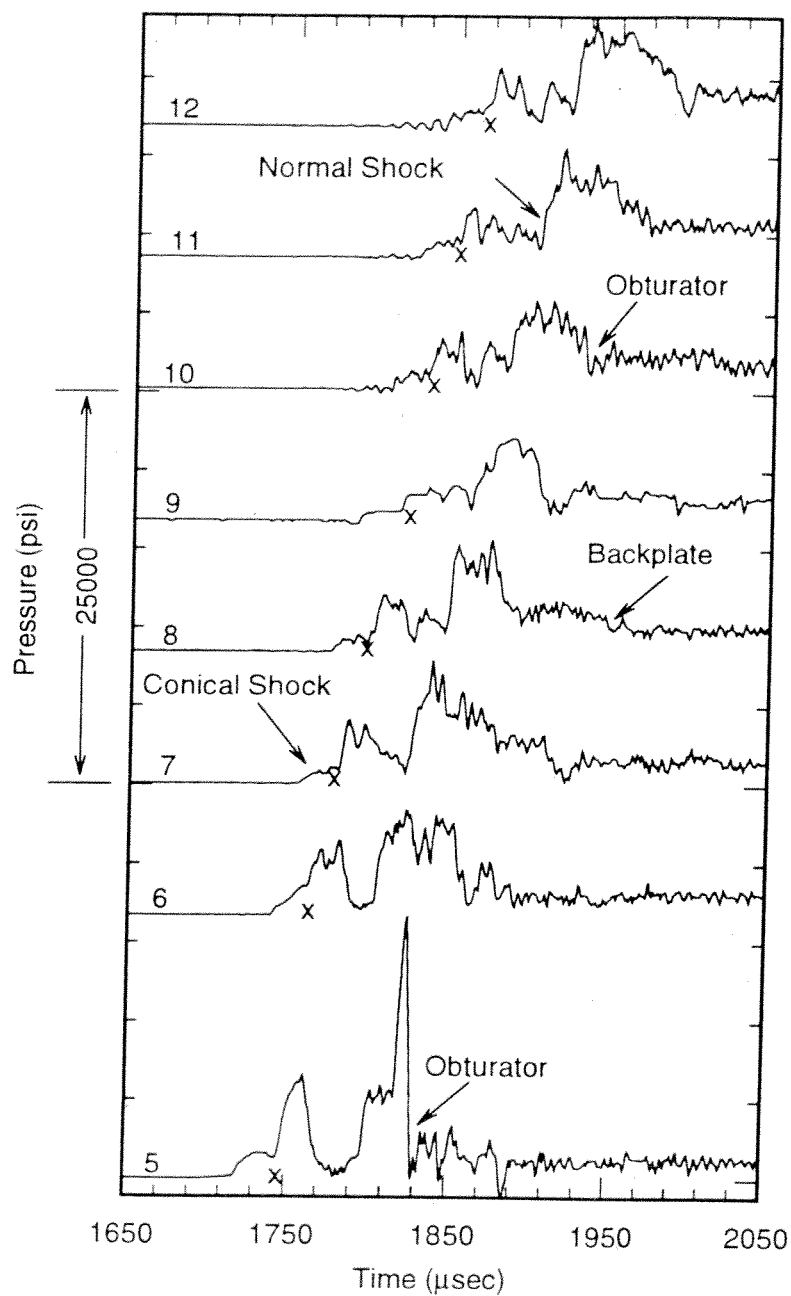


Fig. 4.24 Tube wall pressure traces from the accelerator section for a projectile traveling 1180 m/s in a mixture of $2.7\text{CH}_4 + 2\text{O}_2 + 5.8\text{N}_2$ with 1.0 psi of air in the launch tube and five 0.014" mylar diaphragms.

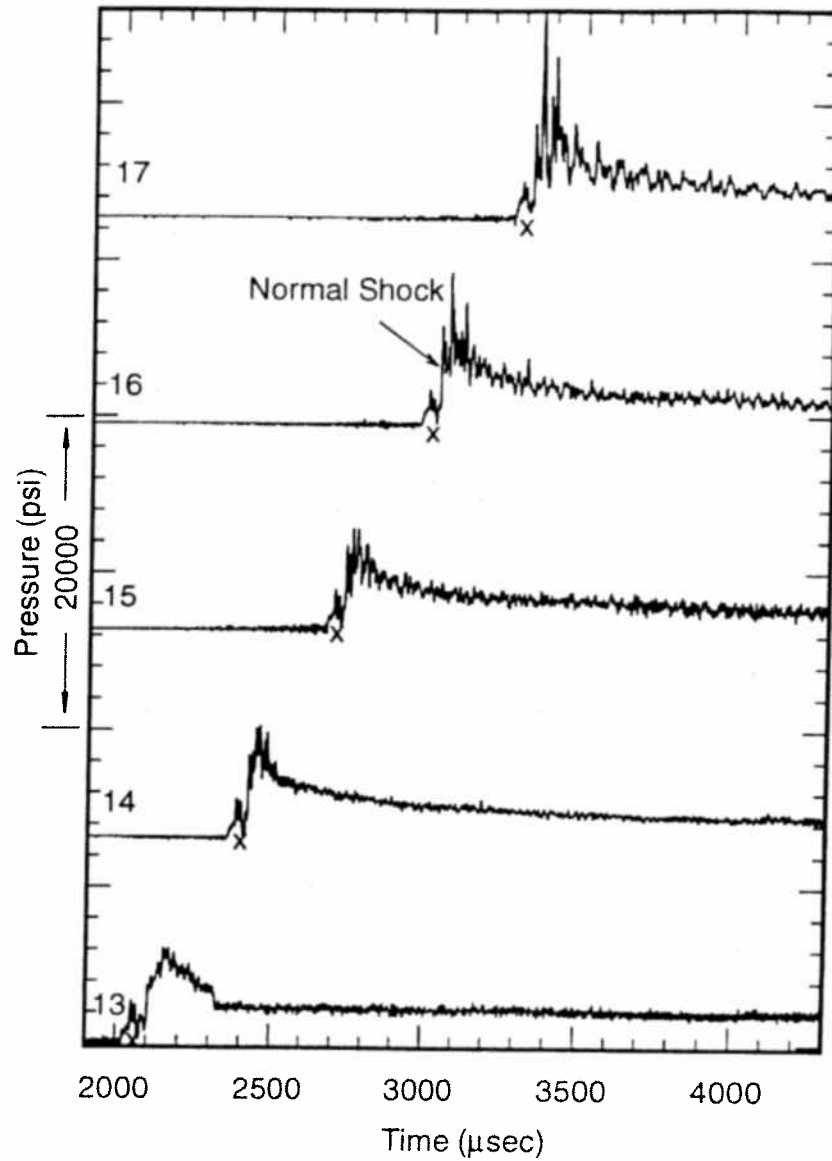


Fig. 4.25 Tube wall pressure traces from farther down the accelerator section for the experiment shown in Figs. 4.23 and 4.24.

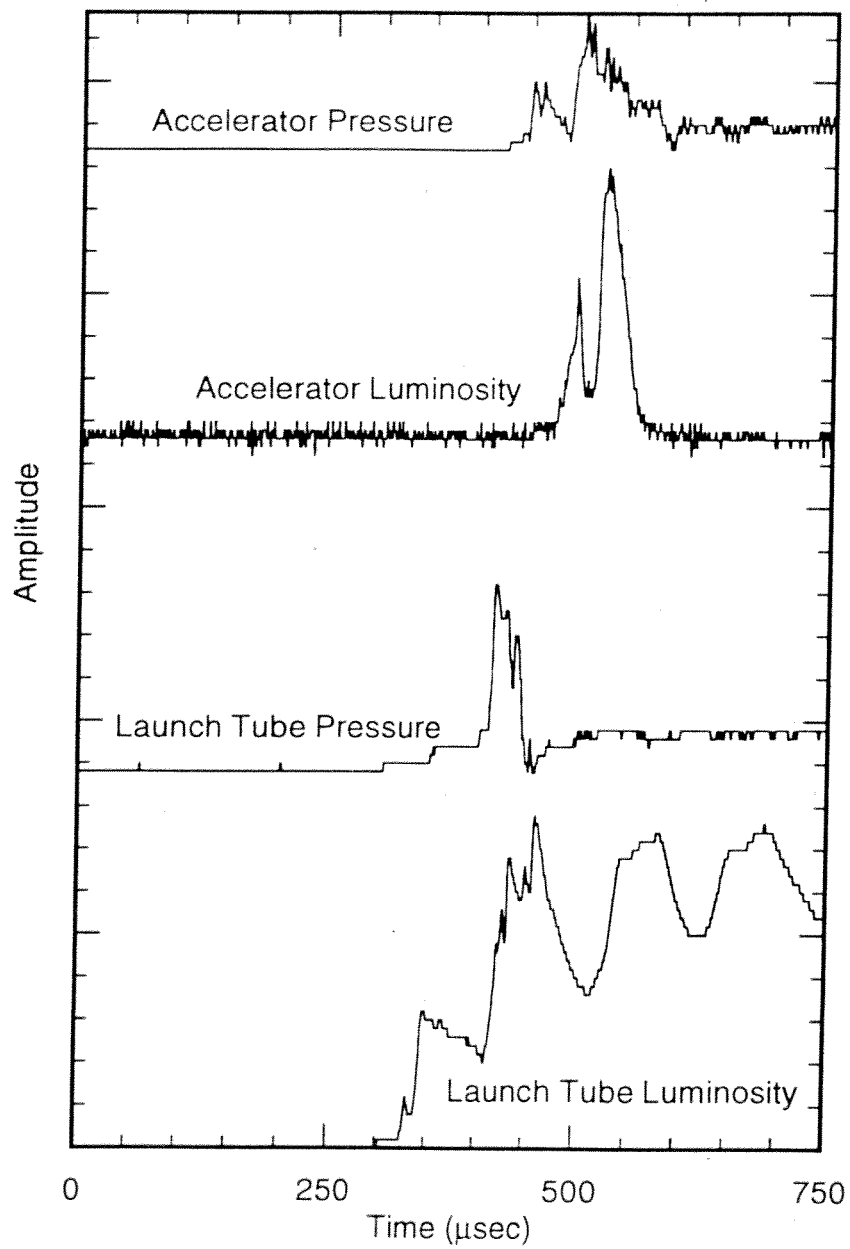


Fig. 4.26 Comparison of tube wall pressure and luminosity data for the experiment shown in Figs. 4.23 and 4.24.

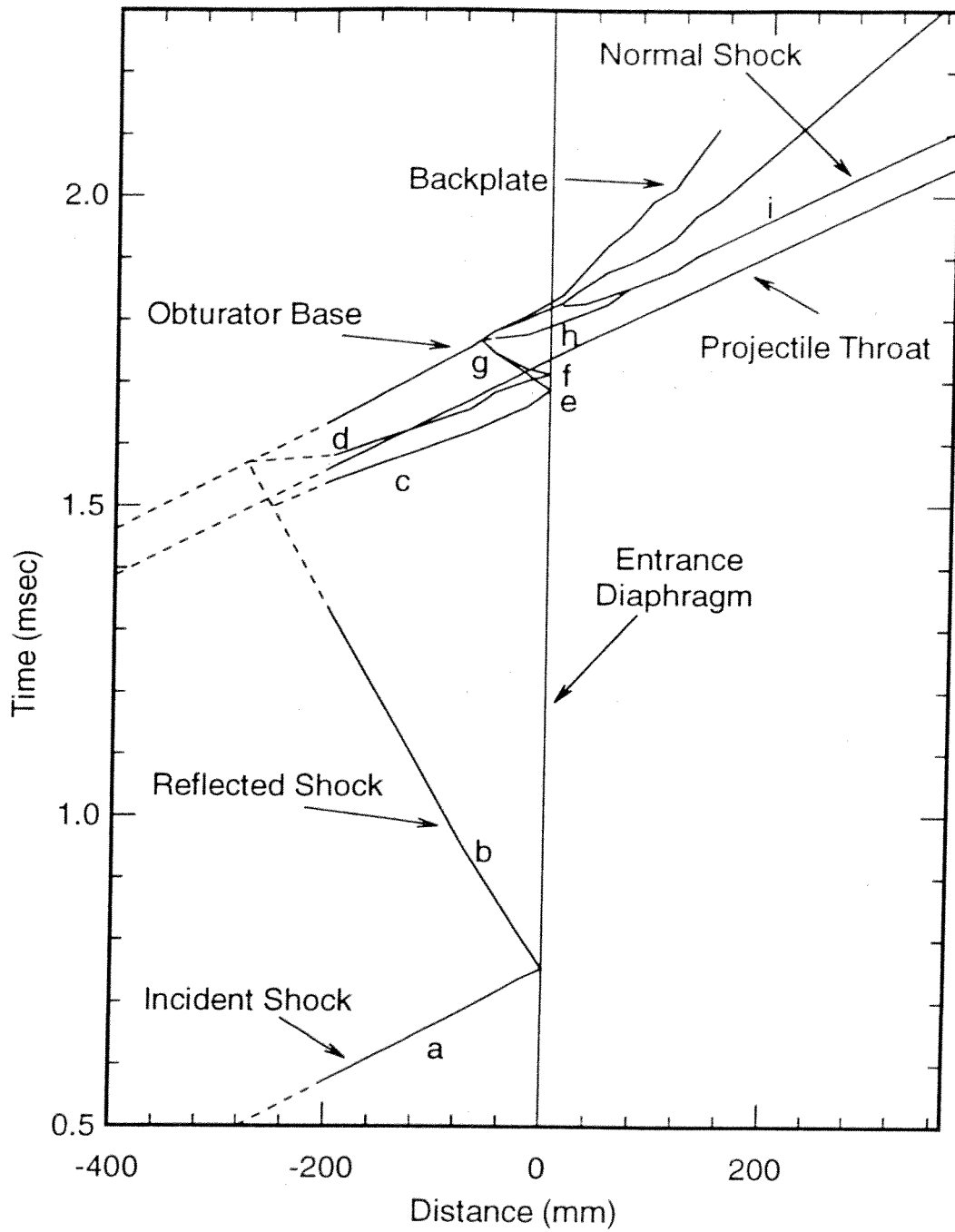


Fig. 4.27 Distance-time (x-t) diagram of the experimental data shown in Figs. 4.23 and 4.24.

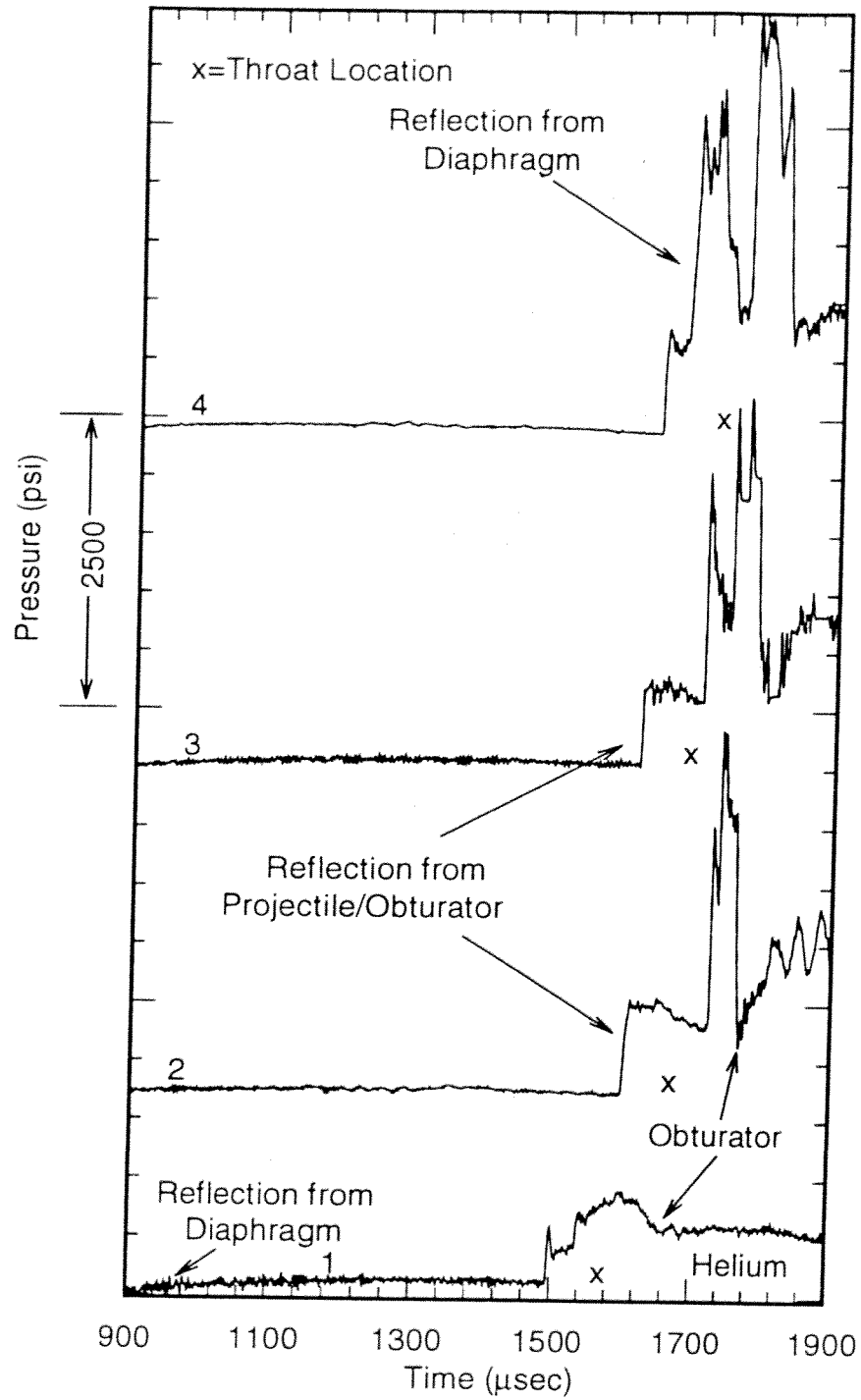


Fig. 4.28 Tube wall pressure traces from the launch tube for a projectile traveling 1140 m/s in a mixture of $2.7\text{CH}_4 + 2\text{O}_2 + 5.8\text{N}_2$ with 1.0 psi of air in the launch tube and two 0.014" mylar diaphragms.

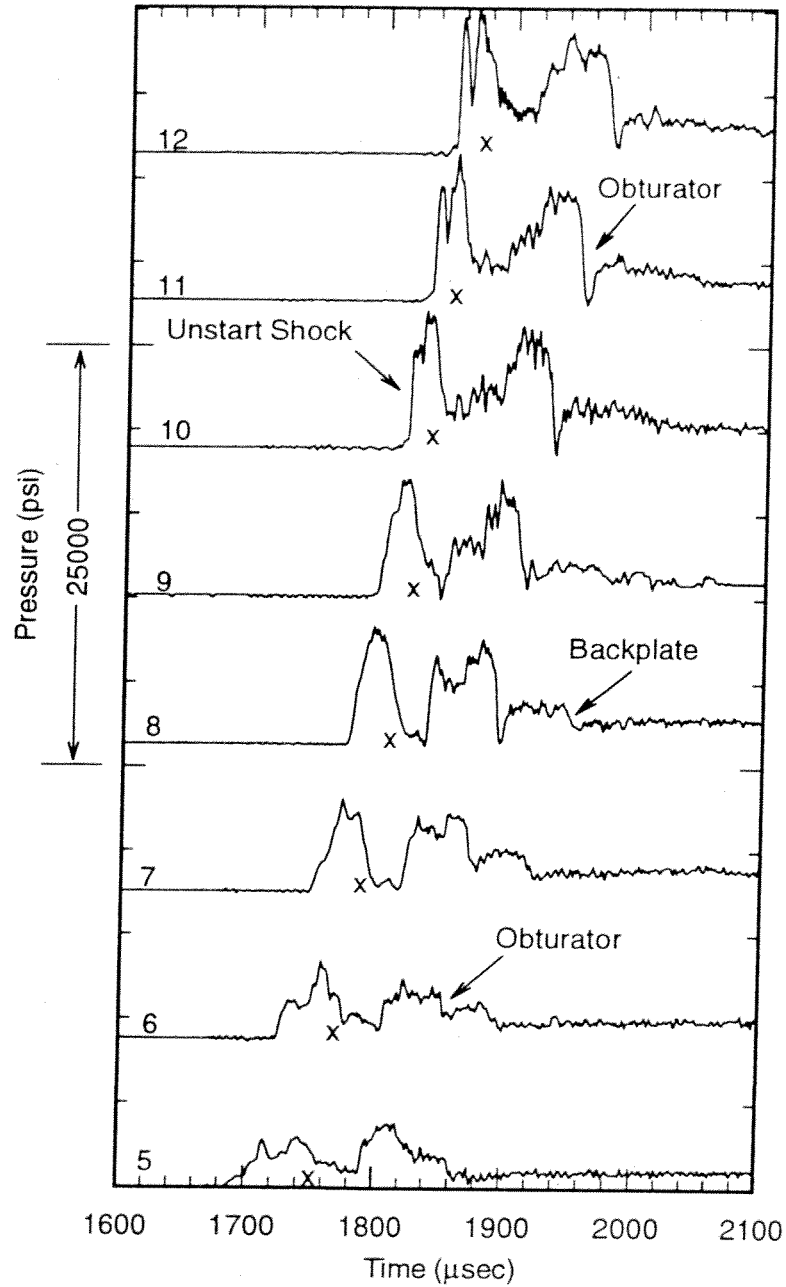


Fig. 4.29 Tube wall pressure traces from the accelerator section for a projectile traveling 1140 m/s in a mixture of $2.7\text{CH}_4+2\text{O}_2+5.8\text{N}_2$ with 1.0 psi of air in the launch tube and two 0.014" mylar diaphragms.

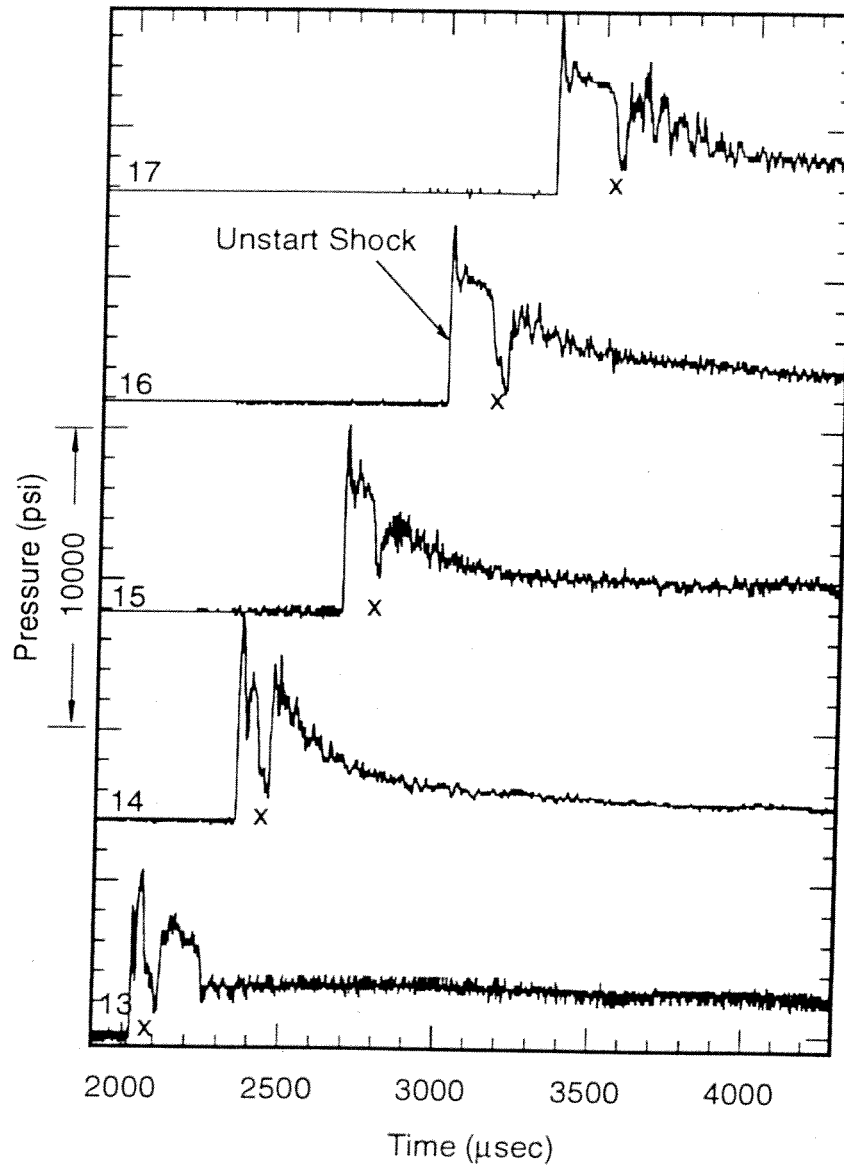


Fig. 4.30 Tube wall pressure traces from farther down the accelerator section for the experiment shown in Figs. 4.28 and 4.29.

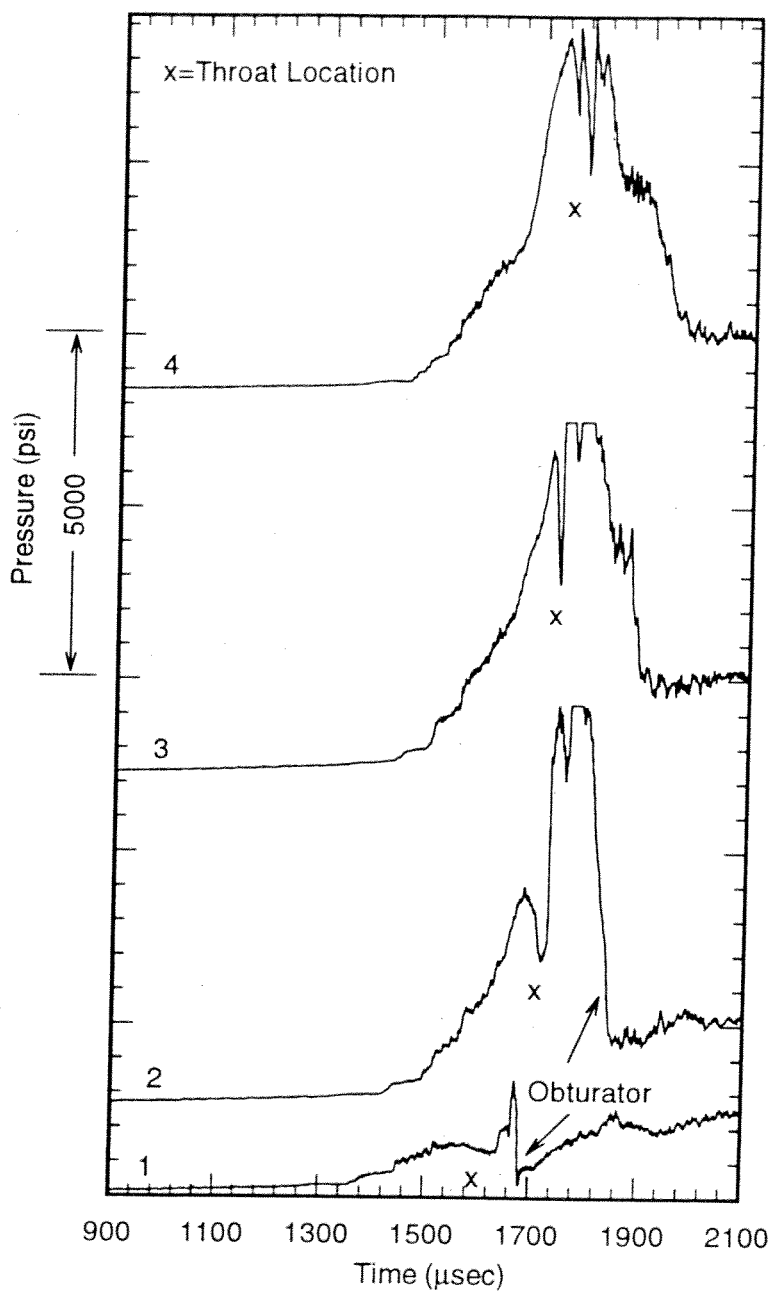


Fig. 4.31 Tube wall pressure traces from the launch tube for a projectile traveling 1100 m/s in a mixture of $2.7\text{CH}_4+2\text{O}_2+5.8\text{N}_2$ with obturator leakage (5%) and 0.1 psi of air in the launch tube and five 0.014" mylar diaphragms.

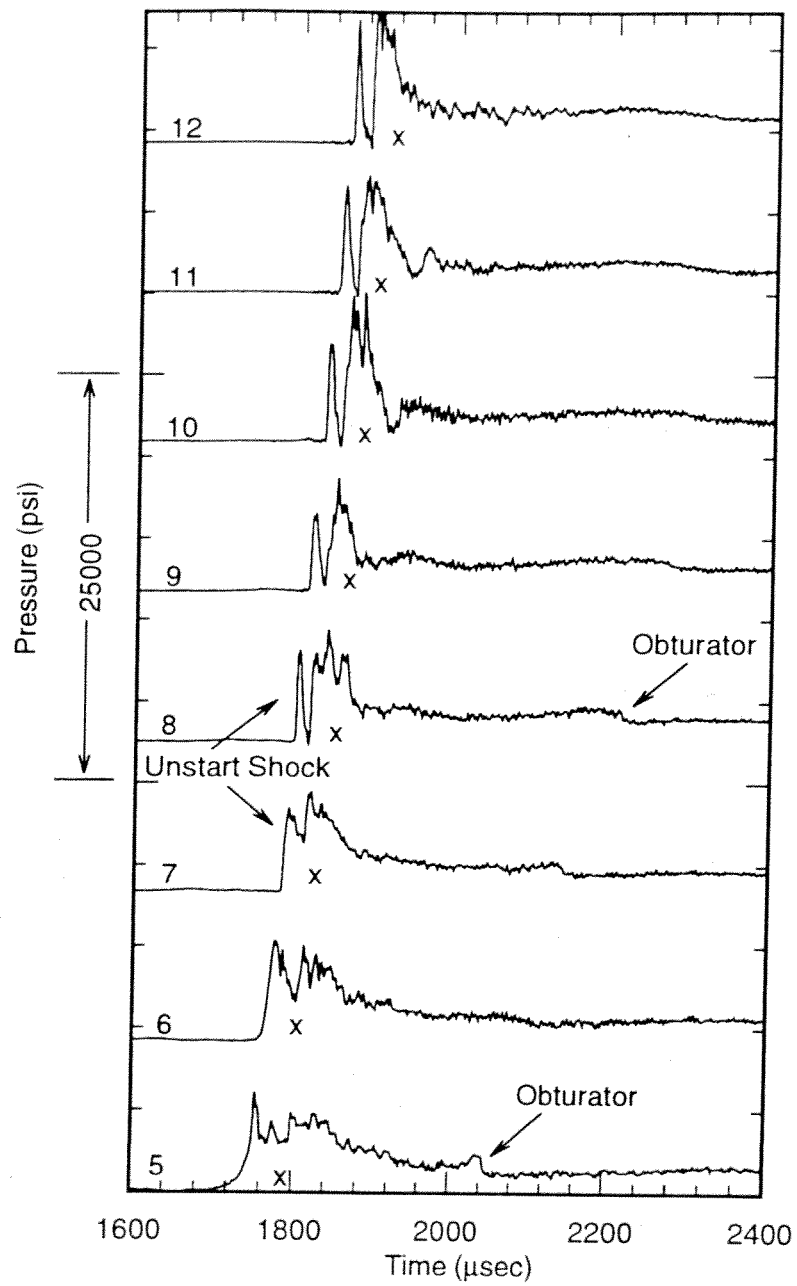


Fig. 4.32 Tube wall pressure traces from the accelerator section for a projectile traveling 1100 m/s in a mixture of $2.7\text{CH}_4 + 2\text{O}_2 + 5.8\text{N}_2$ with obturator leakage (5%) and 1.0 psi of air in the launch tube and five 0.014" mylar diaphragms.

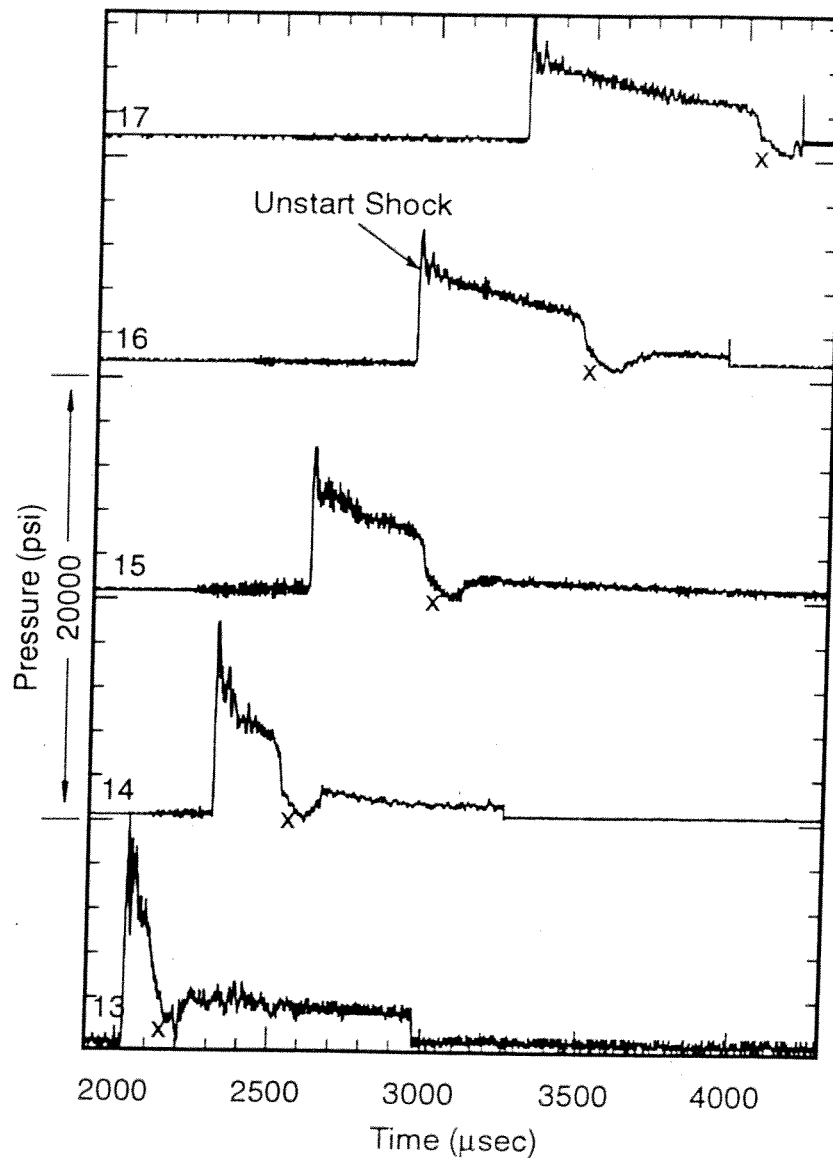


Fig. 4.33 Tube wall pressure traces from farther down the accelerator section for the experiment shown in Figs. 4.31 and 4.32.

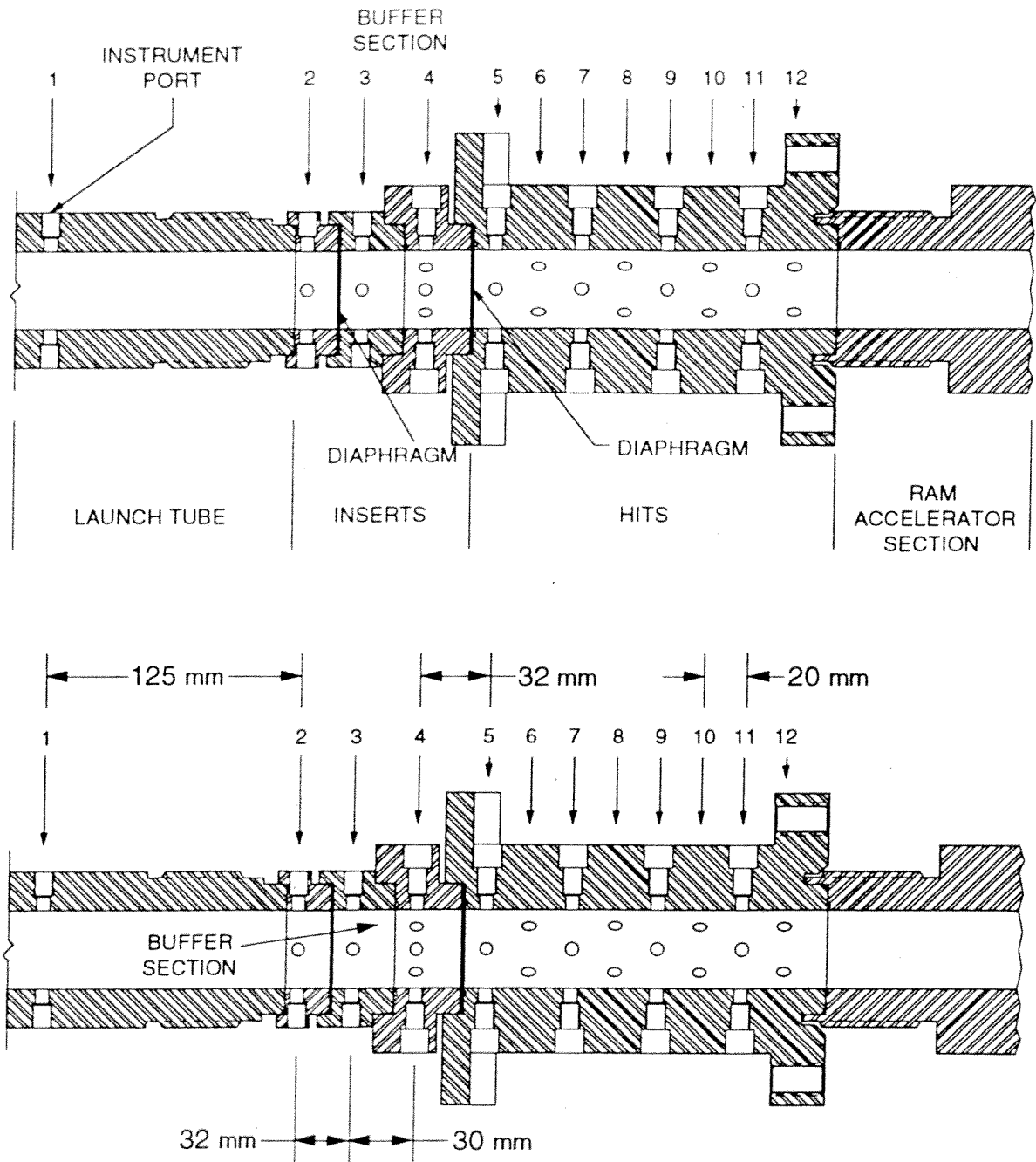


Fig. 4.34 Instrumentation station numbering and diaphragm location for Figs. 4.35 - 4.40.

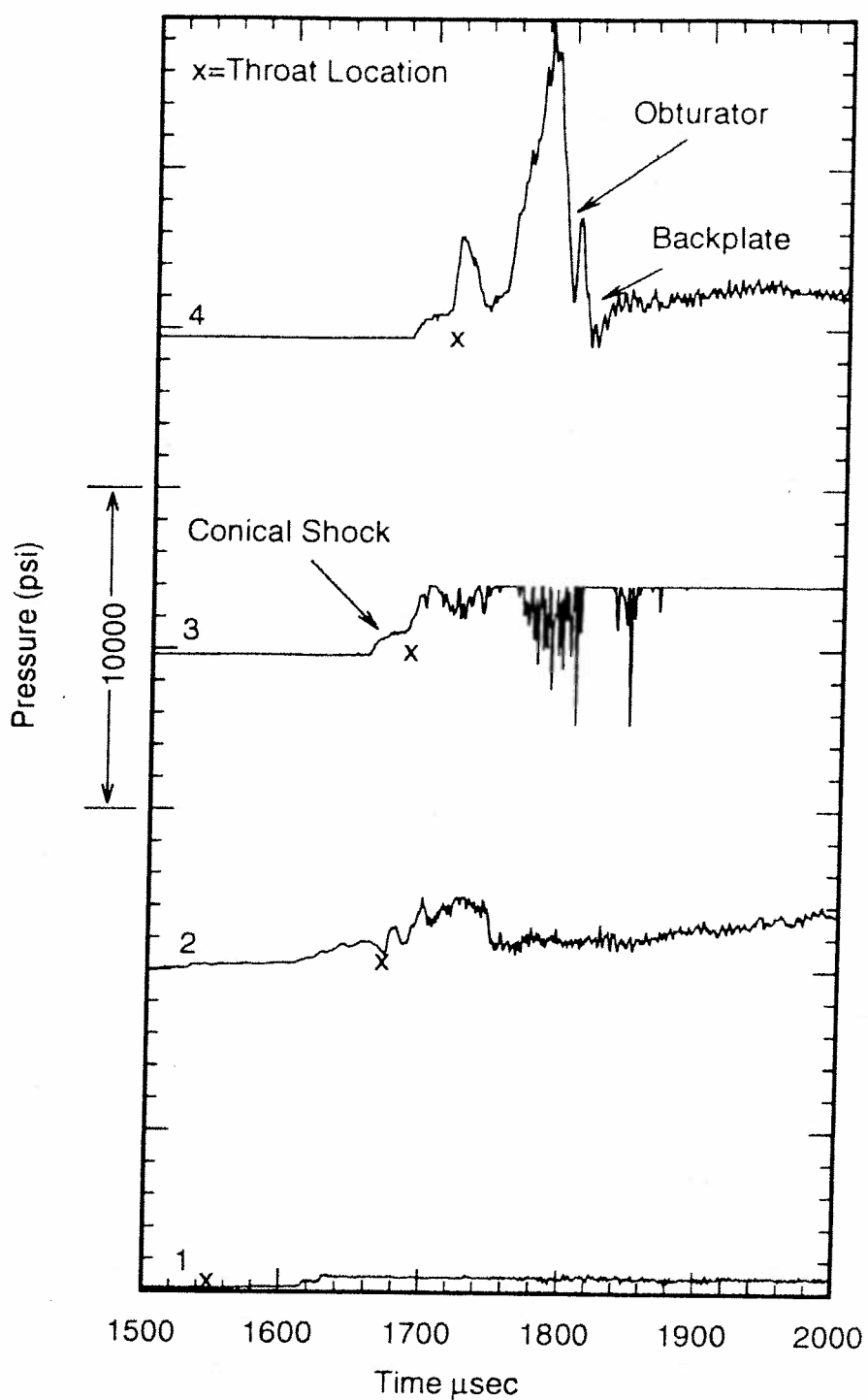


Fig. 4.35 Tube wall pressure traces from the launch tube for a projectile traveling 1150 m/s in a mixture of $2.7\text{CH}_4+2\text{O}_2+5.8\text{N}_2$ with a buffer section filled with a mixture of $2.7\text{CH}_4+2\text{O}_2+5.8\text{N}_2$.

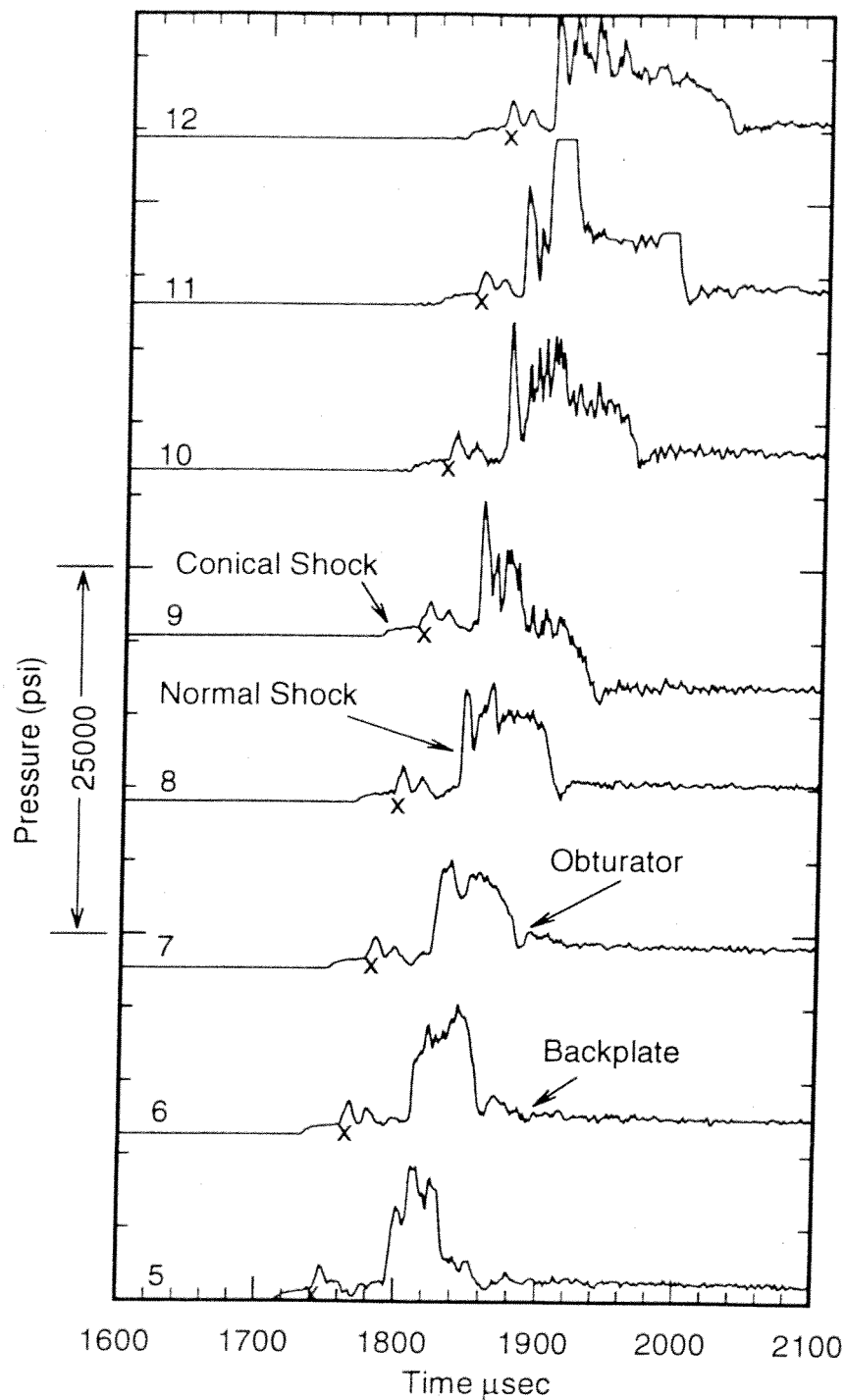


Fig. 4.36 Tube wall pressure traces from the accelerator section for a projectile traveling 1150 m/s in a mixture of $2.7\text{CH}_4+2\text{O}_2+5.8\text{N}_2$ with a buffer section filled with a mixture of $2.7\text{CH}_4+2\text{O}_2+5.8\text{N}_2$.

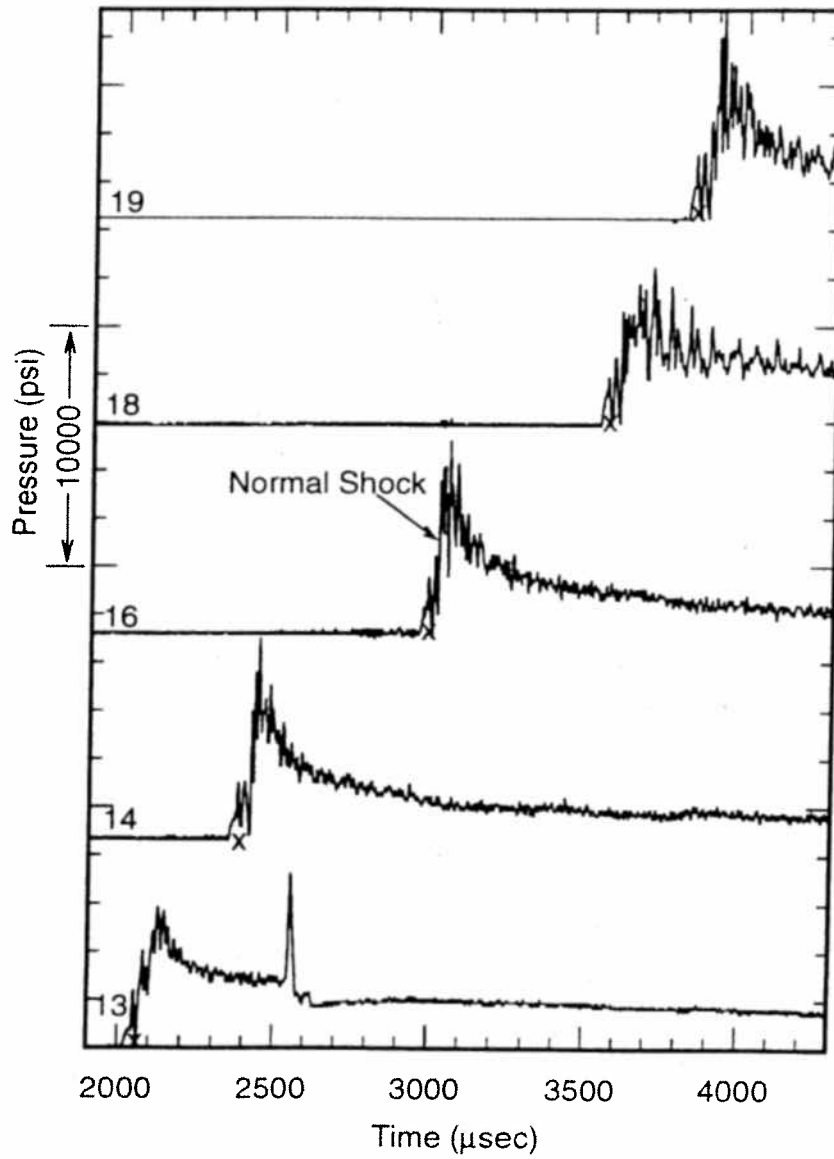


Fig. 4.37 Tube wall pressure traces from farther down the accelerator section for the experiment shown in Figs. 4.35 and 4.36.

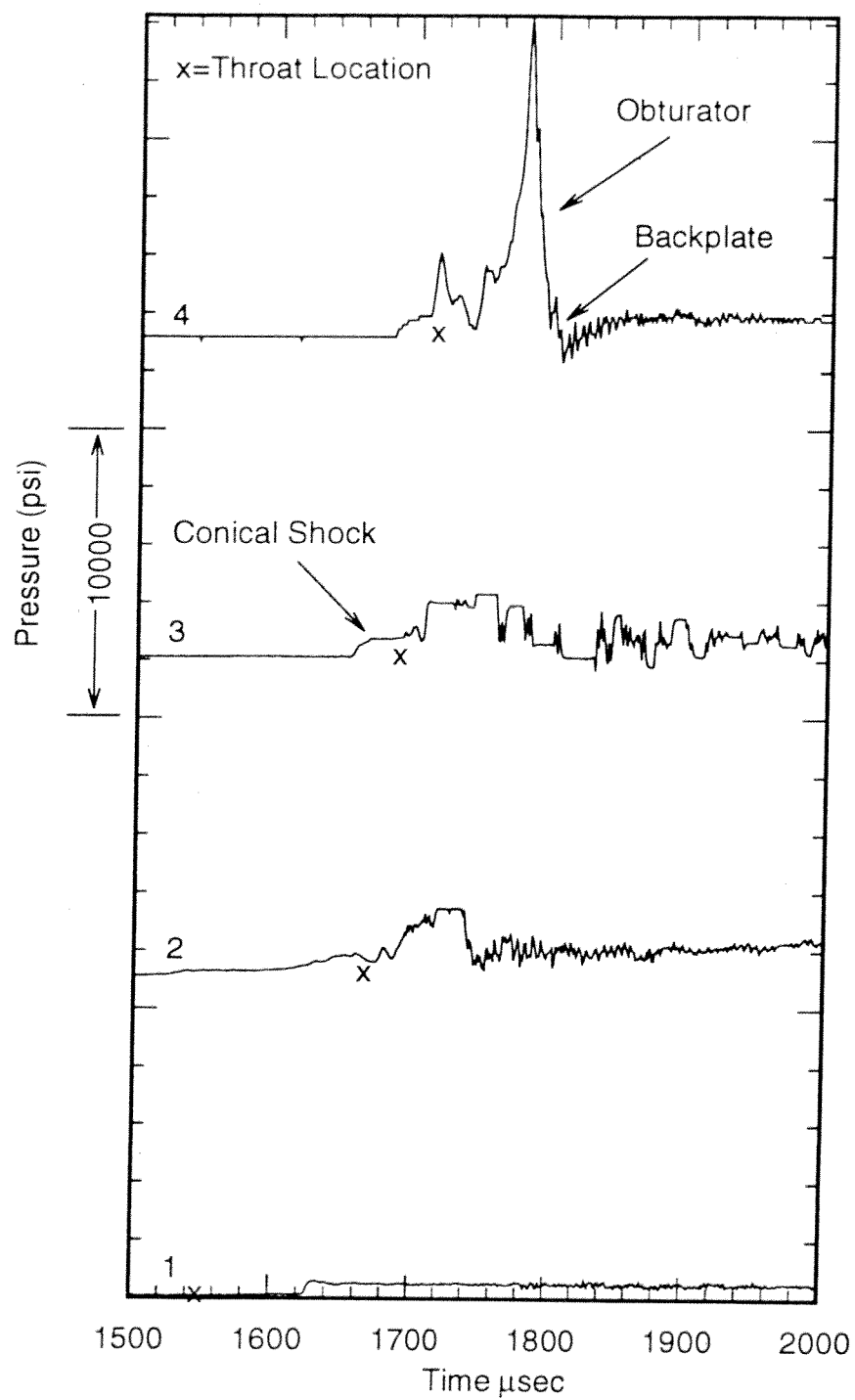


Fig. 4.38 Tube wall pressure traces from the launch tube for a projectile traveling 1150 m/s in a mixture of $2.7\text{CH}_4 + 2\text{O}_2 + 5.8\text{N}_2$ with a buffer section filled with a mixture of $2.7\text{CH}_4 + 7.8\text{N}_2$.

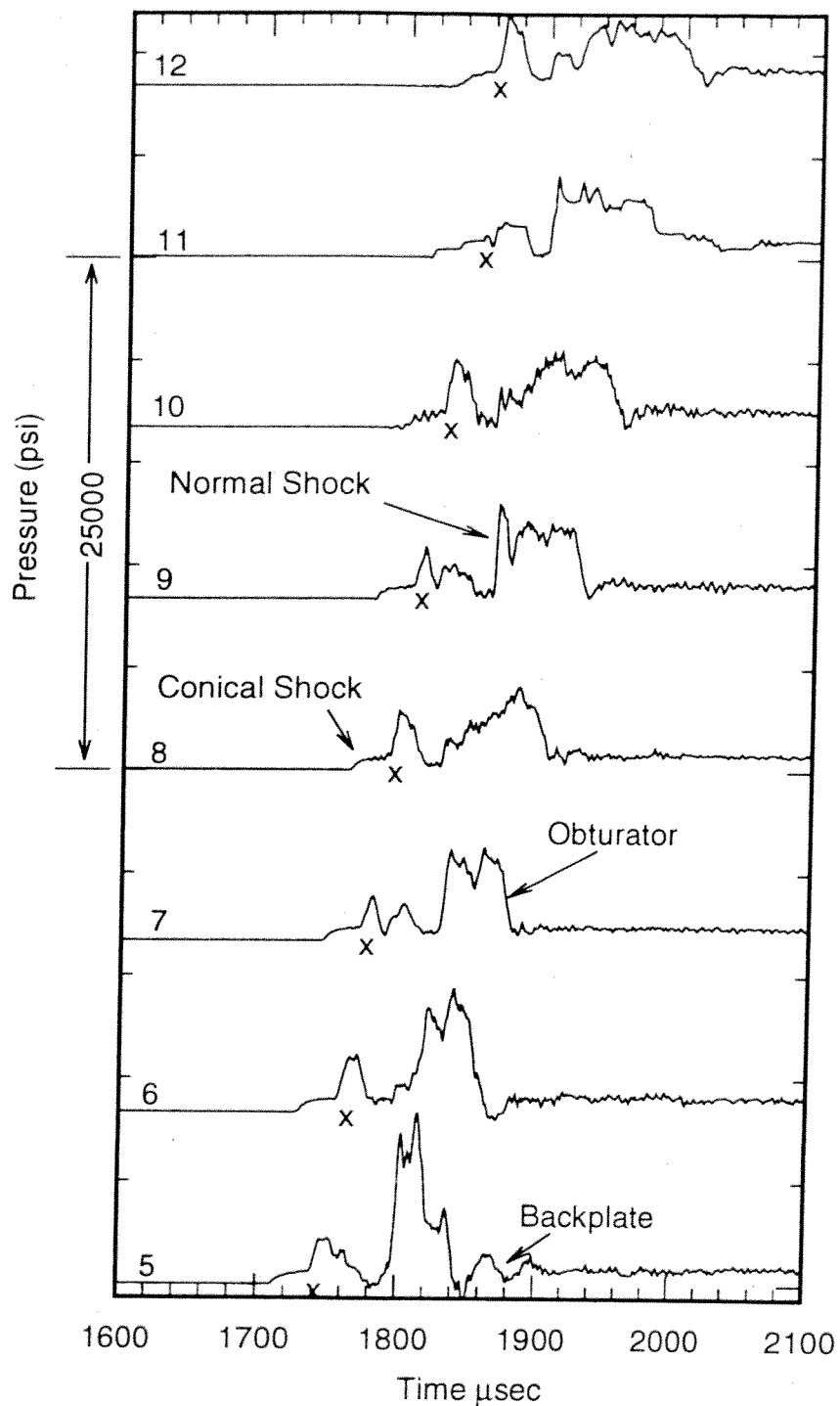


Fig. 4.39 Tube wall pressure traces from the accelerator section for a projectile traveling 1150 m/s in a mixture of $2.7\text{CH}_4 + 2\text{O}_2 + 5.8\text{N}_2$ with a buffer section filled with a mixture of $2.7\text{CH}_4 + 7.8\text{N}_2$.

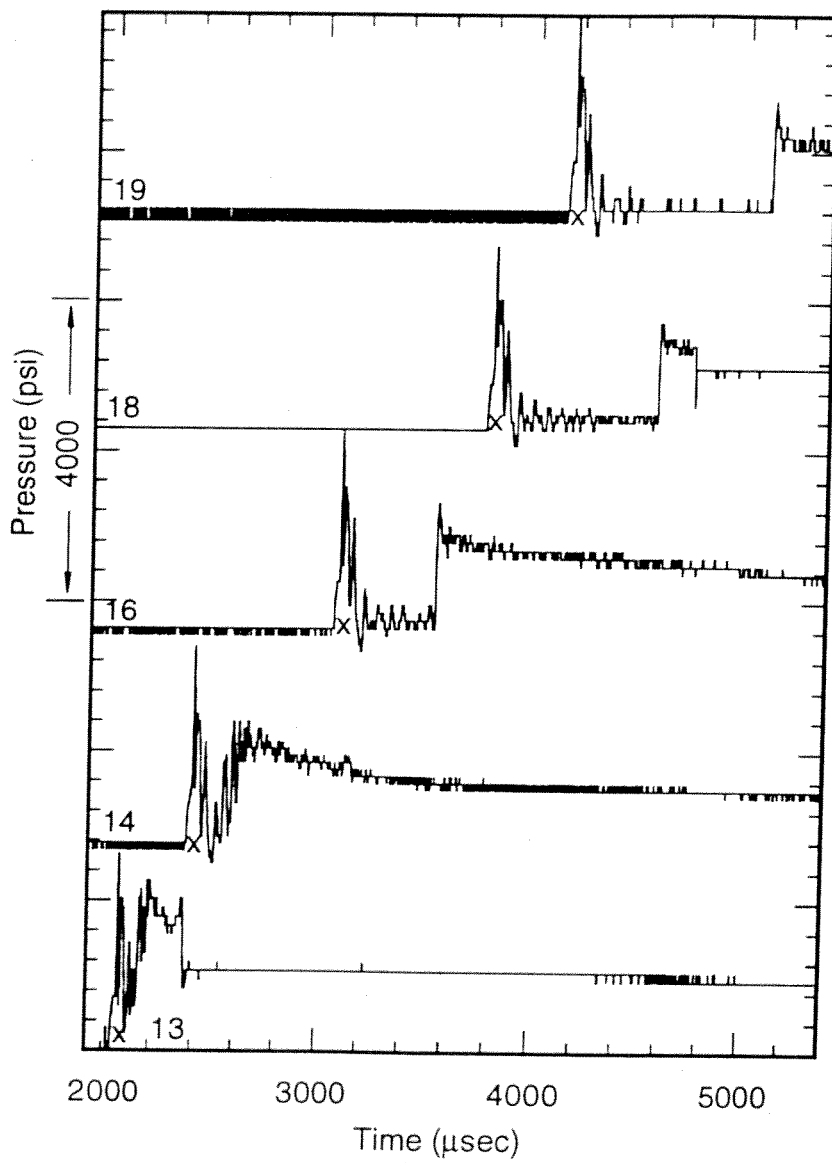


Fig. 4.40 Tube wall pressure traces from farther down the accelerator section for the experiment shown in Figs. 4.38 and 4.39.

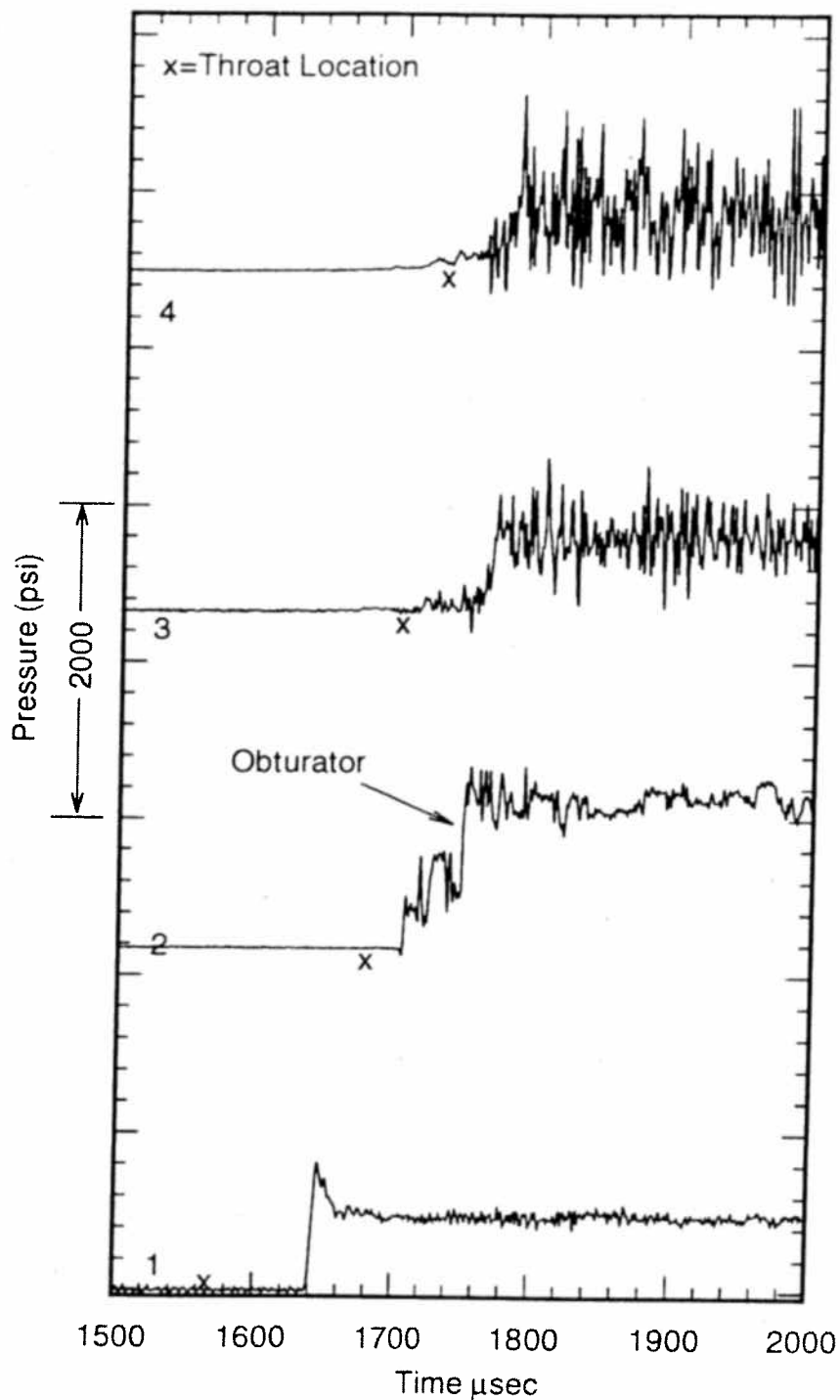


Fig. 4.41 Tube wall pressure traces from the launch tube for a projectile traveling 1190 m/s in a mixture of $2.7\text{CH}_4 + 2\text{O}_2 + 5.8\text{N}_2$ with 0.01 psi of air in the launch tube and a solid non-leaking obturator.

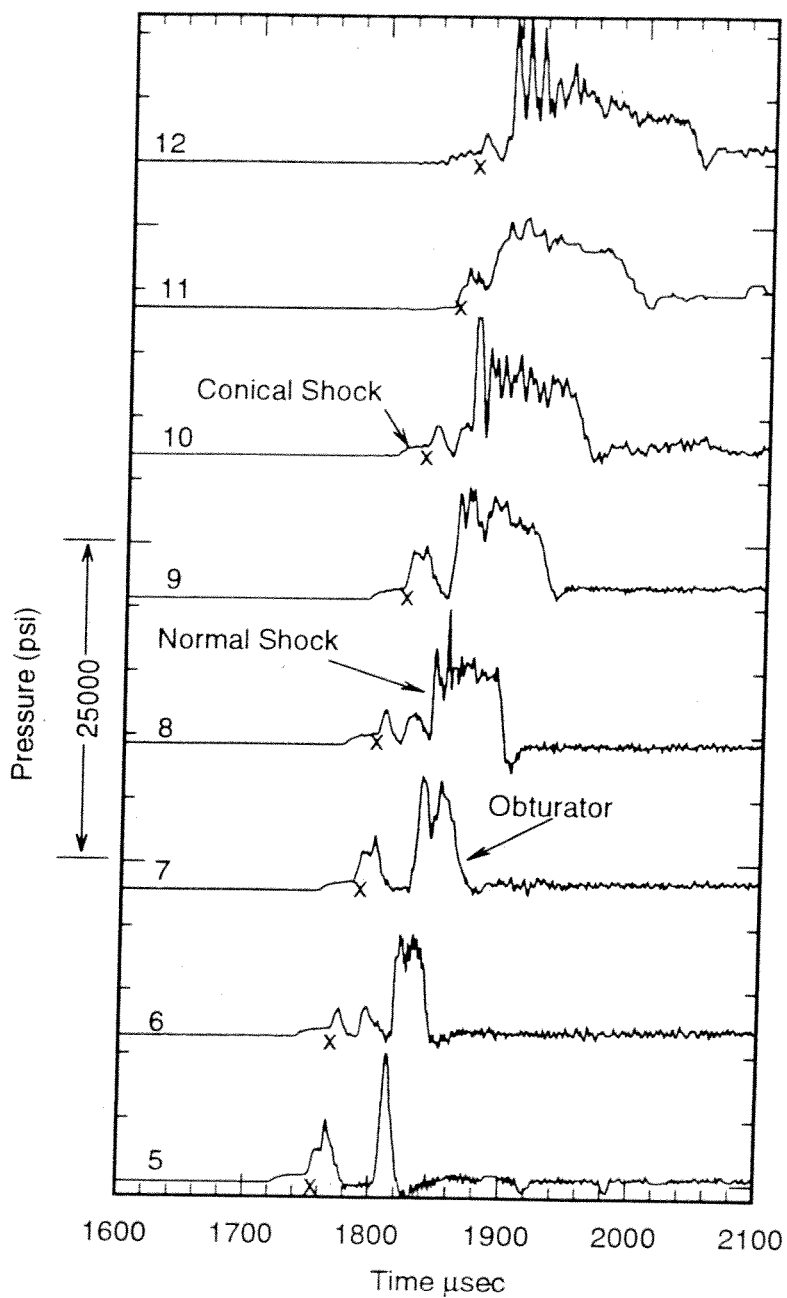


Fig. 4.42 Tube wall pressure traces from the accelerator section for a projectile traveling 1190 m/s in a mixture of $2.7\text{CH}_4 + 2\text{O}_2 + 5.8\text{N}_2$ with 0.01 psi of air in the launch tube and a solid non-leaking obturator.

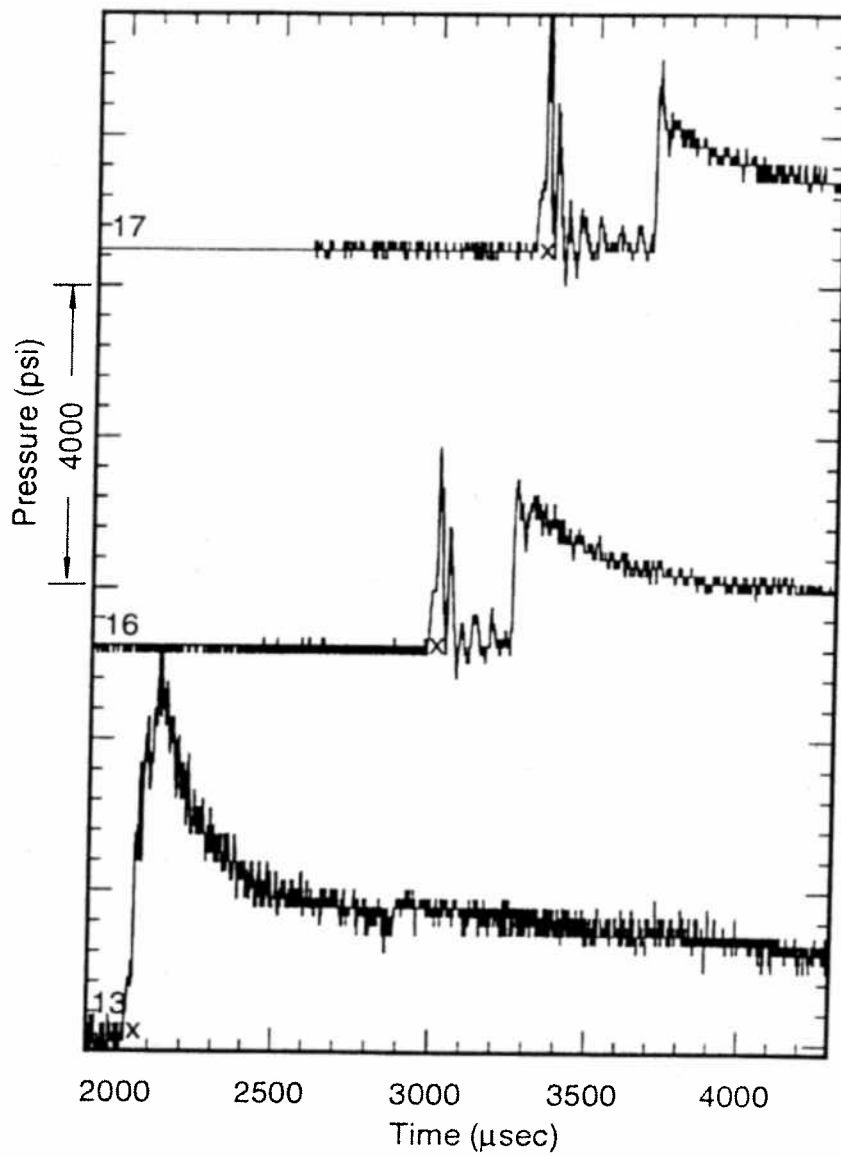


Fig. 4.43 Tube wall pressure traces from farther down the accelerator section for the experiment shown in Figs. 4.41 and 4.42.

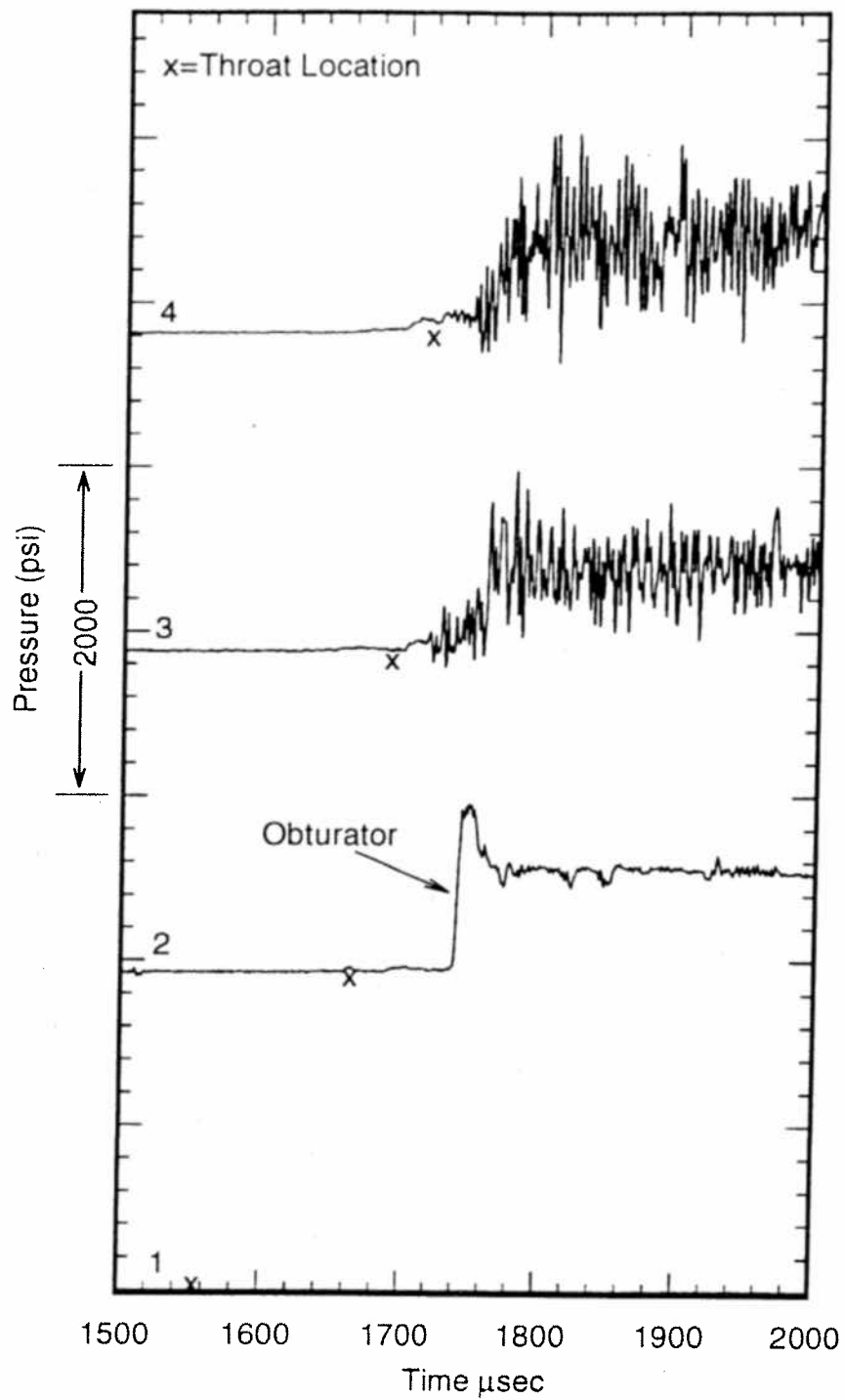


Fig. 4.44 Tube wall pressure traces from the launch tube for a projectile traveling 1170 m/s in a mixture of $2.7\text{CH}_4+2\text{O}_2+5.8\text{N}_2$ with 0.01 psi of air in the launch tube and a solid non-leaking obturator.

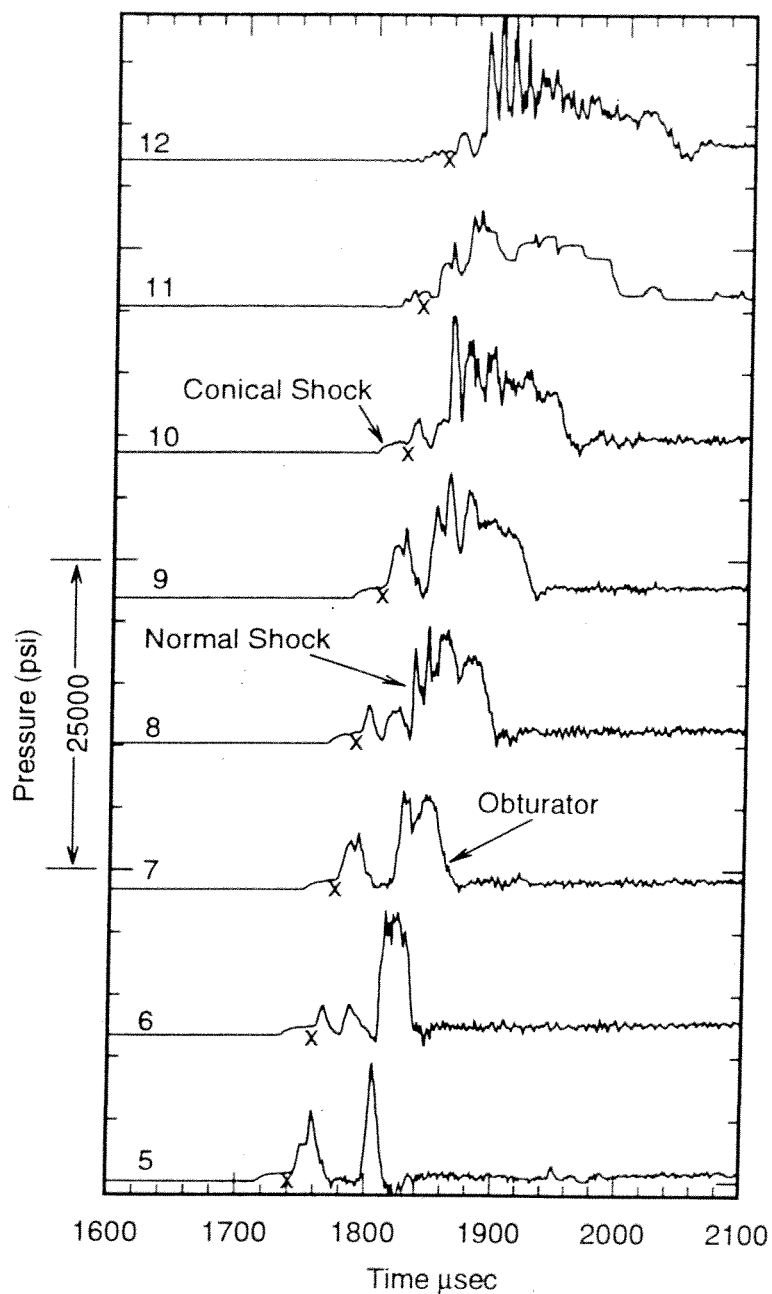


Fig. 4.45 Tube wall pressure traces from the accelerator section for a projectile traveling 1170 m/s in a mixture of $2.7\text{CH}_4+2\text{O}_2+5.8\text{N}_2$ with 0.01 psi of air in the launch tube and a solid non-leaking obturator.

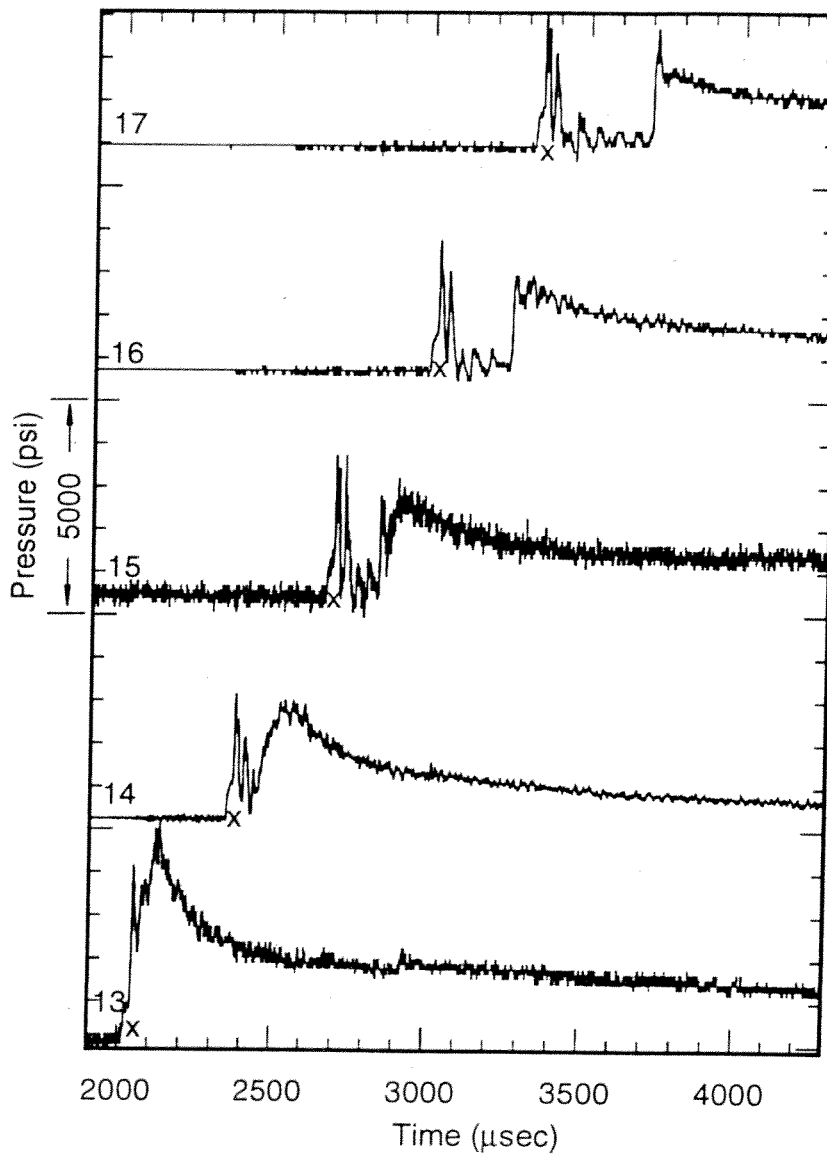


Fig. 4.46 Tube wall pressure traces from farther down the accelerator section for the experiment shown in Figs. 4.41 and 4.42.

V. COMPUTATIONAL MODELING

To enhance the interpretation of the experimental data, a numerical model of the starting process was developed. A numerical model of the starting process requires several features to accurately model the flow. The transients of the ignition process require a good model of the combustion process. Temperatures are sufficiently high so that the gas may not be assumed to be calorically perfect. Both the obturator and projectile accelerate at high g's during starting, so moving boundaries are required. In addition, the entire nature of the starting process is unsteady, so the model must be capable of time accurate modeling of the flow. In many cases a one-dimensional or pseudo-one-dimensional model is sufficient to capture the important details of the flow, such as in the launch tube. Upon entrance to the accelerator section an axisymmetric model is required. To study the effect of the projectile fins on the flow, a steady 3-dimensional model is needed.

5.1 Choice of Methods

An unsteady explicit CFD code which uses either Van Leer splitting or the Advection Upstream Splitting Method (AUSM) was developed. The choices of computational techniques were made primarily for speed and simplicity. The variety of problems simulated ranges from the one-dimensional acceleration of a piston in a tube to the 3-dimensional flow around a ram accelerator projectile.

To enhance the development of the splitting and the solution methods, simplifications were made to the general thermodynamic model.²⁵ The first assumption is that the gas is thermally perfect or the internal energy and enthalpy is a function of temperature only. This gives the equation of state $P = \rho R_m T$ where P is the pressure, ρ is the density, R_m is the gas constant, and T is the temperature. The gas constant can be found from $R_m = R_u/m$ where R_u is the universal gas constant and m is the molecular mass of the gas mixture. The above assumption is good as long as the state of the gas is not near the triple point. High pressures are expected to be modeled (approximately 1000

atm); however, at the same time the temperature will also be high, so this should not cause major problems.

5.2 Heat Release Model - Induction/Reaction

For the study of reacting flow, a realistic method of modeling heat release is needed. Full finite rate chemistry is the most detailed, but it is also the most computationally difficult and time consuming. The results from a finite rate chemistry model are only as good as the rate data that is used in the calculation. Since very little chemical rate data exists for high pressure, fuel rich, methane combustion the rates would have to be extrapolated from lean, low pressure data. The data extrapolation would introduce large errors in the results and therefore remove the incentive to use the more computationally intensive full finite rate chemistry model. For this reason it was decided to use an induction/reaction model of the heat release as has been done by many investigators in the study of hydrogen mixtures.²⁶⁻²⁸ To use this method the induction and reaction times at pressures and temperatures over the region of interest are required. Initially these times were found by integrating a full finite rate chemistry model used by Sloane^{29,30} with a chemical kinetics integrator (CFDK) developed by Pratt.³¹ To find the induction times the equations were integrated until a 1% rise in temperature was found. The reaction time was found by integrating from the induction time and conditions until the final temperature was 1% below the equilibrium temperature. The discrete points were then curve fit using a singular valued decomposition method³² to give continuous values for temperature from 800K to 2300K and pressures from 10 atm to 1000 atm. The coefficients and terms used in the curve fits are shown in Table 5.1. The induction and reaction times are then found from the expression $\text{Time} = \exp(\sum \text{Term} \times \text{Coefficient})$. Figure 5.1 shows the induction and reaction times calculated with this method for various initial temperatures and pressures. For the mixture of interest and considering the accuracy of the kinetic data, it made little difference in reaction

time (approximately 40%) whether constant pressure or constant volume combustion was assumed.

Table 5.1: Induction and Reaction Coefficients

Term	Induction Coefficient	Reaction Coefficient
1	-16.28572	-56.2598
1/T	13472.87	29864.75
ln(P)/T	53.37571	37.22662
ln(P)	-1.053308	-1.060111
T ² /1000000	0.7941329	-5.942833
T/1000	-1.551591	28.33339

In the numerical method additional equations for the induction and reaction parameters are included with the Euler equations.³¹ The induction and reaction parameters vary from 0, nothing has occurred, to 1, the complete time has elapsed. To simplify the solution of the equations, the density multiplied by the reaction and induction parameters are the dependent solution variables. The source terms in the equations are regulated by the local pressure and temperature prior to each time step. If the induction time is less than 1, then the reaction source term is zero. The induction and reaction equations are integrated along with the rest of the fluid equations at each time step. The composition of the gas mixture is now assumed to be a function of the reaction parameter, R , only and is given by $(2.7\text{CH}_4+2\text{O}_2)(1-R) + (2.7\text{CO}+1.3\text{H}_2\text{O}+4.1\text{H}_2)R + 5.8\text{N}_2$. For the pressures and temperatures of interest this is a good approximation to the equilibrium composition of the reacted gas, $R=1$.

With the value of R known and the other conservative variables, the pressure and temperature of the gas are found by iteration beginning with the temperature assuming the specific heat at constant pressure were a constant

and then including the effects of vibrational equilibrium for nonmonatomic species to give a new temperature. Iteration is continued until a very small change in temperature is found.

5.3 Governing Equations

In the following development the flow is assumed to be inviscid and either 2-dimensional or axisymmetric. The inviscid assumption limits the type of problems and the amount of realism that may be obtained from the model. The first order effects of detonations and shock induced combustion can be captured by an inviscid model with less computational difficulty. The extension of this development to 1 or 3 dimensions is straightforward and the axisymmetric case is presented as a representative case.

The governing equations for axisymmetric inviscid flow in terms of generalized coordinates are expressed as³³⁻³⁵

$$\frac{\partial Q}{\partial \tau} + \frac{\partial F}{\partial \xi} + \frac{\partial G}{\partial \eta} + \alpha H = K \quad (\text{Eq. 5.1})$$

where

$$Q = J^{-1} \begin{bmatrix} \rho \\ \rho u \\ \rho v \\ \rho e \\ \rho R \\ \rho I \end{bmatrix} \quad F = J^{-1} \begin{bmatrix} \rho U \\ \rho u U + \xi_x P \\ \rho v U + \xi_y P \\ \rho h U - \xi_t P \\ \rho U R \\ \rho U I \end{bmatrix} \quad G = J^{-1} \begin{bmatrix} \rho V \\ \rho u V + \eta_x P \\ \rho v V + \eta_y P \\ \rho h V - \eta_t P \\ \rho V R \\ \rho V I \end{bmatrix}$$

and

$$H = \frac{J^{-1}}{r} \begin{bmatrix} \rho v \\ \rho uv \\ \rho v^2 \\ \rho vh \\ \rho vR \\ \rho I \end{bmatrix} \quad K = J^{-1} \begin{bmatrix} 0 \\ 0 \\ 0 \\ 0 \\ \rho R_S \\ \rho I_S \end{bmatrix}$$

where Q is the vector of conserved variables, F is the flux vector in the ξ direction, G is the flux vector in the η direction, H is the vector of axisymmetric terms, J^{-1} is the Jacobian, and ξ and η are the generalized coordinates. The contravariant velocities U and V are written as $U = \xi_t + \xi_x u + \xi_y v$ and $V = \eta_t + \eta_x u + \eta_y v$, where the subscripts refer to partial derivatives.

The solution of the equations is done by using either a Van Leer or AUSM type splitting on the F and G fluxes. The Van Leer formulation has continuously differentiable flux contributions that provide smoother solutions near sonic points.³⁶ AUSM differencing splits the convected part of the fluxes separately from the pressure terms. Upwinding allows the differences to be dependent on the local characteristic speeds, and this way positive and negative running waves are properly differenced.

5.3.1 Van Leer equations and discussion

To solve the governing equations (Eq. 5.1) using a Van Leer approach the positive and negative fluxes must be found.³⁶⁻³⁸ For the Van Leer splitting in generalized coordinates the flux (F) in the ξ direction is written as

$$F^\pm = f^\pm \left[\begin{array}{c} 1 \\ \left(\frac{(\bar{\gamma}-1)\bar{U} \pm 2c - \frac{\bar{\gamma}\xi_t}{|\nabla\xi|}}{\bar{\gamma}} \right) \frac{\xi_x}{|\nabla\xi|} - \frac{\bar{v}\xi_y}{|\nabla\xi|} \\ \left(\frac{(\bar{\gamma}-1)\bar{U} \pm 2c - \frac{\bar{\gamma}\xi_t}{|\nabla\xi|}}{\bar{\gamma}} \right) \frac{\xi_y}{|\nabla\xi|} + \frac{\bar{v}\xi_x}{|\nabla\xi|} \\ \frac{((\bar{\gamma}-1)\bar{U} \pm 2c)^2}{2(\bar{\gamma}^2-1)} + \frac{\bar{v}^2}{2} - \frac{\xi_t(\bar{U} + \bar{u})}{2|\nabla\xi|} + \frac{(\bar{U} \mp 2c)\xi_t}{\bar{\gamma}|\nabla\xi|} + q \\ R \\ I \end{array} \right] \quad (\text{Eq. 5.2})$$

with

$$f^\pm = \pm \frac{|\nabla\xi|}{J} \frac{\rho c}{4} (M_\xi \pm 1)^2 \quad \bar{u} = \frac{\xi_x u + \xi_y v}{|\nabla\xi|} \quad \bar{v} = \frac{-\xi_y u + \xi_x v}{|\nabla\xi|}$$

$$M_\xi = \frac{\bar{U}}{c} \quad \bar{U} = \frac{U}{|\nabla\xi|}$$

These equations provide the right and left running fluxes in the ξ direction. In a similar manner the flux (G) in the η direction can be written as

$$G^{\pm} = g^{\pm} \left[\begin{array}{c} \frac{1}{\left(\frac{(\bar{\gamma} - 1)\bar{V} \pm 2c - \frac{\bar{\gamma}\eta_t}{|\nabla\eta|}}{\bar{\gamma}} \right) \frac{\eta_x}{|\nabla\eta|} + \frac{\bar{u}\eta_y}{|\nabla\eta|}} \\ \frac{1}{\left(\frac{(\bar{\gamma} - 1)\bar{V} \pm 2c - \frac{\bar{\gamma}\eta_t}{|\nabla\eta|}}{\bar{\gamma}} \right) \frac{\eta_y}{|\nabla\eta|} - \frac{\bar{u}\eta_x}{|\nabla\eta|}} \\ \frac{((\bar{\gamma} - 1)\bar{V} \pm 2c)^2}{2(\bar{\gamma}^2 - 1)} + \frac{\bar{u}^2}{2} - \frac{\eta_t(\bar{V} + \bar{v})}{2|\nabla\eta|} + \frac{(V \mp 2c)\eta_t}{\bar{\gamma}|\nabla\eta|} + q \\ \text{R} \\ \text{I} \end{array} \right] \quad (\text{Eq. 5.3})$$

with

$$g^{\pm} = \pm \frac{|\nabla\eta| \rho c}{J} \frac{1}{4} (M_{\eta} \pm 1)^2 \quad \bar{u} = \frac{\eta_y u - \eta_x v}{|\nabla\eta|} \quad \bar{v} = \frac{\eta_x u + \eta_y v}{|\nabla\eta|}$$

$$M_{\eta} = \frac{\bar{V}}{c} \quad \bar{V} = \frac{V}{|\nabla\eta|}$$

The solutions obtained using this method contain no oscillations and shocks are captured in 3 or 4 points. In general the results are of acceptable quality but not as crisp as when the AUSM method is used.

5.3.2 Advection Upwind Splitting Method (AUSM)

A method that gives excellent results with little increase in computational difficulty or time is AUSM.³⁹⁻⁴³ This method splits the convective part of the fluxes separate from the pressure portion of the fluxes. The splitting may be dependent on the local velocity or Mach number with the velocity splitting giving better results at moving interfaces.⁴⁰ The Mach number splitting is shown below.

The contravariant velocity and pressure at a cell interface are found from the left and right states as

$$\bar{U}_{\frac{1}{2}} = \bar{U}_L^+ + \bar{U}_R^- \quad \text{and} \quad P_{\frac{1}{2}} = P_L^+ + P_R^- \quad (\text{Eq. 5.4})$$

The contravariant Mach number is given by $M = \bar{U}/c$ which is used to calculate the + and - conditions as

$$\bar{U}^\pm = \begin{pmatrix} \frac{c}{2} (M \pm |M|); \text{if } (|M| \geq 1) \\ \pm \frac{c}{4} (M \pm 1)^2; \text{if } (|M| < 1) \end{pmatrix} \quad (\text{Eq. 5.5})$$

and

$$P^\pm = \begin{cases} P \left(1 \pm \frac{M}{|M|}\right); & \text{if } (|M| \geq 1) \\ \frac{P}{2} (1 \pm M); & \text{if } (|M| < 1) \end{cases} \quad (\text{Eq. 5.6})$$

A third order form of the pressure splitting is available but it may cause small oscillation immediately downstream of a shock. The flux at a 1/2 point in the ξ direction may then be found as

$$F_{i+\frac{1}{2}} = \frac{|\nabla \xi|}{J} \left(\frac{1}{2} \bar{U}_{\frac{1}{2}} (\Phi_L^C + \Phi_R^C) - \frac{1}{2} \left| \bar{U}_{\frac{1}{2}} \right| (\Phi_R^C - \Phi_L^C) + \bar{P}_{\frac{1}{2}} \right) \quad (\text{Eq. 5.7})$$

where

$$\Phi^C = \begin{bmatrix} \rho \\ \rho u \\ \rho v \\ \rho h \\ \rho R \\ \rho I \end{bmatrix} \quad \text{and} \quad \bar{P}_{\frac{1}{2}} = \begin{bmatrix} 0 \\ \xi_x P_{\frac{1}{2}} \\ \xi_y P_{\frac{1}{2}} \\ -\xi_t P_{\frac{1}{2}} \\ 0 \\ 0 \end{bmatrix}$$

A similar expression may be written for the flux in the η direction. This method is computationally fast and gives results that rival those obtained with much more advanced schemes.

5.4 Boundary Conditions

To model a solid obturator, the flow velocity in the x direction at the end boundary must be the obturator velocity. The obturator velocity is found from the pressure on its surface, its mass and its velocity at the last time step. The flow is assumed to be isentropic between the obturator and the points next to it so the Riemann invariants based on the normal velocity to the surface are constant. The speed of sound can therefore be found and used to calculate the density and pressure. The tangential velocity is extrapolated from the interior. The boundary conditions on the projectile are found in a similar manner; however, the normal and tangential velocities to the surface are found from the generalized coordinates.

5.5 Numerical Results

The variety of problems simulated range from the 1-dimensional acceleration of a piston in a tube to the unsteady axisymmetric reacting flow around a ram accelerator projectile. Simulations of detonations and supersonic flows around blunt bodies were also done to test the performance of the induction/reaction model.

5.5.1 Launch tube simulations

A pseudo-one-dimensional version of the above algorithm was used to model the acceleration of the projectile in the launch tube. The pressure in the launch tube was assumed to have no impact on the acceleration of the projectile so first a simulation that modeled the launch of the projectile was made. This gave the acceleration, velocity and position of the projectile in the launch tube as a function of time. These were then curve fit and used in the simulations of the launch tube gas in front of the projectile. Figure 5.2 shows the pressure contours generated by a solid obturator starting at rest and accelerating to the right. The x -axis is the distance from the entrance diaphragm in meters and the y -axis is the time in milliseconds. The entrance diaphragm is at position 0

and is assumed to act as a solid wall. The initial pressure was 0.0068 atm (0.1 psi). The obturator sends out compression waves that coalesce into a shock which reflects from the entrance diaphragm 7.06 msec after launch and in turn reflects from the obturator 7.73 msec after launch. An expanded view of the reflection from the diaphragm and obturator is shown in Fig. 5.3. The reflected shock from the diaphragm reflects from the obturator 0.23 m prior to the entrance diaphragm. It is of some interest to compare this simulation with the experimental data of Fig. 4.7. The difference in relative position on the time axis results from the origin in the simulation beginning when the launch diaphragm breaks versus the triggering of the DAS in the experiment. In the simulation the obturator is much closer to the entrance diaphragm when the shock reflects from it than in the experiment. This indicates that the initial shock in the launch tube is not only caused by the acceleration of the projectile, but also caused by leakage or blow-by of the helium driver gas. In addition, in the simulation a single shock is generated by the reflection of the shock from the obturator while in the experiment two shocks, one from the nose cone and one from the obturator, were generated.

To more accurately model the flow, simulations that include the area change of the projectile are now presented. Figure 5.4 shows the pressure contours generated near the entrance diaphragm for a solid obturator and projectile starting at rest and accelerating to the right. As in the previous figure, the x-axis is the distance from the entrance diaphragm in meters and the y-axis is the time in milliseconds. The entrance diaphragm is at position 0 and is assumed to act as a solid wall. The initial pressure was 0.0068 atm (0.1 psi). The obturator sends out compression waves that coalesce into a shock which reflects from the entrance diaphragm 7.03 msec after launch and in turn partially reflects from the nose cone and then completely reflects from the obturator 7.72 msec after launch. The reflected shock from the diaphragm reflects from the obturator 0.24 m prior to the entrance diaphragm. As can be seen by comparing Figs. 5.3 and 5.4 there is a very slight difference in the

timing of the shocks in the launch tube with the inclusion of the projectile area profile. The major difference is that the projectile area profile causes two shocks to be reflected, one from the nose cone and the other from the obturator, which has been observed in the experiments.

In the simulation presented so far the obturator is much closer to the entrance diaphragm when the shock reflects from it than in the experiments conducted under similar conditions (0.1 psi initial launch tube pressure). To provide more realistic simulations the obturator was allowed to continuously leak helium into the launch tube from a constant pressure reservoir through an area of 1/1000 of the tube area. Figure 5.5 shows the pressure contours generated near the entrance diaphragm for a solid obturator and projectile starting at rest and accelerating to the right with helium leakage through the obturator. The incident shock reflects from the entrance diaphragm 6.3 msec after launch and in turn partially reflects from the nose cone and then completely reflects from the obturator 7.4 msec after launch. The reflected shock from the diaphragm reflects from the obturator 0.62 m prior to the entrance diaphragm. The helium blow-by causes the incident shock in the launch tube to travel faster and to have a greater separation distance from the projectile when it reflects from the entrance diaphragm than in the previous simulation. The reflection from the entrance diaphragm in turn travels farther back into the launch tube before it reflects from the nose cone and obturator. The reflections from the nose cone and obturator coalesce into a single shock as they approach the entrance diaphragm. A single shock is reflected from the entrance diaphragm which then is propagated back into the launch tube. This is a much better representation of the experimental results than the previous simulations. Good agreement is obtained by comparing this simulation with the experimental data shown in Fig. 4.7. The relative timing of the shocks, position of projectile and obturator, and merging of shocks, as well as pressure amplitude, are all accurately modeled when the projectile area profile and helium blow by are included.

The magnitude and timing between shocks is very similar between this numerical simulation and the experimental results of Figs. 4.3, 4.7, and 4.15. Discrepancies between the experiments and the numerical simulation may be accounted for by not knowing the amount of helium blow-by or the exact launch tube initial pressure in the experiments. In addition, the accuracy of the pressure probes at very low pressures is not known. The trends of this pseudo 1-dimensional simulation do show remarkable similarities to the real flow seen in the experiments.

Because the results of the preceding numerical simulation agree very well with the pressure data obtained from experiments, it is of interest to examine the simulated temperature of the gas in the launch tube and qualitatively compare it with the luminosity data. Figure 5.6 shows the temperature contours of the gas near the entrance diaphragm from the previous simulation. The initial temperature is 298 K and jumps to just over 2000 K at the entrance diaphragm when the incident shock reflects. The next jump in temperature occurs when the coalesced shock reflects from the entrance diaphragm and the temperature increases to over 3600 K. Subsequent shock reflections would raise the temperature even more. This gas is surely hot enough to ignite the combustible gas in the accelerator section if steady contact is maintained. The luminosity data in Fig. 4.16 agree well with the simulation. The first rise in luminosity occurs at station 8, which is next to the entrance diaphragm, and follows the reflected shock back into the launch tube with diminishing intensity. The next jump in luminosity is the reflection from the obturator at station 3. The simulation indicates that the gas that was initially in the launch tube is raised to a high temperature and pressure by shock reflections prior to the puncturing of the entrance diaphragm. The conditions of the launch tube gas are important for proper ignition of the combustible gas in the accelerator section. If the pressure and temperature are too high the gas may preignite, while if they are too low, the combustion may not stabilize at the base of the projectile.

With the same helium blow-by it is of interest to examine the effect of increased launch tube pressure. Figure 5.7 shows the pressure contours generated near the entrance diaphragm for a solid obturator and projectile starting at rest and accelerating to the right with helium leakage through the obturator and an initial launch tube pressure of 1.0 psi. The incident shock reflects from the entrance diaphragm 6.88 msec after launch and in turn partially reflects from the nose cone and then completely reflects from the obturator 7.64 msec after launch. The reflected shock from the diaphragm reflects from the obturator 0.32 m prior to the entrance diaphragm. The increase in launch tube initial pressure causes the incident shock in the launch tube to travel slower than in the low pressure case because the effect of blow-by is effectively reduced. This reduced the separation distance between the shock and obturator which reduced the distance that the reflected shock travels back into the launch tube before it reflects from the nose cone and obturator. The reflections from the nose cone and obturator do not, as in the previous simulation, coalesce into a single shock before they reflect from the entrance diaphragm. Two shocks are reflected from the entrance diaphragm which converge as they propagate back into the launch tube. This is a much better representation of the experimental results shown in Fig. 4.27, where 1.0 psi was in the launch tube than the previous simulations with only 0.1 psi. The relative timing of the shocks, position of projectile and obturator, and merging of shocks, as well as pressure amplitude, are all accurately modeled when the projectile area profile, correct initial launch tube pressure, and helium blow-by are included.

5.5.2 Induction/Reaction simulations

The previous simulations did not require a combustion model to accurately model the flow. In the launch tube only air, and possibly helium, were considered. In the accelerator section it is necessary to model the combustion process. The following simulations are for either 2-dimensional or axisymmetric cases where shock induced combustion may occur.

It is of interest to examine the computational results of spheres traveling through a 10 atm combustible gas mixture ($2.7\text{CH}_4+2\text{O}_2+5.8\text{N}_2$) using the induction/reaction model outlined earlier. Extensive work using relatively low pressure hydrogen mixtures and a variety of sphere Mach numbers has been carried out both experimentally and computationally.⁴⁴⁻⁴⁷ These results show that for a particular sphere diameter and a particular mixture, at Mach numbers much higher than the C-J detonation Mach number of the mixture, smooth, stable combustion occurs while at speeds near the detonation Mach number oscillations in the bow shock and combustion front may occur. It is most likely that methane based mixtures would also show this character under the appropriate conditions.

Figure 5.8 shows the steady state density contours generated by a sphere/cylinder body of 38 mm diameter traveling at Mach 6.0 in a 10 atm mixture of $2.7\text{CH}_4+2\text{O}_2+5.8\text{N}_2$ using the induction/reaction model on an 80×100 grid using AUSM differencing. The bow shock and combustion zone are coupled in front of the projectile and decouple at the point where the normal Mach number to the shock is the C-J Mach number.⁴⁸ The bow shock and the reaction zone increase their separation distance as they travel down stream. This computation demonstrates that the induction/reaction model correctly predicts the decoupling point in steady flow.

Figure 5.9 shows a snapshot of the density contours of a Mach 5 flow past the 38 mm diameter sphere/cylinder body. The bow shock and combustion front are decoupled along their length. Along the centerline of the sphere the separation distance of the bow shock and the beginning of the reaction front is related to the induction time of the flow while the width of the reaction zone is related to the reaction time. In this case the flow Mach number is just above the C-J detonation Mach number and there is not a steady state solution. The combustion front continually surges back and forth changing the position of the bow shock. This may be more easily seen by examining the centerline data over a period of time. Figure 5.10 shows an x-t diagram of the centerline density.

Both the bow shock and the reaction front oscillate in position with a frequency of approximately 35 kHz. This is a similar phenomenon as observed in hydrogen mixtures.⁴⁴⁻⁴⁷

These simulations are in no way meant to validate the induction or reaction times obtained from the extrapolated low pressure finite rate chemistry model. The experiments that would be required to make this validation have not been done, or at least not published. The simulations simply show that similar phenomenon to those observed by other authors in hydrogen mixtures may be modeled using a relatively simple induction/reaction model and AUSM differencing in a methane mixture. In fact the finite rate chemistry model does not completely agree with the results obtained from the detonation experiments discussed earlier. For the same conditions the model predicts both induction and reaction times of approximately a factor of 5 smaller than the experimentally determined times, but the ratio of induction to reaction time is approximately the same. The simulations of spheres in combustible mixtures is very sensitive to the method of heat release. Small changes in the induction/reaction model make large changes in the observed phenomenon. Decreasing the induction time by approximately 20% causes an additional high frequency (225 kHz) mode to be superimposed on the bow shock and reaction zone. The preceding simulations are not meant to predict the exact outcome of sphere/cylinder experiments in the high pressure methane mixture but are simply validation tools of the numerical model.

5.5.3 Detonation simulations

The ignition and propagation of a detonation are of some interest because experimental results of these cases exist. The generation of a detonation wave may be done in several ways. In the experimental results of Figs. 2.2 - 2.15 the detonation was initiated by launching a solid obturator into the combustible gas mixture at approximately 1250 m/s. Figure 5.11 shows an x-t diagram of the pressure contours of the centerline of an axisymmetric calculation where a

35 gm solid obturator entered the 23 atm combustible gas mixture at 1250 m/s. The x-axis is in meters and the y-axis is in milliseconds with the entrance diaphragm at $x=0$ and impact occurring at $t=0$. The axisymmetric assumption is appropriate for these conditions because the obturator is solid and it was assumed that there was no gas in the launch tube. The path of the obturator is clearly shown on the left of the figure. The initial shock that is propagated into the combustible gas has a speed of approximately 1500 m/s, a pressure ratio of 19 and a temperature ratio of 3.4. Approximately 65 μsec into the mixture the gas at the obturator face begins to react and propagates a second shock/combustion wave into the already shocked gas. The two shocks meet and couple into a strongly overdriven detonation with a peak speed of approximately 2500 m/s. The delay in ignition is caused by the induction delay time of the numerical model. This is much different than the experimental results shown in Fig. 2.14. In the experiment, combustion had begun by 1.0 cm, station 1, into the HITS. This is because the launch tube gas had acted as an igniter when the obturator entered the combustible gas. If a buffer section had been used to isolate the launch tube gas from the combustible gas as in some of the experiments used to study the ignition behind a projectile, the gas would not have immediately ignited and results similar to the numerical simulation would have been obtained.

A second simulation was done with a less massive obturator and a lower entrance speed. The speed and obturator mass were chosen to be typical of the speeds and masses in experiments where the mixture was ignited and the combustion stabilized behind the projectile. Figure 5.12 shows an x-t diagram of the pressure contours of the centerline of an axisymmetric calculation where a 13 gm solid obturator entered the 23 atm combustible gas mixture at 1125 m/s. As in the previous figure, the x-axis is in meters and the y-axis is in milliseconds with the entrance diaphragm at $x=0$ and impact occurring at $t=0$. The path of the obturator is clearly shown on the left of the figure and a normal shock is seen to propagate into the combustible gas. In this case the lower

entrance speed and the deceleration of the obturator cooling the gas prevented ignition from occurring. This is similar to the experimental results shown in Fig. 4.38 where a buffer section was used to isolate the hot launch tube gas from the combustible accelerator gas and in Figs. 4.42 and 4.45 where there was little launch tube gas and no leakage. The numerical model correctly predicts that with no launch tube gas ignition should not occur.

The use of a buffer section with different initial accelerator fill pressures and obturator entrance velocities could provide detailed measurements of induction and reaction times of this or other combustible mixtures at high pressures. This information would be valuable and possibly more accurate than data from spinning detonations. The data could be used to directly construct an induction/reaction model or provide a benchmark for a full chemical kinetic model. The data from spinning detonations also provides this information; however, the information from many buffered obturator experiments could completely map the pressure and temperature region of interest. For a typical obturator mass and initial accelerator fill pressure, only a few experiments would be required to find the obturator entrance velocity above which an overdriven detonation would occur and below which a nonreacting shock would occur. Simulations could then easily be made around this point to check the validity of the combustion model.

Several investigators have studied the minimum ignition energy required to ignite a premixed combustible gas.^{49,50} This method could also be applied to the impact of the obturator with the combustible gas. The obturator velocity and mass combined with the mixture composition and pressure could provide an estimated interaction time and a bulk energy addition term which would provide a relatively simple method of predicting ignition.

A second method of initiating a detonation is by bulk energy addition to a portion of the flow. Figure 5.13 shows the pressure evolution of a 2-dimensional detonation in a 20 atm methane mixture away from a triangular

region where the initial pressure and temperature were raised by a factor of 5. After 110 μsec the shock is still basically the same shape as it was originally. After 550 μsec the shape of the shock has changed drastically. The top 1/3 of the shock front is very weak and the combustion has decoupled from the shock, while shock and combustion is coupled elsewhere. There is now a transverse shock that is propagating diagonally upward into the unreacted gas behind the weak portion of the shock front. A transverse shock has been observed in experiments and in other numerical simulations of 2-dimensional detonations under a variety of conditions.⁵¹⁻⁵⁴ This transverse shock is very strong, with a pressure ratio relative to the initial pressure of 63, and is similar to the transverse shock observed in the spinning detonation experiments shown earlier in Chapter II. The difference being the 2-dimensional character of the simulated flow and the 3-dimensional character of the spinning detonation. At 1130 μsec the transverse wave is traveling diagonally down. The transverse shock provides the mechanism whereby a stable detonation may be propagated down a tube.

High pressure data from detonations in a methane based mixture are valuable in evaluating combustion models. Only a very limited amount of data is currently available for use in code validation.^{55,56} The experimental results shown in chapter 2 expand the available data for comparison. At high initial pressures more accurate computational models may be required than are shown here.⁵⁷ The compressibility effects of methane based mixture may become important in obtaining an accurate representation of the flow.

5.5.4 Ram Accelerator Starting Simulation

An inviscid numerical model is not capable of stabilizing the combustion at the base of the projectile in any realistic manner. An Euler model is only useful where shock induced combustion is the method of heat release, such as the high Mach number superdetonative regime. Even in this case the boundary layer may play an important role in the location of combustion.¹¹ The incorporation

of viscosity and large eddy simulation with the current induction/reaction model may provide useful information in all areas of ram accelerator operation, in particular the area of starting and transdetonative operation.^{10,11,21} This does not mean that inviscid simulations do not provide useful information on ram accelerator operation. Indeed simple 1-dimensional simulations provide much insight to the ignition source and 3-dimensional simulations accurately reflect the experimentally observed flow.¹⁵⁻¹⁷ The inclusion of an induction/reaction model and viscosity into the 3-dimensional flow simulations may provide useful insights into ram accelerator operation. While the incorporation of viscosity and large eddy simulations in the model would enhance the study of how combustion actually stabilizes at the base of the projectile, it is beyond the scope of this work.

The limitations of an inviscid model do not eliminate the value of simulations of the projectile in the accelerator section. Interesting information on the transition from the shocked launch tube gas to the combustible accelerator gas may be obtained. An axisymmetric simulation was done using the predicted conditions shown in Figs. 5.5 and 5.6 for an initial launch tube pressure of 0.1 psi as the initial conditions in the simulation and progressing in to the combustible accelerator gas. Figure 5.14 shows the pressure and density condition at the tube wall as the projectile enters the combustible gas. A normal shock is driven forward from the obturator toward the throat of the projectile, but does not pass the throat because it encounters the accelerator gas and is swept back onto the projectile body. The reaction front seen on the density contours travels slower than the projectile and is overtaken by the projectile. This is very similar to the experimentally determined x-t diagram shown in Fig 4.7. In both cases the projectile successfully started.

A second simulation was done for the case where the initial launch tube pressure was 1.0 psi and the helium leak was 10 times the previous case. Figure 5.15 shows the tube wall pressure and density contours with the elevated launch tube conditions. A shock is driven forward from the obturator

and passes the projectile throat. The shock created at the original interface of the high pressure launch tube gas and the lower pressure accelerator gas originally travels only slightly slower than the projectile. The shock from the obturator meets the interface shock which creates a shock that travels faster than the projectile. The reaction front seen on the density contours is overtaken more slowly than in the previous case. For the first 0.1 msec it appears that the projectile may start; however, after this time it is obvious that there is no chance of a successful start. When the shock from the obturator combines with the interface shock, the gas is sufficiently heated so that combustion occurs in front of the projectile. This causes an overdriven detonation to be propagated in front of the projectile. This is very similar to the experimental results shown in Figs. 4.28 and 4.29 where the initial launch tube pressure was 1.0 psi and two 0.014" diaphragms were used. In both the simulation and the experiment the projectile failed to start because the launch tube gas preignited the combustible gas.

Even though these simulations were done with an inviscid model the results are very similar to the experimental results. At low initial launch tube pressures and little blow-by, the projectile may successfully start while at higher initial launch tube pressures and greater blow-by starting becomes more difficult. The numerical model can not predict if combustion will stabilize at the base of the projectile, but it is capable of predicting whether it is possible for the projectile to start when it enters the combustible gas.

5.6 Future work

There are many improvements that may be made in future work. More accurate knowledge of induction and reaction times would aid in the prediction of ignition and in overall computational effectiveness. Higher pressure and luminosity probe resolution in spinning detonation experiments could help provide this information. Solid obturator detonation experiments with the launch tube gas isolated from the combustible gas by a buffer section could also

provide this information over a wider variety of conditions and possibly have higher accuracy. Detailed measurements of induction and reaction times at high pressures could be used to directly construct an induction/reaction model or provide a benchmark for a full chemical kinetic model. This information would be valuable in that there is virtually no information for fuel rich high pressure methane mixtures that are used in the majority of current ram accelerator work. The development of a 3-dimensional model using the induction/reaction method to capture the details of spinning detonations would not only improve the understanding of the phenomenon, but would also provide a rigorous test for the computational and heat release models. The incorporation of viscosity and large eddy simulation with the current induction/reaction model may provide useful information on starting and how combustion actually stabilizes at the base of the projectile.

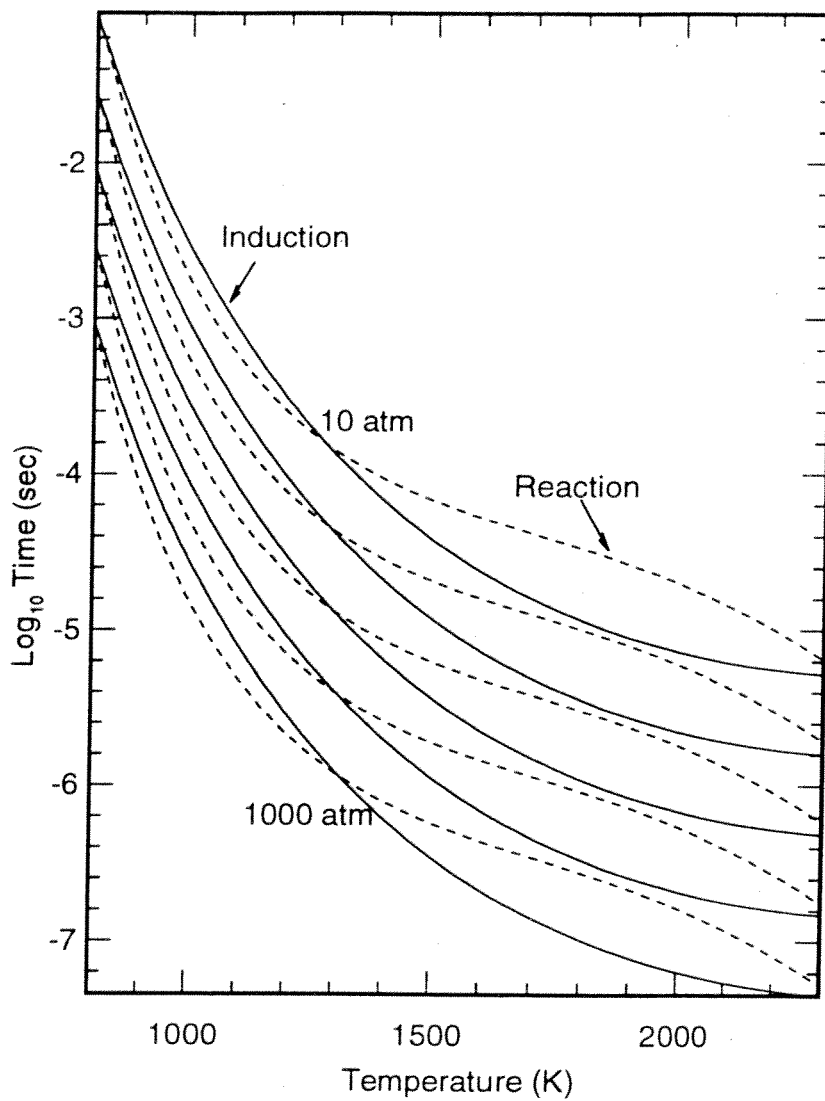


Fig. 5.1 Induction and reaction times for various initial pressures and temperatures.

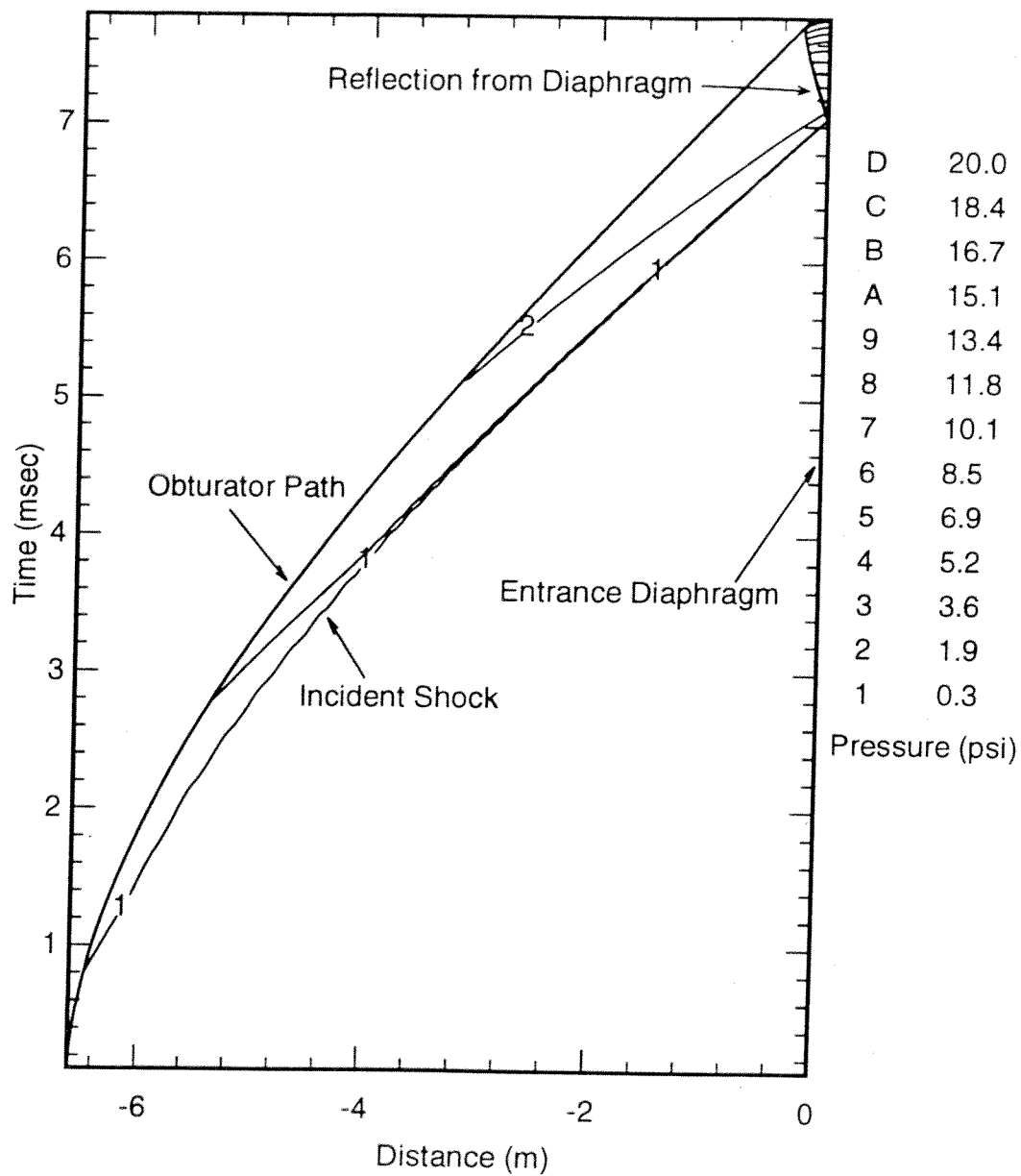


Fig. 5.2 Simulated launch tube pressure contours of a solid obturator accelerated to 1170 m/s in 0.1 psi air.

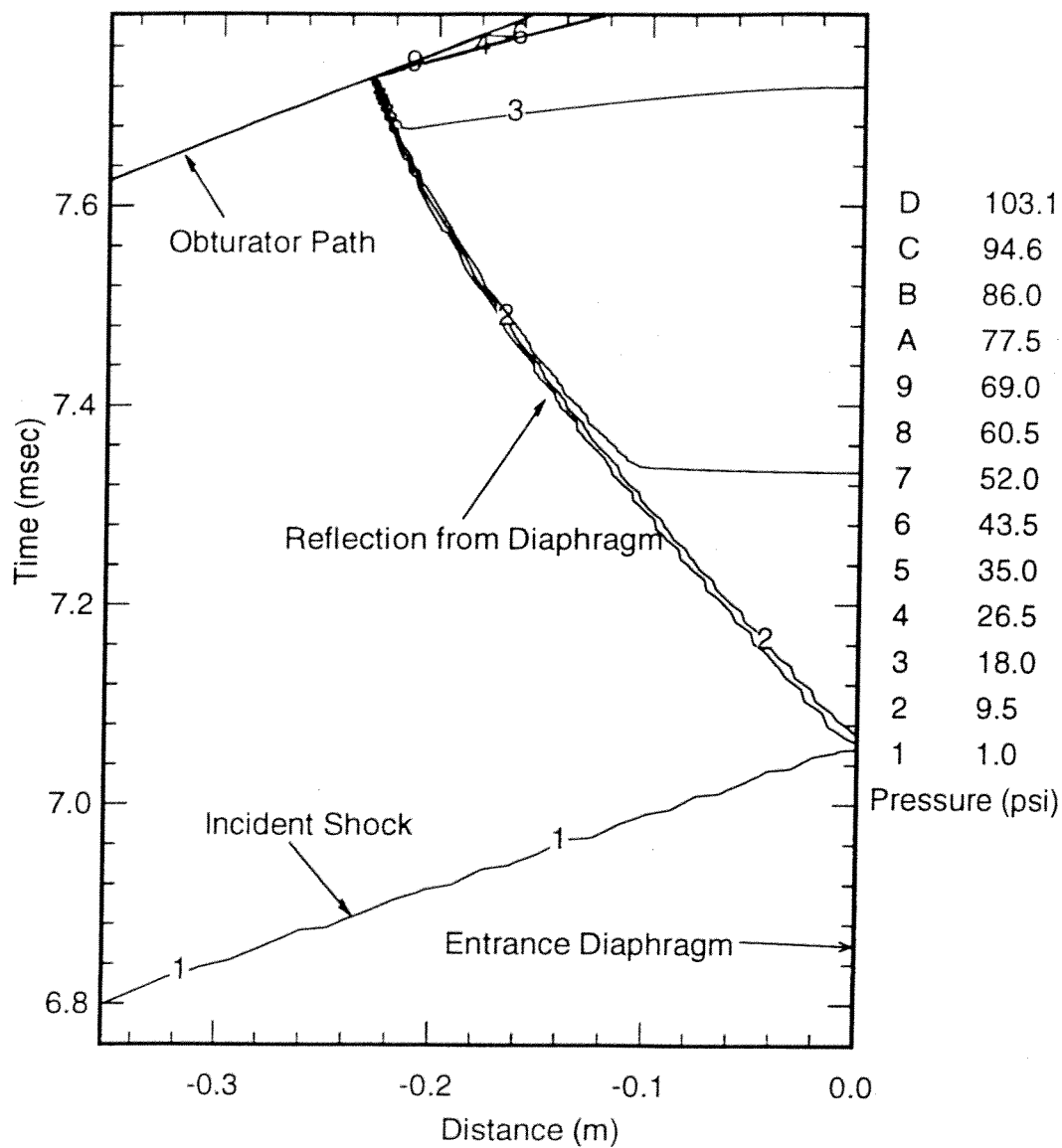


Fig. 5.3 View close to the entrance diaphragm of the simulation shown in Fig. 5.2

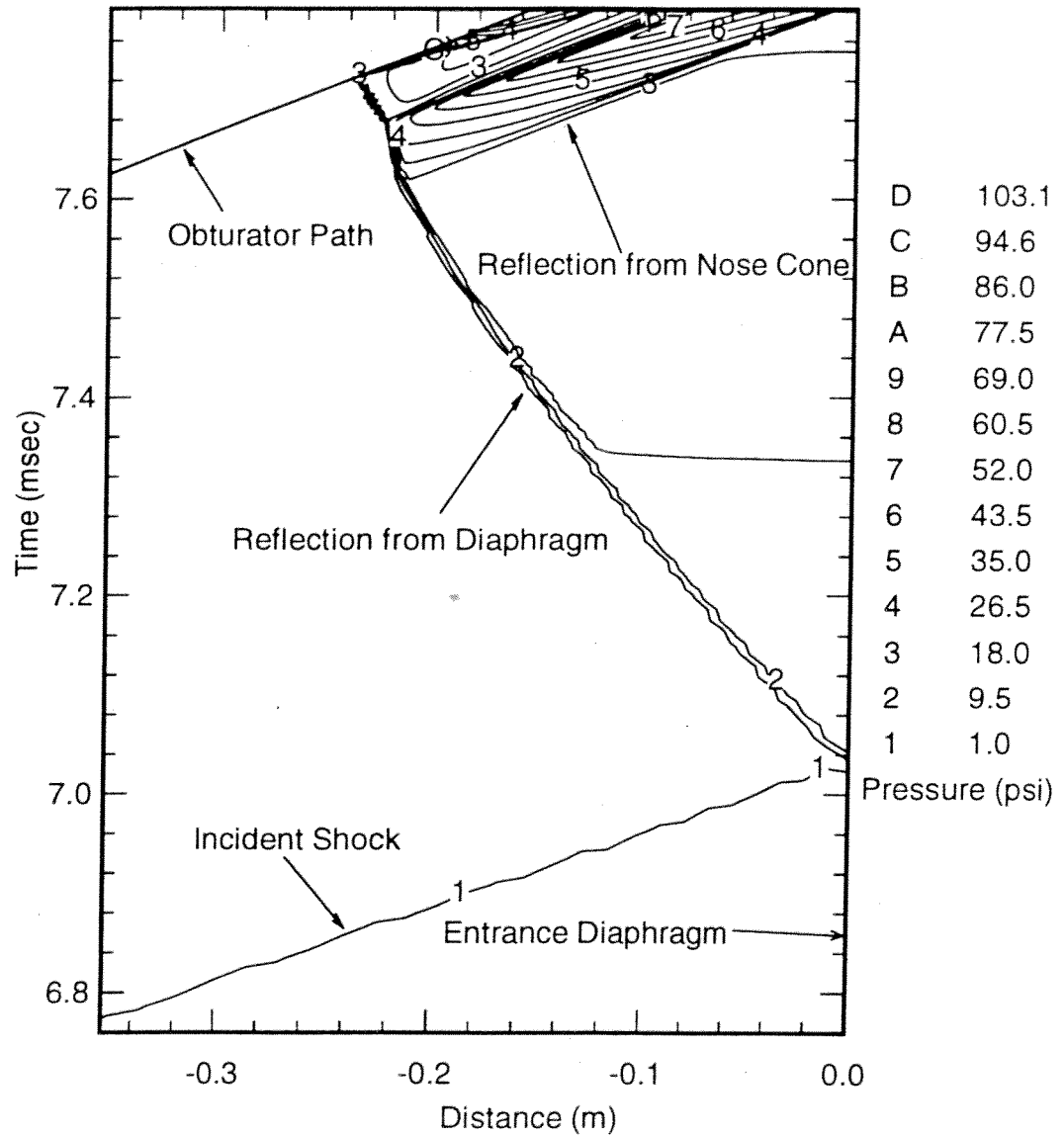


Fig. 5.4 Simulated launch tube pressure contours of a solid obturator and projectile accelerated to 1170 m/s in 0.1 psi air.

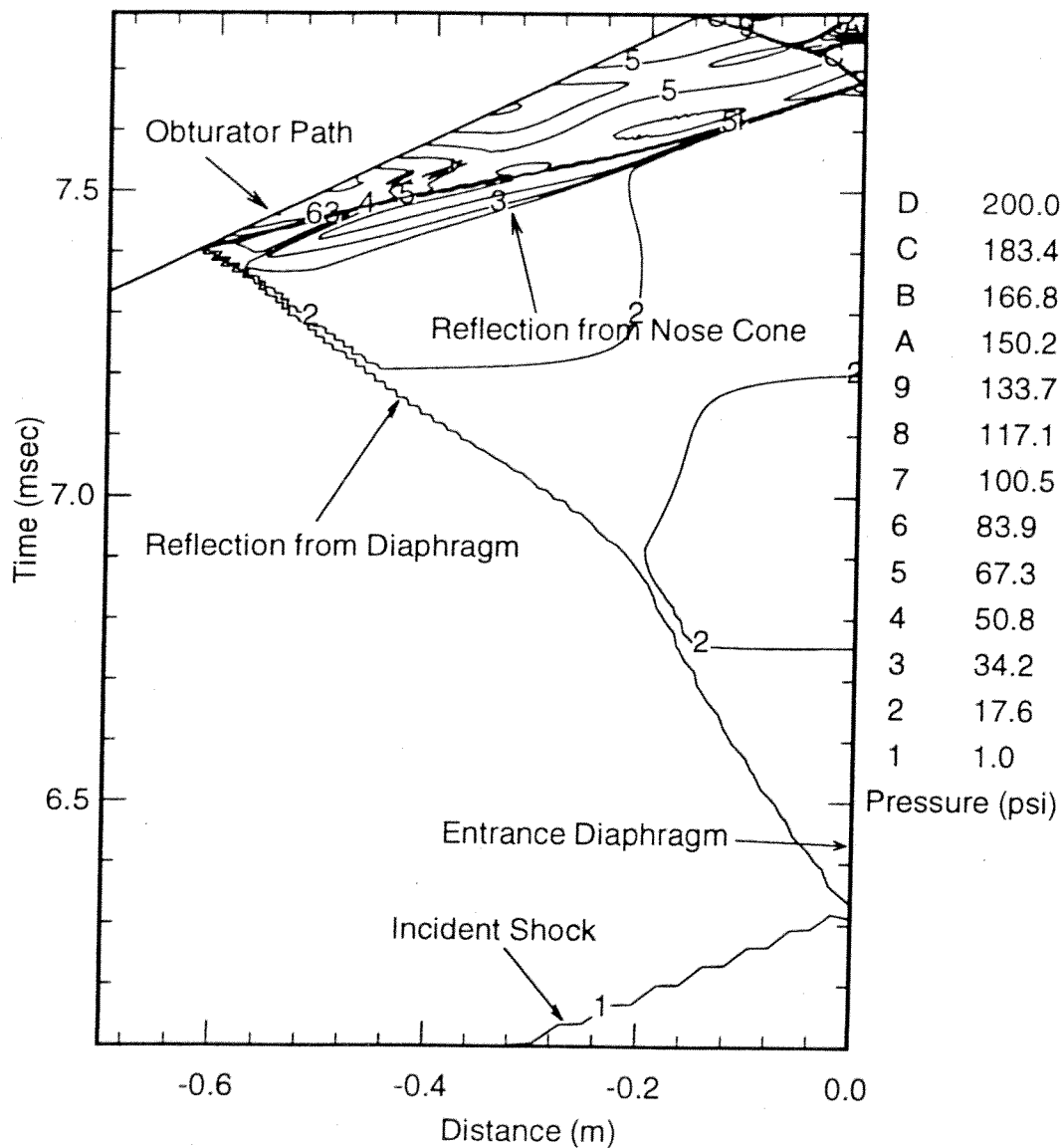


Fig. 5.5 Simulated launch tube pressure contours of a solid obturator and projectile accelerated to 1170 m/s in 0.1 psi air with a 1/1000 obturator area helium leak.

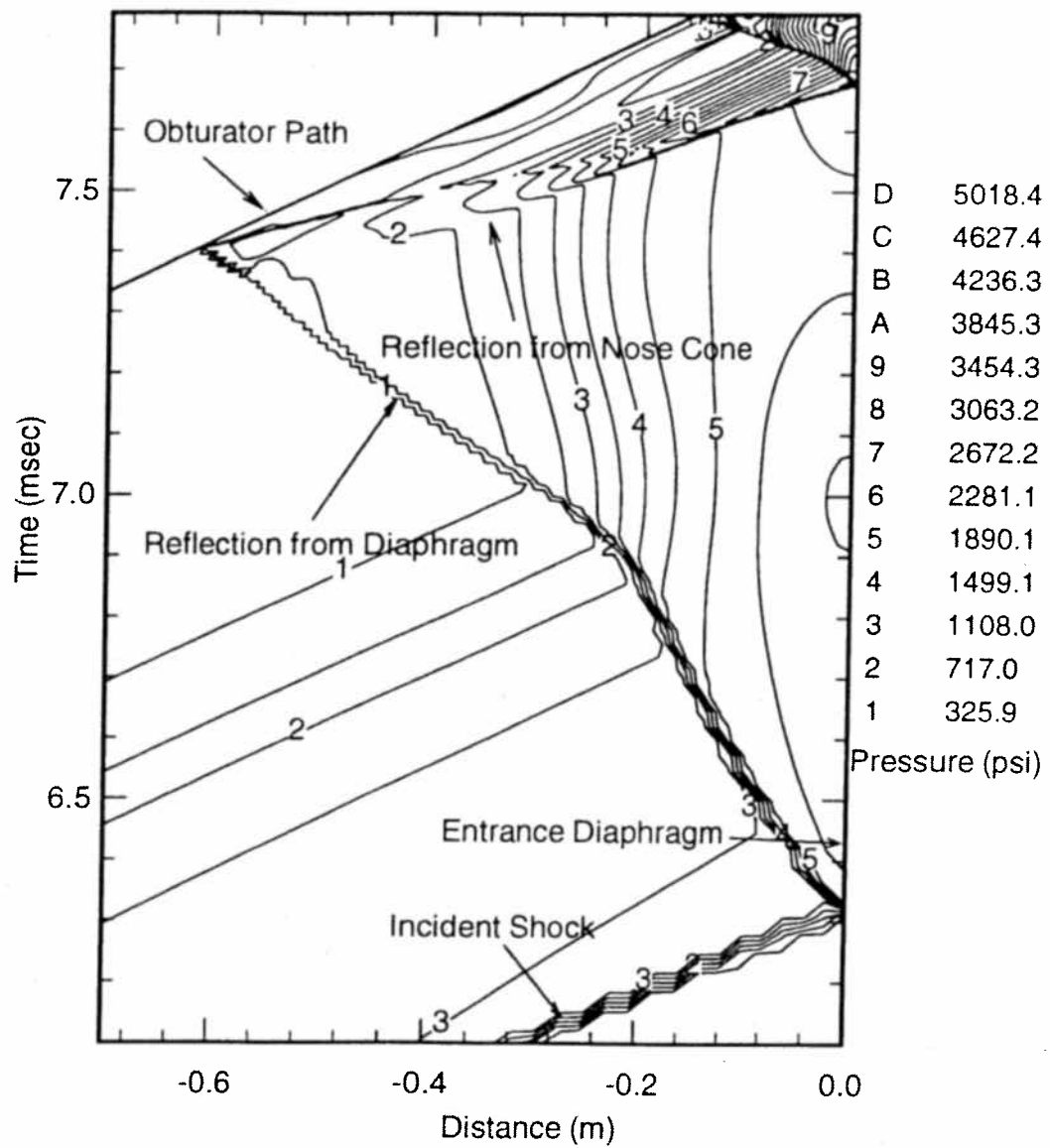


Fig. 5.6 Temperature contours from the same simulation shown in Fig 5.5.

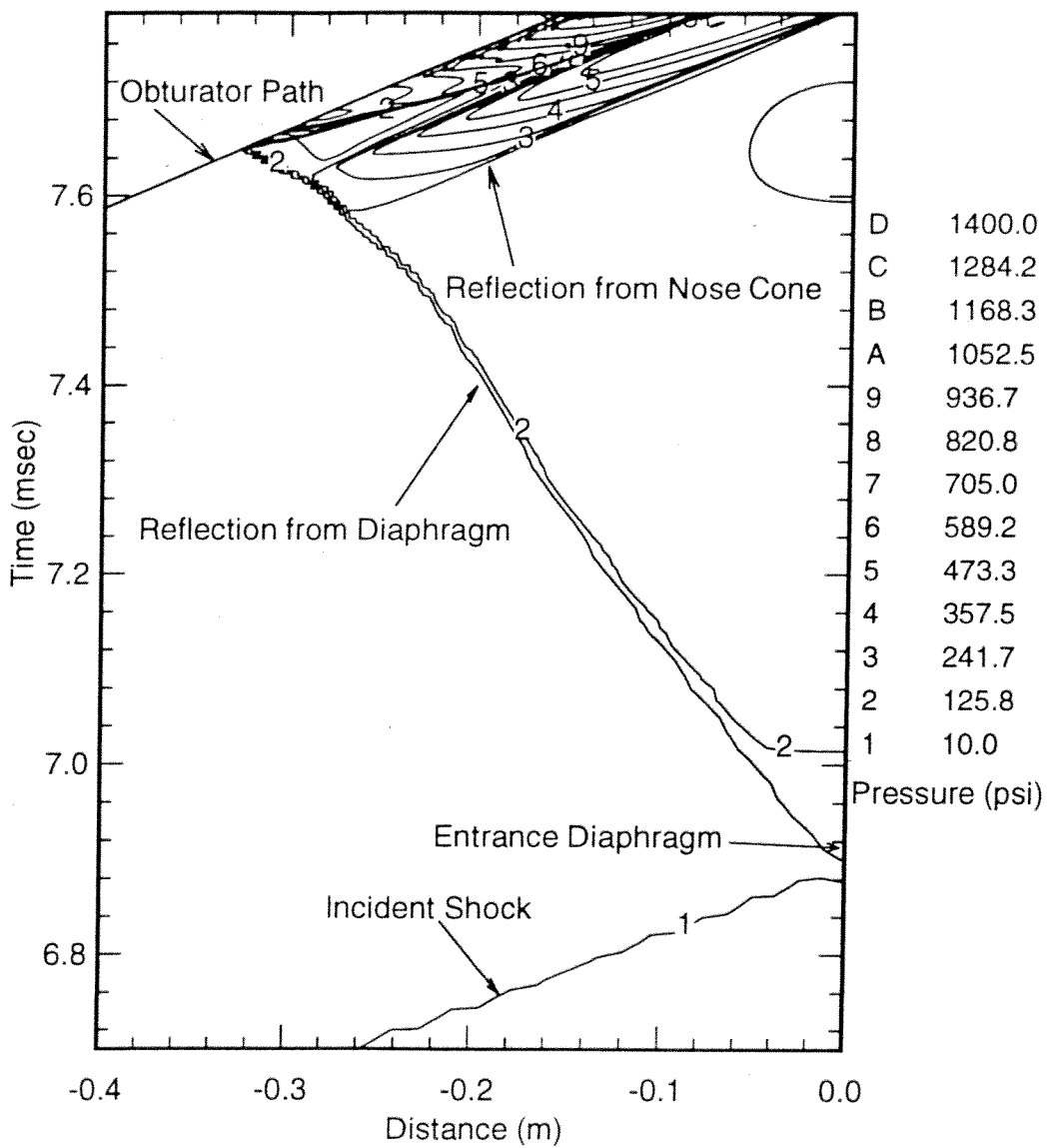


Fig. 5.7 Simulated launch tube pressure contours of a solid obturator and projectile accelerated to 1170 m/s in 1.0 psi air with a 1/1000 obturator area helium leak.

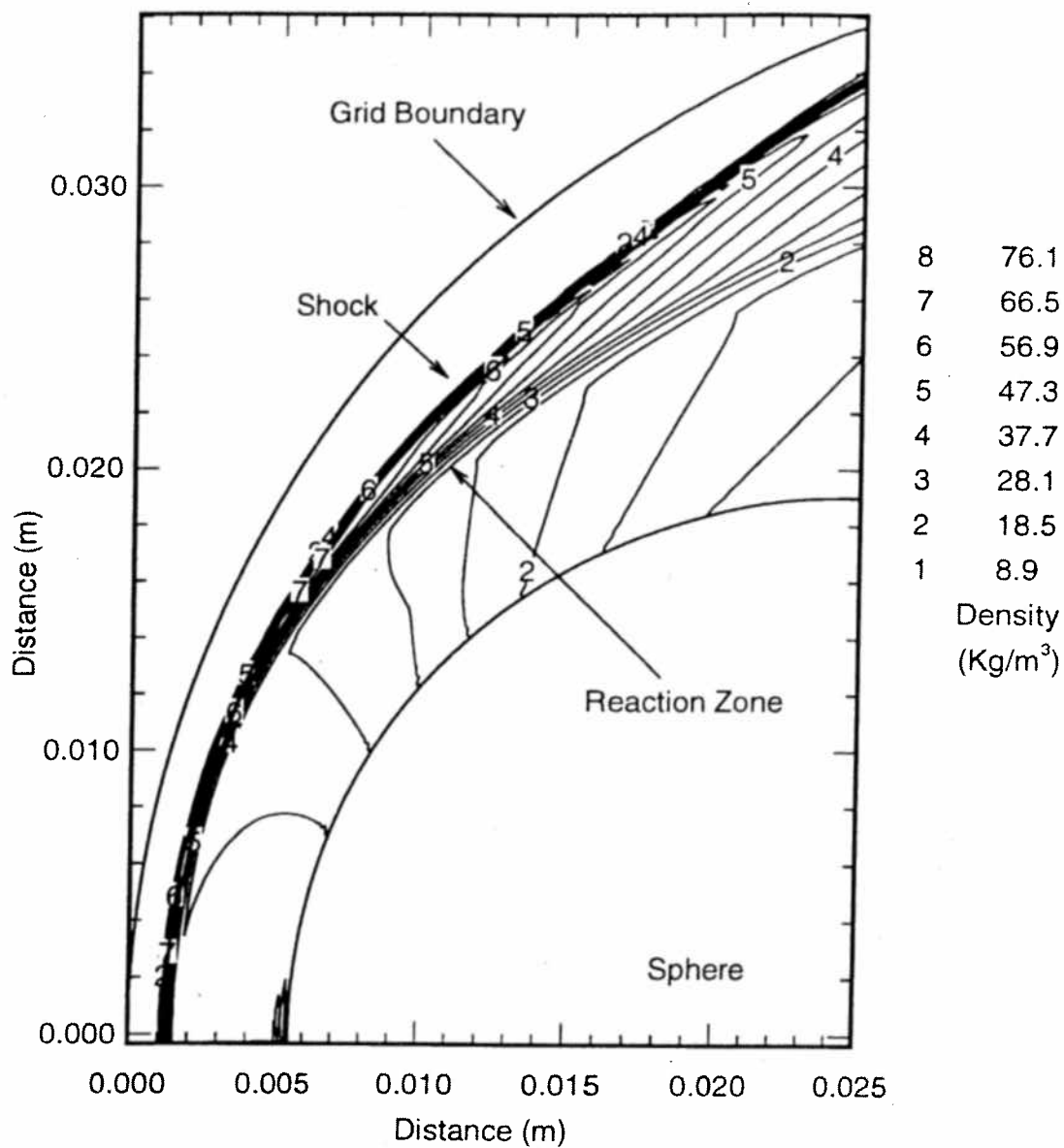


Fig. 5.8 Simulated density contours of a 38 mm diameter sphere/cylinder body traveling Mach 6.0 in a 10 atm mixture of $2.7\text{CH}_4+2\text{O}_2+5.8\text{N}_2$.

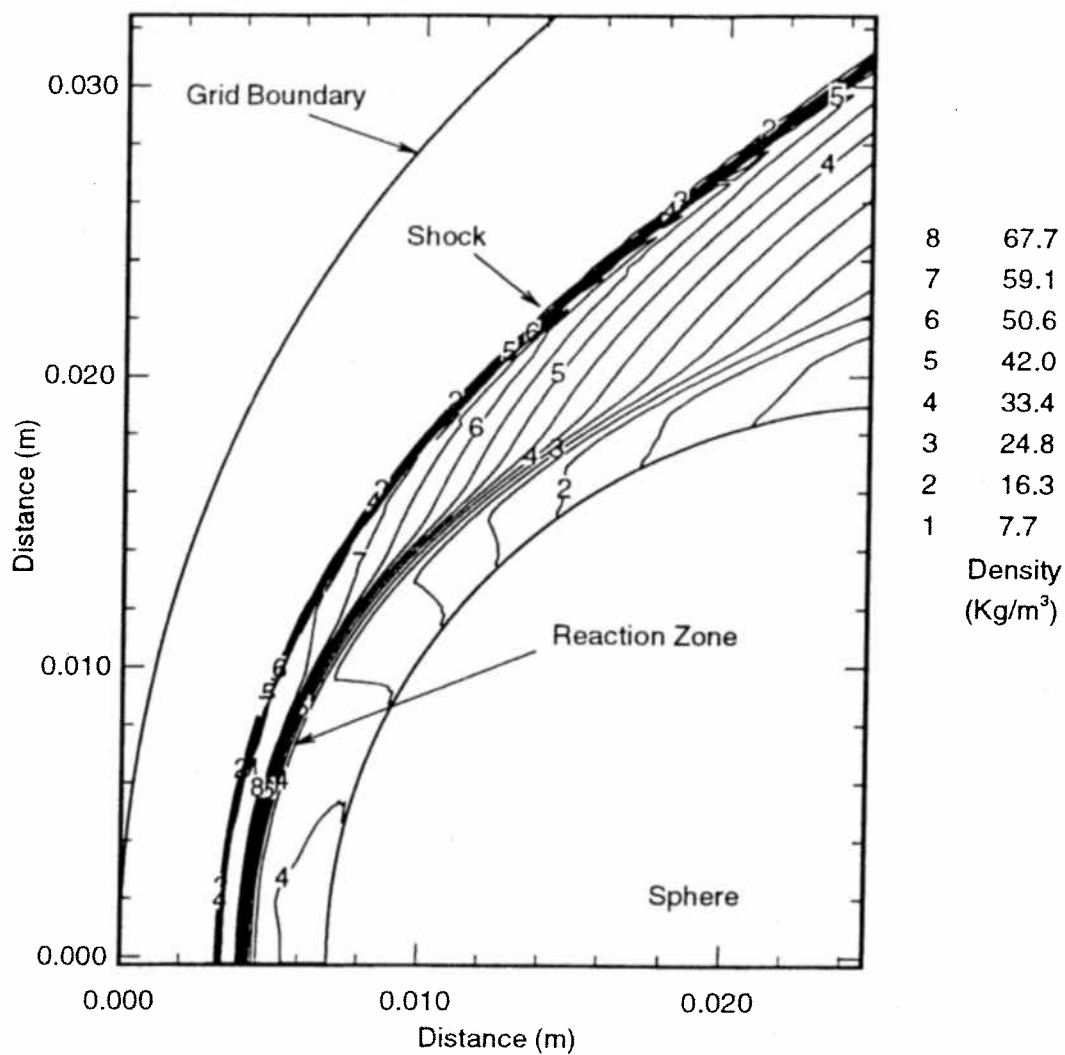


Fig. 5.9 Simulated density contours of a 38 mm diameter sphere/cylinder body traveling Mach 5.0 in a 10 atm mixture of $2.7\text{CH}_4 + 2\text{O}_2 + 5.8\text{N}_2$.

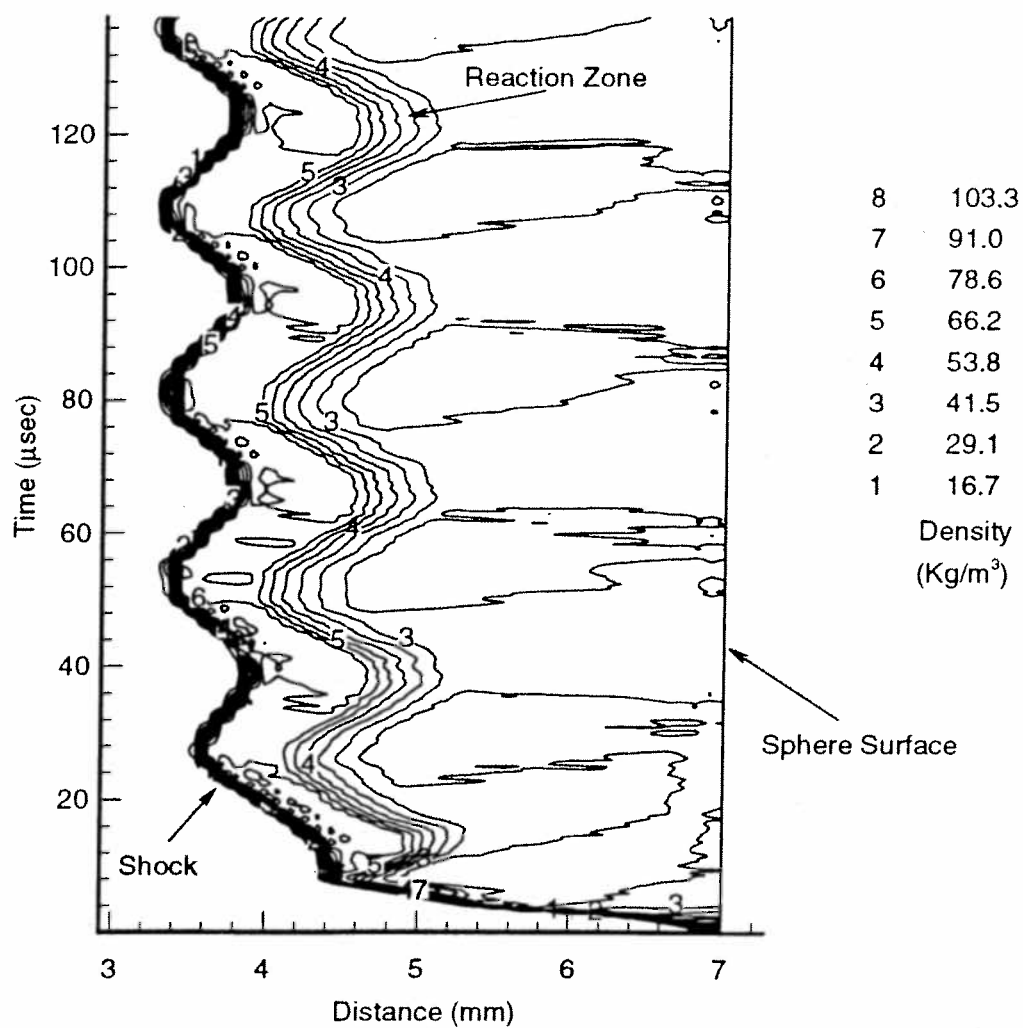


Fig. 5.10 Simulated time evolution of the centerline density contours of a 38 mm diameter sphere/cylinder body traveling Mach 5.0 in a 10 atm mixture of $2.7\text{CH}_4+2\text{O}_2+5.8\text{N}_2$.

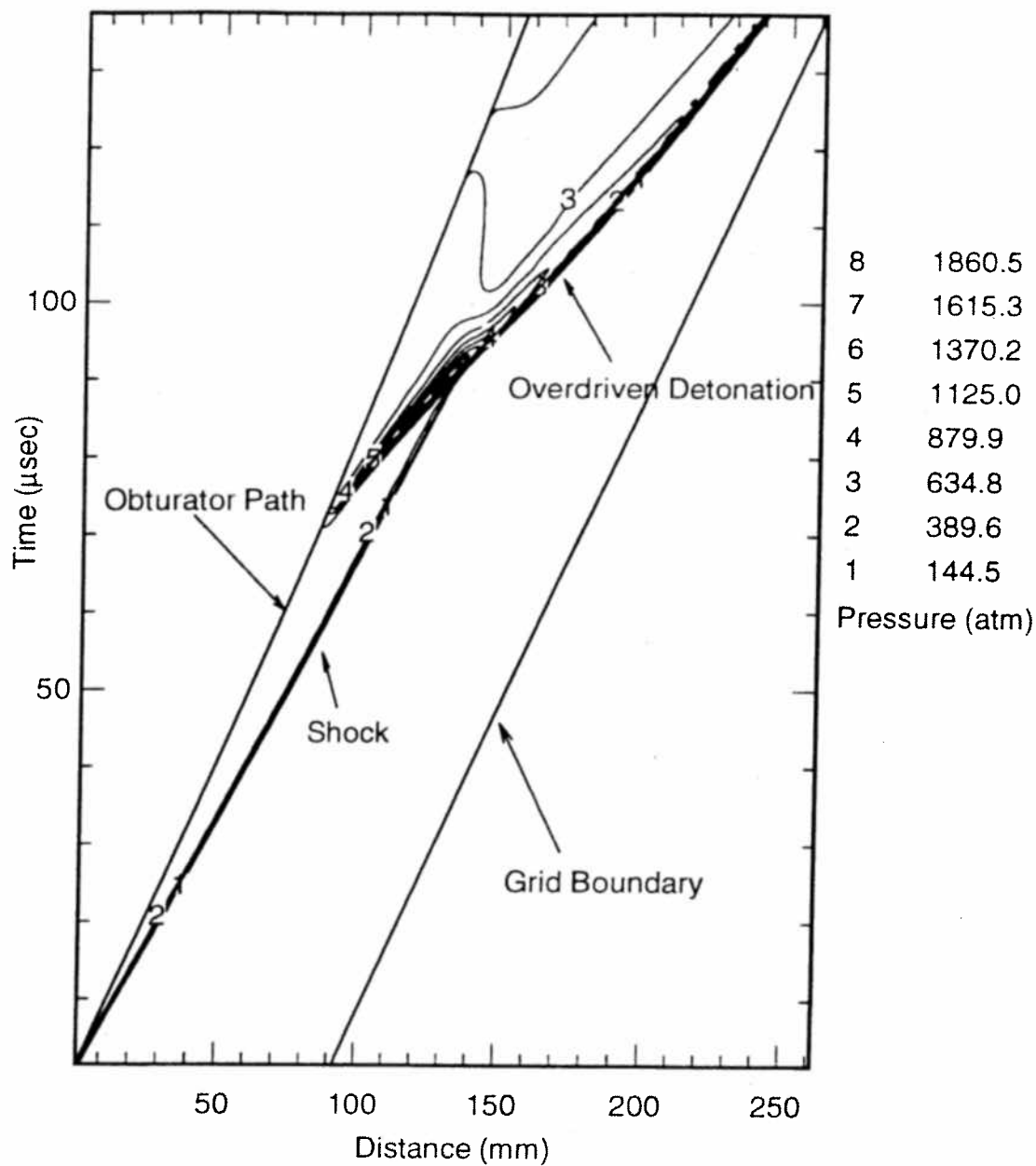


Fig. 5.11 Simulated impact of a 35 gm solid obturator traveling 1250 m/s with a 23 atm stationary mixture of $2.7\text{CH}_4+2\text{O}_2+5.8\text{N}_2$.

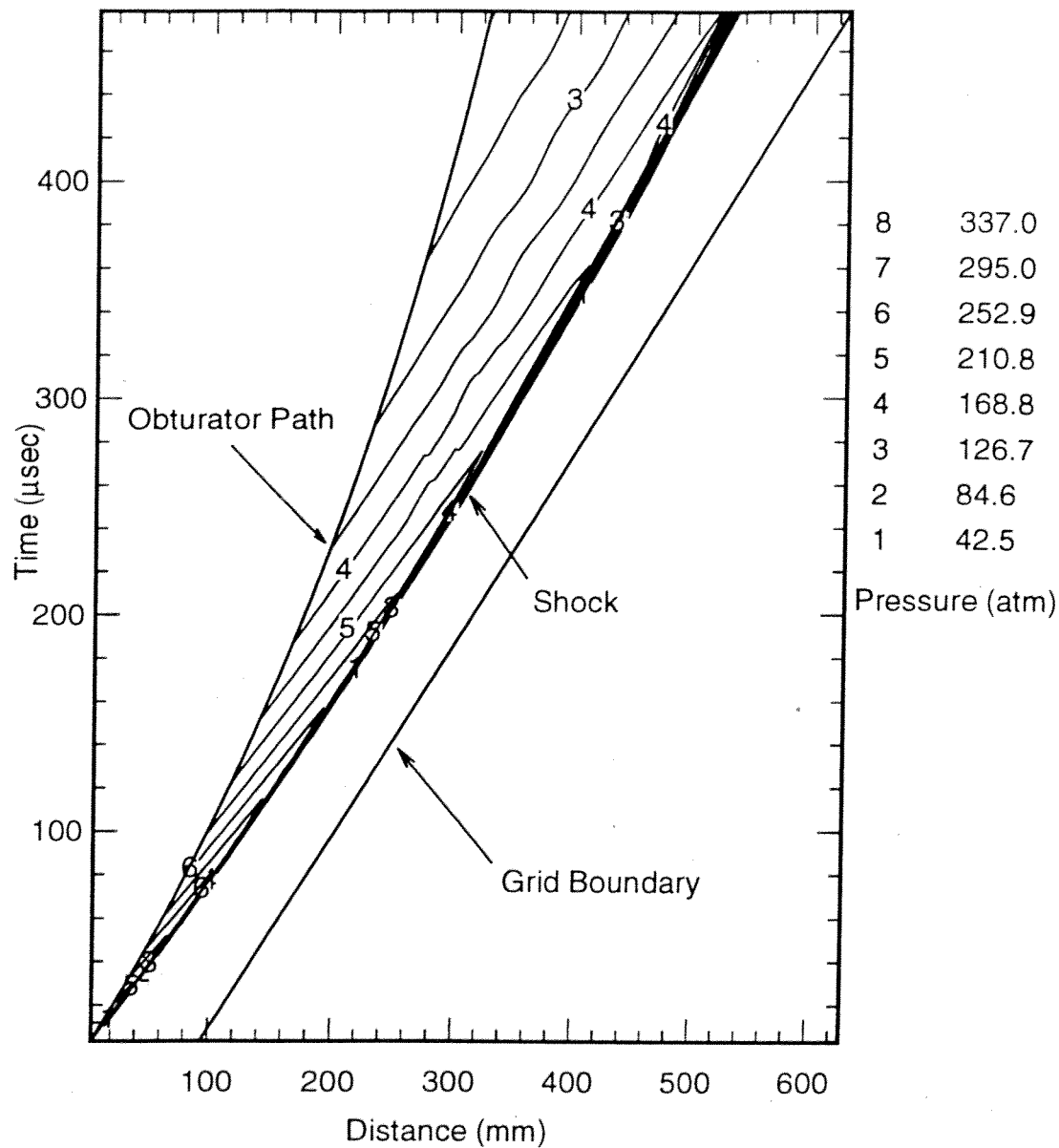


Fig. 5.12 Simulated impact of a 13 gm solid obturator traveling 1125 m/s with a 23 atm stationary mixture of $2.7\text{CH}_4+2\text{O}_2+5.8\text{N}_2$.

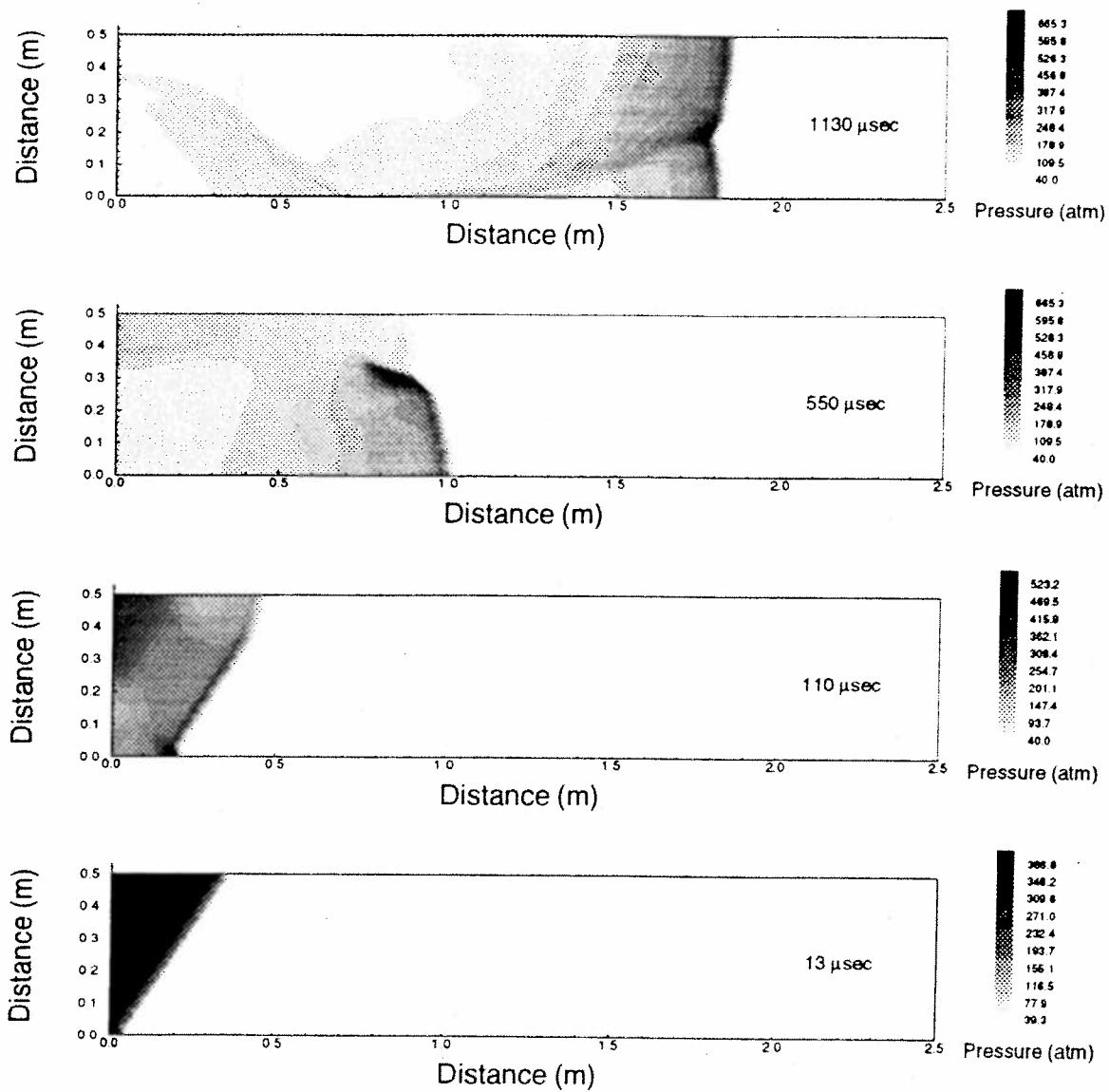


Fig. 5.13 Simulated initiation of a 2-dimensional detonation in a 20 atm mixture of $2.7\text{CH}_4+2\text{O}_2+5.8\text{N}_2$.

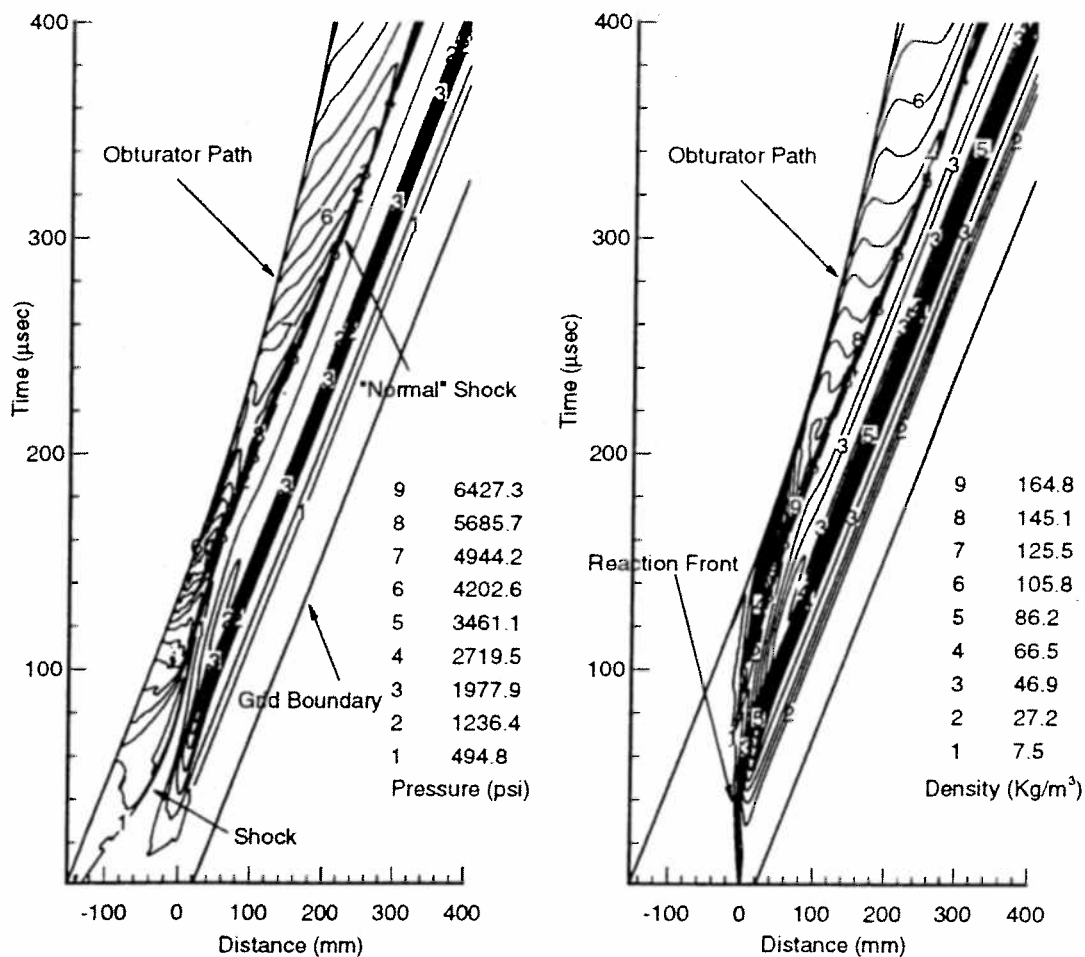


Fig. 5.14 Simulated pressure and density contours for a projectile entering a 23 atm mixture of $2.7\text{CH}_4+2\text{O}_2+5.8\text{N}_2$ from a launch tube initially at 0.1 psi with 1/1000 obturator leakage area.

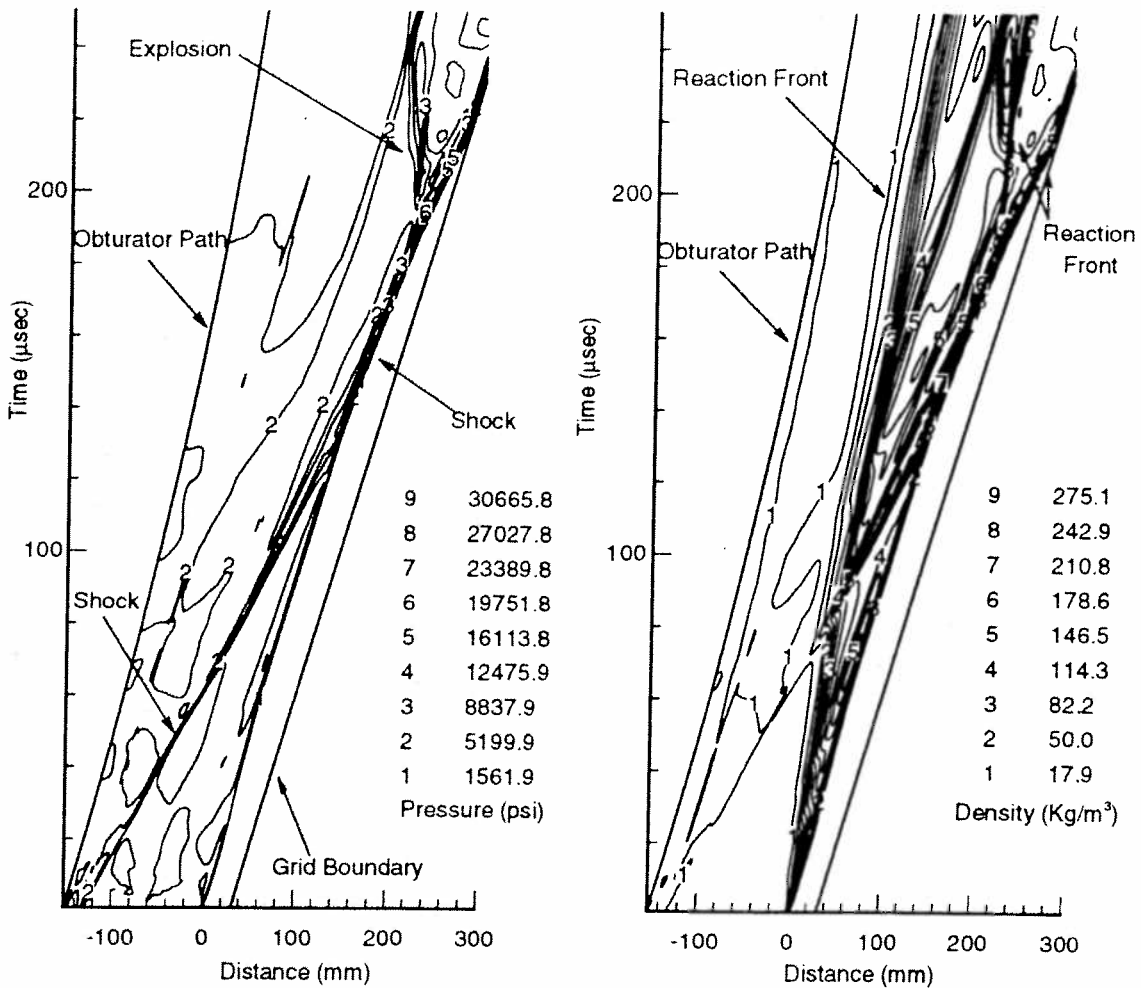


Fig. 5.15 Simulated pressure and density contours for a projectile entering a 23 atm mixture of $2.7\text{CH}_4+2\text{O}_2+5.8\text{N}_2$ from a launch tube initially at 1.0 psi with 1/100 obturator leakage area.

VI. CONCLUSION

The starting transients of the thermally choked ram accelerator and associated phenomena have been discussed. The response of recessed pressure transducers to a normal shock was shown to cause an overshoot in the measured pressure while luminosity sensor responses have been shown to respond to light reflections down the length of the tube. At high pressures the combustible gas mixture was shown to propagate a marginal single headed spinning detonation. Induction and reaction times were measured in the high pressure methane rich mixture by the use of spinning and overdriven detonations. Interpretation of pressure and luminosity sensor responses caused by the 3-dimensional character of the flow around the projectile were also discussed.

Starting the diffuser with low initial launch tube pressure and minimal obturator leakage can be accomplished at any Mach number above the Kantrowitz Mach number. For increased margins of heat release and obturator mass, the starting Mach number is typically higher than the minimum given by the Kantrowitz Mach number. Ignition of a combustible mixture can be accomplished with either a perforated or solid obturator. The solid obturator is stronger and simpler to use while the perforated obturator is more forgiving to variations in starting parameters.

Starting with elevated initial launch tube pressure is possible, but more difficult than with low initial launch tube pressure. Starting with substantial obturator leakage is difficult due to the high pressure obtained prior to entering the combustible gas mixture. Premature bursting of the entrance diaphragm is aggravated by elevated launch tube pressure and blow-by, but is not necessarily detrimental. Stronger entrance diaphragms can reduce the chance of early bursting, but for some cases cannot prevent it. The premature failure of the entrance diaphragm alone does not prohibit the starting of a ram accelerator projectile. Conditions that will prevent starting of the ram

accelerator include if the relative Mach number of the projectile to the accelerator gas is low enough that the diffuser cannot be started, if there is large scale combustion in front of the projectile, if the conditions on and behind the projectile produce an unstart once in the combustible gas mixture, and if ignition or stable combustion cannot be obtained.

The source of ignition was found to be the launch tube gas that was compressed by multiple shock reflections prior to entrance to the accelerator section. An inert buffer section which separated the launch tube gas from the combustible accelerator gas prevented ignition. Extremely low initial launch tube pressure combined with no obturator blow-by also inhibited ignition and prevented combustion from stabilizing at the base of the projectile.

Numerical simulations using Van Leer and AUSM differencing with an induction/reaction chemistry model show good agreement with experimental results. Simulations of the projectile accelerating in the launch tube provide good agreement with experimental results when helium leakage, the projectile geometry and the correct initial launch tube pressure are used. Numerically modeled transitions from the launch tube gas to the accelerator gas correctly predict conditions that result in successful and unsuccessful starting of the projectile.

Information obtained from the hot and cold starting experiments provides important understanding for proper design of new ram accelerator facilities. Special design requirements are needed when using high launch tube pressures or when significant blow-by is anticipated. Knowledge obtained from these starting experiments not only enhance understanding of the ram accelerator, but provide an excellent data base for the evaluation of unsteady, chemically reacting CFD codes.

REFERENCES

1. Hertzberg, A., Bruckner A.P., and Bogdanoff, D.W., "Ram Accelerator: A New Chemical Method for Accelerating Projectiles to Ultrahigh Velocities," *AIAA Journal*, Vol. 26, 1988, pp. 195-203.
2. Hertzberg, A., Bruckner, A.P., and Knowlen, C., "Experimental Investigation of Ram Accelerator Propulsion Modes," *Shock Waves*, Vol. 1, 1991, pp. 17-25.
3. Bruckner, A.P., Knowlen, C., and Hertzberg, A., "Operational Characteristics of the Thermally Choked Ram Accelerator," *Journal of Propulsion and Power*, Vol. 7, 1991, pp. 828-836.
4. Kruczynski, D. L., "Experimental Demonstration of a 120-mm Ram Accelerator," 29th JANNAF Combustion Subcommittee Meeting, Langley Research Center, Hampton, Virginia, October 19-23, 1992.
5. Sinha, N., Dash, S., Drabczuk, R., and Rolader, G., "Progress Toward the Development of Transient RAM Accelerator Simulation and Overview of the U.S. Air Force Armament Directorate Research Program," AIAA Paper 92-3248, AIAA/SAE/ASME/ASEE 28th Joint Propulsion Conference, Nashville, Tennessee, July 6-8, 1992.
6. Giraud, M., Legendre, J.F., Simon, G., and Catoire, L., "Ram Accelerator in 90 mm Caliber. First Results Concerning the Scale Effect in the Thermally Choked Propulsion Mode," 13th International Symposium on Ballistics, Stockholm Sweden, June 1-3, 1992.
7. Srulijes, J., Smeets, G., and Seiler, F., "Expansion Tube Experiments for the Investigation of Ram Accelerator Related Combustion and Gasdynamic Problems," AIAA Paper 92-3246, AIAA/SAE/ASME/ASEE 28th Joint Propulsion Conference, Nashville, Tennessee, July 6-8, 1992.
8. Li, C., Landsberg, A.M., Kailasanath, K., Oran, E.S., and Boris, J.P., "Numerical Simulations of Reactive Flows in Ram Accelerators," 29th JANNAF Combustion Subcommittee Meeting, Langley Research Center, Hampton, Virginia, October 19-23, 1992.
9. Thornhill, L., Scanlon, J., Batteh, J., and Rolader, G., "Performance Modeling of the Ram Accelerator," Science Applications International Corporation, Marietta GA, 29th JANNAF Combustion Subcommittee Meeting, Langely Research Center, Hampton, Virginia, October 19-23, 1992.

10. Soetrisno, M., Imlay, S.T., "Simulation of the Flow Field of a Ram Accelerator," AIAA Paper 91-1915, AIAA/SAE/ASME/ASEE 27th Joint Propulsion Conference, Sacramento, California June 24-26, 1991.
11. Soetrisno, M., Imlay, S.T., and Roberts, D.W., "Numerical Simulations of the Transdetonative Ram Accelerator Combusting Flow Field on a Parallel Computer," AIAA Paper 92-3249, AIAA/SAE/ASME/ASEE 28th Joint Propulsion Conference, Nashville, Tennessee, July 6-8, 1992.
12. Burnham, E.A., Hinkey, J.B., and Bruckner, A.P., "Investigation of Starting Transients in the Thermally Choked Ram Accelerator," 29th JANNAF Combustion Subcommittee Meeting, Langley Research Center, Hampton, Virginia, October 19-23, 1992.
13. Bruckner, A.P., Burnham, E.A., Knowlen, C., Hertzberg, A., and Bogdanoff, D.W., "Initiation of Combustion in the Thermally Choked Ram Accelerator," *Shock Waves*, Vol. 1, edited by K. Takayama, Springer-Verlag, Berlin, 1992, pp. 623-630.
14. Burnham, E.A., "Experimental and Numerical Analysis of the Thermally Choked Ram Accelerator Starting Process," (M.S.A.A thesis, University of Washington), 1989.
15. Hinkey, J.B., Burnham, E.A., and Bruckner A.P., "High Spatial Resolution Measurements of Ram Accelerator Gas Dynamic Phenomena," AIAA Paper 92-3244, AIAA/SAE/ASME/ASEE 28th Joint Propulsion Conference, Nashville, Tennessee, July 6-8, 1992.
16. Hinkey, J.B., Burnham, E.A., and Bruckner A.P., "High Spatial Resolution Measurements in a Single Stage Ram Accelerator," 29th JANNAF Combustion Subcommittee Meeting, Langley Research Center, Hampton, Virginia, October 19-23, 1992.
17. Hinkey, J.B., Burnham, E.A., and Bruckner A.P., "Investigation of Ram Accelerator Flow Fields Induced by Canted Projectiles," AIAA Paper 93-2186, AIAA/SAE/ASME/ASEE 29th Joint Propulsion Conference, Monterey, California, June 28-30, 1993.
18. Knowlen, C., Higgins, A.J., Bruckner, A.P. and Hertzberg, A., "In-Tube Photography of Ram Accelerator Projectile," Proceedings of the 19th International Symposium on Shock Waves, No. 409, 1993.
19. Scott, K.A., "Experimental Investigation of Ram Accelerator Concept Using an Optical Probe," M.S. Thesis, Department of Aeronautics and Astronautics, University of Washington, Seattle, WA, 1988.

20. Prochko, A.E., "Preliminary Spectral Analysis of the Ram Accelerator," M.S. Thesis, Department of Aeronautics and Astronautics, University of Washington, Seattle, WA, 1991.
21. Higgins, A.J., "Gas Dynamic Limits of the Ram Accelerator," M.S. Thesis, Department of Aeronautics and Astronautics, University of Washington, Seattle, WA, 1993.
22. Nettleton, M.A., *Gaseous Detonations: Their Nature, Effects and Control*, Chapman and Hall, New York, 1987.
23. Fickett, W. and Davis, W.C., *Detonation*, University of California Press, Berkeley, 1979.
24. Borisso, A.A. (Ed.), *Dynamic Structure of Detonation in Gaseous and Dispersed Media*, Kluwer Academic Publishers, Norwell, MA, 1991.
25. Grossman, B. and Cinnella, P., "The Computation of Non-Equilibrium, Chemically-Reacting Flows," *Computers and Structures*, Vol. 30, 1988, pp. 79-93.
26. Korobeinikov, V.P., Levin, V.A., Markov, V.V., and Chernyi, G.G., "Propagation of Blast Waves in a Combustible Gas," *Astronautica Acta*, Vol. 17, 1972, pp.529-537.
27. Korobeinikov, V.P., "The Problem of Point Explosion in a Detonation Gas," *Astronautica Acta*, Vol. 14, 1969, pp. 411-419.
28. Oran, E.S., Boris, J.P., Young, T., Flanigan, M., Burks, T., and Picone, M., "Numerical Simulations of Detonations in Hydrogen-Air and Methane-Air Mixtures," Eighteenth Symposium (International) on Combustion, The Combustion Institute, 1981.
29. Sloane, T.M., "Numerical Simulation of Electric Spark Ignition in Atmospheric Pressure Methane-Air Mixtures," *Combustion Science and Technology*, Vol. 73, 1990, pp. 367-381.
30. Sloane, T.M., "Ignition and Flame Propagation Modeling With an Improved Methane Oxidation Mechanism," *Combustion Science and Technology*, Vol. 63, 1989, 287-313.
31. Pratt, D.T., private communication, 1993
32. Forsythe, G.E., Malcom, M.A. and Moler, C.B., *Computer Methods for Mathematical Computations*, Englewood Cliffs, N.J., Prentice-Hall, 1977.

33. Hindman, R.G., "Generalized Coordinate Forms of Governing Fluid Equations and Associated Geometrically Induced Errors," *AIAA Journal*, Vol. 20, 1982, pp. 1359-1367.
34. Thomas, P.D. and Lombard, C.K., "Geometric Conservation Law and Its Application to Flow Computations on Moving Grids," *AIAA Journal*, Vol. 17, October 1979, pp. 1030-1037.
35. Weber, K.F., Thoe, D.W., and Delaney, R.A., "Analysis of Three-Dimensional Turbomachinery Flows on C-Type Grids Using an Implicit Euler Solver," *Journal of Turbomachinery*, Vol. 112, July 1990, pp. 362-369.
36. Anderson, W.K., Thomas, J.L., and Van Leer, B., "Comparison of Finite Volume Flux Vector Splittings for the Euler Equations," *AIAA Journal*, Vol. 24, September 1986, pp. 1453-1460.
37. Pulliam, T.H., "Artificial Dissipation Models for the Euler Equations," *AIAA Journal*, Vol. 24, December 1986, pp. 1931-1940.
38. Grossman, B. and Walters, R.W., "Flux-Split Algorithms for the Multi-Dimensional Euler Equations with Real Gases," *Computers & Fluids*, Vol. 17, 1989, pp. 99-112.
39. Liou, M.-S., "An Extended Lagrangian Method," AIAA Paper 93-3305-CP, 1993.
40. Liou, M.-S., "On a New Class of Flux Splittings," *Lecture Notes in Physics* 414, Springer Verlag, 1993, pp. 115-119.
41. Liou, M.-S., "A New Flux Splitting Scheme," NASA TM 104404, 1991.
42. Welch, G.E. and Chima, R.V., "Two-Dimensional CFD Modeling of Wave Rotor Flow Dynamics," AIAA Paper 93-3318-CP, 1993.
43. Coirier, W.J. and Van Leer, B., "Numerical Flux Formulas for the Euler and Navier-Stokes Equations: II. Progress in Flux-Vector Splitting," AIAA 10th Computational Fluid Dynamics Conference, Honolulu, HI, June 24-27, 1991.
44. Lehr, H.F., "Experiments on Shock-Induced Combustion," *Astronautica Acta*, Vol. 17, 1972, pp. 589-597.
45. Wilson, G.J., "Computation of Steady and Unsteady Shock-Induced Combustion Over Hypervelocity Blunt Bodies," Ph.D. Thesis,

Department of Aeronautics and Astronautics, Stanford University, Palo Alto, CA, 1991.

46. Wilson, G.J. and Sussman, M.A., "Computation of Unsteady Shock-Induced Combustion Using Logarithmic Species Conservation Equations," *AIAA Journal*, Vol 31, February 1993, pp. 294-301.
47. Matsuo, A. and Fujiwara, T., "Numerical Simulation of Shock-Induced Combustion around an Axisymmetric Blunt Body," AIAA Paper 91-1414, AIAA 26th Thermophysics Conference, Honolulu, Hawaii, June 24-26, 1991.
48. Ghorbanian, K., "Superdetonative Flow of Gaseous Propellant Mixtures over Sphere-Cone Bodies," Ph.D. Thesis, Department of Mechanical Engineering, University of Washington, Seattle, WA, 1993.
49. Frendi, A. and Sibulkin, M., "Dependence of Minimum Ignition Energy on Ignition Parameters," *Combustion Science and Technology*, Vol. 73, 1990, pp. 395-413.
50. Sloane, T.M., "Energy Requirements for Spherical Ignitions in Methane-Air Mixtures at Different Equivalence Ratios," *Combustion Science and Technology*, Vol. 73, 1990, pp. 351-365.
51. Peraldi, O., Knystautas, R., and Lee, J.H., "Criteria for Transition to Detonation in Tubes," Twenty-first Symposium (International) on Combustion, The Combustion Institute, 1986.
52. Lee, J.H.S., "Dynamic Parameters of Gaseous Detonations," *Annual Review of Fluid Mechanics*, Vol. 16, 1984, pp. 311-336.
53. Kailasanth, K., Oran, E.S., Boris, J.P. and Young, T.R., "Determination of Detonation Cell Size and the Role of Transverse Waves in Two-Dimensional Detonations," *Combustion and Flame*, Vol. 61, 1985, pp.199-209.
54. Taki, S., and Fujiwara, T., "Numerical Analysis of Two-Dimensional Nonsteady Detonations," *AIAA Journal*, Vol. 16, No. 1, January, 1978.
55. Bauer, P., Presles, H.N., and Dunand, M., "Detonation Characteristics of Gaseous Methane-Oxygen-Nitrogen Mixtures at Extremely Elevated Initial Pressures," in Kuhl, A.L., Leyer, J.-C., Borisov, A.A., Sirignano, W.A. (Eds), *Dynamics of Detonations and Explosions: Detonations*, Vol 133, Progress in Astronautics and Aeronautics, AIAA, Washington, D.C., 1991.

56. Bauer, P.A., Giraud, M., Legendre, J.-F., and Catoire, L., "Detonability Limits of Methane-Oxygen Mixtures at Elevated Initial Pressures," 18th International Pyrotechnics Seminar, Breckenridge, Co, July 13-17, 1992.
57. Heuze, O., Bauer, P., and Presles, H.-N., "Compressibility and Thermal Properties of Gaseous Mixtures at High Temperatures and High Pressures," *High Temperatures-High Pressures*, Vol. 19, 1987, pp. 611-620.

Biographical Note

Edward A. Burnham, Jr. was born July 3, 1964 in Missoula, MT. After graduating from Plains Public High School in 1982, he attended Montana State University for 4 quarters. He then transferred to the University of Washington where he received a Bachelor of Science Degree in Aeronautics and Astronautics in December of 1986. In graduate school at the University of Washington, he worked as a research assistant on the ram accelerator. He performed both experimental and theoretical work and received his Masters of Science in Aeronautics and Astronautics in August of 1989. He spent the remainder of his graduate career characterizing the different regimes of ram accelerator operation, investigating three dimensional effects, and performing experimental and numerical studies of the ram accelerator starting process.